

University of Nottingham

**PHD THESIS**

**THE EFFECT OF HETEROGENEITY IN  
SEDIMENTARY PROPERTIES ON FLUID FLOW  
BEHAVIOUR AT THE PORE-SCALE**

by

**Student Name: Freya Jones**

Student ID: 4295114

27.08.2021

Supervisors: Veerle Vandeginste, David Hargreaves,  
Bagus Muljadi

Programme: PhD

## Abstract

Sandstone reservoir rocks are important for numerous applications, such as oil and gas recovery, CO<sub>2</sub> storage and groundwater aquifers, and understanding how reservoir rock properties influence the dynamics of fluids and gases within reservoir rocks is essential yet difficult to predict. Heterogeneity complicates the identification of viable areas of recovery, potential areas of migration and groundwater catchment planning. To improve accuracy in reservoir flow models further analysis of the impact of heterogeneous reservoir rock properties on fluid transport is required. Pore network analysis is key in understanding fundamental concepts of fluid flow behaviour as pore network geometry is a dominant control on the effectiveness of fluid transport within a reservoir and is strongly associated with porosity and permeability. Despite this, there has been limited research into how heterogeneous rock properties influence fluid flow behaviour at the pore scale and analysis is commonly focused on samples which have homogeneous grain size and mineralogy.

Heterogeneity in sandstone reservoir rocks can be categorised into three main types; 1) sedimentary, 2) structural, and 3) diagenetic. This thesis focuses on sedimentary heterogeneities, which are influenced by the environmental conditions at the time of sediment deposition, and the main aim of this thesis is to quantify the effect of heterogeneity in grain size and mineralogy on pore network geometry (pore diameter, porosity), fluid flow behaviour and mineral dissolution in the pore network. Ten synthetic, glass bead pack samples were designed based on naturally occurring sedimentary heterogeneities identified in cores from the Triassic Sherwood Sandstone and the Permian Rotliegend Group and used in pore-scale permeability experiments which validate the results from 3D visual analysis and simulations conducted in the Avizo®Fire software and CFD simulations conducted in the ANSYS Fluent software.

The experimental methodology for the pore-scale permeability experiments was designed and developed to enable reliable and accurate measurements of flow rate and pressure difference over a 3D customised bead pack sample. In order to achieve this, two degassing techniques were employed to fully purge trapped bubbles of air which occurred in the system/sample. The experiments produce reliable and repeatable data which are in agreement with results from the literature and permeability calculated using the Kozeny-Carman model, Avizo®Fire simulations and ANSYS Fluent CFD simulations.

The results from the experiments and simulations confirm the widely held view that bead size and heterogeneity in bead size influences the pore network geometry, fluid flow behaviour and permeability of a sample. In samples with homogeneous bead size, increasing bead size (54.5%) corresponds to larger mean pore diameter size (35.2%), a larger range in mean pore diameter size, less uniform distribution in pore diameter size, and greater porosity (0.74-3.47%). Less uniformity in pore diameter size increases tortuosity (2.65%) and facilitates high velocity preferential pathways which increases permeability (52.2-98.5% across all homogeneous samples and techniques).

The effect of bead size heterogeneity is determined by the arrangement of the bead size (e.g. smaller beads changing to larger beads) and the mean pore diameter size and range of mean pore diameter size is lower (7.7%) and the distribution of pore diameter size is more uniform when smaller beads transition to larger beads. This is due to the reduction in pore space due to a poorer degree of sorting and increased packing density as smaller beads are able to invade the pore space between the larger beads. Greater uniformity in pore diameter size results in more consistent fluid flow (multiple, well distributed, smaller, low velocity flow pathways) and higher permeability (0.60-55.9% across all techniques) when fluid flow passes a transition from smaller beads to larger beads.

The onset of non-Darcy flow was analysed in the samples with differing homogeneous bead size and heterogeneous bead size and the results suggest that the critical Reynold's number (the Reynold's number which corresponds with the onset of non-Darcy flow) is determined by pore size and greater pore size corresponds to a larger critical Reynold's number due to larger pores being more able to facilitate high velocity flow. In the samples with heterogeneous bead size different factors influence the critical Reynold's number and the critical Reynold's number decreases with decreasing tortuosity when fluid flow passes a transition from smaller beads to larger beads and the critical Reynold's number decreases due to increasing heterogeneity and decreasing permeability when flow crosses a transition from larger beads to smaller beads. The beta factor was also calculated and increases with decreasing bead size and the results from the samples with homogeneous bead size suggest that beta factor increases with decreasing permeability.

The results from samples which present mineralogical heterogeneity show that the addition of kaolinite and dolomite reduces the mean pore diameter size (56.8-68.0%), the range of mean pore diameter size and the porosity (2.2-3.8%). Kaolinite results in a greater reduction in mean pore diameter size (68.0%) and increases the range of mean pore diameter size and this is due to the size and distribution of kaolinite which is more randomly distributed throughout the sample due to its greater range in particle size (0-63  $\mu\text{m}$ ). The impact of kaolinite is reduced when it occurs with dolomite as dolomite content restricts the distribution of kaolinite and this is due to the shape and size of the dolomite grains. Angular grains of dolomite occupy pore cavities and wedge alongside beads which is more destructive to porosity and limits accumulations of kaolinite to fewer pores.

Increased variation in pore diameter size is related to increased tortuosity and longer fluid flow pathways which increases access to reactive minerals and increases dissolution. Kaolinite content is most destructive to permeability (73.4-88.0%), in comparison to dolomite content, as it increases heterogeneity in pore diameter size and reduces pore space the most. The impact of kaolinite on permeability is less severe when kaolinite occurs with dolomite as dolomite limits the random distribution of kaolinite throughout the pore network which limits heterogeneity.

The permeability of the samples which contain dolomite was reduced after acidic flow despite evidence of mineral dissolution and this is interpreted to occur as a result of small particles becoming detached during dissolution and becoming lodged in pores and pore throats. Heterogeneity in bead size and mineralogy decreases the mean pore diameter size (31.6-65.4%) and porosity (3.7-5.7%), increases the range in mean pore diameter (20.3-26.0%) and reduces permeability (75.7%), in comparison to the bead pack samples which present mineralogical heterogeneity.

The bead pack sample which presents heterogeneity in bead size and mineralogy displays comparable pore diameter, porosity and permeability results to the crushed rock sample which indicates that bead pack samples can present realistic pore network geometries. Dolomite dissolution increases (1.4-2.4%) when bead size is heterogeneous and permeability is reduced (76.6%) after acidic flow and the reduction in permeability is greater (44.1%) when heterogeneous bead size and mineralogy occur in a sample together and this is due to local variations in permeability which in turn can result in local fluctuations in reaction rates and mineral dissolution. Local fluctuations in reaction rates and dissolution may enhance the variations in permeability after acidic flow or create a series of permeability contrasts where regions of higher permeability enable a higher rate of reactions and dissolution and the regions of low permeability are less able to facilitate fluid and particle transport meaning that the pore space becomes clogged more easily which reduces permeability further.

## Acknowledgements

I would like to express my greatest thanks and appreciation to Dr Veerle Vandeginste for the continued support and encouragement throughout the entirety of the PhD. The support and guidance from Dr David Hargreaves has been invaluable and key in introducing CFD analysis into the project. I would also like to thank Dr Bagus Muljadi for his input on fluid flow regimes in porous media and Professor Matthew Hall for providing me with this opportunity.

Special thanks to Mark Guyler who was a great help with the experimental set up and to Dr Jacob Uguna who was also of technical assistance.

I would also like to thank my industrial sponsor BP as without them this project would have not been possible and my industrial supervisor Dr Tony Espie whose contributions to the project have been greatly appreciated.

Lastly, I would like to show my appreciation and gratitude to Max, my family and my friends for the unlimited support throughout my education.

# Contents

|          |   |           |
|----------|---|-----------|
| <b>1</b> | <b>Introduction</b>   | <b>1</b>  |
| 1.1      | General Introduction . . . . .  | 1         |
| 1.2      | Background Research . . . . .   | 2         |
| 1.2.1    | The impact of sedimentary rock properties on fluid flow behaviour . . . . . | 2         |
| 1.2.2    | Heterogeneity in sandstone reservoir rocks . . . . .                        | 2         |
| 1.2.3    | Heterogeneity in the pore network . . . . .                                 | 3         |
| 1.2.4    | Geological Background . . . . .   | 3         |
| 1.2.5    | Triassic Sherwood Sandstone Group . . . . .                                 | 4         |
| 1.2.6    | Permian Rotliegend Group . . . . .  | 5         |
| 1.3      | Aims and Objectives . . . . .   | 5         |
| 1.3.1    | Structure of the Thesis . . . . .   | 6         |
| <b>2</b> | <b>Literature Review</b>  | <b>7</b>  |
| 2.1      | Introduction . . . . .  | 7         |
| 2.2      | Properties of Pore Networks in Sandstones . . . . .                         | 7         |
| 2.2.1    | Pore Properties . . . . .   | 8         |
| 2.2.2    | Pore Throat Properties . . . . .  | 8         |
| 2.2.3    | Heterogeneity in pore network properties . . . . .                          | 9         |
| 2.3      | Controls on Pore Network Properties in Sandstones . . . . .                 | 10        |
| 2.3.1    | Depositional Controls on the Pore Network . . . . .                         | 10        |
| 2.3.2    | Diagenetic Controls on the Pore Network . . . . .                           | 13        |
| 2.3.3    | Structural Controls on the Pore Network . . . . .                           | 14        |
| 2.4      | Fluid Flow Behaviour in the Pore Network . . . . .                          | 17        |
| 2.4.1    | Fluid Phase . . . . .   | 17        |
| 2.4.2    | Fluid Flow Regime . . . . .   | 19        |
| 2.4.3    | Fluid Flow Pathways . . . . .   | 22        |
| 2.4.4    | Pore Filling and Fluid Trapping in the Pore Network . . . . .               | 22        |
| 2.4.5    | Fluid Displacement in the Pore Network . . . . .                            | 23        |
| 2.5      | Controls on Fluid Flow Behaviour in the Pore Network . . . . .              | 25        |
| 2.5.1    | Wettability . . . . .   | 25        |
| 2.5.2    | Fluid Chemistry . . . . .   | 26        |
| 2.5.3    | Fluid Viscosity . . . . .   | 28        |
| 2.5.4    | Pressure in the Pore Network . . . . .                                      | 28        |
| 2.6      | Computational Modelling of Fluid Flow in the Pore Network . . . . .         | 29        |
| 2.7      | Pore-Scale Experiments . . . . .  | 31        |
| <b>3</b> | <b>Materials and Methodology</b>  | <b>34</b> |

|          |   |            |
|----------|---|------------|
| 3.1      | Core Characterisation   | 34         |
| 3.1.1    | Core and Thin Section Sample Analysis   | 34         |
| 3.1.2    | Powder X-ray Diffraction (PXRD)   | 35         |
| 3.1.3    | Mercury Intrusion Porosimetry (MIP)   | 36         |
| 3.2      | Synthetic 3D Bead Pack Design and Analysis  | 36         |
| 3.2.1    | Synthetic 3D Bead Pack Construction   | 38         |
| 3.2.2    | Synthetic 3D Bead Pack Analysis   | 38         |
| 3.3      | Pore-Scale Permeability Experiments   | 39         |
| 3.4      | Inductively Coupled Plasma - Optical Emission Spectrometry (ICP-OES)                                      | 39         |
| 3.5      | Avizo® Fire Image Processing and Permeability Simulations   | 41         |
| 3.6      | ANSYS Fluent Simulations  | 42         |
| <b>4</b> | <b>Design and Development of Pore-Scale Permeability Experiments</b>                                      | <b>44</b>  |
| 4.1      | Introduction  | 44         |
| 4.2      | Experimental Design and Development   | 45         |
| 4.3      | System Performance  | 46         |
| 4.4      | Results   | 48         |
| 4.4.1    | Results from the Pore-Scale Permeability Experiments  | 48         |
| 4.4.2    | Results of Permeability using the Kozeny-Carman Model   | 48         |
| 4.5      | Discussion  | 49         |
| 4.5.1    | Evaluation of the Sample Type and Experimental Methodology  | 49         |
| 4.5.2    | Evaluation of the Results   | 53         |
| 4.5.3    | Applicability of the experimental system  | 54         |
| 4.6      | Conclusions   | 56         |
| <b>5</b> | <b>Grain Size Heterogeneity</b>   | <b>58</b>  |
| 5.1      | Introduction  | 58         |
| 5.2      | Results   | 59         |
| 5.2.1    | Core Sample Characterisation  | 59         |
| 5.2.2    | Bead Pack Sample Characterisation   | 62         |
| 5.2.3    | Permeability  | 68         |
| 5.2.4    | Flow Regime and Reynold's Number  | 75         |
| 5.2.5    | Tortuosity and Fluid Flow Pathways  | 78         |
| 5.3      | Discussion  | 84         |
| 5.3.1    | How does heterogeneous bead size alter the pore network geometry?   | 84         |
| 5.3.2    | How does the pore network geometry influence tortuosity and flow pathways?                                | 97         |
| 5.3.3    | How does the pore network geometry, tortuosity and fluid flow pathways control pore scale flow phenomena? | 100        |
| 5.4      | Conclusions   | 104        |
| <b>6</b> | <b>Mineralogical Heterogeneity</b>  | <b>106</b> |
| 6.1      | Introduction  | 106        |
| 6.2      | Results   | 107        |
| 6.2.1    | Core Characterisation   | 107        |
| 6.2.2    | Bead Pack Characterisation  | 108        |
| 6.2.3    | Permeability  | 113        |
| 6.2.4    | Fluid Chemistry Analysis  | 118        |
| 6.3      | Discussion  | 119        |

|          |   |            |
|----------|---|------------|
| 6.3.1    | How does heterogeneous mineralogy impact the pore network geometry? . . .                                 | 119        |
| 6.3.2    | How does heterogeneous mineralogy impact mineral dissolution at the pore scale? . . . . .                 | 120        |
| 6.3.3    | How does heterogeneous mineralogy impact permeability and transport phenomena? . . . . .                  | 121        |
| 6.4      | Conclusions . . . . .   | 124        |
| <b>7</b> | <b>Grain Size and Mineralogical Heterogeneity</b>   | <b>126</b> |
| 7.1      | Introduction . . . . .  | 126        |
| 7.2      | Results . . . . .   | 126        |
| 7.2.1    | Core Characterisation . . . . .   | 127        |
| 7.2.2    | Bead Pack Characterisation . . . . .  | 127        |
| 7.2.3    | Permeability . . . . .  | 130        |
| 7.2.4    | Fluid Chemistry Analysis . . . . .  | 133        |
| 7.3      | Discussion . . . . .  | 133        |
| 7.3.1    | How does heterogeneous grain size and mineralogy influence pore network geometry? . . . . .               | 133        |
| 7.3.2    | How does heterogeneous mineralogy and grain size control mineral dissolution at the pore scale? . . . . . | 134        |
| 7.3.3    | How does heterogeneous mineralogy and grain size affect permeability and fluid flow behaviour? . . . . .  | 135        |
| 7.4      | Conclusions . . . . .   | 138        |
| <b>8</b> | <b>Conclusions</b>  | <b>139</b> |
| 8.1      | Future Work . . . . .   | 141        |
| <b>A</b> | <b>Results from the Pore-Scale Permeability Experiments</b>   | <b>179</b> |
| <b>B</b> | <b>Avizo Fire Simulation Inputs</b>   | <b>185</b> |
| <b>C</b> | <b>CFD Results</b>  | <b>187</b> |

# List of Figures

|     |  |    |
|-----|--|----|
| 1.1 | Examples of heterogeneity in sandstone reservoir rocks. . . . .  | 3  |
| 1.2 | Examples of pore shapes and types. . . . .   | 4  |
| 2.1 | 2D SEM images of some of the types of pores which occur in sandstones; a) intergranular pore, b) dissolved pore in k-feldspar, c) dissolved pore in quartz, d) dissolved pore infilled by clay, e) micro pore in illite, f) micropore in kaolinite. (Taken from Liu et al. (2017)). . . . .  | 8  |
| 2.2 | Examples of the types of pore throats in 2D. . . . .   | 9  |
| 2.3 | Examples of the types of pore throat profiles in 3D; 1) conical, 2) parabolic, 3) hyperbolic, 4) sinusoidal. (Edited from Sochi (2015)). . . . .   | 10 |
| 2.4 | A diagram showing the controls on properties in the pore network. . . . .  | 11 |
| 2.5 | An example of wormholing: Neutron radiographs of different dissolution regimes with different injection regimes. Injection rates increase towards the right. As injection rate increases, wormholing becomes less apparent, and dissolution occurs more uniformly. (Edited from Al-Khulaifi et al. (2017)). . . . .  | 15 |
| 2.6 | Examples of open and filled microfractures (Edited from Perez and Boles (2005)). . .   | 15 |
| 2.7 | Types of deformation bands based on the type of deformation mechanism (Edited from Fossen et al. (2007)). . . . .  | 18 |
| 2.8 | A Forchheimer graph showing the slope used to identify the beta factor (Edited from Muljadi et al. (2016)). . . . .  | 21 |
| 2.9 | The contact angles for various wetting conditions: a) drops of water in oil on a plane, b) drops of oil on a plane, c) water and oil in a capillary tube (Edited from Donaldson and Alam (2008)). . . . .  | 26 |
| 3.1 | Core samples taken from the Rotliegend Group (1-3) and the Sherwood Sandstone Group (4). . . . .   | 35 |
| 3.2 | Thin section image from core sample 3. . . . .   | 35 |
| 3.3 | Schematic of the bead pack samples used in this study. Samples 5 and 6 are meshes used in the CFD simulations in Chapter 5 so the bead pack samples were not numbered consecutively as to avoid confusion. Sample 12 is composed of crushed rock from core sample 3. *Please note: schematic is not to scale, sample dimensions are $1 \times 1 \times 33$ mm. . . . . | 37 |
| 3.4 | Experimental set up for the pore-scale permeability experiments: 1) syringe pump, 2) flow metre, 3) inlet pressure metre, 4) synthetic sample, 5) outlet pressure metre, 6) drain syringe, 7) control box, and, 8) diaphragm vacuum pump. . . . .  | 40 |



|      |   |    |
|------|---|----|
| 3.5  | A schematic of the experimental set up for the pore-scale permeability experiments: 1) syringe pump, 2) flow metre, 3) inlet pressure metre, 4) synthetic sample, 5) outlet pressure metre, 6) drain syringe, 7) control box, and, 8) diaphragm vacuum pump. The blue line represents the route which fluid takes through the experimental system. The green line represents the direction of air when the system is being degassed. The grey line represents electrical connections. . . . . | 40 |
| 3.6  | The $400\ \mu\text{m}^3$ tetrahedral mesh generated in the Avizo®Fire software for sample 1. . . . .  | 42 |
| 4.1  | Unstable pressure results from the original configuration of the experimental system. The inlet pressure continuously increases whereas the outlet pressure does not increase. Additionally, the flow rate also fluctuated consistently. . . . .  | 45 |
| 4.2  | Stabilised pressure results and minimal fluctuation in flow rate after adjustments to the experimental system. Some minor fluctuations are expected in flow rate due to the horizontal movement of the syringe pump. . . . .  | 47 |
| 4.3  | Results from the trial pore-scale permeability experiments. . . . .   | 48 |
| 4.4  | The porosity and Kozeny-Carman permeability throughout the 3D bead pack sample. In the experiments fluid flows horizontally from zone 1 to zone 5. . . . .  | 50 |
| 4.5  | A graph showing the relationship between permeability and particle size. . . . .  | 55 |
| 5.1  | Laminations of finer grained material in core sample 3. . . . .   | 60 |
| 5.2  | Coarser bands of material which has created grain size contrasts in core sample 1. The coarser bands of material are highlighted by the dashed lines. . . . .   | 61 |
| 5.3  | Laminations in core samples 1 and 3 at the thin section scale; A shows the contrast between the overall grain size and a lamination of coarser grains in core sample 1 and B shows the contrast between the overall grain size and a lamination of finer grains in core sample 3. . . . .   | 61 |
| 5.4  | The difference in pore space (blue) between core sample 2 (A) and 4 (B). . . . .  | 62 |
| 5.5  | The range in pore diameter values for each sample. . . . .  | 64 |
| 5.6  | A log presenting the pore network properties of the bead pack samples and how they vary throughout the five zones of the sample. The properties were measured across a $1 \times 1 \times 7$ mm scanned section of the bead pack samples and the porosity used in the log is the porosity measured in the Avizo®Fire software. Fluid flows in the $z$ direction from zone 1 to zone 5. . . . .  | 65 |
| 5.7  | The central section (zone 3) of the four bead pack samples. The 3D image of each sample was taken in the Avizo®Fire software and is a 3D render of the image stack from the XCT scan. . . . .   | 67 |
| 5.8  | An example of smaller beads wedged between larger beads (panel on the left) and an example of a smaller bead infilling the pore space between larger beads (panel on the right). . . . .  | 67 |
| 5.9  | The boundary between larger beads and smaller beads in sample 3 (panel on the left) and an example of smaller beads infilling the pore space between larger beads in sample 3 (panel on the right). . . . .   | 67 |
| 5.10 | The results from the pore-scale permeability experiments for each sample. . . . .   | 69 |

|      |  |    |
|------|--|----|
| 5.11 | The permeability results from the Avizo Fire permeability simulations plotted against porosity (top panel) and pore diameter (bottom panel) which show that permeability increases with increasing porosity and mean pore diameter. The results show that mean pore diameter size has a greater impact on permeability than porosity, and this is especially demonstrated by sample 1, which shows a small range in permeability despite a large range in porosity. This may indicate that porosity is not a reliable property to use to predict permeability. . . . . | 72 |
| 5.12 | The pressure values across the tetrahedral meshes of the transitional zones in samples 2 and 3. . . . .  | 74 |
| 5.13 | The permeability across the tetrahedral meshes of the transitional zones in samples 2 and 3. . . . .   | 75 |
| 5.14 | The results from the CFD simulations showing a gradient change in the linear trend line. . . . .   | 76 |
| 5.15 | The permeability results compared to bead size indicating that permeability increases with increasing bead size in the samples. . . . .  | 77 |
| 5.16 | Permeability plotted against Re from the CFD simulations . . . . .   | 79 |
| 5.17 | The mean pore diameter size plotted against the Re at which permeability begins to decrease in the samples. The results show that the permeability begins to decrease at lower Re when pore diameter is smaller. . . . .   | 80 |
| 5.18 | The Forchheimer graphs for each sample showing the inverse relationship between $1/K_{App}$ and $\rho U/\mu$ . . . . .   | 81 |
| 5.19 | $\beta$ compared to bead size showing that $\beta$ decreases with decreasing bead size. . . . .  | 82 |
| 5.20 | Tortuosity values plotted against the bead size from the samples with homogeneous bead size showing that the tortuosity value increases with increasing bead size. . . . .   | 83 |
| 5.21 | Tortuosity values from samples 2 and 3 showing that tortuosity differs between the different zones of the samples with heterogeneous bead size. . . . .  | 84 |
| 5.22 | The pathlines for sample 1. The legend describes the velocity of the pathlines (m/s) and the size of the mesh is $400 \mu\text{m}^3$ . . . . .   | 85 |
| 5.23 | The pathlines for sample 2 zone 2. The legend describes the velocity of the pathlines (m/s) and the size of the mesh is $400 \mu\text{m}^3$ . . . . .  | 86 |
| 5.24 | The pathlines for sample 2 zone 3. The legend describes the velocity of the pathlines (m/s) and the size of the mesh is $400 \mu\text{m}^3$ . . . . .  | 87 |
| 5.25 | The pathlines for sample 2 zone 4. The legend describes the velocity of the pathlines (m/s) and the size of the mesh is $400 \mu\text{m}^3$ . . . . .  | 88 |
| 5.26 | The pathlines for sample 3 zone 2. The legend describes the velocity of the pathlines (m/s) and the size of the mesh is $400 \mu\text{m}^3$ . . . . .  | 89 |
| 5.27 | The pathlines for sample 3 zone 3. The legend describes the velocity of the pathlines (m/s) and the size of the mesh is $400 \mu\text{m}^3$ . . . . .  | 90 |
| 5.28 | The pathlines for sample 3 zone 4. The legend describes the velocity of the pathlines (m/s) and the size of the mesh is $400 \mu\text{m}^3$ . . . . .  | 91 |
| 5.29 | The pathlines for sample 4. The legend describes the velocity of the pathlines (m/s) and the size of the mesh is $400 \mu\text{m}^3$ . . . . .   | 92 |
| 5.30 | The pathlines for sample 5. The legend describes the velocity of the pathlines (m/s) and the size of the mesh is $400 \mu\text{m}^3$ . . . . .   | 93 |
| 5.31 | The pathlines for sample 6 The legend describes the velocity of the pathlines (m/s) and the size of the mesh is $400 \mu\text{m}^3$ . . . . .  | 94 |

|     |  |     |
|-----|--|-----|
| 6.1 | Thin section images under cross polarisation (XPL) showing the mineralogy in the sandstone samples; A: clusters of pore filling dolomite in sample 4 which are recognisable as the pale pink and green grains; B: Muscovite in sample 3 which recognisable as the brightly coloured and sometimes striped grains. The darker grey grains in both images are quartz. . . . .  | 108 |
| 6.2 | PXRD diffraction patterns indicative of quartz, dolomite and chlorite in the sandstone samples. . . . .  | 109 |
| 6.3 | PXRD diffraction patterns from the clay minerals which occur in the four samples. . . . .  | 110 |
| 6.4 | PXRD diffraction patterns from the samples after chlorite was removed. . . . .   | 111 |
| 6.5 | 2D images of the four bead pack samples discussed in this chapter showing the different mineralogical compositions. Sample 7 is composed of 75 $\mu\text{m}$ glass acid washed beads, sample 8 is composed of 75 $\mu\text{m}$ glass acid washed beads and 5% dolomite, sample 9 is composed of 75 $\mu\text{m}$ glass acid washed beads and 5% kaolinite and sample 10 is composed of 75 $\mu\text{m}$ glass acid washed beads, 5% dolomite and 5% kaolinite. Dolomite is identifiable as the white, angular or acicular grains and kaolinite is identifiable as the dark grey pore filling material. Note: the resolution differs across the samples due to the differing particle sizes (dolomite particle size: 63 $\mu\text{m}$ , kaolinite particle size: 0 - 63 $\mu\text{m}$ . The colour of the glass beads also varies due to the varying contrast settings used for each sample and different contrast settings were used to more easily identify the minerals. . . . . | 112 |
| 6.6 | A log presenting the pore network properties of the bead pack samples discussed in this chapter and how they vary throughout the five zones of the samples. The properties were measured across a $1 \times 1 \times 7$ mm scanned section of the samples. Fluid flows from zone 1 to zone 5. . . . .  | 114 |
| 6.7 | Plots of pressure difference against flow rate for the four samples before and after acidic flow. . . . .  | 116 |
| 6.8 | The Re results plotted against the experimental permeability results. . . . .  | 117 |
| 7.1 | Core sample 3 (left) shows high angle cross laminations of silt which present both a change in mineralogy and a change in grain size. Core sample 4 (right) shows significant grain size heterogeneity and shows the addition of detrital clasts which may have contrasting mineralogy and or provenance. . . . .  | 127 |
| 7.2 | The thin section images of core samples 1, 3 and 4; core sample 1 shows grain size heterogeneity and shows a band of finer material; core sample 3 displays heterogeneity in mineralogy (XPL) and grain size (PPL) and shows sporadic dolomite grains/cement and muscovite mica occurring in clusters local to the band of finer material which infills the pore space between larger grains; core sample 4 shows grain size heterogeneity and various areas of pore space which are cemented. . . . .   | 128 |
| 7.3 | The five zones of sample 11 showing the transition from homogeneous bead size (75 $\mu\text{m}$ ) (zones 1-2) to mixed bead size (75-180 $\mu\text{m}$ ), 2 mg of dolomite and 2 mg of kaolinite (zones 3-5). Zone 3 is the transitional zone between the homogeneous bead size and heterogeneous bead size with the addition of dolomite and kaolinite. . . . .   | 129 |
| 7.4 | The three zones analysed in sample 12; zone 1 is composed of 75-180 $\mu\text{m}$ grains, zone 2 is composed of 0-180 $\mu\text{m}$ grains and zone 3 is composed of 0-75 $\mu\text{m}$ grains. . . . .  | 130 |

|     |  |     |
|-----|--|-----|
| 7.5 | A log presenting the pore network properties of the bead pack samples discussed in this chapter and how they vary throughout the different zones of the samples. The properties were measured across a $1 \times 1 \times 7$ mm scanned section of the samples. Fluid flows in the $z$ direction from zones 1 to zone 5 in sample 11 and from zone 1 to zone 3 in sample 12. . . . . | 132 |
| 7.6 | The results from the pore-scale permeability experiments before and after acidic flow.   | 133 |

# List of Tables

|      |  |    |
|------|--|----|
| 2.1  | Experimental studies at the pore scale. . . . .  | 33 |
| 3.1  | A table showing the scan settings for PXRD. . . . .  | 36 |
| 3.2  | A table showing the composition of the samples used in the pore scale permeability experiments. . . . .  | 38 |
| 5.1  | The grain size characteristics of the core samples at the core scale. . . . .  | 60 |
| 5.2  | The grain size characteristics of the core samples at the thin section scale. . . . .  | 60 |
| 5.3  | The porosity and median pore diameter results from the core samples using MIP. . . . .   | 62 |
| 5.4  | The porosity results from the core samples using ImageJ analysis. Porosity 1 corresponds to the porosity of the homogeneous areas of the sample and porosity 2 corresponds to the porosity of the heterogeneous areas of the samples (e.g. within lamination features or after lamination features) Please note: only one porosity value was taken for core sample 4 as it displayed no clear contrasts in grain size, grain shape or grain sorting at thin section. . . . . | 63 |
| 5.5  | The mean pore diameter results from the bead pack samples. . . . .   | 63 |
| 5.6  | The average porosity results from the bead pack samples and meshes of the bead pack samples. . . . .   | 66 |
| 5.7  | The comparable porosity results from the bead pack samples and meshes of the bead pack samples. . . . .  | 66 |
| 5.8  | The experimental permeability results across the four bead pack samples. . . . .   | 68 |
| 5.9  | The average Kozeny-Carman permeability results across the four bead pack samples. Average K1 corresponds to the K-C permeability using the porosity results from Avizo®Fire and average K2 corresponds to the K-C permeability using the porosity results from ANSYS Fluent R2. . . . .  | 70 |
| 5.10 | The Kozeny-Carman permeability results across the different zones of the four bead pack samples. . . . .   | 70 |
| 5.11 | The average absolute permeability results for each bead pack sample. . . . .   | 71 |
| 5.12 | The average permeability results from the CFD simulations conducted at the experimental scale in the Darcy flow regime. . . . .  | 73 |
| 5.13 | The Re at which permeability decreases for each sample. . . . .  | 78 |
| 5.14 | The $\beta$ for each sample. . . . .   | 80 |
| 5.15 | The tortuosity results from the samples. . . . .   | 82 |
| 5.16 | The average flow velocity from the pathline results from the different meshes which have different pressure drops. The different pressure drops are based on the results from the pore-scale permeability experiments. . . . .   | 95 |

|     |  |     |
|-----|--|-----|
| 6.1 | The mean pore diameter and porosity of the bead pack samples. . . . .  | 113 |
| 6.2 | The range of mean pore diameter results across the five zones in the bead pack samples. There is not much variation between the minimum values and the lowest value measured for samples 7 and 8 is 0.00496307 mm and the lowest value measured for samples 9 and 10 is 0.00496286 mm. . . . .   | 115 |
| 6.3 | The results from the pore-scale permeability experiments for the bead pack samples.  | 117 |
| 6.4 | The averaged permeability results from the Avizo Fire simulations. . . . .   | 118 |
| 6.5 | The averaged permeability results compared to the permeability results from the transitional zone (zone 3). . . . .  | 118 |
| 7.1 | The mean pore diameter and porosity results from the samples. The minimum pore diameter for both samples was 0.00496307 mm. The same value for the minimum pore diameter was also observed in the bead pack samples from the previous chapter (Chapter 6) which contained kaolinite. This suggests one of two things; 1) the mineralogical composition determines the minimum pore size in the sample, or, 2) the Avizo Fire software has a limited resolution where pores below 0.00496307 mm are not detectable. The limited resolution could be due to how the image stack was processed and the bead pack samples which contained minerals proved more difficult to convert into binary images due to the different shades of colour each image contained which was due to the different minerals. For example, the glass beads and dolomite are white and the kaolinite is dark grey which makes it difficult to distinguish the kaolinite from the pore space. . . . . | 131 |
| 7.2 | The simulated permeability results from the samples. . . . .   | 131 |
| A.1 | The data collected from the pore-scale permeability experiments. The values displayed are the mean values from a sampled time period after the pressure had stabilised and the period of sampled time differed between the different experiments. Note: Samples 6A, 7A, 8A and 9A correspond to sample results post acidic flow. . . . .   | 180 |
| B.1 | The inputs for the Avizo Fire Absolute Permeability Experimental Simulations for each sample. The inputs were based on the results from the pore-scale permeability experiments. The inputs for sample 12 were based on the results from sample 11 as experiments were not conducted on sample 12 due to experimental limitations. The inputs from sample 11 were used as it is the most similar sample in terms of composition.   | 186 |
| C.1 | The data collected from the CFD simulations. . . . .   | 188 |

# Chapter 1

## Introduction

### 1.1 General Introduction

Sandstone reservoir rocks are important not only for oil and gas recovery, but also for CO<sub>2</sub> storage and groundwater aquifers. In these applications understanding how reservoir rock properties influence the dynamics of fluids and gases hosted in the reservoirs is critical. Currently, the dynamics of fluid and gas behaviour in reservoir rocks is difficult to accurately predict as most reservoir models are based on assumptions and homogeneous rock properties, or very little heterogeneity in rock properties. Heterogeneity in rock properties is defined by a lack of uniformity in the composition and distribution of properties (Liu et al., 2016). Reservoir flow models are essential in identifying and assessing viable areas of recovery, potential areas of migration and in groundwater catchment planning. To improve accuracy in reservoir flow models further analysis of heterogeneous reservoir rock properties, such as grain size, grain sorting and mineralogy, and their influence on fluid flow behaviour is required. Analysis of the pore network in reservoir rocks is essential in developing a greater understanding of single phase and multiphase fluid flow behaviour as pore network geometry is a dominant control on the effectiveness of fluid transport within a reservoir (Jiang et al., 2013; Thomson et al., 2018; Claes et al., 2018). Within sandstone reservoir rocks little is known about the effect of heterogeneous sedimentary properties on the pore network and how this impacts fluid transport. In comparison to carbonate reservoir rocks, sandstone reservoir rocks show less heterogeneity, however, heterogeneity still occurs across a variety of spatial-temporal scales and is an important factor to consider (Claes et al., 2018). A greater understanding of the impact of heterogeneity in reservoir rock properties on fluid dynamics can provide essential information on fluid transport phenomena under variable conditions, and will increase accuracy in reservoir characterisation and in predicting fluid behaviour throughout reservoirs. Additionally, there is limited understanding on how heterogeneous properties can influence mineral dissolution, and in turn how this influences fluid transport properties and behaviour. Reactive flow in sandstone reservoirs can occur naturally due to mineralogical reactions with meteoric groundwater or hydrothermal fluids, and also artificially through CO<sub>2</sub> injection and matrix acidisation for enhanced oil recovery or removing formation damage (Mou et al., 2019). It is crucial to consider the effects of heterogeneity in sandstone reservoir rock properties due to the increasing demand for energy sources and the increasing popularity of less conventional petroleum sources which often have strong heterogeneity (Qiao et al., 2020). Additionally, there is also an urgent need to increase CO<sub>2</sub> storage capabilities to offset the global carbon footprint.

## 1.2 Background Research

### 1.2.1 The impact of sedimentary rock properties on fluid flow behaviour

Previous research has shown that some sedimentary rock properties, such as grain size, can be associated with increased porosity and permeability (Algive et al., 2012), and therefore favourable reservoir quality. For example, fine grained mudstones are not as permeable as coarse grained sandstones. Furthermore, increased clay mineral content in sandstones is often related to lower permeability (Medici et al., 2019) as it reduces the occurrence and connectivity of large intergranular pores and connected flow pathways (Rosenbrand et al., 2015). Other properties which characterise fluid behaviour, such as tortuosity, fluid flow pathways, pore throat distribution or the Reynold's number, are not as readily associated with sedimentary rock properties such as grain size, grain sorting and mineralogy. Furthermore, there has been limited research into how sedimentary heterogeneities influence fluid flow behaviour at the pore scale, despite porosity and permeability being strongly associated with pore network geometry (Qiao et al., 2020; Pini et al., 2016). Understanding the influence of rock properties, such as grain size or mineral content, on fluid flow behaviour will greatly enhance the accuracy of reservoir characterisation and predictive reservoir flow and storage models. This is also relevant in mapping the impact of reactive flows and solute and contaminant transport, given that if sedimentary properties can indicate preferential flow pathways then the accuracy in prediction and identification of chemical reactions and solute and contaminant fronts will increase. Previous research has recognised that heterogeneities can heavily influence the spreading of solute plumes and contribute towards flow transport in sedimentary rocks (Kurotori et al., 2019; Pini et al., 2016).

### 1.2.2 Heterogeneity in sandstone reservoir rocks

Heterogeneity in sandstone reservoir rocks can be defined by three types; 1) sedimentary, 2) structural, and 3) diagenetic (Fig. 1.1). Sedimentary heterogeneity is influenced by the environmental conditions at the time of sediment deposition, for example, energy levels, rate of sedimentation, climate and biogenic activity, and can be identified by non-uniform grain size, grain sorting, mineralogy and sedimentary structures (e.g. laminations, cross bedding). Structural heterogeneity is largely controlled by tectonic activity and the mechanical properties of the rock, for example, whether the rock is ductile or brittle, and is characterised by non-uniform bedding and structural features (e.g. deformation bands, fractures). Diagenetic heterogeneity is determined by numerous processes including depth of burial, overburden pressure and the original rock properties, and can be demonstrated by non-uniform cement distribution, cement composition and grain compaction. This study focuses on sedimentary heterogeneity which occurs in sandstone reservoirs, including heterogeneity in grain size and mineralogy. Heterogeneity in the sedimentary properties of sandstone reservoir rocks increases the difficulty of accurately characterising and predicting fluid flow behaviour in reservoirs (Pini and Benson, 2013; Qiao et al., 2020). First of all, heterogeneity in sedimentary properties can create permeability contrasts, which can act as baffles, barriers or conduits for fluid flow (Medici et al., 2016; Liu et al., 2016; Haffen et al., 2017), resulting in fluid flow being halted or redirected (Liu et al., 2016). It is also important to consider the size, extent and distribution of sedimentary heterogeneities in sandstone reservoirs, as this can reveal the size, extent and distribution of features which are capable of influencing fluid flow behaviour. Sedimentary heterogeneities in sandstone reservoir rocks can occur at a multitude of scales (Claes et al., 2018) and can occur in many forms, including grain size, grain sorting, sedimentary features (e.g. laminations, mud lenses, cross bedding) and mineralogy (e.g. cements, mineral overgrowths) (Liu et al., 2016; Pini et al., 2016). For example, a series of clay laminations in a well sorted, medium grained sandstone would be identified as a heterogeneity. Heterogeneities within sandstone reservoir rocks can be identified



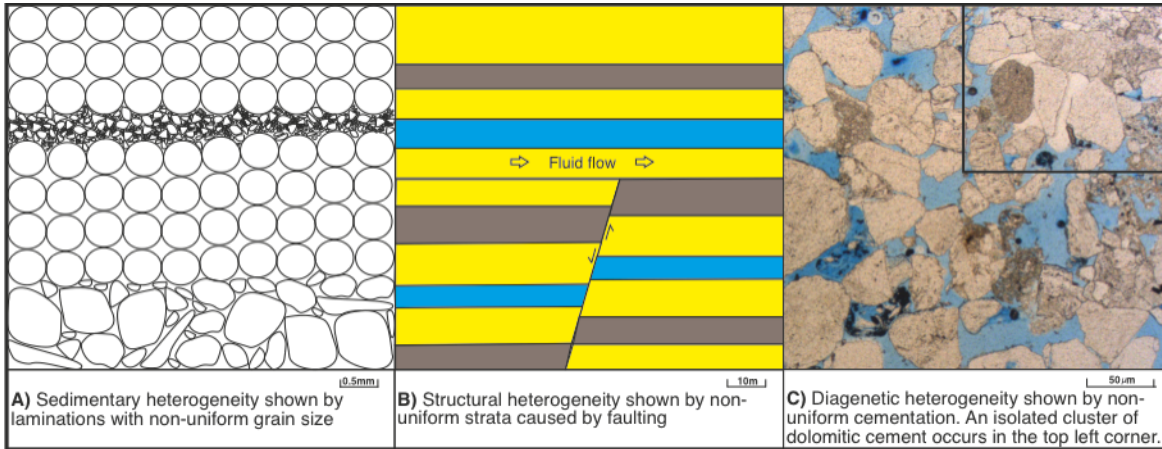


Figure 1.1: Examples of heterogeneity in sandstone reservoir rocks.

during reservoir characterisation, however, the full effect on fluid flow has not been quantified.

### 1.2.3 Heterogeneity in the pore network

Heterogeneity in the pore network can occur within the geometry of the pore network, such as pore shape, pore size, pore diameter and pore throat diameter. Pores can be described as cavities which occur between the grains/minerals and are connected by smaller channels which are commonly defined as pore throats. Pore space within sedimentary rocks can be complex as a result of depositional and diagenetic processes (Thomson et al., 2019; Algive et al., 2012). Pore shape can vary in a pore network and typical pore shapes include round, elliptical, saccate/ink bottle pores and slit pores (Fig. 1.2). The types of pore can also vary as pores can be well connected, such as through pores, or they can be isolated, such as closed pores (Fig. 1.2). The arrangement of pores and pore throats can also vary, and the pore cavity to pore throat ratio is an important factor to consider when analysing the geometry of a pore network. Pore network geometry is important to consider as it is inherently linked to the connectivity of the pore network, permeability, reservoir quality and overall fluid flow behaviour in the pore network (Qiao et al., 2020; Thomson et al., 2018). For example, the fraction of connected pore space increases with overall porosity (Thomson et al., 2018). Homogeneous sandstones can display a simplistic pore geometry, however, heterogeneous sandstones can display much more complex pore geometries (Thomson et al., 2019).

### 1.2.4 Geological Background

This study focuses on quantifying the effect of sedimentary heterogeneities on fluid flow behaviour at the pore-scale and to ensure that the heterogeneities presented in the synthetic samples were realistic, sandstone samples from producing oil/gas reservoirs, primary aquifers and potential CO<sub>2</sub> storage targets were studied. It was important that sedimentary heterogeneities from producing oil/gas reservoirs, primary aquifers or CO<sub>2</sub> targets were studied as it is critical to understand fluid flow in sandstones which are targets for such applications in order to potentially increase productivity and/or increase storage capacity. Furthermore, sandstone samples from different formations were studied to ensure that the heterogeneities analysed in this study were not unique to a specific formation. Due to this, the synthetic bead pack samples were designed to emulate the properties exhibited in the Triassic Sherwood Sandstone Group and the Permian Rotliegend Group.

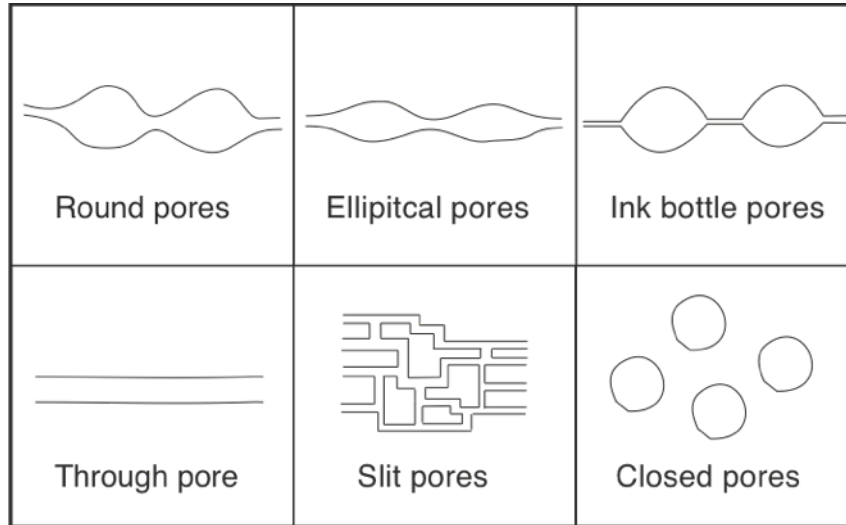


Figure 1.2: Examples of pore shapes and types.

The Triassic Sherwood Sandstone Group was sampled from the University of Nottingham’s GeoEnergy Test Bed facility and has been sampled at 692 ft. The Permian Rotliegend Group sandstones were sampled from wells in the southern North Sea in the Valiant North, Vanguard and Vulcan fields, at 7732, 88149 and 9423 ft. Both of these formations present heterogeneous sedimentary properties which are capable of altering fluid and transport properties, such as carbonate cements, poorly sorted grains and sedimentary structures which present grain size and mineralogy contrasts, however the effect of these properties on fluid flow behaviour is not well understood. Furthermore, both of these formations are targets of interest for oil and gas production, CO<sub>2</sub> storage, and the Triassic Sherwood Sandstone Group is also a regional aquifer in the UK (Smedley et al., 2018). Due to this, the synthetic samples were designed to feature bead size and mineralogy contrasts to analyse how fluid flow behaviour may be altered at the pore-scale. Permeability was analysed using pore-scale permeability experiments, permeability simulations and permeability models (Kozeny-Carman model). Tortuosity and fluid flow pathways were analysed using CFD simulations performed in ANSYS Fluent R2.

### 1.2.5 Triassic Sherwood Sandstone Group

The Triassic Sherwood Sandstone group is an extensive sandstone formation spanning across two sedimentary basins, from offshore west of Ireland, across the East Irish Sea Basin, to the eastern England Shelf (Schmid et al., 2006; Medici et al., 2015). The group forms a major European aquifer and is also the second largest groundwater aquifer in the UK (Smedley et al., 2018; Cronin et al., 2005; Medici et al., 2015). The Sherwood Sandstone Group is also a hydrocarbon reservoir in the East Irish Sea basin, producing both oil and gas (Kirk, 2006). The sandstones are capped by the Mercia Mudstone Group or Quaternary deposits, depending on the location (Smedley et al., 2018; Cronin et al., 2005). For example, the sandstones are capped by the Mercia Mudstone Group in the East Midlands region of the UK (Cronin et al., 2005; Smedley et al., 2018), whereas in the South Yorkshire region of the UK the sandstones are overlain by quaternary deposits (Smedley et al., 2018). The Sherwood Sandstone Group in the East Irish Sea Basin is the main reservoir unit and also demonstrates potential for CO<sub>2</sub> storage up to 1046 million tonnes (Kirk, 2006). Reservoir quality is largely influenced by porosity occluding dolomite cements (Schmid et al., 2004) and the

sedimentology of the sandstones (Wakefield et al., 2015). In the East Irish Sea basin porosity ranges from 8-30% and permeability ranges from 0.05 mD - 10 D (Kirk, 2006). The sandstones in this group include lithic arkoses, quartz arenites and subordinate breccia-conglomerates, and are largely fluvial and aeolian in origin and were deposited in an arid – semi arid climate (Medici et al., 2019; Schmid et al., 2006; Meadows, 2006; Wakefield et al., 2015). The fluvial sandstones are associated with high heterogeneity (Meadows, 2006). The cements which occur within the sandstones are commonly composed of dolomite, quartz, K-feldspar, calcite, clay minerals and grain coating haematite (Cronin et al., 2005; Medici et al., 2019; Schmid et al., 2006). The cements composed of dolomite, clay minerals, K-feldspar and haematite occur as a result of geochemical interactions with meteoric groundwater during early diagenesis (Schmid et al., 2004). Quartz overgrowths occurred during burial diagenesis (Schmid et al., 2006).

### 1.2.6 Permian Rotliegend Group

The Rotliegend group is a sedimentary rock succession located in north western Europe, extending from the eastern UK to Poland, and has been extensively studied to aid exploration and production activities in the oil and gas industry (Vincent et al., 2018). The group hosts the main reservoir for multiple gas fields in the Netherlands, UK, Poland and Germany (Molenaar et al., 2015). The group is categorised into three subgroups; the Lower Rotliegend, Upper Rotliegend, and the Zechstein (Vincent et al., 2018), which acts as cap rock for the underlying reservoir units. Many important gas reservoirs occur within the Lower Rotliegend group (Zwingmann et al., 1999; Gluyas and Leonard, 1995), and the gas is sourced from Upper Carboniferous Coal Measures (Zwingmann et al., 1999). Reservoir quality and fluid transport properties are strongly associated with the conditions and environment at the time of sediment deposition and diagenetic processes (Vincent et al., 2018; Ganzer et al., 2014; Pudlo et al., 2011; Rosenbrand et al., 2015). Quartz and carbonate cements and clay mineralogy are determined to be contributing controlling factors on porosity and permeability (Vincent et al., 2018; Ganzer et al., 2014; Pudlo et al., 2011; Rosenbrand et al., 2015). Most producing reservoirs of the Rotliegend Group have porosities ranging from 9-19% and moderate to high permeability of 1 mD – 1 D (Rosenbrand et al., 2015; Hannis, 2016). The lower and upper Rotliegend groups mostly comprise of quartzose sandstone (Molenaar et al., 2015) and were deposited in a large non-marine basin in fluvial and aeolian settings (Gluyas and Leonard, 1995; Vincent et al., 2018) under semi-arid conditions on a continental flood plain (Pudlo et al., 2012). The aeolian sandstones have higher porosity and permeability due to favourable grain size and sorting and mineral dissolution (Pudlo et al., 2012), and the fluvial sandstones have lower porosity and permeability as a result of higher clay mineral content and pore filling cements (Pudlo et al., 2012). The sandstones have a variable and complex diagenetic history, demonstrated by the prevalent carbonate pore filling cements, feldspar dissolution and quartz overgrowths (Pudlo et al., 2012; Vincent et al., 2018; Pudlo et al., 2011), which results in areas with strong heterogeneity. Areas of strong heterogeneity means that sections of this group are also a target for unconventional plays and geothermal applications (Molenaar et al., 2015).

## 1.3 Aims and Objectives

The aim of this study is to quantify the effect of heterogeneity in grain size and mineralogy on the pore network geometry and fluid flow behaviour before and after a reactive flow by using a combination of experimental and computational modelling techniques. The synthetic samples in this study are used as analogues for sandstone pore networks.

The objectives for this study are as follows:

1. Investigate the impact of heterogeneous grain size and mineralogy on pore network geometry, porosity, permeability and fluid flow behaviour.
2. Measure the effect of heterogeneous grain size and mineralogy on mineral dissolution after a reactive flow.
3. Analyse the impact of mineral dissolution on fluid flow behaviour in samples with heterogeneous grain size and mineralogy.

### 1.3.1 Structure of the Thesis

In order to achieve the objectives stated above this thesis has been structured into eight chapters. Chapter 1 is the introduction which demonstrates the importance of understanding the relationship between heterogeneous sedimentary rock properties and fluid flow behaviour. Chapter 2 details a literature review of relevant publications. In chapter 3 the materials used and created for this project and the methodology used is discussed. Chapter 4 focuses on the design and development of the pore-scale permeability experiments, which were designed specifically for this project and essential to the completion. Chapter 5 presents the impact of heterogeneous grain size on pore network geometry, tortuosity, flow paths and pore-scale flow phenomena. Chapter 6 addresses the effect of heterogeneous mineralogy on pore network geometry, dissolution, permeability and fluid transport phenomena and how this is altered after a reactive flow. Chapter 7 discusses how heterogeneity in both grain size and mineralogy alters the pore network geometry, dissolution and fluid flow behaviour and how this is altered after a reactive flow. Chapter 8 concludes the findings of this study and provides recommendations for future work.

# Chapter 2

## Literature Review

### 2.1 Introduction

Pore networks which occur in sandstone rocks can be described as a series of cavities (pores) which are connected by smaller channels (pore throats). Sandstone pore networks can vary greatly and are often intricately complex (Song et al., 2016; Chen and Song, 2002; Algive et al., 2012). The properties in sandstone pore networks are governed by the characteristics of sandstones, such as grain size, grain sorting and mineralogy, which are determined by processes of sediment deposition, diagenesis and/or structural deformation. The properties in sandstone pore networks can influence properties such as porosity, permeability, tortuosity, fluid flow pathways, fluid regime transitions and wettability. These properties at the pore scale can impact reservoir quality and recovery efficiency (Peng et al., 2012; Song et al., 2016; Cai et al., 2019).

### 2.2 Properties of Pore Networks in Sandstones

Properties of the pore network which are outlined in the literature include the arrangement of pore type, pore shape, pore size, pore throat type, pore throat shape, pore throat size and pore connectivity (Faruk Civan, 2011). It is essential to understand the type, shape/size, distribution and the connectivity of the pores and pore throats as fluid flow behaviour and contaminant transport can be sensitive to the pore structure and the distribution of pore structures (Bloomfield et al., 2001; Anovitz et al., 2015). For example, the geometry of the pore space controls the uniformity of fluid flow behaviour, where a non-uniform pore geometry is likely to result in non-uniform fluid flow behaviour (Datta et al., 2013). Additionally, pore networks with disordered geometries can be associated with tortuous flows which are disadvantageous in EOR and CO<sub>2</sub> storage as they are associated with lower permeability (Datta et al., 2013; Cai et al., 2019). Idealistic pore networks in sandstone reservoirs would consist of large, well connected pores with a low pore cavity/throat ratio, however, this is not always realistic, as pores in granular media are often described as irregular and variable in size (Schmitt et al., 2015b; Sufian et al., 2015; Bernabé et al., 2010; Hall et al., 2016). Furthermore, the pore network can also be described as a multi scale network, and may be host to other contrasting smaller scale networks which can result in different magnitudes of porosity, effective porosity and permeability (Blunt, 2017).

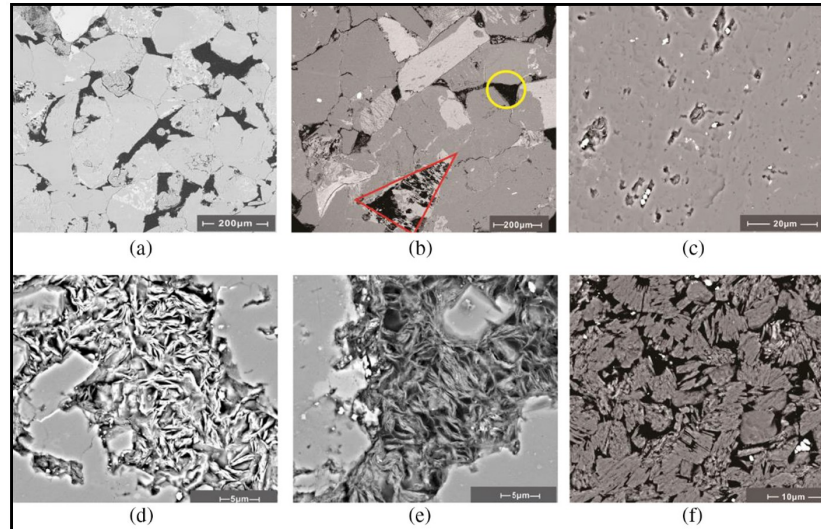


Figure 2.1: 2D SEM images of some of the types of pores which occur in sandstones; a) intergranular pore, b) dissolved pore in k-feldspar, c) dissolved pore in quartz, d) dissolved pore infilled by clay, e) micro pore in illite, f) micropore in kaolinite. (Taken from [Liu et al. \(2017\)](#)).

### 2.2.1 Pore Properties

A variety of different pore types/shapes which occur in pore networks are described in the literature which include uniform pores, through pores, funnel shaped pores, band shaped pores, ball shaped pores, ink bottle pores, intergranular pores, intercrystalline pores and moldic pores (Fig. 1.2). The types of pores which commonly occur within sandstones range from the micro-pore to macro-pore scale and include intergranular pores, intercrystalline pores, clay cemented pores, vuggy pores, dissolved pores and fracture pores (Fig. 2.1). Some pore types may restrict fluid flow, such as ink bottle pores, and some pore types support fluid flow, such as uniform pores or through pores. Pores at the micro-pore scale can restrict fluid movement as fluid is not able to pass through unless exposed to a high-pressure gradient ([Hall et al., 2016](#)). Ink bottle (saccate) pores can also restrict fluid transport and displacement as they can result in a large pore throat-pore cavity ratio which can reduce permeability ([Hall et al., 2016](#); [Cai et al., 2019](#)). The size of pores is linked to the size of grains, where pore diameter and pore radius is roughly equal to the grain diameter ([Revil et al., 2012](#); [Cai et al., 2019](#)). Furthermore, pores at the micro-pore scale are often associated with very fine grained sandstones or sandstones which have a high clay content in pore throats. The size of pore radius and the configuration of pores is also expected to influence the permeability ([Cai et al., 2019](#)). The distribution of pore size can also influence critical flow pathways, where a non-uniform distribution of pore size can result in a higher frequency of fluid flow pathways ([David, 1993](#)). The distribution of pore shapes and the geometry of the pore space overall is linked to tortuosity in the pore network, for example, pore networks which have disordered geometries increase the tortuosity of fluid pathways ([Datta et al., 2013](#)).

### 2.2.2 Pore Throat Properties

Pore throats occur in many forms, such as sheet like, belt like, a crooked flake like appearance, tubular, spherical, pore-shrinking, neck-contracted, slice shaped, micro throats and cluster throats (Fig. 2.2) ([Bai et al., 2013](#); [Mi et al., 2019](#); [Liu and Sun, 2020](#)). Sheet like, pore-shrinking, neck-contracted, slice shaped and cluster pore throats are associated with tight sandstone reservoirs ([Bai](#)

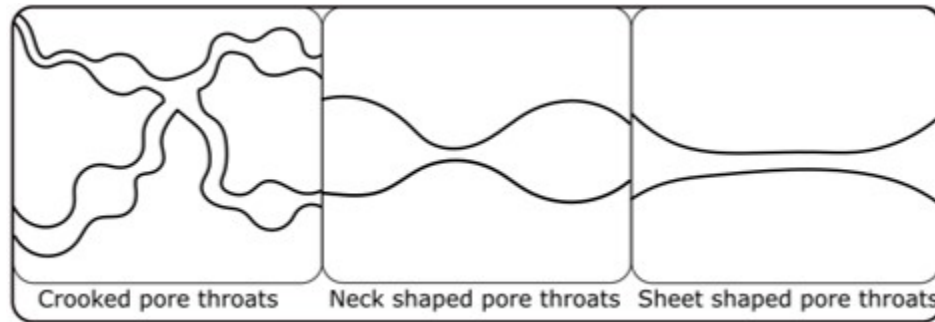


Figure 2.2: Examples of the types of pore throats in 2D.

et al., 2013; Mi et al., 2019). The size of pore throats in sandstones is associated with grain size, where the size of pore throats decreases with decreasing grain size (Nelson, 2009). Furthermore, grain size also impacts the range of pore throat sizes, where the range increases with increasing grain size (Nelson, 2009). Additionally, pore throat size is also related to porosity, where the size of pore throats increase with increasing porosity (Nelson, 2009). The size, distribution and combination of pore throat types and size can vary greatly even on a small scale and can be localised, occur in strips or be well distributed throughout the pore network (Bai et al., 2013). The size, distribution, combination and connectivity of pore throat types is important to consider when evaluating fluid flow in the pore network as the percolation, distribution and displacement efficiency of fluid flow is controlled by the pore throat structure which subsequently influences permeability, connectivity, tortuosity, reservoir quality and the migration and accumulation of oil and gas (Mi et al., 2019; Liu and Sun, 2020; Xi et al., 2016; Wang et al., 2020a; Bloomfield et al., 2001; Zahid et al., 2019). For example, smaller, narrower pore throats (e.g. micro throats) are associated with lower permeability and well connected, wider pore throats are associated with higher permeability (Liu and Sun, 2020; Bloomfield et al., 2001; Bernabé et al., 2016; Wang et al., 2020a). The size of pore throats is also related to storage capacity and smaller pore throats are more effective in storage than in reservoir flow (Xi et al., 2016). The profile of pore throats is also important to consider, especially when modelling pore scale fluid flow. Types of pore throat profile include conical, parabolic, hyperbolic and sinusoidal (Veyskarami et al., 2016) (Fig. 2.3). The types of pore throat profile can also be related to porosity and permeability, for example, sinusoidal pore throat profiles have greater porosity than parabolic pore throat profiles (Veyskarami et al., 2016). Furthermore, pore networks which are dominated by conical pore throat profiles show greater permeability than pore networks which are dominated by parabolic pore throat profiles (Veyskarami et al., 2016). Complex and diverse pore throat structures are expected to restrict production and development processes thus impacting the recovery rate (Zhang et al., 2019).

### 2.2.3 Heterogeneity in pore network properties

Heterogeneity can occur in pore network properties such as pore size, pore shape, pore throat size, pore throat shape and pore cavity - pore throat ratio, and heterogeneity can also occur in the distribution of these properties. Heterogeneity in pore network properties can heavily influence fluid transport properties and increases the difficulty of accurately predicting fluid flow behaviour as a heterogeneous pore network can result in heterogeneous fluid flow behaviour (Tang et al., 2019; Sufian et al., 2015; Bernabé et al., 2010; Datta et al., 2013; Al-Khulaifi et al., 2017). For example, increasing heterogeneity in pore size distribution can result in an increased occurrence of steady eddies which increase tortuosity (Muljadi et al., 2016). Additionally, heterogeneous pore networks

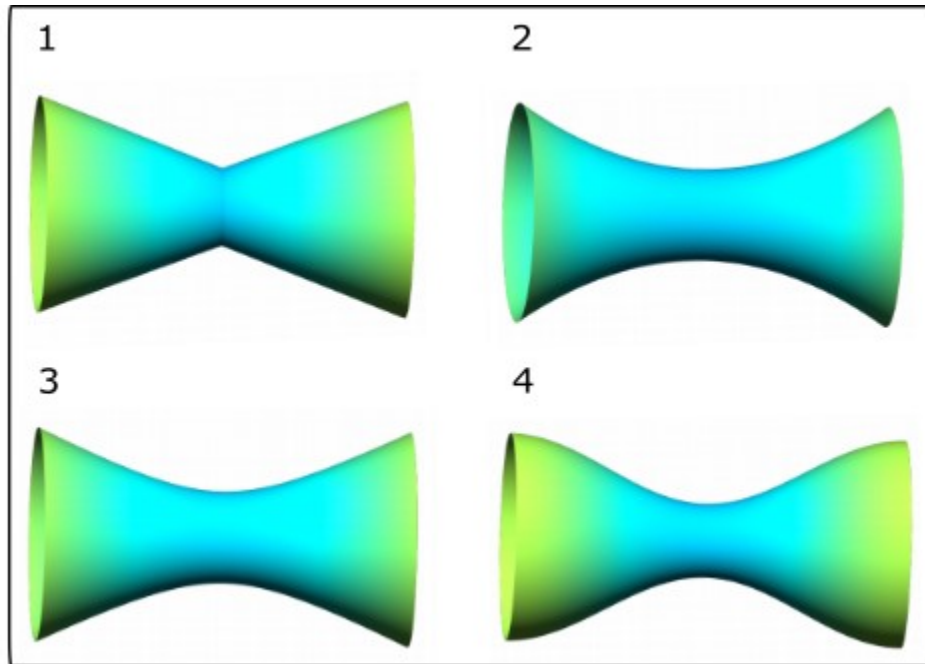


Figure 2.3: Examples of the types of pore throat profiles in 3D; 1) conical, 2) parabolic, 3) hyperbolic, 4) sinusoidal. (Edited from [Sochi \(2015\)](#)).

can also show thicker fingering patterns than homogeneous pore networks, increase flow channelling and influence fluid displacement patterns ([Ellis and Bazylak, 2012](#); [Tang et al., 2019](#); [Liu et al., 2015](#)). Furthermore, the transition from the laminar flow regime to the turbulent flow regime occurs earlier in pore networks which have a greater degree of heterogeneity in pore network properties ([Muljadi et al., 2016](#); [El-Zehairy et al., 2019](#)). Reactive transport, such as diffusion, in the pore network can also be affected by heterogeneous pore network properties, where the diffusion constant decreases with increasing heterogeneity in pore radius ([Adloo et al., 2019](#)).

## 2.3 Controls on Pore Network Properties in Sandstones

Pore networks within sandstone reservoir rocks can be complex and can possess variable distributions of different properties, such as pore type, pore throat type. Such factors contribute towards the overall geometry of the pore network and are commonly accepted to occur as a result of depositional, diagenetic and structural processes (Fig. 2.4) ([Schmitt et al., 2015a](#); [Lian, 2011](#); [Nabawy et al., 2009](#)).

### 2.3.1 Depositional Controls on the Pore Network

The depositional controls on the pore network derive from the depositional controls on the sedimentary rock, which influence grain packing, grain size, grain sorting, grain roundness and grain sphericity, mineralogy and sedimentary structures (e.g. cross bedding, laminations) ([Nabawy et al., 2009](#)). Depositional controls on the host rock include paleoenvironment, energy levels in the environment of deposition (e.g. fast flowing water, stagnant water), rates of sedimentation, climate, provenance and the path from the sediment source.



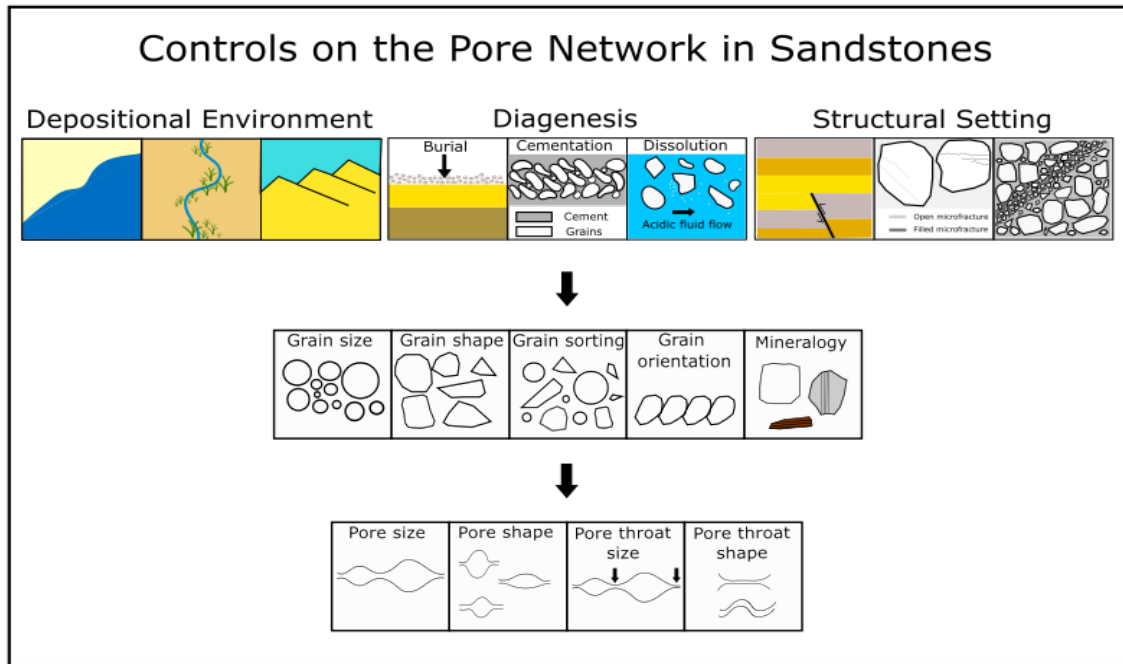


Figure 2.4: A diagram showing the controls on properties in the pore network.

The packing of grains can greatly impact the geometry of the pore network and the volume of pore space in the pore network (Pal et al., 2018). The packing of grains is variable and can occur in many forms such as cubic, hexagonal, rhombohedral, orthorhombic, tetragonal and triclinic (Pal et al., 2018; Tiab and Donaldson, 2012). The different packing types is demonstrated best by spheres, and cubic packing shows the greatest potential for porosity (40%) whereas triclinic and rhombohedral packing show the least potential for porosity (26%) (Tiab and Donaldson, 2012). Porosity is also impacted by the packing density, where increasing packing density results in decreasing porosity (Weltje and Alberts, 2011). The packing of grains depends on other properties such as grain size, grain shape and sorting (An and Nie, 2021). For example, round particles are expected to pack more densely than other particle shapes (An and Nie, 2021).

Grain size, and the distribution of grain size, is recognised as a key controlling factor in the geometry in the pore network and grain size is often linked to pore size. In simple granular pore networks the length of pores is associated with the diameter of grains, where pore length increases with increasing grain diameter (Revil et al., 2012). The size and distribution of the grains also controls the packing density where packing density increases with decreasing uniformity in grain size (Desmond and Weeks, 2014). Furthermore, grain size can also influence pore connectivity, porosity and tortuosity. Smaller grains are expected to have a greater impact on pore connectivity and can result in lower porosity and higher tortuosity (Kashif et al., 2019; Yusuf and Padmanabhan, 2019). Grain size in sandstones varies depending on the conditions of deposition which include hydrodynamic conditions, mode of transportation and energy levels (Baiyegunhi et al., 2017). The size and distribution of grains is indicative of energy levels, where finer grain size corresponds to lower energy levels and larger grain size corresponds to higher energy levels (Baiyegunhi et al., 2017). Energy levels relates to the transport process which occur in different environments, for example, high energy environments include beach/shore line environments and fast flowing rivers where wave action and river flow are the sediment transport processes. On the other hand, examples of low energy environments include

lakes and swamps, where sediment transport is dominated by particles settling out of suspension.

Grain sorting is another property which can impact the pore network and is capable of influencing packing density, porosity and permeability. The sorting of grains influences packing density, where well sorted grains will be less densely packed in comparison to poorly sorted grains (Desmond and Weeks, 2014). Furthermore, poor grain sorting is also associated with reduced porosity and permeability and increased tortuosity in opposition to grains which are well sorted (Al-hasani et al., 2018; Yusuf and Padmanabhan, 2019). The degree of grain sorting also determines the effect of processes which occur during diagenesis, deformation and weathering, such as cementation and grain compaction. For example, less cementation can occur during diagenesis if there is less pore space to cement as a result of well sorted and less densely packed grains. Grain sorting is dependent on the conditions and environment of deposition, for example, aeolian sandstones are frequently associated with good grain sorting due to the method of grain transport (wind).

Grain shape, roundness and sphericity also has a role in the geometry of the pore network and the shape of grains can influence the pore size distribution and subsequently influence hydraulic conductivity and headloss (Sperry and Peirce, 1995). Furthermore, a disordered distribution of angular and round grains can result in a range of diverse diverging-converging pore to pore throat geometries (e.g. ink bottle pores) (Chaudhary et al., 2013a). Converging pore to pore throat geometries can contribute towards a broader distribution of flow velocity, where flow velocity will be higher in the narrower, diverging pore throats and lower in the larger, converging pore space (Chaudhary et al., 2013a; Yan et al., 2011; Datta et al., 2013).

Grain orientation and sedimentary anisotropic structures such as laminations also contribute to the structure of the pore network (Nabawy et al., 2009; Basniev et al., 2012). Areas of lamination will impose different flow properties than areas without lamination, typically resulting in fluids flowing in the direction perpendicular to the plane of lamination (Basniev et al., 2012).

The minerals which occur within sandstone reservoirs are largely a result of depositional conditions and can heavily influence the pore network geometry, porosity, permeability, connectivity and tortuosity. Clay mineral content in the pore network can be a significant control on pore network geometry, porosity and permeability as it can impact the size, connectivity and distribution of pores and pore throats (Wang et al., 2020a; Zahid et al., 2019; Qiao et al., 2020; Schmitt et al., 2015a). Clay minerals can block, clog, fill and line pores and pore throats which reduces connectivity in the pore network (Wang et al., 2020a; Wilson et al., 2014). Clay minerals are mostly destructive to intergranular porosity and reduce overall pore size, which increases heterogeneity in pore size throughout the network (Qiao et al., 2020). Clays can further constrict pores by swelling during fluid flow (Sharifipour et al., 2019). Common clay minerals which swell during fluid flow include montmorillonite, kaolinite, chlorite and illite, and illite is often recognised as the clay mineral with the strongest influence on reservoir quality (Qiao et al., 2020). The amount of swelling differs between the different clay minerals, for example, kaolinite and illite will show less swelling than montmorillonite, which can swell up to 1500%, and this is determined by the clay mineral chemical composition and structure (Farrokhpay et al., 2016). Furthermore, a high clay content can also result in a more complex pore network geometry (Zahid et al., 2019). On the other hand, clay minerals can be beneficial to porosity and permeability if they are grain coating and common grain coating clay minerals include illite, chlorite and kaolinite (Verhagen et al., 2020). Grain coating clays can prevent quartz overgrowths during diagenesis and preserve original porosity and permeability (Qiao et al., 2020; Olivarius et al., 2015b; Arribas et al., 2012; Wang et al., 2020c), however, grain coating clays are only beneficial to porosity and permeability if the coating is thin (Verhagen et al., 2020). The mineralogy of sandstones is dependent on the provenance, transport mechanisms (e.g. wind, water),

weathering, tectonic setting, climate and the environmental conditions during sediment deposition (Yalysheva and Maslov, 2013; Anani et al., 2018). Additionally, the mineralogy of sandstones can be altered during diagenesis due to mineral dissolution and precipitation from fluids (Mahmud et al., 2018).

### 2.3.2 Diagenetic Controls on the Pore Network

Diagenetic controls on the pore network include compaction (chemical and mechanical), mineral overgrowths, mineral precipitation and mineral dissolution (Algive et al., 2012; Claes et al., 2018; Nader et al., 2016). These processes can both increase and reduce porosity and permeability, influence pore size distribution and alter the pore structure (Scott et al., 2019; De Boever et al., 2012; Nader et al., 2016). Diagenetic processes occur in sedimentary rocks after deposition during burial, where increasing temperature and pressure induce physical and chemical changes in the rock.

Compaction, both chemical and mechanical, is a reduction in volume and porosity (Mørk and Moen, 2007). Mechanical compaction is recognised as a primary control on reservoir quality and microscopic pore structure (Wang et al., 2020b), and is characterised by grain rearrangement including grain rotation and grain slippage, grain deformation, breaking of grains and squeezing of ductile grains, which results in denser packing of grains, reduced pore throat radii and lower porosity (Zhang et al., 2013; Mørk and Moen, 2007; Dou et al., 2018; Wang et al., 2020b). In sandstones, mechanical compaction commonly occurs at shallow - intermediate burial (< 2.5 km) whereas chemical compaction occurs during deeper burial (Fisher et al., 1999; Mørk and Moen, 2007). Chemical compaction may also involve dissolution, element transport and cementation (Mørk and Moen, 2007; Zhang et al., 2013). The extent of compaction is influenced by burial rate and depth, mineralogy, temperature, pressure and stress conditions, grain size and sorting, and the mechanical properties of the rock (Mørk and Moen, 2007; Wang et al., 2020b; Nader et al., 2016).

Mineral precipitation and dissolution are also diagenetic processes which can significantly alter the pore network. This is especially evident when cycles of dissolution and precipitation repeatedly occur which causes repeated alteration of porosity and permeability (Algive et al., 2012). Furthermore, cycles of dissolution and precipitation may not be constant which can lead to heterogeneity in the pore network geometry (Algive et al., 2012). Mineral dissolution occurs as a result of geochemical reactions which occur between reservoir fluids and a mineral. Common minerals which are involved in dissolution include carbonate minerals (e.g. calcite, dolomite, ankerite) and feldspars. Fluids can become acidic when exposed to molecules such as carbon dioxide or minerals such as pyrite, which can originate from organic rich hydrocarbon source rocks (Dawson et al., 2015). The rate of dissolution is dependent on mineralogical reaction rates which are determined by the surface area of the mineral, fluid flow rate, the reaction time, fluid chemistry and temperature (Liu et al., 2018). Some minerals, such as feldspar and calcite, are more reactive than others, such as quartz, which may result in non-uniform alterations in the pore network geometry and permeability and result in dissolution patterns such as wormholing (Fig. 2.5) (Parmigiani et al., 2011; Dawson et al., 2015; Liu et al., 2018). Dissolution patterns can occur in many forms, such as wormholing, compact dissolution and uniform dissolution, and are determined by the mineralogical composition, degree of cementation and fluid flow properties (e.g. propagation, velocity, viscosity) (Soulaine et al., 2017; Claes et al., 2018). For example, if the propagation of the acidic fluid is limited then it is likely that a compact dissolution pattern will occur (Soulaine et al., 2017). Furthermore, if the flow velocity is high instabilities can occur and develop wormholes which can result in channelised flow in the pore network (Soulaine et al., 2017; Ott and Oedai, 2015). The type of dissolution pattern which occurs can strongly influence the porosity-permeability relationship, rate of chemical reactions and

transport phenomena. For example, wormholing is associated with a fast permeability increase (Kang et al., 2014; Chen et al., 2014). Dissolution can be beneficial to the porosity and permeability of pore networks as it may result in a large volume of secondary pores, especially if it occurs after mineral precipitation, however, the dissolution of some minerals, for example feldspars, can create secondary minerals as bi-products such as illite, kaolinite and smectite (Wang et al., 2020c; Arribas et al., 2012; Yuan et al., 2017; Jalilavi et al., 2014). This can reduce permeability and the extent of permeability reduction is dependent on how the mineral forms, for example, if the mineral forms as a clast it can act as a detrital grain and fluid flow may not be as affected as the fluid can still flow around it (Olivarius et al., 2015b). On the other hand, intergranular clay can have a damaging effect on the pore network as it is capable of blocking pore throats (Olivarius et al., 2015b). The type of mineral which forms as a result of feldspar dissolution is largely dependent on the chemistry of the mineral assemblage (Yuan et al., 2017). Mineral assemblages which have a low silica content typically favour the formation of kaolinite, whereas assemblages which have a high silica content typically support quartz formation (Yuan et al., 2017). Additionally, the carbonate mineral content also contributes to the formation of secondary minerals (Liu et al., 2011). If carbonate within the rock is dissolved due to reactive processes it may be later precipitated as new carbonate (Liu et al., 2011). Furthermore, the formation of secondary minerals can also affect future dissolution as a result of altered fluid composition (Wigley et al., 2013). For example, if the rates of kaolinite precipitation are low then the fluid is closer to equilibrium with plagioclase, and therefore the rates of plagioclase dissolution are lower (Wigley et al., 2013). This is especially evident when the fluid pH is low (Wigley et al., 2013). Precipitated minerals are often referred to as cements, and can occur in a variety of shapes and may occur as pore filling, rhombs, patches, nodules, fibres, ribbon like, concretions or grain coating (Olivarius et al., 2015b; Arribas et al., 2012; Zhang et al., 2013; Jalilavi et al., 2014). Quartz cement is often considered as the most detrimental to porosity (Mørk and Moen, 2007) as quartz overgrowths occur at grain contacts and boundaries (Zhang et al., 2013). Quartz overgrowths may also occur in a fibrous form (Anovitz et al., 2015) and reduce pore space, narrow pore throats and reduce connectivity (Wang et al., 2020b). On the other hand, eogenetic (early diagenesis) and grain coating cements may preserve reservoir quality as they can prevent and limit quartz overgrowths and preserve pore space and pore connectivity and the original porosity and permeability (Olivarius et al., 2015b; Arribas et al., 2012; Wang et al., 2020c).

### 2.3.3 Structural Controls on the Pore Network

Pore networks which occur in sandstones can also be influenced by structural features such as microfractures and deformation bands. The structures within in a pore network can alter the pore network geometry and may result in porosity and permeability contrasts.

Microfractures in the pore network can range from nanometres up to 100 micrometres in size and can be open, infilled or partially infilled by cement (Fig. 2.6) (Wang et al., 2018; Sun et al., 2019; Mørk and Moen, 2007; Perez and Boles, 2005). The type of microfracture which occurs depends on tectonic conditions, lithology, erosion and ductile vs brittle grain content (Perez and Boles, 2005). Open microfractures can occur as a result of tensional stress and tensional fractures may develop within open fractures which can exhibit a stylolitic texture (Chentnik, 2012). A stylolitic texture can form as a result of pressure solution and will only develop if pores and pore throats are open and have high connectivity (Chentnik, 2012). Cemented and partially cemented microfractures indicate tensile failure which can also lead to pore pressure changes and mineral vein formation (Perez and Boles, 2005). The properties of microfractures, such as aperture, length, dip angle and roughness, can contribute towards fluid flow behaviour in the pore network (Sun et al., 2019). The aperture of a microfracture is recognised as having the strongest influence over fluid flow, as pore and pore

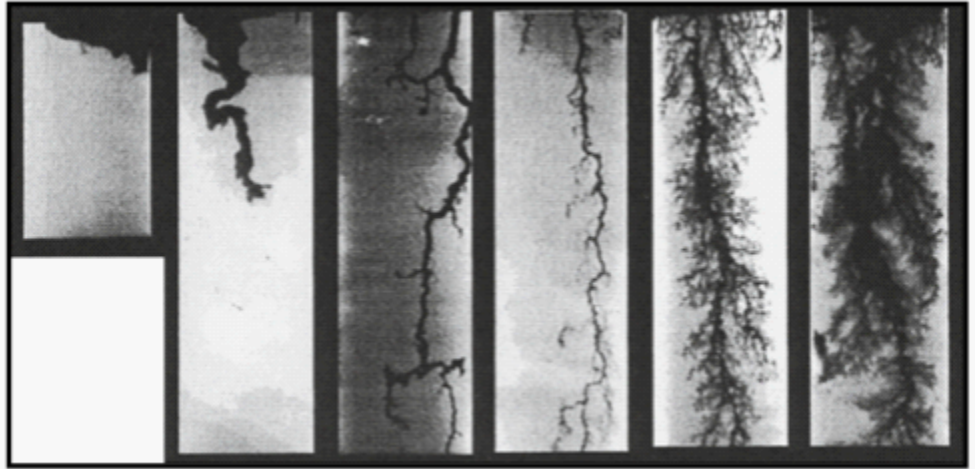


Figure 2.5: An example of wormholing: Neutron radiographs of different dissolution regimes with different injection regimes. Injection rates increase towards the right. As injection rate increases, wormholing becomes less apparent, and dissolution occurs more uniformly. (Edited from Al-Khulaifi et al. (2017)).

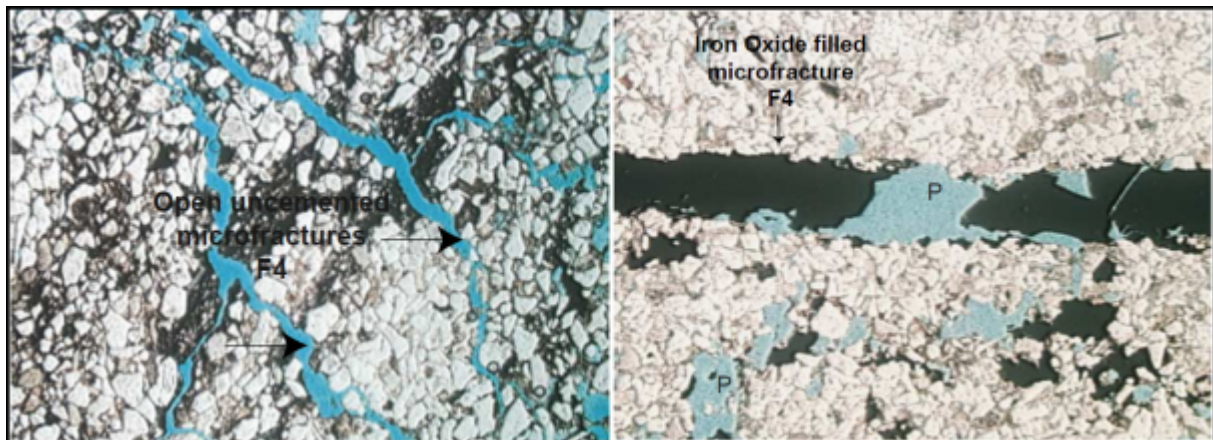


Figure 2.6: Examples of open and filled microfractures (Edited from Perez and Boles (2005)).

throat radius distribution increases with increasing aperture size (Sun et al., 2019). Additionally, permeability and aperture length share a linear relationship, where permeability increases with increasing aperture length (Yang et al., 2018; Sun et al., 2019). Permeability also has a linear relationship with microfracture cosine dip angle, where permeability increases with a greater cosine dip angle (Sun et al., 2019). Microfractures exist within intergranular pores, intragranular pores and mineral grains (Wang et al., 2018; Mørk and Moen, 2007). Most microfractures which occur within mineral grains occur within quartz as a result of mechanical compaction which occur at depths greater than 4.5km (Mørk and Moen, 2007). A pore network which has a combination of open, partially infilled and infilled microfractures can exhibit heterogeneity in porosity and permeability (Perez and Boles, 2005). When microfractures are open they can increase connectivity between pores and act as conduits for fluid flow, however when microfractures are cemented they can act as zones of low porosity and permeability and baffles or barriers to fluid flow (Bai et al., 2013; Chentnik, 2012).

Deformation bands are another type of structure which impacts the pore network and they are capable of altering the geometry of the pore network and reducing porosity (Ballas et al., 2015; Exner et al., 2013). Deformation bands are zones of localised strain in porous sedimentary rocks which can occur isolated or in clusters and can develop as a result of mechanical deformation which includes grain rotation and translation, which can further lead to grain crushing, grain rotating, or frictional sliding along grain boundaries (Lommatzsch et al., 2015; Exner et al., 2013; Ballas et al., 2015; Fossen et al., 2007). They are fault like structures which are planar and appear as thin bands (1mm thick) which produce small offsets in the order of a few mm to a few cm (Antonellini et al., 1994). The extent, distribution and type of deformation band which occurs depends on tectonic regime, burial depth, porosity, grain size, grain sorting, grain shape, mineralogy, cementation and lithification (Ballas et al., 2015; Exner et al., 2013; Gambino et al., 2019). Deformation bands can be classified either by kinematics or by deformation mechanism. In the kinematic classification there are three types of deformation bands, 1) dilation bands, 2) shear bands, 3) compaction bands, and hybrids of all three types of bands can also occur (Gambino et al., 2019). Dilation bands can develop from localised low confining pressure and can occur as fully cemented or loosely cemented (Lommatzsch et al., 2015). The cementation in dilation bands strongly contributes to porosity reduction (Lommatzsch et al., 2015). Shear bands form as a result of grain crushing, grain cracking and fracturing processes and can often exhibit dilation and compaction features (Gambino et al., 2019; Charalampidou et al., 2011). Compaction bands develop from grain breakage and porosity reduction, and are also associated with reduced permeability (Charalampidou et al., 2011). The reduction in porosity occurs as a result of pore collapse due to grain breakage and the movement of grain fragments into the pore space (Charalampidou et al., 2011). In the deformation mechanism classification there are four types of deformation bands; 1) disaggregation bands, 2) cataclastic bands, 3) phyllosilicate bands, and, 4) solution and cementation bands (Fig. 2.7) (Gambino et al., 2019; Fossen et al., 2007). Disaggregation bands occur as a result of shear-related displacement activities such as grain rolling, grain boundary sliding and granular flow due to stress concentrations at grain contacts from shear and compression (Philit et al., 2017; Fossen et al., 2007). Disaggregation bands can be recognised crossing/offsetting laminae (Fossen et al., 2007) and formation is promoted by a high clay content and poor mechanical compaction/low packing density (Ballas et al., 2015). Cataclastic bands form from mechanical grain fracturing and the degree of deformation is dependent on the degree of grain fracturing (Chentnik, 2012). They are characterised by poorly sorted angular grains and typically occur within coarse grained, well sorted and angular deposits (Fossen et al., 2007; Ballas et al., 2015). They can have a strong impact on the pore network as they can inhibit pore space and compact and destroy any remaining open pores (Fossen et al., 2007; Ballas et al., 2015). Additionally, cataclastic bands also promote grain rearrangement and grain interlocking which limits pore space (Ballas et al., 2015; Fossen et al., 2007). Furthermore, they can also result in preferential fluid pathways and can increase flow tortuosity (Ballas et al., 2015). Phyllosilicate bands are recognised as a type of disaggregation band but require a lower content ( 5-10 %) of platy minerals to occur (Fossen et al., 2007). Platy mineral content can lead to an increased chance of frictional grain boundary sliding and a higher content of platy minerals results in a higher chance that this type of deformation will occur (Fossen et al., 2007; Chentnik, 2012; Ballas et al., 2015). Phyllosilicate bands are commonly characterised by a band of finer material which aligns to form a localised fabric within the band (Fossen et al., 2007). This type of deformation band is detrimental to porosity in the pore network as they fill the surrounding pores (Fossen et al., 2007). Additionally, if the clay content is high enough the band may develop into a clay smear, which further reduces porosity and permeability (Fossen et al., 2007). Solution bands occur as a result of chemical compaction and/or pressure and formation is promoted by clay minerals at grain boundaries (Fossen et al., 2007). Solution bands can be recognised by tightly packed grains which are finer than the matrix (Fossen

*et al.*, 2007). Cementation bands develop from fresh, reactive surfaces produced by grain crushing or grain boundary sliding (Fossen *et al.*, 2007). In this type of deformation band porosity is reduced by the precipitation of cement within the band which can lead to fluid flow compartmentalisation from the pore to reservoir scale (Exner *et al.*, 2013). Deformation bands maintain or increase cohesion and are not typically associated with an increase in porosity and permeability (Fossen *et al.*, 2007; Ballas *et al.*, 2015) but with a reduction in fluid storage capacity which decreases with decreasing pore size and pore throat size (Ogilvie *et al.*, 2001). Pore size and pore throat size are reduced during mechanical deformation during the formation of deformation bands as a result of compacted grains which are more densely packed (Ogilvie *et al.*, 2001). Consequently, porosity and permeability will decrease with increasing deformation (Ballas *et al.*, 2015). Porosity and permeability in deformation bands and the transitional areas typically have lower porosity and permeability than the host reservoir rock (Chentnik, 2012; Ballas *et al.*, 2015) and permeability can reduce by as much as six orders of magnitude (Liu *et al.*, 2020a), which can create porosity and permeability contrasts (Ogilvie *et al.*, 2001). Additionally, porosity and permeability across deformation bands and the transitional area are variable at the pore scale, which is caused by variation in mechanical deformation (Chentnik, 2012; Ogilvie *et al.*, 2001). On the other hand, some deformation bands may act as fluid flow conduits or preferential pathways as a result of changes in the rock microstructure from grain rearrangement (Liu *et al.*, 2020a). This is especially evident in deformation bands which are associated dilatancy or evolve into fractures (Liu *et al.*, 2020a).

## 2.4 Fluid Flow Behaviour in the Pore Network

Fluid in the pore network can occur as a single phase or in multiple phases and fluid flow can be laminar or turbulent and in some circumstances reactive, however, this is determined by the composition of the fluid and the mineralogy of the pore network. The geometry of the pore network is commonly regarded as a primary controlling factor in fluid flow behaviour and the distribution of fluid within the pore network, as the geometry controls physical parameters such as imbibition and drainage (Endres *et al.*, 1991). The geometry and fabric of pore networks in sandstones are complex and often irregular which can both enhance and/or hinder fluid flow, and a heterogeneous pore structure can result in heterogeneous fluid flow (Sufian *et al.*, 2015; Bernabé *et al.*, 2010; Datta *et al.*, 2013; Al-Khulaifi *et al.*, 2017).

### 2.4.1 Fluid Phase

Single phase flow is when a single fluid occurs within a pore network and is often used in microfluidic experiments and simulations to simplify fluid flow behaviour to allow focus on specific areas of interest such as solute transport or dissolution rates. Furthermore, single phase simulations can be used as an alternative to two-phase flow simulations as they have shown good comparison with results from two-phase flow models and have a shorter computational time (Martinelli *et al.*, 2011; Zha *et al.*, 2018).

Multiphase flow is a flow of two or more phases, two of which can be distinguished as the wetting and non-wetting fluid. The wetting fluid is the fluid which saturates the pore network whereas the non-wetting fluid does not. Non-wetting fluids can reduce permeability and connectivity in the pore network as non-wetting fluids can trap/isolate the wetting fluid, especially when the non-wetting and wetting fluid have differing buoyancies (Parmigiani *et al.*, 2011). Typically the non-wetting fluid will occupy larger pores, unlike the wetting fluid which occupies smaller pores (Reynolds *et al.*, 2017). At low flow rates both the wetting and non-wetting fluid can flow throughout the pore network in

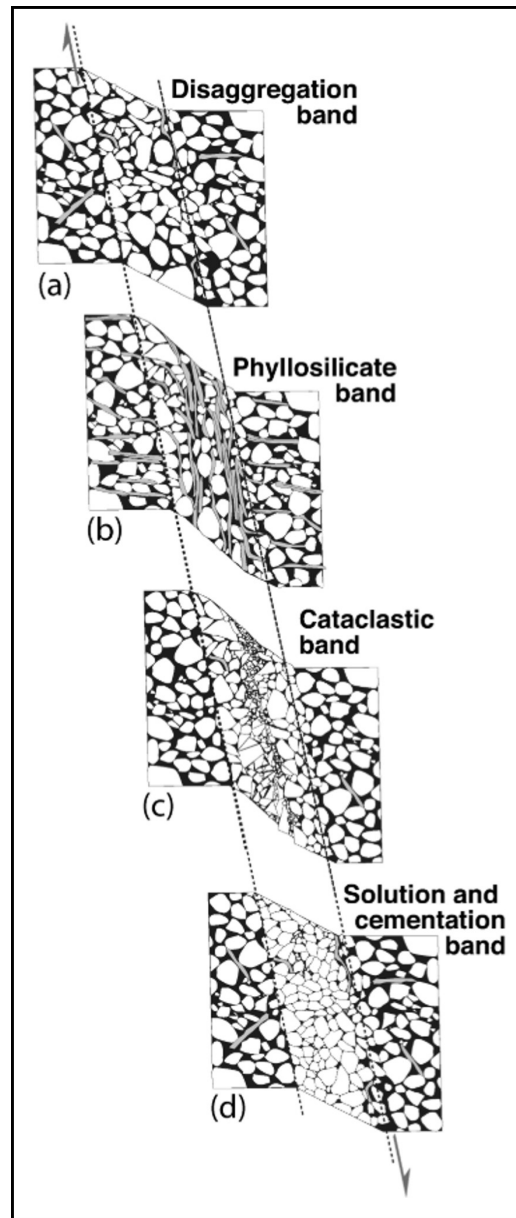


Figure 2.7: Types of deformation bands based on the type of deformation mechanism (Edited from Fossen et al. (2007)).



separate, stable fluid pathways (Reynolds et al., 2017). The behaviour of multiphase fluid flow is strongly associated with capillary pressure and relative permeability (Andrew et al., 2014; Singh et al., 2017), which are controlled by wettability, pore geometry, interfacial tension and the contact angle (Shojai Kaveh et al., 2016; Andrew et al., 2014). Multiphase fluids can also be associated with reactive processes, as the presence of multiphase flow can cause reactions at the fluid-fluid interface and/or the fluid-solid interface (Parmigiani et al., 2011). Reactions can influence the development of displacement within multiphase fluids, for example, dissolution rates have a strong control over the evolution of capillary fingers (Parmigiani et al., 2011).

### 2.4.2 Fluid Flow Regime

The type of fluid flow regime can be divided into three main regimes; 1) laminar flow, 2) turbulent flow, and, 3) the transitional regime between the laminar and turbulent flow regimes. The type of fluid flow regime is quantified by the Reynold's number,  $Re$ ,

$$Re = \frac{\rho V L}{\mu}, \quad (2.1)$$

where  $\rho$  is the fluid density,  $\mu$  is the dynamics dynamic viscosity,  $V$  is the velocity and  $L$  is a characteristic length scale. The characteristic length scale varies in the literature and the length of pore diameter is often used. The Brinkman length may also be used which is defined as  $\sqrt{K_D}$ , where  $K_D$  is the Darcy permeability (Muljadi et al., 2016). A Reynold's number greater than one typically indicates a transition into the turbulent flow regime (Blunt, 2017), however, the exact number where transition into the turbulent regime occurs is currently not well defined (Kumar et al., 2011). Furthermore, the  $Re$  is also related to fluid velocity where larger  $Re$  is expected to correspond to a greater fluid velocity (Kumar et al., 2011). High  $Re$  also suggests a deviation from Newtonian fluid behaviour (e.g. non-Newtonian fluid behaviour) as a result of greater variation in shear rates which increase with increasing velocity (Fayed et al., 2016). Typical Newtonian fluid behaviour presents a linear relationship between viscous stresses and the local strain rate, whereas non-Newtonian fluid behaviour does not.

The laminar flow regime is observed when fluid flows in parallel layers with no disruption. Laminar flow is also typically associated with low flow velocities and is expected to occur in the main body of a reservoir. This regime is desirable in oil recovery as layers of fluid provide continuity and prevent trapping (Blunt, 2017). This regime is dominated by viscous forces and inertial effects are negligible (Lage and Antohe, 2000; Macini et al., 2011). Additionally, the type of flow which occurs in this regime is associated with a degree of hydrodynamic stability and has low  $Re$  (Humphry et al., 2009). Two types of flow can occur during the laminar flow regime - Darcy flow and creeping flow (also known as Stokes flow). Darcy's law occurs towards the upper range of laminar Reynolds numbers and is given by

$$Q = \frac{K_D A}{\mu L} \Delta P, \quad (2.2)$$

where  $Q$  is the volumetric flow rate,  $\mu$  is the dynamic viscosity,  $L$  is a length over which there is a pressure drop  $\Delta P$  and  $A$  is the cross-sectional area. The (Darcy) permeability,  $K_D$ , is a fundamental property of the porous media. At the lowest Reynolds numbers, creeping flow can be described by the Navier-Stokes equations

$$\mu \nabla^2 \mathbf{u} - \nabla p + \mathbf{f} = 0 \quad (2.3)$$

$$\nabla \cdot \mathbf{u} = 0, \quad (2.4)$$

where  $\nabla p$  is the pressure gradient,  $\mathbf{u}$  is the fluid velocity and  $\mathbf{f}$  is an external body force (Wu et al., 2019). Both Darcy and creeping flow exhibit a linear relationship between fluid flow rate and pressure difference (Orgéas et al., 2006; Rivière, 2008).

The turbulent flow regime is seen when fluid flow undergoes constant irregular fluctuations in velocity, magnitude, pressure and direction. This flow regime is dominated by inertial forces and can also be referred to as non-Darcy flow or Forchheimer flow as there is a non-linear relationship between fluid flow rate and pressure difference (Berawala and Andersen, 2020; Chaudhary et al., 2013a). The turbulent flow regime is associated with high ( $Re > 1$ ) and is governed by the Forchheimer quadratic term (Eq. 2.5) which accounts for significant inertial effects and non-linearity in Darcy's law when  $Re \gg 1$  (Blunt, 2017; Chaudhary et al., 2013a; Berawala and Andersen, 2020). The onset of the turbulent flow regime can be estimated by using the non-Darcy flow coefficient,  $\beta$  in the Forchheimer term, which can be identified from the slope of the Forchheimer graph (Fig. 2.8) when the reciprocal of apparent permeability is plotted against  $Re$  (Macini et al., 2011; Muljadi et al., 2016). Additionally, when  $Re \gg 1$  viscous eddies can grow due to the increased fluid flow velocity which can result in reduced permeability (Chaudhary et al., 2013a).

The Forchheimer permeability is given by

$$K_F = \left( \frac{\mu QL}{\nabla P A} \right) + \beta \rho |Q|^2 \eta \quad (2.5)$$

where  $\mu$  is the dynamic viscosity,  $Q$  is the flow rate,  $L$  is the length,  $\nabla P$  is the pressure difference,  $A$  is the area,  $\beta$  is the non-Darcy coefficient,  $\rho$  is the fluid density,  $\eta$  is the unit vector in the direction of the pressure difference

The transitional regime separates the laminar and turbulent flow regimes and displays features of both regimes. Currently, the Reynolds numbers at which the transitional regime begins and ends is not well defined (Berawala and Andersen, 2020; Kumar et al., 2011) and is varies with the geometry of the pore network (Lage and Antohe, 2000).

Fluid flow can also be further described as either reactive flow or non-reactive flow. Reactive flow is capable of altering the pore network by increasing pore volume, porosity and permeability as a consequence of geochemical reactions at the fluid-solid interface in both liquid and solid phases which can cause mineral dissolution (Kim and Lindquist, 2013; De Boever et al., 2012; Raoof et al., 2013). Additionally, sufficient breakdown of minerals by reactive flow in the pore network can also contribute to the formation of new fluid pathways (Kim and Lindquist, 2013). The effects of reactive flow may not be uniform as a consequence of variable flow velocity, dispersion, pressure, mineralogy, extent of fluid saturation, pore network geometry, fluid flow pathways, fluid acidity and reaction rates (Kim and Lindquist, 2013; Raoof et al., 2013; De Boever et al., 2012). For example, low fluid velocity in an area with low reactive mineral content will show minimal mineral dissolution, whereas high fluid velocity in an area with high reactive mineral content will show a greater rate of mineral dissolution (Kim and Lindquist, 2013; De Boever et al., 2012). This is a result of prolonged reaction times which is due to the circulation of fresh reactive fluid. Furthermore, rates of dissolution can also vary between pore cavities and pore throats, which may lead to or enhance ink bottle shaped pores which have a large pore throat/cavity ratio. A large pore throat-cavity ratio is detrimental to fluid flow in the pore network as it limits fluid movement and displacement (Hall et al., 2016).

The flow in the pore network can be also be classified as reactive or non-reactive, and is quantified by the Peclet number,  $Pe$ ,

$$Pe = \frac{\langle u \rangle l_0}{D}, \quad (2.6)$$

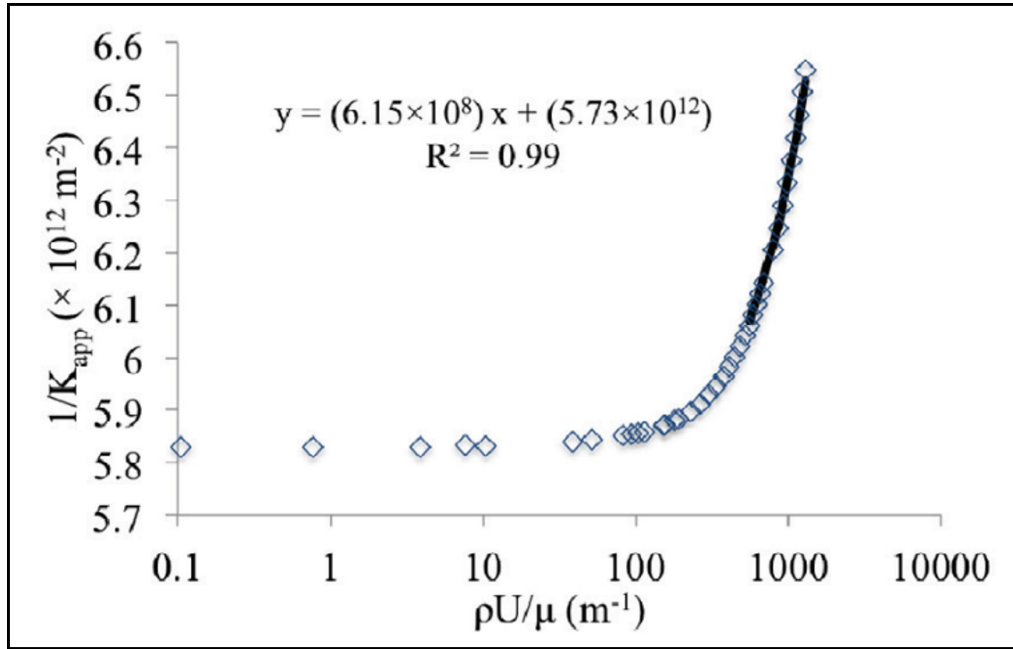


Figure 2.8: A Forchheimer graph showing the slope used to identify the beta factor (Edited from [Muljadi et al. \(2016\)](#)).

where  $\langle u \rangle$  is the mean velocity,  $l_0$  is the pore length and  $D$  is the diffusion coefficient and the Damkohler number,  $Da$ ,

$$Da = KC_0^{n-1}\tau, \quad (2.7)$$

where  $K$  is the kinetic reaction rate constant,  $C_0$  is the initial concentration,  $n$  is the reaction order and  $\tau$  is a time scale.

The  $Pe$  is the ratio of the advective transport rate to the diffusive transport rate ([Rastegar and Gu, 2017](#); [Dentz et al., 2018](#)). At low  $Pe$  diffusion dominates ([Kalashnikova et al., 2011](#); [Kirby, 2012](#)) whereas at high  $Pe$  ( $>1$ ) advection is dominant and diffusion is negligible ([Dentz et al., 2018](#); [Kirby, 2012](#)). Additionally, high  $Pe$  is associated with slow reaction rates and heterogeneous invasion fronts with regions of low solute concentration next to regions of high solute concentration ([Boccardo et al., 2018](#); [Dentz et al., 2018](#)). The  $Da$  is defined as the ratio of the net rate of reaction to the rate of advective transport ([Fredd and Scott Fogler, 1998](#); [Brondolo, 2019](#); [Yu and Hunt, 2017](#)). A large  $Da$  ( $\gg 1$ ) is associated with rapid chemical reactions whereas a small  $Da$  ( $\ll 1$ ) corresponds to slow chemical reactions and rapid diffusion ([Brondolo, 2019](#); [Sanchez-Vila et al., 2007](#); [Gervais and Jensen, 2006](#)). Additionally, when  $Da \gg 1$  the reactive transport system is close to local equilibrium at all points ([Sanchez-Vila et al., 2007](#)). The  $Da$  is inversely proportional to the injection rate and is capable of influencing dissolution patterns such as wormholes ([Fredd and Scott Fogler, 1998](#)). For example, wormholing typically occurs when the  $Da$  is high and a decreasing  $Da$  changes the wormhole structure from a conical shaped channel with large diameter to a highly ramified channel ([Kang et al., 2014](#); [Chen et al., 2014](#); [Fredd and Scott Fogler, 1998](#)). Decreasing  $Da$  can also be associated with an increase in permeability as a result of uniform or channelised dissolution ([Fredd and Scott Fogler, 1998](#); [Chen et al., 2014](#)).

### 2.4.3 Fluid Flow Pathways

Fluid flow pathways, also referred to as flow paths, critical pathways and preferential flow channels, are recognised as the main routes for fluid flow through the pore network and transmit the greatest flow via the shortest route (van der Linden et al., 2019; Sufian et al., 2019; Ju et al., 2018). It is important to study fluid flow pathways as they can largely influence predictions and measurements of permeability and increase fluid flow in the pore network (Hall et al., 2016; Vo et al., 2013). Fluid flow pathways can be described as either major or minor, where the major pathways distribute the majority of the flow in the pore network and the minor pathways connect the major pathways and provide alternative flow routes (van der Linden et al., 2019). Some fluid flow pathways may only occur periodically whereas some can be fixed, however, this only occurs within multiphase systems. Fixed fluid flow pathways usually occur in pores which are occupied by the non-wetting fluid, however, some connections to other pathways may periodically open and close (Reynolds et al., 2017). Fluid flow pathways can be influenced by many factors within the pore network, including pore size, pore throat size, connectivity, tortuosity, flow rate, fluid phase, wettability, flow stability, fluid temperature and fluid density (Reynolds et al., 2017; Parmigiani et al., 2011; van der Linden et al., 2019; David, 1993; Ju et al., 2018). The size of pores is recognised as a key controlling factor in the occurrence of fluid flow pathways, and larger pores are expected to increase the occurrence of fluid flow pathways (van der Linden et al., 2019). Additionally, pore size is also expected to have a greater influence than pore throat size, and a large pore size can offset the effect of small pore throats (van der Linden et al., 2019). Tortuosity in the pore network also impacts fluid flow pathways and the geometry of fluid flow pathways is determined by tortuosity, pore space geometry and connectivity (David, 1993).

### 2.4.4 Pore Filling and Fluid Trapping in the Pore Network

Pore filling and fluid trapping in the pore network can occur as a result of multiple processes and is strongly related to the pore network geometry. Local capillary pressure controls the velocity of fluid displacement, the order of pore filling, the sequence of pore filling and trapping of fluid (Blunt, 2017). Understanding the sequence that pores and pore throats are filled, and the fluid configuration within pores and pore throats can aid in understanding how much fluid is recoverable and how the fluids move (Blunt, 2017). Pore filling in multiphase systems can result in the wetting phase displacing the non-wetting phase, often by piston-like advance, unless it is trapped by snap-off (Singh et al., 2017; Blunt, 2017).

Pore filling in the pore network is a linked process, where the filling of one single pore will impact any adjoining pores (Blunt, 2017). Different types of pore filling mechanisms may occur in the pore network including piston-like advance and cooperative pore filling, (Blunt, 2017; Ruspini et al., 2017; Bultreys et al., 2016). Piston-like advance is where an invading wetting phase displaces the non-wetting phase and when a pore is filled the adjoining pore throats are also likely to be filled (Ruspini et al., 2017; Blunt, 2017). Piston like advance is a function of pore space geometry and size (Singh et al., 2017) and the invading wetting phase preferentially fills the narrowest regions of the pore (Ruspini et al., 2017; Krevor et al., 2015). The capillary pressure required for piston like advance to occur is higher than that required for snap-off to occur (Singh et al., 2017). Cooperative pore filling occurs when an invading wetting phase displaces the non-wetting phase from the pore cavity when multiple pore throats are filled with the non-wetting phase (Ruspini et al., 2017; Bultreys et al., 2016). Cooperative pore filling can also be recognised as a temporary drainage event during imbibition (Helland et al., 2017).

Fluid trapping in the pore network can occur as a result of pore filling events and can be advantageous in some applications such as CO<sub>2</sub> storage, however, it can also be disadvantageous in applications such as oil recovery (Singh et al., 2017). Capillary pressure is strongly linked to the trapping of fluid, and it is often regarded as capillary trapping (Tanino and Blunt, 2012). Capillary trapping is governed by the pore geometry, pore cavity - pore throat ratio, flow rate, wettability, surface tension and non-wetting phase saturation (Ruspini et al., 2017; Tanino and Blunt, 2012; Singh et al., 2017; Krevor et al., 2015; Deng et al., 2015). Furthermore, the capillary number,  $Ca$ , which describes the relationship between viscous and capillary forces, is also associated with the extent of capillary trapping which occurs. For example, a small  $Ca$  in water-wet systems can result in a constant amount of trapping in the non-wetting phase (Ruspini et al., 2017). Capillary trapping can be further described by processes such as snap-off and roof snap-off.

Snap-off is where the pore throat becomes invaded by a non-wetting phase and blocked by the wetting phase (Singh et al., 2017; Ruspini et al., 2017; Blunt, 2017). If all pore throats which surround the pore become blocked then the non-wetting phase becomes trapped inside the wider region of the pore and cannot be displaced (Blunt, 2017). Snap-off occurs as a result of capillary instability (Tanino and Blunt, 2012; Deng et al., 2015) where the non-wetting phase pressure remains constant but capillary pressure increases, which consequently results in a rapid decrease in the wetting phase pressure (Blunt, 2017; Singh et al., 2017). This results in the wetting phase filling and blocking the pore throat and the narrower areas of the adjoining pores and a further increase in local capillary pressure (Rossen, 2003; Blunt, 2017).

Roof snap-off can be observed during drainage when the non-wetting phase invades a pore throat and rapidly fills the adjoining pore which generates a drop in local capillary pressure (Blunt, 2017; Rossen, 2003). The local capillary pressure is higher in the pore throat than in the pore cavity, which results in the wetting phase occupying the narrowest regions of the pore closest to the pore walls, also referred corners of the pore, to swell and eventually snap-off when the capillary pressure has been sufficiently reduced (Deng et al., 2014), which leads to trapped ganglion in pores (Blunt, 2017). Snap-off and roof snap-off are strongly influenced by the pore geometry and less snap-off is expected to occur in pores which have a large contact angle or in pore throats with a contact angle close or at 90° (Blunt, 2017). Additionally, both types of snap-off favour round pores and pore throats with large pore cavity - pore throat ratios (Blunt, 2017; Tanino and Blunt, 2012; Rossen, 2003). When snap-off and roof snap-off are seen extensively across the pore network it is extremely detrimental to effective porosity and permeability and restricts fluid displacement (Blunt, 2017).

### 2.4.5 Fluid Displacement in the Pore Network

Fluid displacement at the pore scale is influenced by permeability, fluid viscosity, wettability, buoyancy, solubility, the flow rate of the invading fluid, capillary pressure, the capillary number, the viscosity ratio (the ratio between the viscosity of the invading non-wetting phase to the viscosity of the defending wetting phase) and the geometry of the pore network (Lee and Karpyn, 2012; Bakhshian et al., 2019; Zhang et al., 2011a; Tsuji et al., 2016). Additionally, fluid displacement in the pore network occur is determined by whether the fluids are miscible or immiscible. In miscible displacement no interface exists between the miscible fluids, whereas in immiscible fluids displacement, an interface separates the immiscible fluids. Furthermore, at constant temperature and pressure separate miscible fluids can merge into one single phase fluid, whereas immiscible fluids cannot (Danesh, 2003; Donaldson et al., 1985). Miscible fluids can also become partially soluble and produce a mixture of separate fluids, for example, two miscible fluids can generate a mixture of two separate miscible fluids with different fluid composition to the original miscible fluids (Donaldson et al., 1985). If the

altered miscible fluids are mainly composed the original miscible fluid and only a small amount of the other original miscible fluid then the altered miscible fluid will be single phase (Donaldson et al., 1985). However, if the altered miscible fluids are composed of equal amounts of the original miscible fluids then the altered miscible fluids will become separate phases (Donaldson et al., 1985).

Miscible fluid displacement occurs from imbibition and unstable displacement mechanisms such as viscous fingering and capillary fingering (Wang et al., 2013). Imbibition is recognised by an increase in the wetting phase saturation and occurs during fluid displacement when the advancing phase has a contact angle  $< 90^\circ$  (Wang and Sheng, 2018; Blunt, 2017) and is strongly influenced by the capillary number and capillary pressure (Li et al., 2017b). During imbibition fluid displacement is determined by snap-off and cooperative pore filling process (Blunt, 2017). The rate of imbibition is determined by permeability, pore network geometry, capillary pressure, initial water saturation, boundary conditions, viscosity, interfacial tensions and wettability (Alyafei and Blunt, 2018; Shi et al., 2018). Imbibition processes include primary imbibition, spontaneous imbibition and forced imbibition (Wang and Sheng, 2018; Blunt, 2017; Palakurthi et al., 2018). Primary imbibition occurs when the direction of saturation is reversed, and the wetting phase is imbibed into the pore network by displacing the non-wetting phase (Palakurthi et al., 2018). Spontaneous imbibition is the invasion of the wetting phase due to capillary forces, and only occurs in water-wet and mixed-wet systems (Alyafei and Blunt, 2018; Wang and Sheng, 2018). When additional external forces are included in this process it is recognised as forced imbibition (Wang and Sheng, 2018). Spontaneous imbibition is characterised by snap-off and piston-like advance pore filling and the non-wetting phase can become trapped by the pore filling wetting phase (Blunt, 2017). Spontaneous imbibition has two macroscopic fronts, one which leads into narrow pores and one which lags into wider pores (Ashraf et al., 2018). Spontaneous imbibition can be divided into two types; counter-current and co-current spontaneous imbibition (Wang and Sheng, 2018; Alyafei and Blunt, 2018). Counter-current spontaneous imbibition occurs when the flow directions of the wetting and non-wetting phases are opposite (Wang and Sheng, 2018; Alyafei and Blunt, 2018). Co-current spontaneous imbibition occurs when the flow directions of both phases are the same (Wang and Sheng, 2018; Alyafei and Blunt, 2018). Fluid displacement of miscible fluids can also occur via viscous and capillary fingering occur during unstable conditions. Viscous fingers occur due to instability in viscosity between the first and second phase fluids, where the less dense, less viscous fluid penetrates the denser, more viscous fluid (Torrealba et al., 2016; Parmigiani et al., 2011; Yuan and Azaiez, 2014; Tsakiroglou et al., 2003). This type of instability is often characterised by narrow, progressing flow paths shaped like fingers (Wang et al., 2013; Yuan and Azaiez, 2014; Medici and Allen, 2009). Capillary fingering occurs due to instability in capillary forces, where capillary forces dominate and cause the wetting phase to creep along the pore wall and the non-wetting phase to occupy the centre of the pore (Torrealba et al., 2016). Capillary fingering can also be recognised by the formation of finger shaped flow paths which vary in size (Medici and Allen, 2009). Fingering patterns can be problematic in enhanced oil recovery as pockets of the defending phase can become trapped and unable to remobilise due to the lack of fluid continuity (Holtzman, 2016).

The displacement of immiscible fluids occurs via drainage which occurs due to decreasing saturation of the wetting fluid (Mahabadi et al., 2020). Drainage processes include primary drainage, secondary drainage, tertiary drainage and stable displacement (Hammond and Unsal, 2012; Wang et al., 2013; Blunt, 2017). Primary drainage is where the wetting phase is displaced by the non-wetting phase (Wang et al., 2013; Blunt, 2017). Invasion of the non-wetting phase is restricted by ingress through pore throats and displacement occurs via a piston-like advance (Blunt, 2017). Displacement can occur as a result of increased pressure in the non-wetting phase or from injection of a non-wetting phase (Palakurthi et al., 2018). Secondary drainage occurs when the wetting phase is displaced or

trapped due to an invading non-wetting phase (Blunt, 2017). The wetting phase can become trapped on the pore wall surface in thick films, in pore constrictions or in the middle of the pore body and pore throats (Yadali Jamaloei et al., 2010). Tertiary drainage can also occur as a result of the trapped wetting phase becoming mobilised (Yadali Jamaloei et al., 2010). Stable displacement happens when both viscous and capillary forces are in equilibrium, resulting in primary fluid being swept away rapidly by the secondary fluid (Torrealba et al., 2016). Stable displacement is characterised by uniform fluid permeation and the retainment of the interface shape as the front moves (Medici and Allen, 2009), however, this can be influenced by significant surface tension which can result in non-circular shapes (Kim et al., 2015).

## 2.5 Controls on Fluid Flow Behaviour in the Pore Network

Fluid behaviour in the pore network is influenced by wettability, fluid composition, viscosity, flow rate, fluid saturation, water pressure, capillary pressure and threshold pressure, (Blunt, 2017; Andrew et al., 2014; Singh et al., 2017; Basniev et al., 2012; Reynolds et al., 2017).

### 2.5.1 Wettability

Wettability is a key contributing factor in how fluid in the pore network is distributed (Rabbani et al., 2018; Yadali Jamaloei et al., 2011; Rücker et al., 2020). Wettability is defined by the contact angle between a fluid and a surface and can be recognised when a droplet of fluid preferentially spreads along the surface of a pore (Donaldson and Alam, 2008; Rabbani et al., 2018; Arshadi et al., 2020; Abdallah et al., 2007). Wettability of reservoirs can be described as water-wet, oil-wet, mixed wettability, and fractional wettability (Donaldson and Alam, 2008; Yadali Jamaloei et al., 2011; McDougall et al., 1997; Abdallah et al., 2007). When a pore network is water-wet 50 % of its surfaces are wet by water and water occurs as a film in larger pores whereas oil occurs as droplets or in irregular streaks (Donaldson and Alam, 2008; Abdallah et al., 2007; Yadali Jamaloei et al., 2011). Water is identified as the continuous, mobile wetting phase and oil is identified as the non-wetting phase which is susceptible to trapping (Abdallah et al., 2007; Donaldson and Alam, 2008; Yadali Jamaloei et al., 2011). In an oil-wet pore network 50% of surfaces are wet by oil and oil occurs as a film whereas water occurs in droplets (Abdallah et al., 2007; Donaldson and Alam, 2008). As opposed to a water-wet pore network, oil is the wetting phase and water is the non-wetting phase (Donaldson and Alam, 2008). The displacement phase and conditions will differ between water-wet and oil-wet systems, for example, in a water-wet system, oil droplets are more diverse and heterogenous whereas in an oil-wet system, oil droplets are wider (Yadali Jamaloei et al., 2011). Mixed wettability occurs when smaller pores are water-wet and saturated with water and larger pores are oil-wet and saturated with oil (McDougall et al., 1997; Donaldson and Alam, 2008; Tiab and Donaldson, 2012). Mixed wettability can also be regarded as ‘neutral wettability’ or ‘intermediate wettability’ (Donaldson and Alam, 2008; Tiab and Donaldson, 2012). Fractional wettability is observed when the wetting of the pore surfaces is heterogeneous and preferential wetting is randomly distributed (McDougall et al., 1997; Donaldson and Alam, 2008; Tiab and Donaldson, 2012). Furthermore, wettability in pore networks can also be described as strongly water-wet, strongly oil-wet, weakly water-wet, weakly oil-wet or partially-wet (Tiab and Donaldson, 2012; Rabbani et al., 2018). Wettability in the pore network is controlled by the size and distribution of the contact angles in the pore network, pore geometry, mineralogy and fluid composition (Tiab and Donaldson, 2012; Blunt, 2017; Yadali Jamaloei et al., 2011; Qiao et al., 2020; Bultreys et al., 2016; Heydari et al., 2019). In reservoirs the size of the contact angle can determine wetting conditions (Fig. 2.9), for example, if the contact angle is  $< 90^\circ$  then the system will be water-wet whereas if the

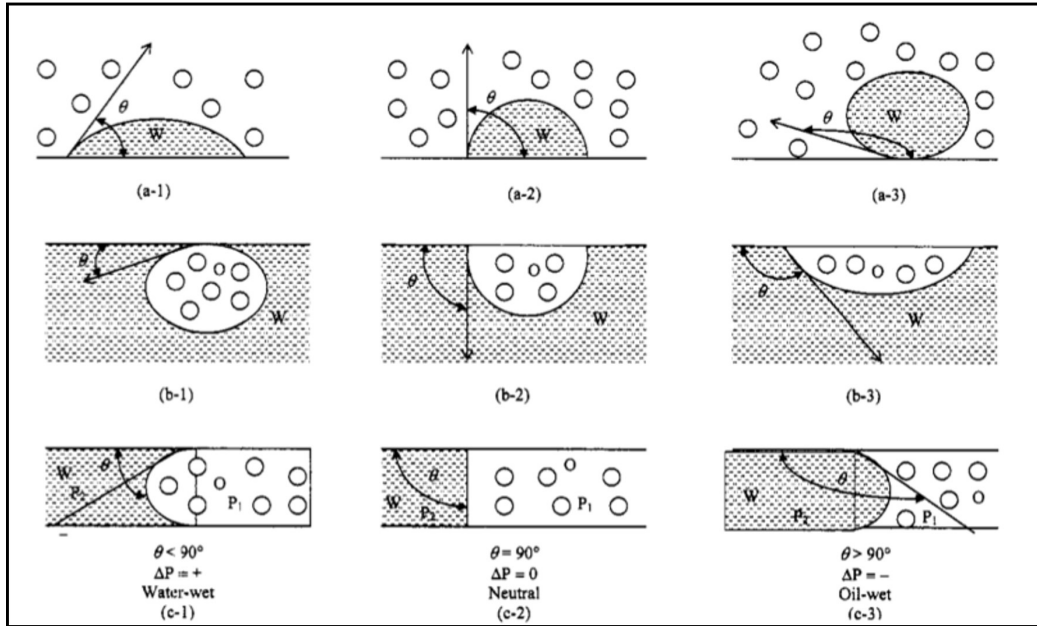


Figure 2.9: The contact angles for various wetting conditions: a) drops of water in oil on a plane, b) drops of oil on a plane, c) water and oil in a capillary tube (Edited from Donaldson and Alam (2008)).

contact angle is  $> 90^\circ$  then the system will be oil-wet (Tiab and Donaldson, 2012). When the contact angle is zero the system is neutrally wet (Tiab and Donaldson, 2012). The mineralogy of a pore network will also influence wettability. For example, quartz and feldspars are hydrophilic minerals and exhibit similar wettability under the same temperature and pressure conditions (Qiao et al., 2020), and minerals such as calcite and dolomite are naturally water-wet (Bultreys et al., 2016). On the other hand, graphite, talc and some clay minerals are hydrophobic (Rücker et al., 2020; Javaheri et al., 2018). Wettability in the pore network can be altered and the degree of alteration is determined by the mineralogy of the pore network, surface roughness, fluid composition and capillary pressure during drainage (Al-Futaisi and Patzek, 2004; Blunt, 2001). Some polar compounds which occur in non-aqueous phase liquids (e.g. oil) can alter the wettability (Kallel et al., 2017; Bultreys et al., 2016; Blunt, 2001; Abdallah et al., 2007), for example, when compounds such as carboxylates adsorb onto carbonate minerals the surface can become oil-wet (Heydari et al., 2019). Furthermore, the wettability of quartz can be altered towards less water-wet when exposed to supercritical  $\text{CO}_2$  (Mutailipu et al., 2019; Saraji et al., 2013). Wettability is important to consider as it can influence capillary pressure, relative permeability and the distribution of the phases in the pore network which controls fluid displacement and the storage capability of the pore network (Javaheri et al., 2018; Qiao et al., 2020).

## 2.5.2 Fluid Chemistry

The chemical composition of fluids in the pore network can influence the type of fluid flow in the pore network and it is capable of altering properties in the pore network which influence fluid flow behaviour, such as wettability, porosity and permeability. The properties of fluids which can influence fluid flow behaviour and the properties in the pore network include salinity and acidity. Saline fluid can occur naturally in the pore network as a result of interactions between fresh water



or brackish water and saline minerals such as halite and gypsum or from formation fluids originating from seawater and saline depositional environments (e.g. playa lakes, sabkhas) (Regenspurg et al., 2016). Furthermore, saline fluid can also be injected into petroleum reservoirs to increase oil recovery (Hassenkam et al., 2011; Ding and Rahman, 2017). Low salinity fluids (200 – 8000 ppm) impact on oil recovery as they can reduce adhesion and interfacial tension between the fluid and grain surfaces and alter the wettability (Hassenkam et al., 2011). Wettability can also be altered due to the interactions between clay minerals and low salinity fluids (Aminian and ZareNezhad, 2019; Hassenkam et al., 2011), and can occur due to a change in concentration of divalent cations which stimulates the release of organic polar components from clay surfaces (Hassenkam et al., 2011). Saline fluids can also create issues in CO<sub>2</sub> storage, especially when dry CO<sub>2</sub> is injected. Continuous injection of dry CO<sub>2</sub> can result in water evaporation which can lead to the increase of aqueous sodium chloride and precipitation of salt (Cui et al., 2018). The precipitation of salt is detrimental to fluid flow as it can block pore space and reduce porosity and permeability (Cui et al., 2018; Rathnaweera et al., 2016). Furthermore, the solubility of CO<sub>2</sub> can be influenced by the salinity, where solubility increases with decreasing salinity (Abbaszadeh and Shariatipour, 2018).

The pH of fluids in the pore network can also impact fluid flow behaviour and pore network properties. Low pH, acidic fluids can occur in the pore network naturally from hydrocarbon source rocks and can also occur as a result of injection (Dawson et al., 2015). Injected CO<sub>2</sub> rich fluids can develop into carbonic acid after reacting with resident brines which can lead to dissolution and precipitation of minerals in pore networks (Al-Khulaifi et al., 2017; Menke et al., 2014; Singh et al., 2018). The chemical reactions between fluids and minerals in the pore network, which can result in dissolution or precipitation, are dependent on mineralogy, pore network geometry, flow velocity, fluid pH, temperature and rate of renewal of fresh reactive fluid (Al-Khulaifi et al., 2017; Noiriél and Daval, 2017; Yuan et al., 2017; Menke et al., 2014; Singh et al., 2018). Carbonic acid can react with multiple minerals including calcite, dolomite, feldspars and clay minerals (Rathnaweera et al., 2016; Jalilavi et al., 2014). The extent of dissolution depends largely on the uniformity of mineralogy or the lack of heterogeneity in mineralogy. Heterogeneity in the mineralogy can lead to inconsistent dissolution and dissolution patterns such as wormholing (Fig. 2.5) (Noiriél and Daval, 2017; Menke et al., 2014), which can lead to heterogeneous porosity and permeability values throughout the pore network (Tang et al., 2016). The type of dissolution pattern is determined by the flow conditions of the acidic fluid, the properties of the pore network, temperature and pressure (Menke et al., 2014). Dissolution can occur in multiple phases, for example, the first phase of dissolution primarily leads to a uniform growth of fluid pathways, whereas the second phase of dissolution may only affect the growth of a single flow pathway (Al-Khulaifi et al., 2017). Dissolution can generate secondary porosity yet it may also reduce porosity (Ma et al., 2017). For example, the dissolution of feldspars by CO<sub>2</sub> rich brine can produce secondary minerals such as illite, albite, authigenic quartz and kaolinite which can fill pores, block pore throats, therefore redistributing and reducing porosity and permeability (Ma et al., 2017; Tang et al., 2016; Steinwinder and Beckingham, 2019). However, the secondary minerals can also be transported out of pores, but this is largely dependent on the geometry of the pore network, flow rate and permeability (Tang et al., 2016; Ma et al., 2017). Furthermore, the injection of CO<sub>2</sub> also provides a source of carbon for carbonate mineral precipitation (Jalilavi et al., 2014). In solution carbonate ions readily react with divalent calcium and magnesium ions to precipitate carbonate minerals (Jalilavi et al., 2014). Mineral precipitation can occur uniformly or non-uniformly, and is determined by pore size, grain size and mineralogy (Steinwinder and Beckingham, 2019).

### 2.5.3 Fluid Viscosity

Viscosity describes the resistance of a fluid to flow and strongly influences how fluid flow behaves (Guo et al., 2008; Bear, 1972). Higher viscosity results in more stable fluid displacement and in some applications, such as oil recovery, the viscosity can be altered by surfactants and polymers to enhance oil displacement (Lopez et al., 2003). Viscosity can also determine convective heat transfer and the pressure drop in laminar fluid flow (Mishra et al., 2014) and can vary locally (Hoang and Galliero, 2012). Viscosity is governed by cohesion and the rate of transfer of molecular momentum, which generates inertial forces, and both are heavily influenced by temperature (Shaughnessy et al., 2005; Granger, 1995; Bear, 1972). Increasing temperature results in decreasing strength of cohesive forces and overall viscosity decreases (Shaughnessy et al., 2005; Bear, 1972). Pressure is also a contributing factor however it is marginal until very high pressures, where viscosity increases with increasing pressure and constant temperature (Bear, 1972). Viscosity can be classified as dynamic viscosity or kinematic viscosity where dynamic viscosity is the measure of resistance between adjacent layers of fluid and kinematic viscosity is the ratio of the dynamic viscosity to density (Granger, 1995). Viscosity can also be described as shear viscosity and bulk viscosity (Shaughnessy et al., 2005). Shear viscosity is a resistance to shear forces and is predominantly controlled by temperature (Shaughnessy et al., 2005). Bulk viscosity occurs when fluids which have a complex molecular structure compress or expand and exhibit a secondary viscosity which can vary from the initial viscosity of the fluid (Shaughnessy et al., 2005). The viscosity ratio between fluid phases can also determine how fluid flow behaves and controls the relative permeability (Blunt, 2017). The viscosity ratio is the ratio between the viscosity of the invading phase and the viscosity of the displaced phase (Blunt, 2017; Wang et al., 2013; Zhang et al., 2011a). The viscosity ratio is unfavourable for fluid displacement when the value is  $> 1$  as this causes instability (Tzimas et al., 1997; Blunt, 2017; Zhang et al., 2011a; Holtzman, 2016). For example, when a less viscous fluid displaces a fluid with higher viscosity instabilities such as viscous fingering can develop (Blunt, 2017; Wang et al., 2013; Tzimas et al., 1997; Wang et al., 2019a). Furthermore, the effects of viscosity are variable and depend on whether the fluid is Newtonian or non-Newtonian. The viscosity of Newtonian fluids (e.g. water) is not affected by shear rate whereas the viscosity of non-Newtonian fluids is (Fayed et al., 2016; Chang et al., 1995; Petrak and Rauh, 2009), however, at higher shear rates viscosity can change and fluid flow can display non-Newtonian behaviour (Fayed et al., 2016). Non-Newtonian fluids have a non-linear relationship between viscosity and shear rate and can also be described as inelastic, shear thinning and shear thickening (Tsakiroglou, 2002; Chang et al., 1995; Fayed et al., 2016; Galindo-Rosales et al., 2011). Shear thinning fluids present a decrease in viscosity when shear rate is increased, and have high viscosity and are stable at low injection velocities (Rodríguez de Castro et al., 2019). Shear thickening fluids display a linear relationship between viscosity and shear, where viscosity increases with increasing shear rate after a critical value is reached (Galindo-Rosales et al., 2011). Shear behaviour in fluids is strongly influenced by the interactions between the fluid and geometry of the pore network (Rodríguez de Castro et al., 2019), and the relationship between the shear rate and viscosity is expected to be non-linear (Rodríguez de Castro et al., 2019).

### 2.5.4 Pressure in the Pore Network

Fluids can exert different types of pressure; normal and tangential. Normal pressure is exerted by a fluid on surfaces when fluid is stationary or moving, whereas tangential pressure is only exerted by a fluid when the fluid is moving (Shaughnessy et al., 2005). Pressure in a stationary fluid can also be referred to as hydrostatic pressure, which is strongly related to the weight of the column of fluid (Shaughnessy et al., 2005). In subsurface conditions fluid can exceed the hydrostatic pressure and reach the lithostatic pressure and cause the rock to break. The pressure in a fluid can cause a

fluid to flow, and the pressure will differ at different positions within the flow (Shaughnessy et al., 2005). Pressure is a local property and it must be defined at each point of the flow field (Granger, 1995). Pressure controls fluid displacement processes in the pore network and is further classified as capillary pressure and viscous forces (Blunt, 2017; Parmigiani et al., 2011; Singh et al., 2017; Andrew et al., 2014; Tanino and Blunt, 2012; Torrealba et al., 2016). In two phase flow capillary pressure is the difference in pressure between two phases (Adegbule and Kibbey, 2020; Abbasi et al., 2018) and is dominant at low capillary numbers (the relationship between viscous and capillary forces) ( $Ca < 10$  to 5) (Suh et al., 2017). Capillary pressure is not expected to be consistent throughout the pore network and is a function of saturation (Blunt, 2017; Gu and Bazant, 2019; Rücker et al., 2020; Abbasi et al., 2018). Furthermore, capillary pressure is controlled by the properties of the pore network (e.g. pore and pore throat size) and the properties of the fluids within the pore network (Tsyphkin and Shargatov, 2018; O’Carroll et al., 2010; Suh et al., 2017). Capillary pressure,  $P_c$  influences fluid displacement mechanisms such as imbibition and determines the position of the meniscus (Alyafei and Blunt, 2018; Blunt, 2017; Abbasi et al., 2018; Cueto-Felgueroso and Juanes, 2016). The Young-Laplace equation,

$$P_c = \sigma \left( \frac{\nabla A}{\nabla V} \right) \quad (2.8)$$

where  $\sigma$  is the interfacial surface tension,  $\nabla A$  is the change in surface area and  $\nabla V$  is the change in volume,

is commonly used to calculate capillary pressure (Blunt, 2017). When viscous forces are dominant pressure distributions become non-uniform and can force the non-wetting phase into smaller pore throats (Zhang et al., 2011a; Cottin et al., 2010). Furthermore, when viscous forces are dominant in the pore network fluid displacement processes such as viscous fingering can occur (Sivanesapillai and Steeb, 2018). Viscous forces typically dominate when  $Re < 1$  (Kuwata and Suga, 2015; Chaudhary et al., 2011). Additional flow characteristics such as viscous eddies and viscous coupling can also occur during viscous dominated flows (Chaudhary et al., 2013a; Xie et al., 2017). Viscous eddies can occupy 1/5 of the pore volume and increase in size with increasing  $Re$  (Chaudhary et al., 2011; Muljadi et al., 2016; Linsong et al., 2018). Viscous eddies are influenced by the pore network geometry and permeability, where a reduction in pore volume and permeability can lead to the growth of eddies (Chaudhary et al., 2011; Muljadi et al., 2016). Additionally, the frequency and growth of eddies is also related to tortuosity, where the frequency and growth of eddies increases with increasing tortuosity (Muljadi et al., 2016). Viscous coupling occurs when one phase impacts another phase as a result of momentum transfer and can influence fluid velocity distribution and flow rates (Xie et al., 2017; Li et al., 2005; Qiao et al., 2018). Viscous coupling is controlled by fluid saturation, capillary number, wettability and the viscosity ratio (Li et al., 2005). Viscous forces control properties including capillarity, porosity and permeability (Reynolds et al., 2014).

## 2.6 Computational Modelling of Fluid Flow in the Pore Network

An accurate representation of fluid flow behaviour within pore networks is important in order to understand microstructure and flow properties, which is key in petroleum engineering, oil recovery, CO<sub>2</sub> storage and hydrogeology (Song et al., 2016; Wang et al., 2015; Qin et al., 2019). Many models have been proposed and the key objective is to readily display the connectivity of the pore space which controls fluid flow (Blunt, 2017). Generally, all models simulate and quantify fluid

displacement in a porous medium to understand multi-phase flow at pore scale (Song et al., 2016; Blunt, 2017). Pore network modelling is based on three key components:

1. the description of the pore network geometry and structure
2. the definitions and solution of the governing equations
3. a selection of macroscopic properties (Martínez-Mendoza et al., 2019)

Fluid flow in the pore network is typically modelled using one of two computational methods; 1) pore network models (PNM) and 2) direct numerical simulation (DNS) methods (Mehmani and Tchelepi, 2018; Wang et al., 2015; Wu et al., 2019; Kohanpur et al., 2020; Blunt, 2017).

PNMs aim to relate pore structures to fluid flow properties and use a simplified, approximated version of the pore space geometry (Mehmani and Tchelepi, 2018; Wang et al., 2015; Wu et al., 2019). PNMs can use many approaches and can often adopt parameters used in DNS, such as the permeability of pore throats (Mehmani and Tchelepi, 2018; Blunt, 2017). They are capable of simulating transient behaviour of flow with time for various capillary numbers and viscosity ratios (Joekar-Niasar and Majid Hassanizadeh, 2011). Some PNMs will develop specialised algorithms to target the governing physics within pore networks (Mehmani and Tchelepi, 2018; Joekar-Niasar et al., 2009). The PNM was first described by Fatt (1956), where he assigned radii to the two-dimensional regular lattice (Song et al., 2016; Wu et al., 2019). Fatt used the Young-Laplace equation (Eq. 2.8) to fill pores and pore throats and produce qualitative forms of capillary pressure and relative permeability curves (Li et al., 2017b). Subsequently PNMs have become more realistic and have been used to predict pore-scale displacement processes, capillary pressure saturation and relative permeability of drainage and address the topology and pore and pore throat distribution (Wu et al., 2019; Blunt, 2017; Song et al., 2016; Joekar-Niasar et al., 2009). PNMs typically use Poiseuille’s law (Eq. 2.9) to govern fluid flow behaviour and imaging technology (e.g. SEM,  $\mu$ CT, laser confocal microscopy) to capture images which are used for information on pore network topology (Song et al., 2016; Joekar-Niasar et al., 2009). This approach can display the pore network well where pores and pore throats are represented by nodes and bonds (Wu et al., 2019; De Boever et al., 2012). PNMs are unable to provide or control the estimates of prediction error, however, they are more computationally efficient than DNS (Mehmani and Tchelepi, 2018; Qin et al., 2019). Additionally, they involve assumptions and approximations of the pore network, such as the size of pores and pore throats (Kohanpur et al., 2020). PNMs typically adopt one of three main techniques, such as statistical methods, process based methods and image based methods (Sharqawy, 2016). Furthermore, PNMs can be classified as either quasi-static or dynamic (Wang et al., 2015; Li et al., 2017b). Quasi-static displacement systems assume that pore-scale fluid configuration and displacement are dependent on capillary pressure and ignore the dynamic effect created by viscous forces (Wang et al., 2015; Li et al., 2017b). Dynamic drive systems are governed by the rationale of volume conservation and non-linear Poiseuille’s law (Wang et al., 2015).

$$Q = \frac{\pi \nabla P r^4}{8\mu L} \quad (2.9)$$

where  $Q$  is the fluid velocity,  $\nabla P$  is the pressure difference,  $r$  is the radius,  $\mu$  = dynamic viscosity and  $L$  is length.

DNS are governed by partial differential equations (PDEs) which are solved from using a detailed representation of the pore space geometry, such as  $\mu$ -CT images (Mehmani and Tchelepi, 2018). This approach solves the governing equations of mass and momentum balances at a sub-particle/sub-pore

scale which gives detailed and accurate information on fluid flow behaviour such as flow conditions and fluid velocity distribution (Wu et al., 2019). Furthermore, capillary and viscous forces can also be accounted for in this type of model (Raeini et al., 2015). The DNS approach is commonly regarded as more accurate as it can preserve pore structures in porous media well (Qin et al., 2019). Additionally, DNS are also computationally efficient and can easily incorporate a variety of scales (Oostrom et al., 2016; Kohanpur et al., 2020). However, this method is also computationally expensive and is not always representative of the whole porous medium (Mehmani and Tchelepi, 2018; Wu et al., 2019; Rodríguez de Castro et al., 2020). The representation of the porous medium can vary and is determined by the quality and size of the input image, image processing and segmentation, which leads to user-dependent results (Rodríguez de Castro et al., 2020; Raeini et al., 2015). DNS can also be referred to as dynamic numerical simulations and use computational fluid dynamics (CFD) techniques such as lattice Boltzmann, level set method, volume of fluid, finite element, smoothed particle hydrodynamics and immersed boundary method (Wang et al., 2015; Wu et al., 2019; Sadeghi et al., 2020; Kohanpur et al., 2020; Zhao et al., 2020).

## 2.7 Pore-Scale Experiments

Experimental work at the pore scale is increasing with the development of new technologies, such as  $\mu$ -CT. Experimental work at the pore scale is important as it can reveal the fundamental behaviour of fluid flow, as this is where fluid navigates through the porous medium (Song et al., 2016; Blunt, 2017).

Experimental studies described in the literature present a variety of methods and samples (Table 2.1). The experimental work can be divided into three categories which are based on specific measurable factors; 1) fluid flow visualisation 2) measuring overall pressure and fluid velocity and, 3) fluid flow visualisation and measuring the pressure drop over a sample.

Experimental studies can further be characterised by the type of samples which are used and based on the literature six types of samples can be identified; 1) 2D bead packs, 2) 3D bead packs, 3) encased plates with etched 2D pore network patterns, 4) natural rock samples, 5) microfluidic channels, and, 6) flow cells. The type of sample used in experiments is dependent on the experimental system available and the desired outcome, for example, encased plates containing etched 2D pore networks patterns, often also referred to as micromodels (Zhang et al., 2010; Buchgraber et al., 2012; Perrin et al., 2006) are popularly used in 2D fluid flow visualisation as they are cost effective, especially when using materials such as polydimethylsiloxane (PDMS), and can be designed specifically to meet the experimental objectives and requirements (Zhang et al., 2013; Dawe et al., 2011). For example, pore structures and sizes can be controlled and varied to create a network as homogenous or heterogeneous as required (Zhang et al., 2013). Core samples can also be used in fluid flow experiments as they have genuine pore network properties which can provide more accurate results. Microfluidic channels and flow cells are useful to use in pore scale flow experiments as they allow visualisation of the processes which occur at the pore scale (Carroll et al., 2014; Imhoff et al., 1996) and assist with additional applications such as particle tracking velocimetry (PTV), fluorescence photobleaching (Carroll et al., 2014). The type of sample used in pore scale experiments is further discussed in chapter 4.

Experimental methodologies can also be categorised by their methods of degassing or lack thereof. Most methodologies include a technique for degassing the system to prevent the occurrence of trapped gas bubbles, which can erroneously influence pressure readings. The experimental methodologies which degas their systems prior to experiments use the following techniques; vacuum cham-

bers/pump, CO<sub>2</sub> injection, system/sample saturation, and, flooding/flushing. Some methodologies use more than one technique to ensure that the system/sample is fully vacuum saturated ([Buchgraber et al., 2012](#); [Singh et al., 2017](#); [Krummel et al., 2013](#); [Perrin et al., 2006](#); [Kim et al., 2012](#); [Datta et al., 2013](#); [Imhoff et al., 1996](#); [Chomsurin and Werth, 2003](#)). The types of experimental methodology used to degas pore scale experiments is further discussed in Chapter 4.

Table 2.1: Experimental studies at the pore scale.

| Reference                   | Objective                       | Degassing Method                      | Sample Type          |
|-----------------------------|---------------------------------|---------------------------------------|----------------------|
| Abate et al., 2009          | Flow visualisation              | -                                     | 2D micromodel        |
| Baumann and Niessner, 2006  | Flow visualisation              | CO <sub>2</sub> injection, vacuum     | 2D micromodel        |
| Berejnov et al., 2009       | Flow visualisation              | -                                     | 2D micromodel        |
| Buchgraber et al., 2012     | Flow visualisation              | CO <sub>2</sub> injection, saturation | 2D micromodel        |
| Carroll et al., 2014        | Flow visualisation              | Vacuum                                | Microfluidic channel |
| Cottin et al., 2010         | Flow visualisation              | -                                     | 2D micromodel        |
| Chang et al., 2009          | Flow visualisation              | -                                     | 2D micromodel        |
| Cheng et al., 2004          | Flow visualisation, pressure    | -                                     | 2D micromodel        |
| Chomsurin and Werth, 2003   | Flow visualisation              | CO <sub>2</sub> injection, saturation | 2D micromodel        |
| Chung and Lin, 2017         | Flow visualisation              | -                                     | 3D bead pack         |
| Culligan et al., 2006       | Flow visualisation, pressure    | Saturation                            | 3D bead pack         |
| Datta et al., 2013          | Flow visualisation              | CO <sub>2</sub> injection             | 3D bead pack         |
| Datta et al., 2014          | Flow visualisation, pressure    | Vacuum, CO <sub>2</sub> injection     | 3D bead pack         |
| Dawe et al., 2011           | Flow visualisation              | Saturation, vacuum                    | 2D micromodel        |
| Ferer et al., 2004          | Flow visualisation              | -                                     | 2D micromodel        |
| Grate et al., 2010          | Flow visualisation              | -                                     | 2D micromodel        |
| Imhoff et al., 1996         | Flow visualisation, pressure    | CO <sub>2</sub> injection, saturation | Flow cell            |
| Kim et al., 2012            | Flow visualisation              | Vacuum, saturation                    | 2D micromodel        |
| Krummel et al., 2013        | Flow visualisation, pressure    | Vacuum, CO <sub>2</sub> injection     | 3D bead pack         |
| Lenormand et al., 1983      | Flow visualisation              | -                                     | 2D micromodel        |
| Lenormand et al., 1988      | Flow visualisation              | -                                     | 2D micromodel        |
| Lovell et al., 2010         | Flow visualisation              | -                                     | 2D bead pack         |
| Meghdadi et al., 2017       | Pressure and flow velocity      | Saturation                            | 2D micromodel        |
| Perrin et al., 2006         | Pressure and flow velocity      | Vacuum                                | 2D micromodel        |
| Sharifpour et al., 2017     | Flow visualisation              | Saturation                            | 2D micromodel        |
| Singh et al., 2017          | Flow visualisation              | CO <sub>2</sub> injection             | Natural rock         |
| Theodoropoulou et al., 2005 | Flow visualisation, pressure    | -                                     | 2D micromodel        |
| Tsakiroglou et al., 2003    | Flow visualisation and pressure | -                                     | 2D micromodel        |
| Willingham et al., 2008     | Flow visualisation              | -                                     | 2D micromodel        |
| Willingham et al., 2010     | Flow visualisation              | -                                     | 2D micromodel        |
| Zhang et al., 2011          | Flow visualisation              | Saturation                            | 2D micromodel        |
| Zhang et al., 2011          | Flow visualisation              | CO <sub>2</sub> injection, saturation | 2D micromodel        |
| Zhang et al., 2013          | Flow visualisation              | Fluid injection, saturation           | 2D micromodel        |
| Zhang et al., 2014          | Flow visualisation              | Saturation                            | 2D micromodel        |

# Chapter 3

## Materials and Methodology

This chapter details the materials and experimental and computational techniques used in this study. Reservoir sandstone samples and synthetic 3D bead packs were used in the experiments and computational work, and the 3D synthetic bead packs were designed on properties identified during sandstone sample characterisation. A combination of experimental and computational analysis has been undertaken at the pore-scale to observe fluid flow properties and behaviour in the Darcy flow regime and to predict fluid flow properties and behaviour in the Forchheimer flow regime.

### 3.1 Core Characterisation

Four reservoir sandstone samples were taken from the Permian Rotliegend Group and the Triassic Sherwood Sandstone Group (Fig. 3.1). The Permian Rotliegend Group samples (samples 1 - 3) originate from wells in the southern North Sea, at 7732, 88149 and 9423 ft, from the Valiant North, Vanguard and Vulcan fields. The Triassic Sherwood Sandstone Group sample (sample 4) originates from the University of Nottingham's GeoEnergy Test Bed facility and has been sampled at 211 ft. Four samples were analysed macroscopically at the core scale and microscopically by thin section petrography.

#### 3.1.1 Core and Thin Section Sample Analysis

Each sample has been analysed at the core scale to identify grain size, grain sorting, mineralogy and sedimentary structures. Core samples have been analysed and a thin section sample was taken from each core. Four polished, 30 mm thin section samples were taken and impregnated with blue resin to highlight the pore space (Fig. 3.2). The thin section samples were analysed using a Zeiss petrographic microscope and grain size, grain sorting, mineralogy and sedimentary structures were recorded. The properties of the thin section samples were observed from grain to grain contact points along three transects taken along the y axis (the longest axis of the thin section sample). Images of the thin section sample were taken at each contact point and used for porosity calculation using the ImageJ software. Prior to porosity calculation the images are processed in the software. First of all the images are converted to RGB colour, which changes the image from colour to black and white, and then the 'split channels' option was selected. This provides three images of the sample and each image represents a different channel. The channel which showed the greatest contrast between the grains, which are represented by lighter colours, and the pore space, which is represented by darker colours, was selected. This contrast was enhanced by using the thresholding tool which further



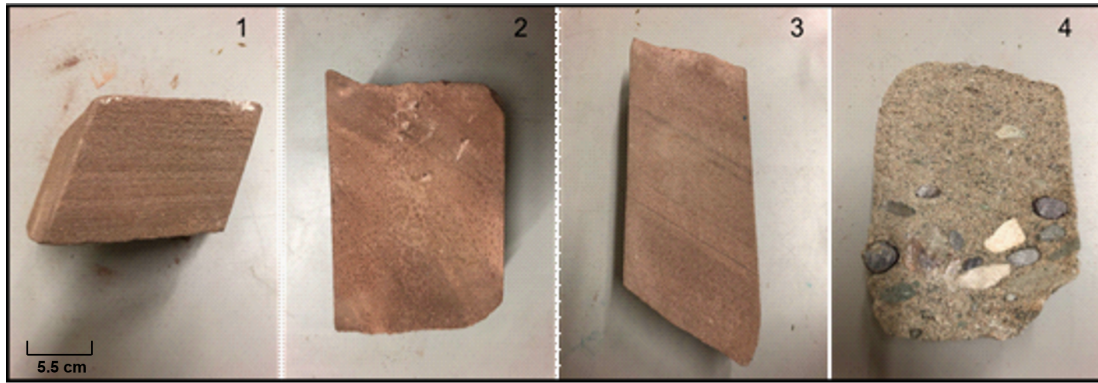


Figure 3.1: Core samples taken from the Rotliegend Group (1-3) and the Sherwood Sandstone Group (4).

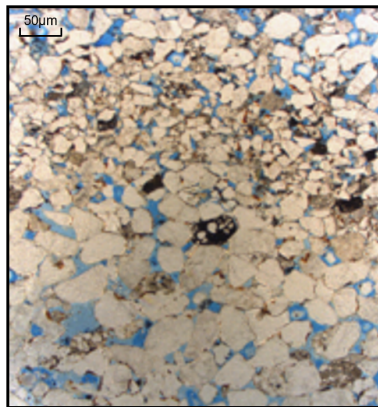


Figure 3.2: Thin section image from core sample 3.

segments the image. The image was then analysed using the ‘Analyse particles’ tool which gives the area of the pore space. This process was repeated three times on each image of every contact point and averaged. The results from all of the images for each sample were also averaged at the end of porosity calculation to give an average porosity value for each thin section sample.

### 3.1.2 Powder X-ray Diffraction (PXRD)

PXRD was used to determine the bulk and clay mineralogy of each sample. Four samples (6x3cm) were taken from each core sample and crushed using a Retsch jaw crusher and pulverised into a fine powder using a Tema disc mill. The crusher and disc mill were cleaned with an air gun before and after each sample to eliminate any contamination between samples. The powdered samples were placed into the sample holder for PXRD until a level surface was created and inserted into the instrument (Hilton Brooks PW1050). The sample holder was cleaned before and after each use with industrial methylated spirit (IMS) to avoid contamination. The instrument was set at 40 kV and 20mA and the settings for the scans are detailed in Table 3.1. After scanning the data was analysed in the Diffrac.Eva software, which displays the results of PXRD and allows identification of minerals. Each mineral presents a different diffraction pattern which enables identification, for example, quartz displays peaks at  $26.6 2\theta$ . For clay mineral analysis, the denser grains in the sample were separated from the finer grains ( $< 2 \mu\text{m}$ ). 5g of each sample was added to a solution of

Table 3.1: A table showing the scan settings for PXRD.

| $\theta$ | Speed ( $^{\circ}2\theta$ /second) | Step Size |
|----------|------------------------------------|-----------|
| 10-70    | 1                                  | 0.05      |

deionised water (25 ml), hydrogen peroxide (5 ml) and sodium hexa meta phosphate (0.2 g). These chemicals are added to remove organics and sulphates out of the sample. This solution was then placed in an ultra-sonic water bath for 2 hours. The samples were subsequently transferred from a beaker into centrifuge tubes and placed into a centrifuge for 25 minutes at 4500 RPM. The top fluid from the samples was drained and deionised water was added. This process is used to clean the sample powder with deionised water and to remove the initial solution and separates the fluid from the solid. The samples were again placed into a centrifuge for 25 minutes at 4500 RPM. The top fluid from the samples was again drained and deionised water was added. The samples were placed into the centrifuge for 2 minutes at 1000 RPM. This separates the clay-size particles from the silt and sand size particles, which are pushed to the bottom of the sample tube by centrifugal forces. 500  $\mu$ l of fluid was extracted from the sample tube and deposited onto a glass slide. 300  $\mu$ l of acetone was added to the slide to prevent the thin clay layer from curling during drying. The samples were then left to air dry. The remaining sample solution was used in further clay mineral analysis. To remove chlorite the sample solution (1ml) was added to HCl (417  $\mu$ l) and Milli-Q water (3583  $\mu$ l). The samples were then heated on a Teflon heater at 100 $^{\circ}$ c for 2 hours, where a reaction will occur between the clay and HCl. Once cooled, the samples were transferred to centrifuge tubes and centrifuged for 25 minutes at 4500 RPM. The samples were subsequently rinsed and added back to the centrifuge for 25 minutes at 4500 RPM. Next, the samples were drained and 1ml of deionised water was added. The samples were then extracted and deposited onto a glass slide to air dry. The samples were then scanned using the X-ray diffractometer.

### 3.1.3 Mercury Intrusion Porosimetry (MIP)

MIP was used to calculate the average porosity, pore size and pore diameter for each sample. A small core sample (2  $\times$  3 cm) was placed inside the penetrometer and weighed. The weight of the penetrometer was inputted into the instrument software and then the penetrometer was placed into the instrument. During MIP mercury is forced into the sample by pressure and the amount of pressure required is controlled by the size of the pores. For example, larger pores require lower pressure than smaller pores. The volume of mercury which intrudes the sample is measured by the penetrometer. The volume of mercury intruded into the sample corresponds to the volume of pore space in the sample.

## 3.2 Synthetic 3D Bead Pack Design and Analysis

Ten synthetic 3D bead packs have been designed and constructed for the work in this study. The 3D bead packs have been designed to emulate properties which have been identified in the reservoir sandstone samples, such as grain size and mineralogy. The design of each bead pack differs due to different experimental objectives, for example, experiments which include reactive fluid flow require samples which include reactive minerals, such as dolomite and kaolinite. The details of sample composition are recorded in Table 3.2 and a schematic of each sample is shown in Fig. 3.3.

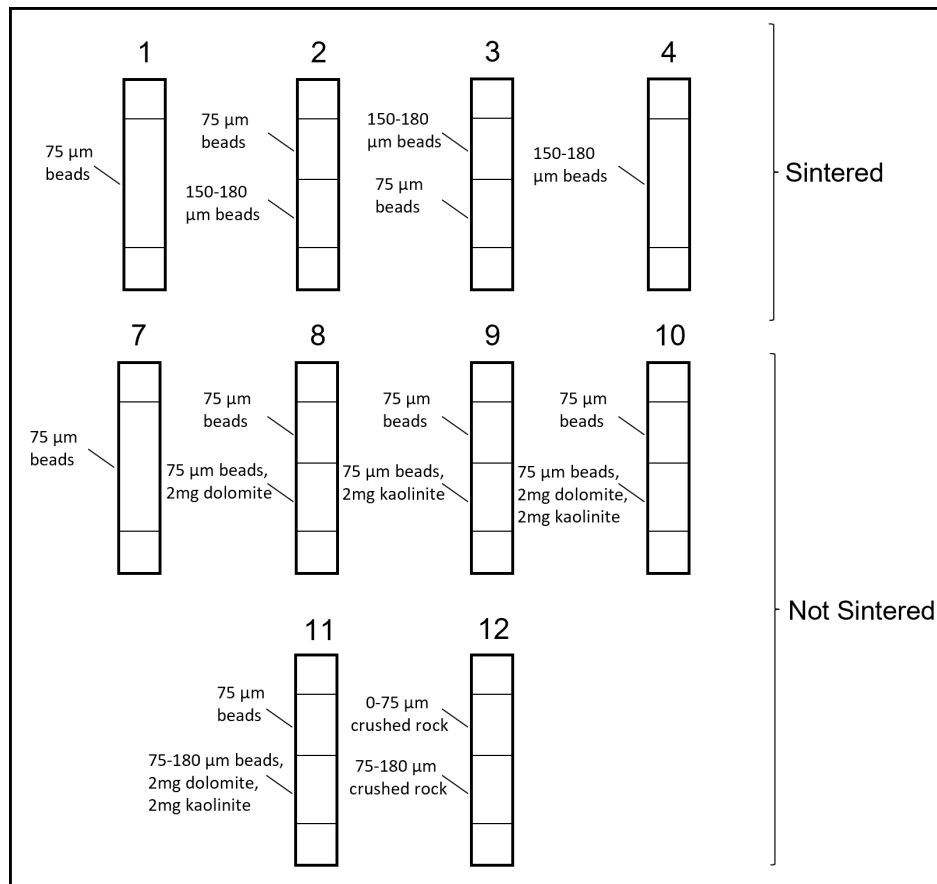


Figure 3.3: Schematic of the bead pack samples used in this study. Samples 5 and 6 are meshes used in the CFD simulations in Chapter 5 so the bead pack samples were not numbered consecutively as to avoid confusion. Sample 12 is composed of crushed rock from core sample 3. \*Please note: schematic is not to scale, sample dimensions are  $1 \times 1 \times 33$  mm.

Table 3.2: A table showing the composition of the samples used in the pore scale permeability experiments.

| Sample | Composition   |
|--------|---|
| 1      | 75 $\mu\text{m}$ acid washed glass beads                                    |
| 2      | 75 - 180 $\mu\text{m}$ acid washed glass beads                              |
| 3      | 75 - 180 $\mu\text{m}$ acid washed glass beads                              |
| 4      | 150 - 180 $\mu\text{m}$ acid washed glass beads                             |
| 7      | 75 $\mu\text{m}$ acid washed glass beads                                    |
| 8      | 75 $\mu\text{m}$ acid washed glass beads, 2mg dolomite                      |
| 9      | 75 $\mu\text{m}$ acid washed glass beads, 2mg kaolinite                     |
| 10     | 75 $\mu\text{m}$ acid washed glass beads, 2mg dolomite, 2mg kaolinite       |
| 11     | 75 - 180 $\mu\text{m}$ acid washed glass beads, 2mg dolomite, 2mg kaolinite |
| 12     | 75 - 180 $\mu\text{m}$ rock powder (core sample 3)                          |

### 3.2.1 Synthetic 3D Bead Pack Construction

The samples are created by first adding quartz or stainless steel wool to the bottom of a 1x1x33mm quartz capillary tube, which acts as a vessel for the sample. The type of wool used varies between samples due to the sample composition (Table 3.2, Fig. 3.3) and whether the sample was sintered or not. Quartz wool was used if the sample was sintered and stainless steel wool was used if the sample was not sintered. The sample contents (e.g. glass acid washed beads, mineral powders, rock powder) was inserted into the quartz capillary tube and either quartz or stainless steel wool was added to the top of the tube. The packing density of the sample was enhanced by tapping the tube several times during filling and the amount of tapping was consistent for every sample. The samples which were sintered were placed into a furnace for 6 minutes at 720°C and afterwards the quartz wool was removed. The sintering process emulates the lithification process which occurs in sedimentary rocks. The samples which contain minerals and have stainless steel wool were not sintered and the wool was not removed. The samples which contain minerals were not sintered to prevent any mineralogical reactions or alteration from occurring. The stainless steel wool which was used was extra fine so it did not impact fluid flow but prevented the sample from moving. The samples were then attached to 1/16" PTFE tubing using a small amount of superglue. The connection between the tubing and the sample was reinforced by heat shrink tubing.

### 3.2.2 Synthetic 3D Bead Pack Analysis

The porosity and permeability of each 3D bead pack sample was analysed using images acquired from X-ray computed tomography (XRCT). Each synthetic sample was scanned using XRCT from the  $z$  axis with a resolution of 2 $\mu\text{m}$  at intervals of 8 $\mu\text{m}$ . The samples were scanned from the  $z$  axis as during the pore-scale experiments fluid flows along the  $z$  axis. The image stack of each scan was divided into five smaller image stacks to increase accuracy during analysis. Each image stack was imported into the ImageJ software, smoothed and converted into 32-bit image type. The contrast and brightness settings for each image stack was enhanced and the image stack was then thresholded to increase the contrast between the beads and pore space and to separate the beads and pore space into different binary categories (beads = 0, pore space = 1). The Analyse particles tool was then used to analyse the area of pore space. This process was repeated three times for each image stack to ensure the results were reliable. The porosity results were then inputted into the Kozeny-Carman equation (Eq. 3.1) to calculate permeability. The Kozeny-Carman equation was used to compare

the reliability of the permeability results from the pore scale permeability experiments.

$$K_{K_C} = \left( \frac{\phi^3}{(Sv)^2 K (1 - \phi)^2} \right) \quad (3.1)$$

where  $\phi$  = porosity,  $Sv = 6/D_P$  (where  $D_P$  = particle diameter),  $K$  = the Kozeny-Carman constant (which is 5 for spherical beads)

### 3.3 Pore-Scale Permeability Experiments

The pore-scale permeability experiments were conducted using a closed system consisting of a New Era NE-1000 syringe pump, 20ml syringe, Bronkhorst mini cori-flow™ series ML120 flow metre, 2 Bronkhorst IQ+ Flow® pressure metres, synthetic sample and a 12ml syringe (Figs. 3.4 and 3.5). The instruments and sample were connected by 1/16" PEEK PTFE tubing and 1/16" air tight zero dead volume (ZDV) unions, tees and Luer fittings. The unions/tees were also fitted with ferrules to prevent leakage. The fluid drained into a 12ml syringe at the end of the system which regulated back pressure and stabilised pressure throughout the system. The o-ring in both syringes were coated with vacuum grease to ensure the system was air tight. The syringe pump provided continuous, horizontal fluid flow at the following rates; 0.010, 0.015, 0.02, 0.025, 0.03 ml/min. The flow metre and pressure metres provided accurate readings of flow rate ( $\pm 0.2\%$ ) and input/output pressure ( $\pm 0.5\%$ ). The flow rate was limited to 0.05 mm/s and the pressure metres were limited to 300 kPa. Prior to each experiment the system was evacuated using a diaphragm vacuum pump for 20 minutes to prevent trapped bubbles of air. Trapped bubbles of air can result in erroneously high pressure values. The vacuum pump was attached to the system with a tee union with a Luer fitting and a valve. The valve allowed the syringe to be closed off from the system during evacuation, and the vacuum pump to be closed off during flooding/experiments. After the system was evacuated the system was flooded with deionised water at the desired flow rate. Once saturated, flow rate, inlet pressure and outlet pressure were measured by the Bronkhorst mini cori-flow™ series ML120 flow metre and the 2 Bronkhorst IQ+ Flow® pressure metres. The instruments were connected to a Bronkhorst control box, which communicated with the FlowWare software which recorded the data from the experiments. Two experiments were conducted for each flow rate and the data from the experiments was used to calculate Darcy permeability (Eq. 2.2) and Re (Eq. 2.1). The fluid used in the experiments varied depending on the sample and the experimental objective. For the non-reactive fluid flow experiments, using synthetic samples 1-4, deionised water was used. For the reactive fluid flow experiments, using synthetic samples 8-11, both deionised water and HCl were used. Deionised water was initially used in experiments to collect data on the samples prior to reactive fluid flow. The samples were then flooded with HCl (pH 3.1) at a constant flow rate, 0.03 ml/min, for three hours. Afterwards the sample and experimental system were flushed with deionised water at a constant flow rate, 0.03 ml/min, for one hour to ensure all acidic fluid was removed and any mineralogical reactions were stopped. Deionised water was then used again in experiments to collect data on each sample (8-11) after reactive fluid flow.

### 3.4 Inductively Coupled Plasma - Optical Emission Spectrometry (ICP-OES)

The flow output from each reactive fluid flow experiment was analysed using ICP-OES. ICP-OES assesses the chemical composition of the fluid, which determines which minerals have been affected

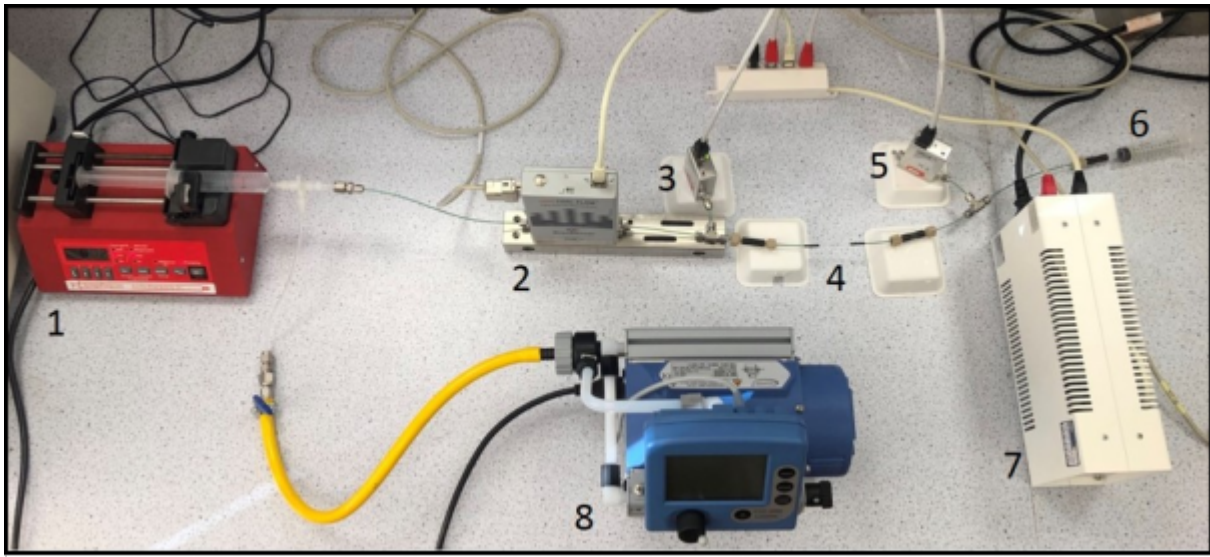


Figure 3.4: Experimental set up for the pore-scale permeability experiments: 1) syringe pump, 2) flow metre, 3) inlet pressure metre, 4) synthetic sample, 5) outlet pressure metre, 6) drain syringe, 7) control box, and, 8) diaphragm vacuum pump.

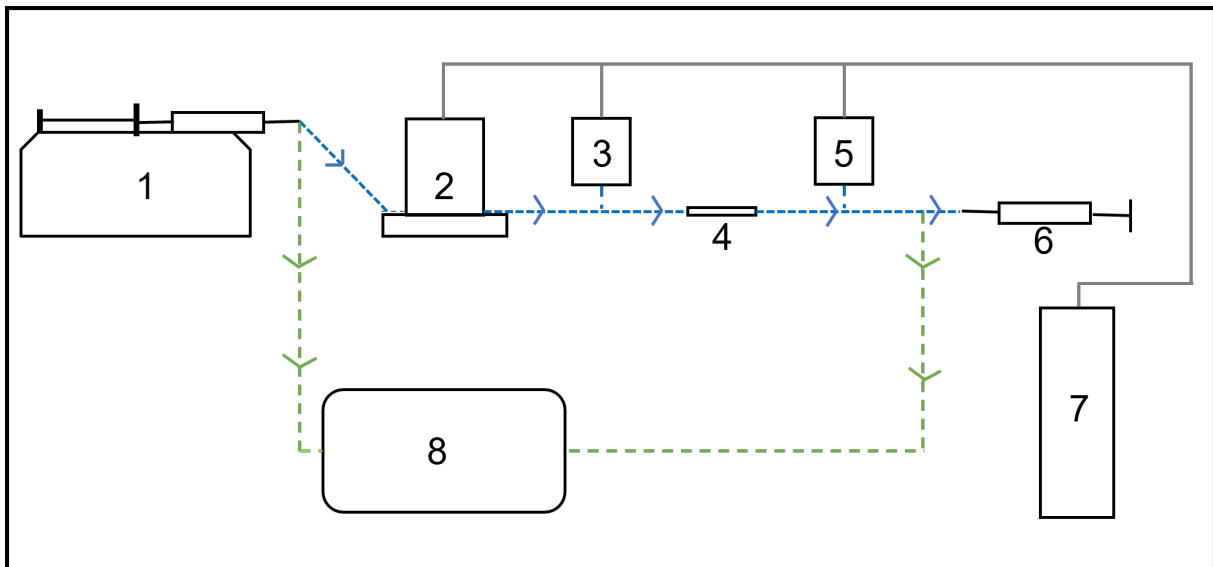


Figure 3.5: A schematic of the experimental set up for the pore-scale permeability experiments: 1) syringe pump, 2) flow metre, 3) inlet pressure metre, 4) synthetic sample, 5) outlet pressure metre, 6) drain syringe, 7) control box, and, 8) diaphragm vacuum pump. The blue line represents the route which fluid takes through the experimental system. The green line represents the direction of air when the system is being degassed. The grey line represents electrical connections.

by reactive fluid flow induced dissolution. ICP-OES is a multi-elemental analysis technique which uses inductively coupled plasma to produce atoms and ions that emit electromagnetic radiation at wavelengths. For analysis, flow outputs were injected into a radio frequency – induced argon plasma. After injection, the sample dries and becomes vaporised and energised through collisional excitation at a high temperature. The emitted wavelength is collected by a lens and imaged. Each element has a characteristic wavelength and the intensity of the wavelength correlates with the concentration of the element. The combination of elements identified in the flow output are used to identify minerals. For example, if the results show high calcium and magnesium concentrations it is likely that dolomite has been dissolved from the sample. A Perkin Elmer Inductively Coupled Plasma Optical Emission Spectrometer was used to conduct elemental analysis and the instrument has a detection limit of 0.1 mg/L and analytical uncertainties within the order of  $\leq 5\%$ . Calibration standards from 0.1 to 30 mg/L were prepared from 100 mg/L standard solution from Fischer Chemical, for the elements Si, Al, Ca, and Mg. For the fluid samples measuring Ca and Mg, 1/2 dilutions are made with 2% HNO<sub>3</sub> and measured, along with the full concentration fluids. The fluid samples measuring Si and Al were not diluted as only low levels of Si and Al were expected in the fluid samples. Duplicate samples (from duplicate reactive fluid flow experiments) were analysed to ensure reliable results.

### 3.5 Avizo® Fire Image Processing and Permeability Simulations

The XRCT scanned images of the synthetic samples were inputted into the Avizo® Fire 8.1 software for image processing and analysis. The image stack was smoothed to remove excessive noise from the images using a non-local means edge preserving filter before segmentation occurred. Segmentation into binary images was performed by using the Interactive Thresholding module. Once processed the image stack was analysed to gain information on porosity and pore diameter. Porosity was measured using the ASBMR Porosity module which measures the porosity of the image stack slice by slice. Pore diameter was measured by creating a label field of the image stack. 3D fluid flow simulations were performed using the Absolute Permeability Experimental Simulation module, which is part of the Avizo XLab Hydro Pack. The fluid flow simulations calculated absolute permeability for single phase fluid flow by solving a simplification of the Navier-Stokes equations:

$$\begin{aligned}\nabla \cdot \vec{V} &= 0 \\ \mu \nabla^2 \vec{V} - \vec{\nabla} P &= 0\end{aligned}\tag{3.2}$$

where  $\vec{V}$  is the velocity vector,  $\mu$  is the dynamic viscosity and  $P$  is the pressure. The assumptions are: a) an incompressible fluid with a constant density, b) a Newtonian fluid with constant dynamic viscosity, c) a steady state flow, and, d) a laminar flow. After this, Darcy's Law (Eq. 2.2) is applied and the permeability is calculated. The boundary conditions for the fluid flow simulations are specified by: a) a no-slip condition at fluid-solid interfaces and b) one voxel wide plane of solid phase (with no slip condition) is added on the faces of the images that are not perpendicular to the main flow direction. Two of the following boundaries can be selected by the user; input pressure, output pressure, fluid flow rate. The third boundary is estimated from the chosen two. In this study input pressure and output pressure was selected, leaving fluid flow rate to be estimated by the software. The pressure values inputted were recorded from the pore-scale permeability experiments (Appendix B) and the simulations were conducted in the  $z$  direction. The advanced settings of the simulation were also modified and the convergence criterion was set at  $1 \times 10^{-6}$  and minimum iterations was set at 500 and maximum iterations was set at 15000.

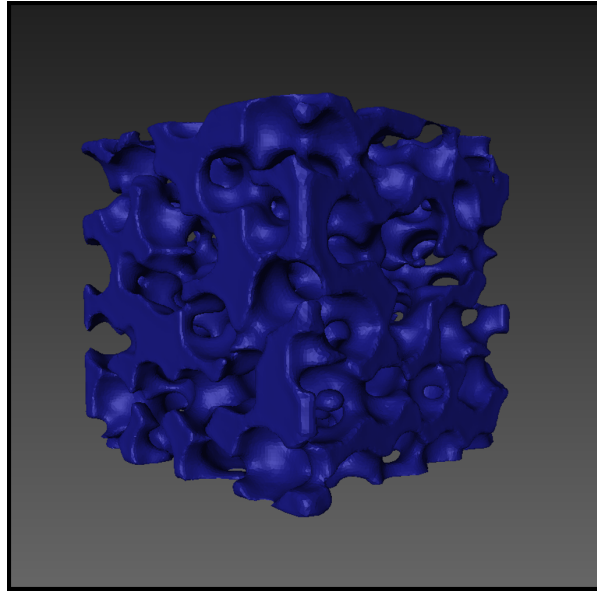


Figure 3.6: The  $400\ \mu\text{m}^3$  tetrahedral mesh generated in the Avizo®Fire software for sample 1.

The fluid flow simulations were conducted on five zones throughout the sample to ensure that the results were representative of the sample. The five zones within each sample correspond to the five image stacks used in 2D porosity analysis in the ImageJ software. The Avizo®Fire software was also used to generate  $400\ \mu\text{m}^3$  tetrahedral meshes (Fig. 3.6) representative of selected zones in the synthetic samples. The meshes were made by applying the Generate a Surface module to the segmented image stack, which was then smoothed and enhanced using the surface editor. After this the Generate a Tetrahedral Grid module was applied and the mesh was exported into the ANSYS Fluent software. It was essential for the tetrahedral meshes not to exceed  $400\ \mu\text{m}^3$  due to the time constraints and to maintain high resolution. The bead pack samples present complex geometries and mesh generation was a time consuming and difficult process which could take between 4 - 48 hours depending on the complexity of the sample. The more complex samples required more processing before mesh generation could occur. Additionally, numerous meshes had to be remade after fluid flow simulations failed in the ANSYS Fluent software and this is interpreted to be a result of the occurrence of closed pores in the samples which may have blocked fluid flow in the simulations and resulted in failure. The occurrence of closed pores is random and therefore difficult to predict when selecting areas of the samples to generate into meshes.

### 3.6 ANSYS Fluent Simulations

Computational fluid dynamics (CFD) was used to study the impact of variable bead pack sample properties at the pore-scale and to analyse the impact of changing properties on fluid flow behaviour. The CFD simulations were performed using the ANSYS Fluent R2 2020 software to calculate the pressure drop and velocity of fluid and from those the permeability, Re and flow regime and tortuosity could be deduced. Tetrahedral meshes were generated in the Avizo®Fire software, which can export meshes directly in ANSYS Fluent format. The flow direction was aligned with the  $z$ -axis.

Steady state, laminar simulations were performed using water with a viscosity of  $1.00 \times 10^{-3}$  Pa.s and density of  $998.2\ \text{kg/m}^3$ . The static pressure on the inlet plane (at  $z = 0$ ) was fixed at a particular



value and was fixed at 0 Pa on the outlet plane. These pressures are effectively gauge pressures, since it is the pressure gradient which drives the flow. Since the mesh used was only a small portion of the sample used in the experiments, the approximate pressure drop across the mesh was calculated, scaled down from the pressure drops seen in the experiments. It was possible to increase the pressure on the inlet plane beyond the limits of the experimental campaign in order to explore the onset of non-Darcian flow. The parameters for the simulations for each mesh are recorded in Appendix C.

The simulations were run for 4000 iterations to ensure the results (pressure, velocity) had stabilised prior to data collection and once completed the area-weighted average pressure on the inlet and outlet of the sample was computed (to confirm it was close to the values set on the boundaries) and, most crucially, the mass flow rate through the inlet plane of the sample was calculated. The latter, combined with the pressure gradient across the mesh, leads directly to the permeability.

In addition, in some case, planes were created at various distances through the meshes, which could be used to show the transition between of pressure in the streamwise direction, allowing the effects of changing bead diameter, for example, to be analysed.

Using the results from the simulations permeability was calculated using Darcy's Law (Eq. 2.2) and tortuosity,  $\tau$ , was calculated by

$$\tau = \frac{\langle u \rangle}{\langle u_x \rangle} \quad (3.3)$$

where  $\langle u \rangle$  is the average magnitude of the intrinsic velocity over the entire system volume and  $\langle u_x \rangle$  is the volumetric average of its component along the macroscopic flow directions.

The computer used to conduct the simulations was a Lenovo ThinkStation P330 with an Intel I5-9500 CPU (3 GHz) with 6 cores. The computer also had a NVIDIA Quadro P2000 GPU which was required to conduct the Avizo®Fire permeability simulations.

## Chapter 4

# Design and Development of Pore-Scale Permeability Experiments

### 4.1 Introduction

The permeability and controls on permeability in sedimentary reservoir rocks have been extensively studied using a variety of techniques across a range of scales for applications such as ground water modelling, enhanced oil recovery and carbon capture and storage (Datta et al., 2013). Permeability is an important property to understand as it is considered as one of the governing factors on oil and gas production rates (Bernabé et al., 2016). Despite this, there is little information about permeability at the pore scale, and how pore network geometry, permeability and fluid behaviour impacts the fundamental processes of transport phenomena at the pore scale even though pore scale processes control larger scale processes (Culligan et al., 2006). Furthermore, many of the controls on reservoir rock permeability and fluid flow characteristics are typically analysed at the core-reservoir scale although many of the properties which contribute towards permeability occur at the pore-scale ( $\mu\text{m}$ ), such as pore size, pore throat size and pore connectivity. Additionally, analysis at the pore-scale provides more detailed information about porosity, permeability, flow properties and fluid transport phenomena than analysis at the core or reservoir scale (Algive et al., 2012). Common experimental methods of studying the permeability of reservoir rocks include core flooding experiments and pore-scale flooding experiments (Reynolds et al., 2014; Rathnaweera et al., 2015). Core flooding experiments provide realistic conditions to study permeability and other flow transport properties, however, core flooding experiments can only provide measurements and analysis of the influences on permeability at the core scale. Additionally, natural samples cannot be preferentially altered (e.g. to isolate specific properties) so the results display the effect of a specific combination of properties on permeability and fluid flow behaviour and the effect of isolated properties cannot be analysed independently. This limits the breadth of analysis and the applicability of the results as properties can vary from pore to reservoir scale and therefore the combination of properties contributing towards permeability and fluid flow behaviour may not be representative of the sample, core or reservoir. On the other hand, pore-scale permeability experiments can provide measurement and analysis of permeability at the pore-scale and many experimental studies use synthetic samples. The type of synthetic sample used varies from 2D samples, such as micromodels or 2D bead packs, flow cells and 3D bead pack samples. Some experimental methodologies can be restricted by the type of sample used, for example, if 2D samples are used, such as micromodels or 2D bead packs, the results are less realistic as permeability is impacted by properties which occur in 3D rather than 2D. Furthermore,

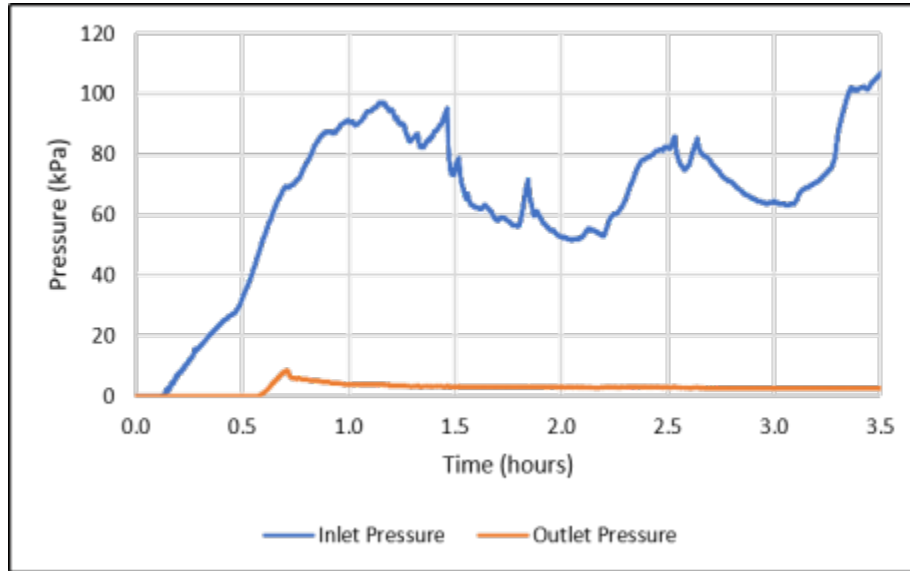


Figure 4.1: Unstable pressure results from the original configuration of the experimental system. The inlet pressure continuously increases whereas the outlet pressure does not increase. Additionally, the flow rate also fluctuated consistently.

many experimental methodologies use different techniques to degas the experimental system, which ensures that pressure is stable during experiments. Different techniques can produce variable results and less effective techniques may produce erroneous data, which limits the reliability of results from the experimental system. Often, the technique(s) used for degassing an experimental system is based on the experimental objective(s), for example, flushing a fluid through the system prior to the experiments is often used for multi-phase experiments. Due to this, this chapter evaluates the existing methodologies and sample types used in pore-scale permeability experiments and proposes a new experimental methodology and sample type which have been designed and developed for pore-scale permeability experiments. The aim of the experimental methodology is to measure and analyse the effects of different reservoir rock properties, which are often characterised at the core scale (e.g. grain size, grain sorting, mineralogy), on pore network geometry, permeability and fluid flow transport properties (e.g. Reynold's number) in 3D and how these are altered after a reactive fluid flow. The type of synthetic samples used in the experiments were designed to isolate the effect of different sedimentary rock properties (e.g. mineralogy, grain size) on pore network geometry, permeability and fluid flow transport behaviour at the pore scale in 3D. The final developed methodology used for the pore scale permeability experiments is detailed in Chapter 3.

## 4.2 Experimental Design and Development

The main requirement for the experimental system is to continuously pump a single phase fluid through a sample and measure the flow rate and pressure drop over a 3D bead pack sample. The experimental system was also required to be compatible with fragile and small scale samples which could be easily changed ( $1 \times 1 \times 33$  mm).

The first design for the experimental system included a syringe pump, flow metre, inlet pressure metre, synthetic sample and an outlet pressure metre. Initial tests using this design produced unreliable results as pressure continuously increased with time and did not stabilise (Fig. 4.1).

To stabilise the pressure in the system a number of solutions were employed, which included increasing the duration of sample/system flooding, alteration of flow rates used prior and during the experiments, syringe pump calibration, alteration of unions and connections between the tubing and instruments, addition of a syringe at the end of the system, addition of vacuum grease, addition of a vacuum pump and alteration of the evacuation times prior to experiments. The first solution trialled to stabilise pressure in the system was increasing the duration of flooding. Experiments were conducted for up to a period of 7 hours, however, no effect on pressure was recorded and the pressure continued to increase with time. The next solution trialled was to alter flow rates during flooding. Flow rate was increased to the highest flow rate used in the experiments (0.030 ml/min) and left running for up to 7 hours to purge the experimental system of air, however, this method also did not impact the pressure in the experimental system. To eliminate another potential contributing factor towards pressure instability the syringe pump used in the experiments was calibrated and a second syringe pump was also trialled. The syringe pumps were calibrated by the flow metre and also manually by recording the amount of fluid ejected from the system over a length of time. Furthermore, all unions, connections and tubing between the instruments were replaced to ensure no damage had occurred, which could have resulted in blockages and caused a build up in pressure. Additionally, the replacement unions and connections were changed from PEEK PTFE fittings to steel Swagelok fittings to ensure the system was airtight. Despite these changes pressure in the experimental system remained unstable. The next solution trialled was the addition of a syringe at the end of the system to regulate back pressure and collect fluid from the experiments. This syringe was also inserted into an additional syringe pump which withdrew air from the system, however, this also did not impact pressure readings. A vacuum pump was then connected to the system and used to evacuate the system over different periods of time (10-40 minutes). Vacuum grease was added to the o-ring of each syringe to ensure the system was airtight. It was found that 20 minutes of evacuation was a sufficient amount of time to stabilise the system. After evacuation the system and sample were flooded and the pressure stabilised (Fig. 4.2), but the length of time required for pressure stabilisation was dependent on the flow rate used in flooding. Higher flow rates resulted in pressure stabilisation occurring sooner, for example, for the lowest flow rate (0.010 ml/min) stabilisation occurred on the second day of the experiment, after approximately 8-10 hours of fluid flow, whereas at the highest flow rate (0.030 ml/min) stabilisation occurred after approximately 1-2 hours. Despite this, the experiments were still conducted over the course of 2-3 days to give the system optimal time to saturate and stabilise even if fluid was not pumping. The flooding flow rate was kept consistent with the flow rate used in the experiments to minimise disruption in the experiments and to preserve sample structure. When a higher flow rate was used to flood the system prior to an experiment with a lower flow rate the system required additional time and fluid to re-stabilise to the lower flow rate, which resulted in the system filling too quickly for results to be taken. Additionally, the samples used are fragile and experiments with higher flow rates were conducted last to maintain the sample integrity and avoid any possible damage from faster fluid flow and higher pressure levels within the sample.

### 4.3 System Performance

The system was flooded with deionised water from 2 - 10 hours for each experiment prior to data collection. Deionised water was used as the glass beads which compose the samples are water wet so deionised water occurs as the wetting phase. Additionally, using deionised water prevents any potential alterations of the sample as it is a non-reactive, neutral fluid. Whilst the system was flooded, and the sample was becoming saturated, the flow rate, inlet pressure and outlet pressure

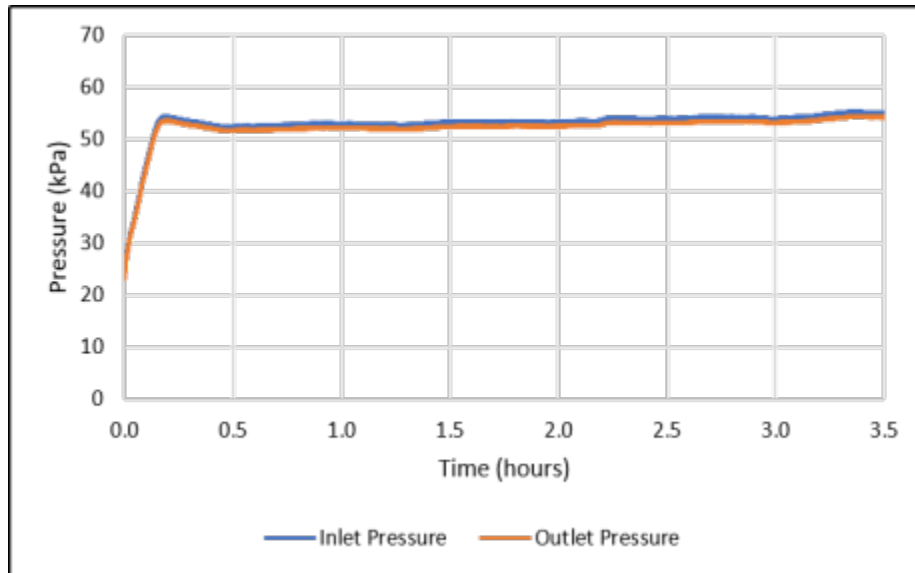


Figure 4.2: Stabilised pressure results and minimal fluctuation in flow rate after adjustments to the experimental system. Some minor fluctuations are expected in flow rate due to the horizontal movement of the syringe pump.

values were variable. After flooding was completed, and the system and sample were saturated, pressure stabilised and results were recorded for a minimum period of 30 minutes. The system is capable of running for as long a period of time as required, as long as there is sufficient fluid to pump, a sufficient catchment for the fluid to drain into and the pressure limit (300 kPa) and flow rate limit (3.267 ml/min) are not exceeded. If the syringe which collects the drained fluid becomes filled, the pressure values begin to increase rapidly. A 20 ml syringe was selected to pump the fluid through the system. This size was selected as it was the largest syringe which was compatible with the syringe pump, thus allowing the experiments to run over long periods of time without interruption. A 12 ml syringe was used to collect the fluid draining from the system and to regulate back pressure. This size was chosen as it had minimal effect on the pressure values and fluid flow. A larger syringe (60 ml) was trialled, however, this initially required a much higher pressure to push the syringe plunger so that the fluid could drain into the syringe, resulting in a back log of fluid flow which caused the syringe pump to stall. The experiments ran from 8 - 17 hours depending on the flow rate. The experiments were conducted at five flow rates; 0.010 ml/min, 0.015 ml/min, 0.020 ml/min, 0.025 ml/min and 0.030 ml/min. Multiple flow rates were used in the experiments to analyse and predict how flow rate influences fluid flow behaviour and patterns. Low flow rates were chosen as when using a syringe pump lower flow rates are expected to be more consistent and stable than higher flow rates. Additionally, lower flow rates were also chosen as typical reservoir flow rates are also very low ( $< 1$  m/day or  $< 0.7$  mm/minute) (Dawe et al., 2011). During the trial experiments to assess the reliability of the experimental methodology the sample used was a sintered 3D bead pack (discussed in Chapter 3) composed of 75  $\mu$ m acid washed glass beads.

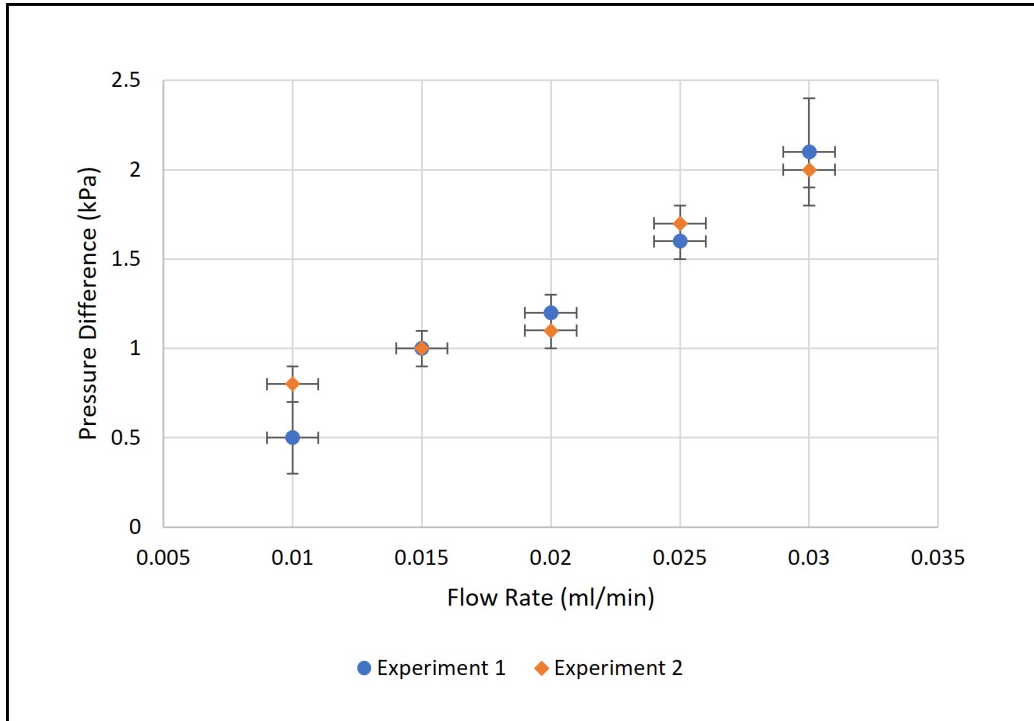


Figure 4.3: Results from the trial pore-scale permeability experiments.

## 4.4 Results

### 4.4.1 Results from the Pore-Scale Permeability Experiments

Two sets of experiments were conducted to assess the reliability of the data acquired from the experimental system. The results from the experimental system include the flow rate and pressure drop over the sample which were used to calculate permeability and the Reynold's number ( $Re$ ).

The results from both sets of experiments show a linear relationship between pressure difference and flow rate, where pressure difference increases with increasing flow rate (Fig. 4.3). The error bars shown in Figure 4.3 were calculated from the standard deviation in the results for flow rate (horizontal error bars) and pressure difference (vertical error bars) after the system had stabilised for a minimum of 30 minutes. Results were recorded every 0.1 seconds. The  $R^2$  value for the linear trend line between pressure difference and flow rate is high for both experiments; experiment 1 has a  $R^2$  value of 0.98 and experiment 2 has a  $R^2$  value of 0.93. The permeability for experiment 1 is 3.06 D and the permeability for experiment 2 is 3.05 D which presents a difference of 0.3%. The  $Re$  is also calculated from each experiment and is calculated using the pore diameter length (9.13  $\mu\text{m}$ ). The  $Re$  ranges from  $1.52 \times 10^{-3}$  -  $4.56 \times 10^{-3}$ .

### 4.4.2 Results of Permeability using the Kozeny-Carman Model

The permeability of the sample was also calculated using the Kozeny-Carman model (Eq. 3.1) to assess the reliability of the results from the pore-scale permeability experiments. The Kozeny-Carman model uses the porosity of the sample to calculate permeability. The porosity of the sample was calculated from XRCT images of the sample in the Avizo®Fire software (see Chapter 3). Porosity was measured for five zones and the porosity ranges from 16.39 to 21.15% (Fig. 4.4) and

the average porosity for the sample is 18.72%. The range in porosity may have occurred due to the sintering process and beads in the lower half of the sample may have been more greatly sintered than the beads in the upper half of the sample. Due to this, the porosity may be lower in the lower half of the sample and greater in the upper half of the sample. The permeability of the sample was also calculated for five zones of the sample and ranges from 2.40 to 4.59 D (Fig. 4.4) and the average permeability for the sample is 3.20 D. This result corroborates the results from the pore-scale permeability experiments and there is 4.3-4.7% difference between the experimental and Kozeny-Carman model results.

## 4.5 Discussion

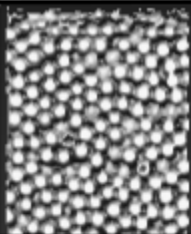
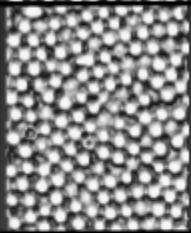
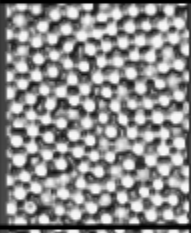
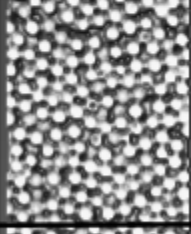
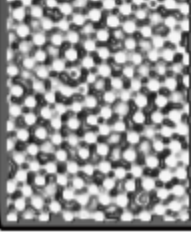
### 4.5.1 Evaluation of the Sample Type and Experimental Methodology

Numerous approaches detailing how to inject steady state fluid flow into a porous sample are described in the literature and each approach is tailored to the type of sample used in the experiments and the user specific objectives for the experiments.

#### Evaluation of Sample Type

3D synthetic bead pack samples were used in the experiments in this study but other sample types described in the literature include 2D bead packs, 2D micromodels, microfluidic channels, flow cells and rock samples. 3D bead pack samples were chosen as they can represent a simplified version of a sandstone pore network and the properties of the 3D bead pack sample (e.g. particle size, particle shape, composition, wettability) can be modified to mimic realistic rock properties which can be easily controlled to focus analysis on different properties and the complexity of the sample can be gradually increased. Additionally, the wettability of the 3D bead pack sample can also be determined by controlling the composition and construction of the sample. For example, the sample was composed of hydrophilic acid washed glass beads to create a water-wet system and the sintering process of the 3D bead pack sample also creates a water-wet system as any impurities in the sample are burnt off or oxidised (Dawe et al., 2011). Furthermore, 3D bead pack samples also allow 3D visualisation of fluid flow through the sample and support additional analysis for the corroboration of experimental results. For example, the results from the permeability experiments can be compared and validated with the permeability results calculated from the Kozeny-Carman model. The Kozeny-Carman model calculates permeability for materials with spherical particles so this would not be applicable for samples such as 2D micromodels, rock samples and microfluidic channels. 2D bead packs can also represent a simplified version of a sandstone pore network and they allow one to design a sample specifically to the experimental objectives, however, 2D bead pack samples only allow analysis over two dimensions rather than three dimensions.

Micromodels, similarly to 2D bead packs, can also represent a simplified version of a sandstone pore network yet limit visualisation and analysis to two dimensions. 2D samples are disadvantageous as fluid will behave differently in two dimensions than in three dimensions and 2D samples can prevent analysis of some aspects of fluid flow, such as relative permeability (Dawe et al., 2011). On the other hand, micromodels are advantageous as they are cost effective, especially when using low cost materials such as polydimethylsiloxane (PDMS), and can be designed specifically for each experimental objective (Zhang et al., 2013; Dawe et al., 2011). For example, the properties in the pore network, such as pore size, pore shape and pore throat size, can be specified and micromodels can be constructed using transparent materials (e.g. glass) to allow visualisation and analysis of fluid flow in the pore network (Sharifpour et al., 2017). The geometry of the pore network in micromodels can

| Sample  | Zone | Porosity (%) | Permeability (D) |
|---|------|--------------|------------------|
|    | 1    | 20.57        | 4.29             |
|    | 2    | 21.15        | 4.59             |
|   | 3    | 16.58        | 2.47             |
|  | 4    | 16.39        | 2.40             |
|  | 5    | 18.92        | 3.47             |

1 mm

Figure 4.4: The porosity and Kozeny-Carman permeability throughout the 3D bead pack sample. In the experiments fluid flows horizontally from zone 1 to zone 5.



be designed using computer graphics software which can be printed using 3D printers or lithography machines. The printed geometry can then be used as a mask to make templates for etching or used for moulds which can be filled with resin or PDMS (Buchgraber et al., 2012; Dawe et al., 2011). Pore network geometry can also be etched onto the chosen material via reactive ion or laser etching processes and the depth of the pattern can also be controlled (Zhang et al., 2011b; Buchgraber et al., 2012). PDMS is often a popular choice for micromodels, but materials such as silicon and glass are also used. PDMS and silicon models are popular to use as they improve the quality of the micromodel as these materials increase the accuracy and precision during the etching of pore network patterns and accommodate smaller pore sizes (few  $\mu\text{m}$  width) (Buchgraber et al., 2012; Perrin et al., 2006). Additionally, some micromodels are composed of two materials, for example, the geometry of the pore network can be designed on one material, such as silicon, and then a glass slide can be attached over the silicon to seal the model and allow visualisation of fluid flow behaviour (Grate et al., 2010). Furthermore, unlike bead pack samples, the wettability of micromodels can also be specified prior to experiments and is controlled either by applying hydrophobic/hydrophilic gel coatings, exposing the micromodel to polymerisation reactions induced by exposure to UV light patterns or soaking the micromodel in solution, such as dimethyldichlorosilane, and then heating (Abate et al., 2010; Buchgraber et al., 2012; Dawe et al., 2011). Alternatively, 3D bead packs are also cost effective and can be designed specifically for each experimental objective, as done in this study, and allow visualisation and analysis of fluid flow in the pore network across three dimensions rather than two.

Microfluidic channels are also used in pore scale experiments and are micrometre sized flow channels which are efficient in visualising fluid flow velocity with minimal interference. Microfluidic channels can also occur in stacks, consisting of an interface layer, a flow layer and a bottom layer (Gale et al., 2018). Microfluidic channels are commonly used to support additional applications, such as particle tracking velocimetry (PTV), as they can easily be attached to microscope slides for microscopic analysis. Moreover, they can also be cost effective to use as they can be designed from inexpensive materials such as PDMS. Microfluidic channels are also relatively simple and quick to fabricate and allow control over layer depths (Gale et al., 2018). However, using microfluidic channels can limit analysis and experimental objectives as microfluidic channels often present unrealistic and idealised conditions for fluid flow.

Flow cells are also used in studies which focus on fluid flow across 2D or 3D samples. Flow cells are similar to bead packs and micromodels as the composition/design of the sample can be specified for each experiment. However, flow cells are much larger than bead packs and micromodels (cm-m scale) and the sample used cannot be as easily changed between experiments as they are often encased between instruments (Imhoff et al., 1996).

Rock samples can also be used in fluid flow experiments and are advantageous as they represent realistic conditions. Despite this, rock samples can increase complexity during analysis as contributing factors on fluid flow behaviour, such as wettability or pore size, cannot be controlled. Therefore, the results from experiments which use rock samples are unique to that particular sample and the unique set of properties that the sample has. On the other hand, influencing factors on fluid flow and the pore network geometry, such as particle size, particle shape, composition and wettability, can be controlled in synthetic samples, such as 3D bead packs, 2D beadpacks and 2D micromodels, which allows analysis of the direct impact of individual properties on fluid flow behaviour.

Due to the reasons outlined and the aims of this study a 3D bead pack sample was used as this sample type provides an interchangeable, controlled environment to study pore-scale permeability and supports pore network and fluid flow visualisation. Using 3D bead pack samples enables analysis

of the effects of different sedimentary properties found in reservoir rocks, such as particle size, particle sorting and mineralogy, on permeability at the pore-scale as each sample can be tailored to focus on different independent properties or different combinations of properties. The effect of the different sedimentary properties can be isolated when using 3D bead pack samples as other influencing factors can be controlled. Furthermore, 3D bead pack samples are composed of transparent materials (e.g. glass beads, quartz capillary tubes) which allow 3D visualisation of fluid flow and the pore network allowing the effect of pore network geometry on pore-scale permeability to be analysed.

### Evaluation of the experimental methodology

The methodology used in this study was designed to measure a single phase flow rate and the pressure drop over a 3D bead pack sample. Single phase fluid flow was used in the experiments to reduce complexity when analysing the complicated dynamic between heterogeneous sample properties and fluid flow behaviour. The objective of the experiments was to measure the effect of variable pore network geometry, as a result of variable sample properties (e.g. particle size, mineralogy), on permeability at the pore-scale. The methodology used was designed and developed to record reliable and repeatable results from a flow metre, inlet pressure metre and outlet pressure metre. Additionally, the experimental system was required to be compatible with small scale samples (mm). The literature details multiple methodologies to study fluid flow behaviour at the pore-scale, which can be characterised either by the experimental objectives of the study or the method of degassing used in the experimental system, recorded in table 2.1 in chapter 2. In water saturated porous media gas phases (e.g. air) can develop in-situ when the porous media is injected with an aqueous phase (e.g. water) (Enouy et al., 2011). During the injection process the porous medium becomes super saturated with the aqueous phase which can lead to the activation of nucleation sites on solid surfaces and the occurrence of bubbles (Enouy et al., 2011). Increased transport of the aqueous phase leads to an increase in bubble growth and pressurisation of bubbles which is confined in pores by local capillary forces (Enouy et al., 2011). Degassing the experimental system and sample is a vital component of the experimental methodology as it removes the gaseous phase which ensures that the system remains single phase and removes trapped bubbles of air within the system and sample which can cause instabilities in flow rate, prolonged disequilibrium in pressure, increase fluid resistance and interrupt continuous fluid flow. Due to this, a considerable amount of time was spent on the design and development of the experimental methodology to ensure the pressure was stable and the system remained single phase.

In this study a vacuum pump was used to evacuate air from the system and afterwards the system/sample was flooded with deionised water. The results were recorded once the system/sample was saturated, which was indicated by the stabilisation of pressure. Previous studies which measure flow rate and/or pressure drop across a porous sample have used other techniques to degas the system, such as fluid or gas injection. Additionally, some studies do not use a method to degas the system and other studies use multiple methods (e.g. vacuum pump and flooding) to degas the experimental system. The methodologies which do not degas the experimental system and sample prior to experiments are typically experiments which involve multi-phase fluid flow, where the system is initially saturated with the wetting phase which is then displaced by an injected non-wetting phase (Ferrer et al., 2004). Using a vacuum pump, or vacuum chamber, is one method used to withdraw air residing in the experimental system and sample and vacuum pumps/chambers can also be used to saturate experimental systems and samples with fluid which also displaces trapped air bubbles (Perrin et al., 2006). Degassing using a vacuum pump/chamber is effective because of the phenomenon described by Henry's law, which states that the amount of dissolved gas is proportional to its partial pressure above the liquid. Using a vacuum pump/chamber reduces the partial pressure

and solubility of the gas (e.g. air). Saturation is another method used to degas a system/sample and it is popular as it is easily incorporated into the experimental apparatus typically used in pore scale experiments (e.g. syringe pump, fluid reservoir). Saturation occurs as a result of continuous flooding which displaces any trapped air (Chomsurin and Werth, 2003; Dawe et al., 2011; Meghdadi Isfahani and Afrand, 2017) and allows the experimental system/sample to reach equilibrium prior to experiments (Sharifipour et al., 2017). Fluid or gas injection can also be used as a degassing technique and operates similarly to the saturation process as it is dependent on displacement mechanisms. Fluid or gas is injected into the system/sample and displaces trapped air bubbles (e.g. CO<sub>2</sub>) (Krummel et al., 2013; Singh et al., 2017).

Some methodologies may use multiple techniques to degas the experimental system and sample, for example, some studies use a vacuum pump to evacuate the system and then inject CO<sub>2</sub> to further eliminate the occurrence of trapped air (Datta et al., 2014). Using a combination of techniques to degas experimental systems/samples is thorough and effective but it can also be costly in terms of price, time and space, and can be dependent on laboratory facilities and capabilities. The combination of some techniques used to degas an experimental system/sample are more efficient than others, for example, when a system/sample is evacuated using a vacuum pump/chamber the solubility of the gaseous phase is reduced. If the system/sample is then saturated with the aqueous phase after the solubility of the gaseous phase has been reduced then the gaseous phase is easier to displace. Using degassing techniques which use different mechanisms to remove gas is advantageous as it increases the efficiency of gas removal. On the other hand, degassing using a combination of fluid/gas injection and saturation can be less effective as the degassing technique is similar. Using degassing techniques which use similar mechanisms to remove gas is disadvantageous as the efficiency of gas removal is limited. Due to the size of the sample and the instruments the experimental system can be difficult to degas and the trapping of air can occur more readily due to the pressure required for displacement. Capillary pressure increases with decreasing pore size and displacement processes will require a higher pressure than the local capillary pressure for displacement to occur (Kim et al., 2018). This was evident during the development of the experimental methodology, where pressure was unstable when only flooding was used as a method of degassing. Pressure did not reach equilibrium until the system and sample was evacuated with a vacuum pump and the system and sample were flooded. Due to this, it is recommended that two or more different types (e.g. vacuum and saturation or flooding) of degassing techniques which use different mechanisms to remove trapped gas are required when working at the pore scale to ensure reliable results.

#### 4.5.2 Evaluation of the Results

The results from the pore-scale permeability experiments have been evaluated and compared to the results from three different methodologies, including other experimental systems in the literature which measure the permeability of 3D bead pack samples, permeability simulations in the literature and calculations of permeability using the Kozeny-Carman model from this study and from the literature. The comparison of results from three different approaches further validates the results obtained from the experimental system used in this study.

The results for pressure difference and permeability from both experiments are very similar (Fig. 4.3) suggesting that the experimental procedure is repeatable and reliable. The R<sup>2</sup> value for both trend lines is over 0.93 which indicates minimal variation in the results. The permeability results from the experiments are further supported by the permeability results from the Kozeny-Carman model. The Kozeny-Carman permeability results for five zones throughout the sample are consistent and are very compatible with the results from the experiments as there is less than 5% difference between

the average permeability values from both experiments and the average permeability value from the Kozeny-Carman model. Therefore, the experimental system is deemed a reliable and accurate methodology for permeability studies as it has been supported by repeatable results from duplicate experiments and additional results from alternative methods (Kozeny-Carman model).

The results from the experiments are also in strong agreement with the results in the literature. [Muljadi et al. \(2016\)](#) present a permeability of 5.65 D for a lightly sintered 3D bead pack using a numerical simulation at low velocities (0 - 0.0279 m/s) and a permeability of 6.25 D from the Kozeny-Carman equation, which is similar to the average permeability results from the experiments, 3.05, 3.06 D, and the average permeability result from the Kozeny-Carman model, 3.20 D in this study. The slight variation in permeability from each study is due to variation in the methodology used (e.g. experimental methodology or numerical simulation) and the properties of each bead pack sample. Each experiment or numerical simulation will have different objectives and conditions so it is to be expected that results will differ slightly. The bead pack sample used in this study was composed of beads which have a diameter of 75  $\mu\text{m}$ , whereas the bead pack sample used in [Muljadi et al. \(2016\)](#) was composed of beads with a diameter of 100  $\mu\text{m}$ . Particle size is expected to contribute largely to the geometry of the pore network and is associated with pore size, where pore length increases with increasing particle diameter ([Revil et al., 2012](#)). The impact of particle size on permeability is also evident in the results from the literature. [Datta et al. \(2014\)](#) use a lightly sintered bead pack sample composed of beads with a smaller diameter 19  $\mu\text{m}$  than the beads used in this study and in [Muljadi et al. \(2016\)](#) and have a lower experimental permeability (1.64 D) and Kozeny-Carman permeability (1.56 D). [Bijeljic et al. \(2013\)](#), alike [Muljadi et al. \(2016\)](#), use beads which have a diameter of 100  $\mu\text{m}$  and have a very similar permeability of 5.70 D. The results from this study conform with the linear relationship between particle size and permeability (Fig. 4.5) which further validates the results from the experimental system. In addition to validating the experimental results from the pore scale permeability experiments, the results from [Datta et al. \(2014\)](#) and [Muljadi et al. \(2016\)](#) also support the use of the Kozeny-Carman model to validate permeability results. The results from this study, [Datta et al. \(2014\)](#) and [Muljadi et al. \(2016\)](#) all present permeability results acquired from the Kozeny-Carman model which are very similar to the permeability results from numerical simulations or experimental methods (Fig. 4.5), suggesting it is an effective method to use to compare permeability values in homogeneous bead pack samples which have been lightly sintered. Overall, the permeability values from the literature and Kozeny-Carman model are agreeable to the permeability values acquired from the pore-scale permeability experiments used in this study, which further supports the reliability and credibility of the results gained from the experimental system.

### 4.5.3 Applicability of the experimental system

This experimental system enables the measurement of flow rate and pressure drop across interchangeable 3D bead pack samples and the system is also able to incorporate additional techniques such as fluid flow visualisation and fluid chemistry analysis (e.g. inductively coupled plasma - optical emission spectrometry (ICP-OES)). The experimental system is also adaptable to different sample sizes which supports analysis at different scales (e.g. from  $\mu\text{m}$  to cm).

The current set up of the experimental system does not include visualisation, however, this can be easily incorporated. The tubing used between instruments is flexible and the length of the tubing between instruments can be varied, however, this would result in longer evacuation and saturation periods. To visualise fluid flow in the experiments a confocal microscope with imaging capabilities can be included into the experimental system, where the sample resides underneath the microscopic lens. Characterisation of the flow field can then be achieved using particle image velocimetry (PIV),

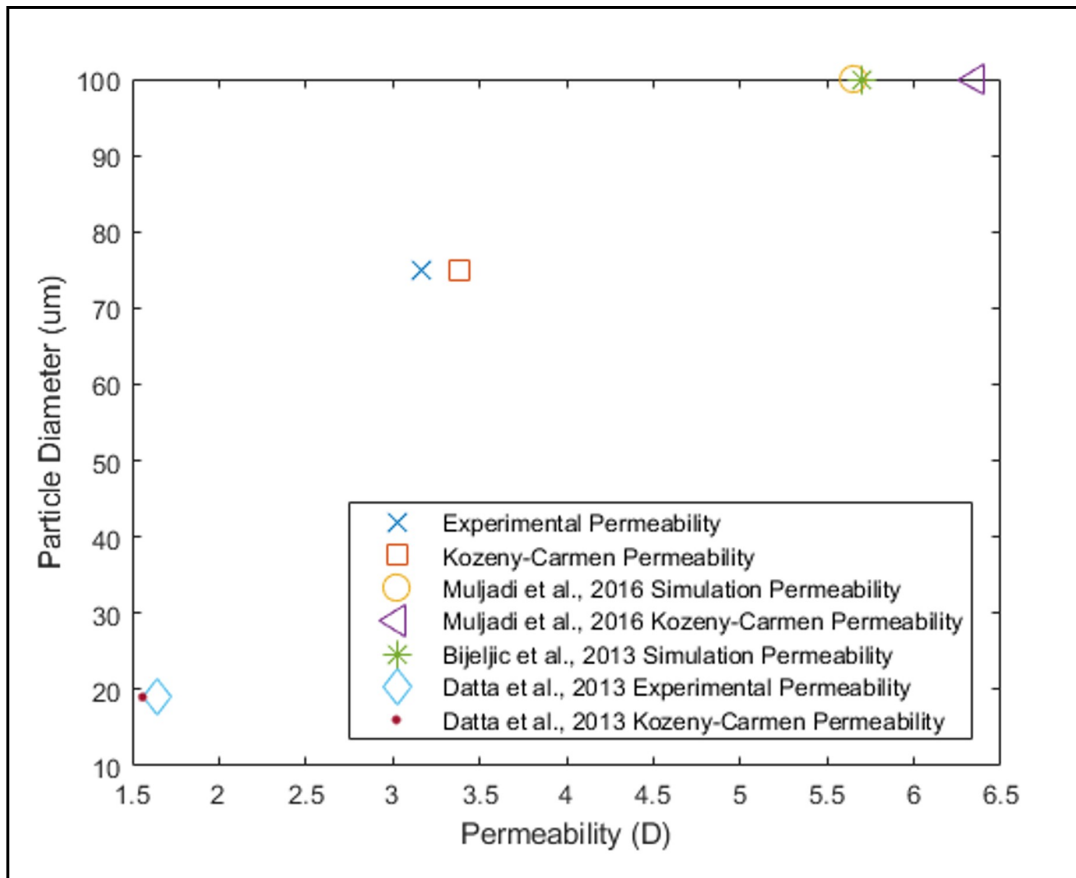


Figure 4.5: A graph showing the relationship between permeability and particle size.

where the fluid flow is seeded with tracer particles prior to the experiment and the velocity field can be characterised by calculating the displacement of tracer particles between each image slice, as described by [Datta et al. \(2013\)](#). Visualisation of multi-phase displacement processes can also be achieved easily using this experimental methodology and sample type with a confocal microscope. A multi-phase system can be created by flushing either a gas or fluid through the system via the syringe pump until saturation is achieved after the system has been evacuated. Once the system is saturated, the second phase can be injected via the syringe pump and analysis can begin. Either phase can be dyed to allow visualisation of displacement processes ([Datta et al., 2014](#)). Analysis of fluid chemistry is also supported by this experimental system. In the experimental set up the output fluid drains into a syringe where it accumulates until the experiment is finished. The output fluid can then be collected for analysis such as ICP-OES, which analyses the chemical composition of the fluid, which is useful in analysing the effects of reactive flow and for contaminant/pollutant tracing.

The experimental system is also capable of supporting studies which use samples with different lengths and scales. In this study the samples used were 1x1x33 mm, however, larger samples can also be used in this experimental system. Larger bead packs, using larger capillary tubes, can be connected by fitting the correct adapters, which would allow analysis in a range of sample sizes from 1 - 6mm diameter. Conducting experiments using samples with increasing size is significant in identifying and validating trends in data and is important for upscaling results, which is typically performed using numerical simulations based on multiple assumptions.

## 4.6 Conclusions

Duplicate experiments have been conducted under the same conditions to verify the reliability and accuracy of the experimental system and the type of sample used.

The experiments which have been conducted confirm that the system complies with the original requirements; 1) introduction of a variable steady state single-phase fluid flow at the pore scale, 2) measurement of fluid flow rate, inlet pressure and outlet pressure at the pore scale, and, 3) easy withdrawal/substitution of small scale, fragile samples without damaging or compromising the integrity of the system.

The experimental methodology enables a user to measure and analyse the pore scale permeability in 3D. Furthermore, the experimental system and type of sample allow a user to measure and analyse the effects of specific reservoir rock sedimentary properties, and different combinations of properties, on the pore network geometry and on pore scale permeability. The type of sample used in this study, a 3D bead pack, also allows the user to isolate the effect of the studied property/properties as other influencing factors on fluid flow behaviour can be controlled.

During the development of the experimental methodology it was observed that a combination of two different types of degassing techniques were required to fully stabilise pressure during the pore scale permeability experiments. The degassing techniques used in this experimental methodology were successful and allowed pressure to stabilise for each experiment ensuring accurate and reliable data was produced from the experimental system.

The experiments have produced reliable and repeatable data. The data from the duplicate experiments shows minimal variation and both sets of experimental data present a linear trend line with a  $R^2$  value  $> 0.93$ . The permeability difference between each experiment was 0.3% and the experimental permeability results are further supported by the permeability values calculated using the Kozeny-Carman model which also show negligible variation from the experimental permeability

results (0.15%).

The experimental permeability and the permeability calculated using the Kozeny-Carman model are strongly corroborated by other permeability studies in the literature. Related studies in the literature show similar permeability results (1.64 - 5.65 D) from experimental and numerical methods and indicate that the pore-scale permeability in 3D bead pack samples increases with increasing bead size. Lower permeability (1.64 D) is observed when the bead size is lower (19  $\mu\text{m}$ ) and higher permeability (5.65 D) is observed when the bead size is higher (100  $\mu\text{m}$ ). The Kozeny-Carman permeability values in the literature further support this trend and also present similar permeability results (1.56 - 6.25 D). This further confirms that the pore-scale permeability experiments are a reliable method to measure permeability at the pore scale.

The experimental system is also able to incorporate additional techniques such as fluid flow visualisation and ICP-OES. Additionally, the experimental system can be used for single-phase or multi-phase studies and can accommodate samples with varying sizes (1 - 6 mm diameter).

## Chapter 5

# How does grain size heterogeneity impact pore network transport properties?

### 5.1 Introduction

Grain size is a sedimentological property in reservoir rocks and the size and distribution of grain size can vary at a multitude of scales ( $\mu\text{m}$ - $\text{km}$ ). The size and distribution of grains can be variable as a result of variable conditions during the time of sediment deposition, structural features, such as faults which may cause displacement of different facies or formations and result in non-uniform grain size distribution, or due to diagenetic processes such as dissolution and precipitation. Variations in grain size can be observed as gradational or abrupt depending on the cause of the grain size variation (e.g. depositional conditions, structural features or diagenetic processes) (Ogbe, 2021). Grain size and the underlying processes which control grain size and distribution of grains are important to understand in reservoir rocks as they contribute towards reservoir quality as they are capable of influencing properties such as packing, porosity, pore system, permeability, hydraulic conductivity, tortuosity and fluid flow pathways (Tiab and Donaldson, 2012; Weltje and Alberts, 2011; Yusuf and Padmanabhan, 2019; Revil et al., 2012; Datta et al., 2013; Yang et al., 2020). Different grain packing types relate to different porosity ranges and porosity also increases with increasing packing density (Weltje and Alberts, 2011). The size of grains can also influence pore connectivity and tortuosity where smaller grains are linked to less pore connectivity and greater tortuosity (Kashif et al., 2019; Yusuf and Padmanabhan, 2019). Furthermore, the size of grains is also associated with the size of pore throats, which in turn is related to the shear resistance to flow (Sperry and Peirce, 1995). Additionally, in recent pore scale experimental and numerical studies it has been well established that grain size influences pore diameter and permeability, where pore diameter and permeability increases with increasing grain size / particle size (Revil et al., 2012; Muljadi et al., 2016; Datta et al., 2013; Bijeljic et al., 2013). However, this relationship is only observed in samples with homogeneous grain size, and it is not well understood how heterogeneous grain size directly impacts porosity, pore diameter or permeability, and how this in turn impacts fluid transport behaviour despite that heterogeneous textures in sandstones are expected to play a vital element in transport behaviour of reservoir fluids and the prediction strategies in petroleum exploration and exploitation (Sun et al., 2007). Additionally, microtextural properties (e.g. pore lining/filling patterns, grain sorting, grain shape and packing density) of sandstones are commonly observed to differ between wells in oil fields so understanding how microtextural properties influence flow properties at the pore scale can aid in future prediction of how microtextural properties influence flow properties at the core and reservoir



scale (Sun et al., 2007). Therefore, this chapter analyses and discusses the results from pore scale permeability experiments and fluid transport simulations performed at the pore - core scale using samples which have different bead sizes and present bead size contrasts (samples 1 - 4) (Fig. 3.3, Table 3.2). Sample 1 is composed of 75  $\mu\text{m}$  beads, samples 2 and 3 are both composed of 75 - 180  $\mu\text{m}$  beads and present bead size contrasts, where sample 2 presents a contrast from larger beads to smaller beads and sample 3 presents a contrast from smaller beads to larger beads, sample 4 is composed of 150 - 180  $\mu\text{m}$  beads. The bead size contrasts within the synthetic samples were based off grain size contrasts identified in the natural rock samples at the core and thin section scale.

## 5.2 Results

The results detailed in this chapter include core characterisation, bead pack characterisation, pore network geometry, permeability from the pore-scale permeability experiments, the Avizo®Fire absolute permeability simulations and from the ANSYS Fluent simulations, the flow regime, fluid flow pathways, permeability and tortuosity.

### 5.2.1 Core Sample Characterisation

The four reservoir sandstone core samples were analysed to identify grain size characteristics. Grain size characteristics were analysed to ensure that the synthetic 3D bead pack samples presented realistic grain size properties. Grain size was analysed at the core and thin section scale. Analysis at the core scale revealed that grain size ranges from 375  $\mu\text{m}$  (lower medium sand sized grains) - 4 cm (large pebbles). Core sample 1 shows the least variation in grain size, 500  $\mu\text{m}$ , and core sample 4 shows the greatest variation in grain size, 187  $\mu\text{m}$  - 4cm (Table 5.1) and consequently, core sample 1 shows a greater level of grain sorting and core sample 4 shows a lower level of grain sorting. Core samples 1, 3 and 4 also display features such as cross bedding, laminations and bands of coarser material, which present grain size contrasts (Fig. 5.1). Core sample 1 (Fig. 5.2) presents 3 bands of coarser material across 2.5 cm section with varying thickness; the top band is 4 mm thick, the middle band is 3 mm thick, and the bottom band is 3 mm thick. In this section the bands of coarser material occur frequently, 8 - 10 mm apart. In core sample 3 the laminations of finer material are thinner and occur less frequently than the bands of coarser material in core sample 1. In core sample 3 across a 16 cm section 6 laminations occur, 5 of which occur in 2 clusters. At the top of the core section a single lamination occurs which is >1 mm thick, then there is a 7 cm gap until an additional 2 laminations occur, which are only 1 mm apart. After a 8 mm gap a cluster of 3 laminations occur which are >1 mm apart. Core sample 4 displays one band of coarser material (2 - 40 mm) which is 30 mm thick across a 7.5 cm core section. Analysis at the thin section scale shows that grain size ranges from 200  $\mu\text{m}$  - 8mm (Table 5.2). Core sample 4 has the greatest range in grain size, 500  $\mu\text{m}$  - 8mm, and core sample 1 shows the lowest range in grain size, 250 - 500  $\mu\text{m}$ . Correspondingly, core sample 4 shows the poorest grain sorting and core sample 1 shows the greatest grain sorting. Core sample 1 shows laminations of coarser grains, 200 - 1000  $\mu\text{m}$ , and core sample 3 shows laminations of finer grains (clay sized < 68  $\mu\text{m}$ ) (Fig. 5.3).

The porosity and median pore diameter of the reservoir sandstone core samples were measured using mercury intrusion porosimetry (MIP) and the porosity ranges from 15.23 - 25.27% (see Table 5.3). Core sample 4 has the highest porosity and core sample 3 has the lowest porosity. The median pore diameter also varies across the four core samples, and ranges from 0.0103 - 0.0169  $\mu\text{m}$ . Core sample 1 has the lowest median pore diameter and core sample 4 has the largest median pore diameter.

Table 5.1: The grain size characteristics of the core samples at the core scale.

| Sample | Grain Size                            | Grain Sorting     | Features                             |
|--------|---------------------------------------|-------------------|--------------------------------------|
| 1      | 500 $\mu\text{m}$                     | Very well sorted  | Moderate angle cross laminations     |
| 2      | 375 - 750 $\mu\text{m}$               | Moderately sorted | -                                    |
| 3      | 500 - 750 $\mu\text{m}$               | Very well sorted  | Clay sized laminations               |
| 4      | 187 $\mu\text{m}$ - 750 $\mu\text{m}$ | Poorly sorted     | Band of coarser material (2 - 40 mm) |

Table 5.2: The grain size characteristics of the core samples at the thin section scale.

| Sample | Grain Size               | Grain Sorting     | Features  |
|--------|--------------------------|-------------------|---|
| 1      | 250 - 500 $\mu\text{m}$  | Well sorted       | Bands of coarser material (200 - 1000 $\mu\text{m}$ ) |
| 2      | 250 - 710 $\mu\text{m}$  | Moderately sorted | Dolomite concretions                                  |
| 3      | 500 - 1000 $\mu\text{m}$ | Well sorted       | Clay sized laminations                                |
| 4      | 500 $\mu\text{m}$ - 8mm  | Moderately sorted | Clusters of dolomite nodules                          |

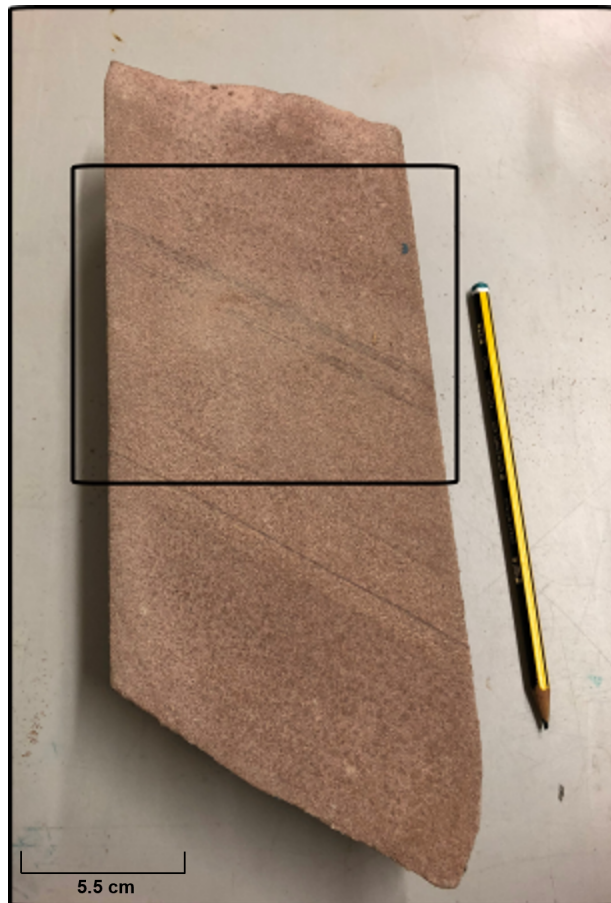


Figure 5.1: Laminations of finer grained material in core sample 3.

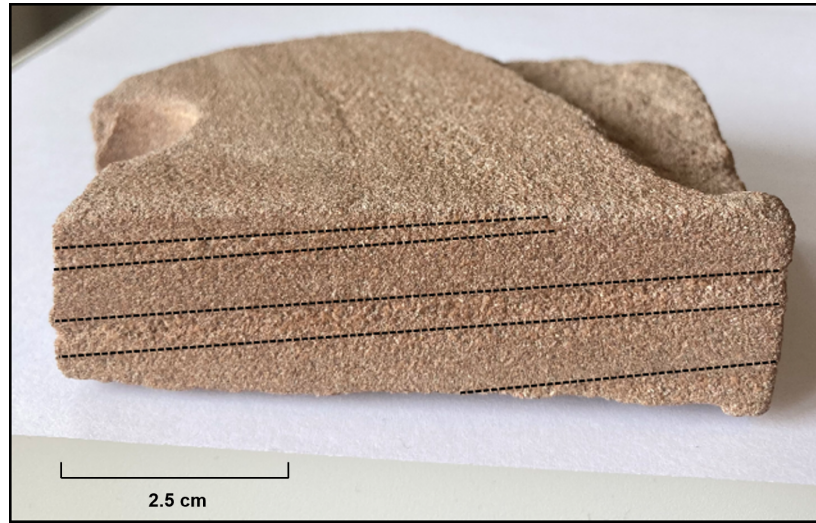


Figure 5.2: Coarser bands of material which has created grain size contrasts in core sample 1. The coarser bands of material are highlighted by the dashed lines.

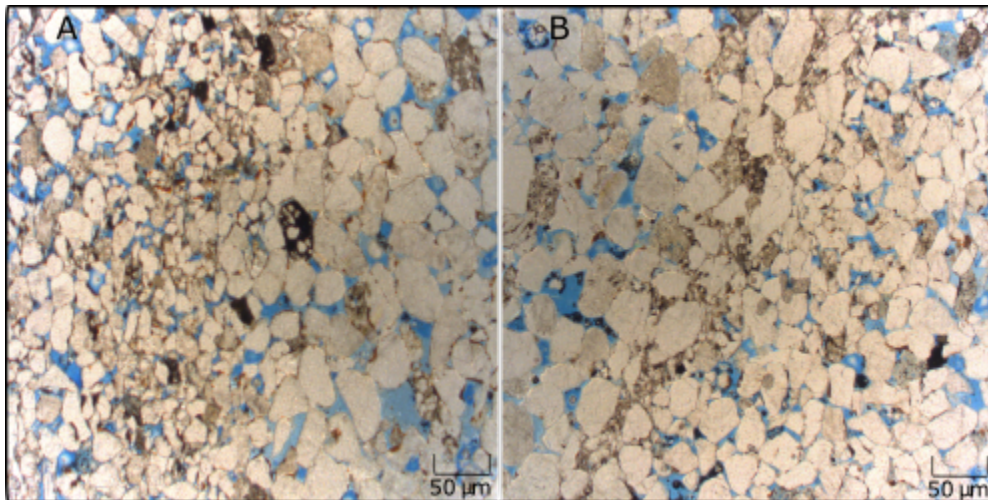


Figure 5.3: Laminations in core samples 1 and 3 at the thin section scale; A shows the contrast between the overall grain size and a lamination of coarser grains in core sample 1 and B shows the contrast between the overall grain size and a lamination of finer grains in core sample 3.

Table 5.3: The porosity and median pore diameter results from the core samples using MIP.

| Sample | Porosity (%) | Median Pore Diameter ( $\mu\text{m}$ ) |
|--------|--------------|--|
| Core 1 | 17.45        | 0.0103                                 |
| Core 2 | 17.50        | 0.0147                                 |
| Core 3 | 15.23        | 0.0146                                 |
| Core 4 | 25.27        | 0.0169                                 |

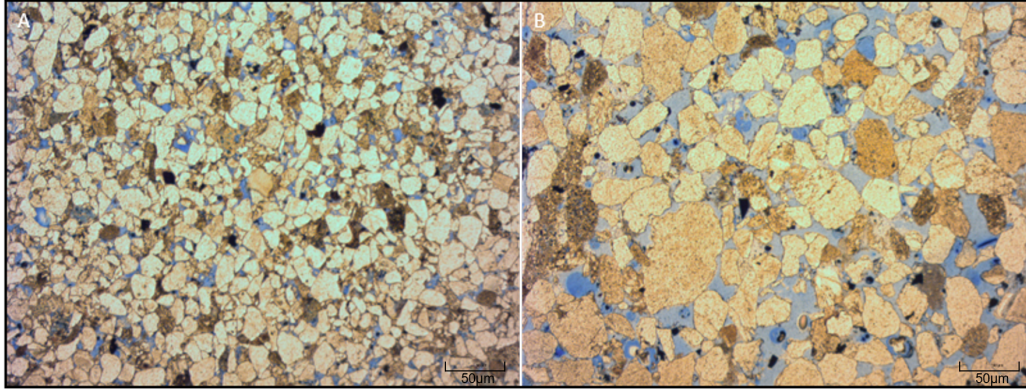


Figure 5.4: The difference in pore space (blue) between core sample 2 (A) and 4 (B).

The porosity of the core samples was also assessed from thin section images using the ImageJ software and core sample 4 has the largest average porosity and core sample 2 has the lowest average porosity and this is demonstrated at the thin section scale by Figure 5.4, where core sample 4 evidently has more pore space (impregnated with blue resin) than core sample 2. The range of porosity values in the core samples was also analysed, and core sample 4 shows the biggest range in porosity values across the thin section sample and core sample 2 shows the smallest range in porosity values across the thin section sample (Table 5.4). The porosity was also measured in another two sections of the core samples 1, 2 and 3 as the properties in the samples were variable at the thin section scale due to the occurrence of a lamination of finer material (Fig. 5.3), and this is reflected by the variability in porosity results. In core samples 1 and 3 the porosity was assessed before (porosity 1) and after (porosity 2) a lamination feature and in core sample 2 porosity was assessed in a homogeneous section (porosity 1) and within a lamination feature (porosity 2). Core sample 2 presents the largest range in porosity, 14.19% - 24.35% and core sample 1 presents the smallest range in porosity, 22.92% - 26.48%.

### 5.2.2 Bead Pack Sample Characterisation

The Avizo<sup>®</sup> Fire software was used to calculate the range of pore diameter size and the pore diameter size ranges from 0.005 - 0.253 mm for sample 1, 0.005 - 0.254 mm for sample 2, 0.005 - 0.276 mm for sample 3, and from 0.005 - 0.297 mm for sample 4 (Fig. 5.5, Fig. 5.6, Table 5.5). Samples 1 and 4 present a bimodal distribution of pore diameter size despite having a unimodal distribution of bead size. This may be due to the type or degree of contact between the beads and the capillary tube wall, which may present a different pore diameter size in comparison to the pore diameter size between sintered, packed beads.

Table 5.4: The porosity results from the core samples using ImageJ analysis. Porosity 1 corresponds to the porosity of the homogeneous areas of the sample and porosity 2 corresponds to the porosity of the heterogeneous areas of the samples (e.g. within lamination features or after lamination features) Please note: only one porosity value was taken for core sample 4 as it displayed no clear contrasts in grain size, grain shape or grain sorting at thin section.

| Sample | Average Porosity (%) | Porosity 1 (%) | Porosity 2 (%) |
|--------|----------------------|----------------|----------------|
| Core 1 | 21.98                | 26.48          | 22.92          |
| Core 2 | 17.10                | 24.35          | 14.19          |
| Core 3 | 18.41                | 17.19          | 14.99          |
| Core 4 | 24.43                | -              | -              |

Table 5.5: The mean pore diameter results from the bead pack samples.

| Sample | Mean Pore Diameter (mm) |
|--------|-------------------------|
| 1      | 0.070                   |
| 2      | 0.072                   |
| 3      | 0.078                   |
| 4      | 0.108                   |

Sample 4 has the largest range in pore diameter and sample 1 has the smallest range in pore diameter. The mean pore diameter size for each sample was also measured, and ranges from 0.067 - 0.108 mm. Sample 4 has the largest mean pore diameter (0.108 mm) and sample 1 has the smallest mean pore diameter (0.070 mm). The mean pore diameter size was also measured throughout the different zones of each sample (Fig. 5.6) and sample 3 shows the greatest variation in the mean pore diameter size across the zones (0.055 mm) and sample 1 shows the smallest difference in mean pore diameter values across each zone (0.009 mm).

When the samples with bead size contrasts (samples 2 and 3) are compared the mean pore diameter size is variable in the zones which have the same bead size. Samples 2 and 3 contain the same range of bead sizes but the arrangement of the bead size is different, as demonstrated in Figure 3.3. This means that certain zones of the samples have the same bead size but occur in a different section of the sample. For example, sample 2 zones 1 and 2 will have the same bead size as sample 3 zones 4 and 5. Despite having the same bead size, (75  $\mu\text{m}$ ) sample 3 zone 5 has 6% larger mean pore diameter than sample 2 zone 1. Additionally, sample 3 zone 1 has a 15.45% larger mean pore diameter than sample 2 zone 5 and both zones have a composition of 150 - 180  $\mu\text{m}$  beads. Furthermore, sample 2 zone 4 has a larger mean pore diameter than sample 3 zone 3 (6.36%) Sample 2 zone 2 shows a minimal variation with sample 3 zone 4 (0.001%) and this is also observed with sample 2 zone 3 and sample 3 zone 3 (0.24%).

The porosity of the bead pack samples was measured using the Avizo® Fire software and the ANSYS Fluent R2 software (see Chapter 3). In the Avizo® Fire software the porosity was measured across five zones (Fig. 5.6), where zone 1 occurs at the top of the sample and zone 5 occurs at the bottom of the sample. The porosity of the ten tetrahedral meshes was also measured using the ANSYS Fluent R2 2020 software and the tetrahedral meshes originate from sample 1 zone 3, sample 2 zones 2-4, sample 3 zones 2-4 and sample 4 zone 3. The porosity of two additional meshes, samples 5 and 6, was also measured in the ANSYS Fluent software and the porosity for sample 5 is 44% and the porosity for sample 6 is 45%.

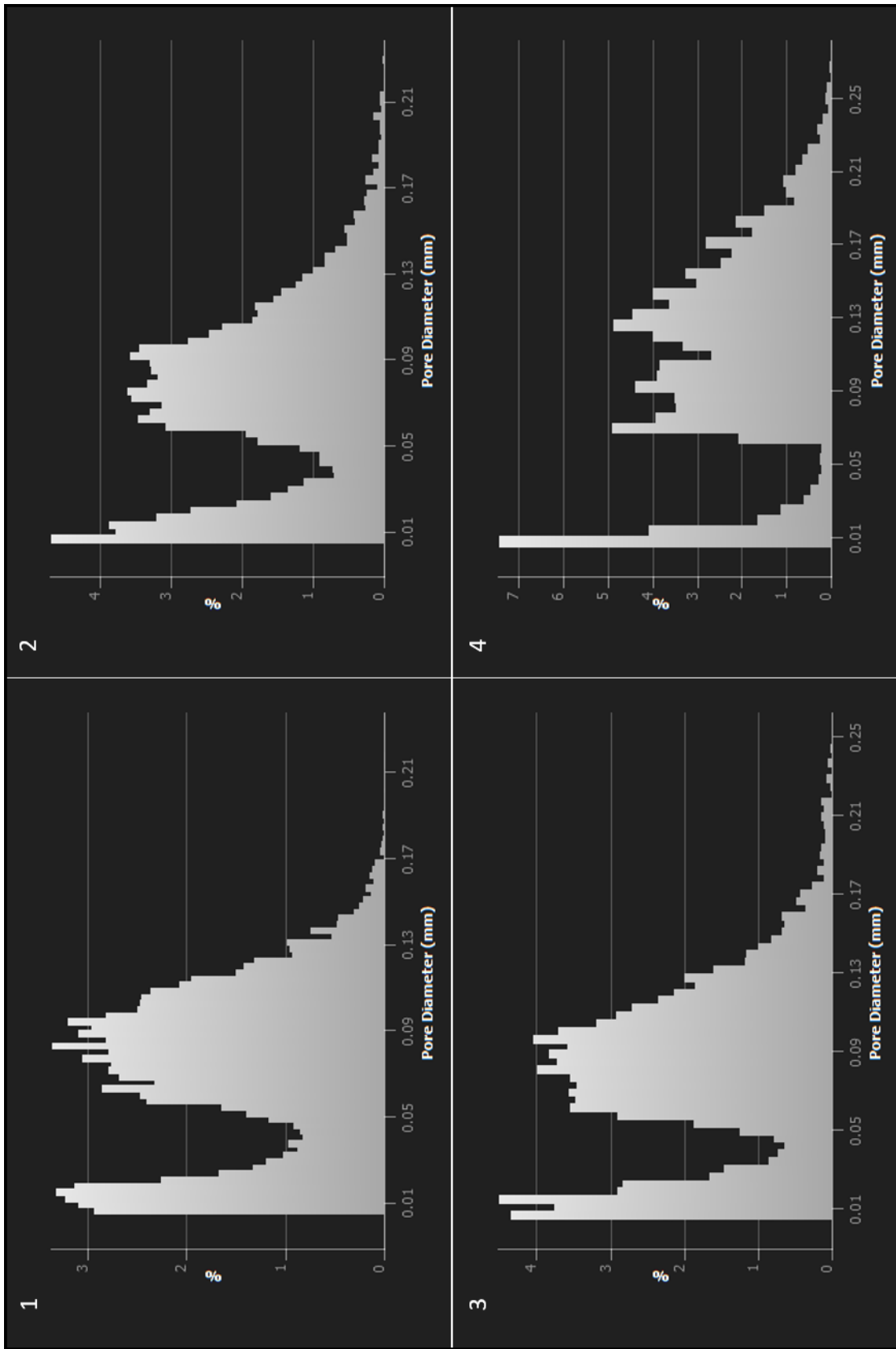


Figure 5.5: The range in pore diameter values for each sample.

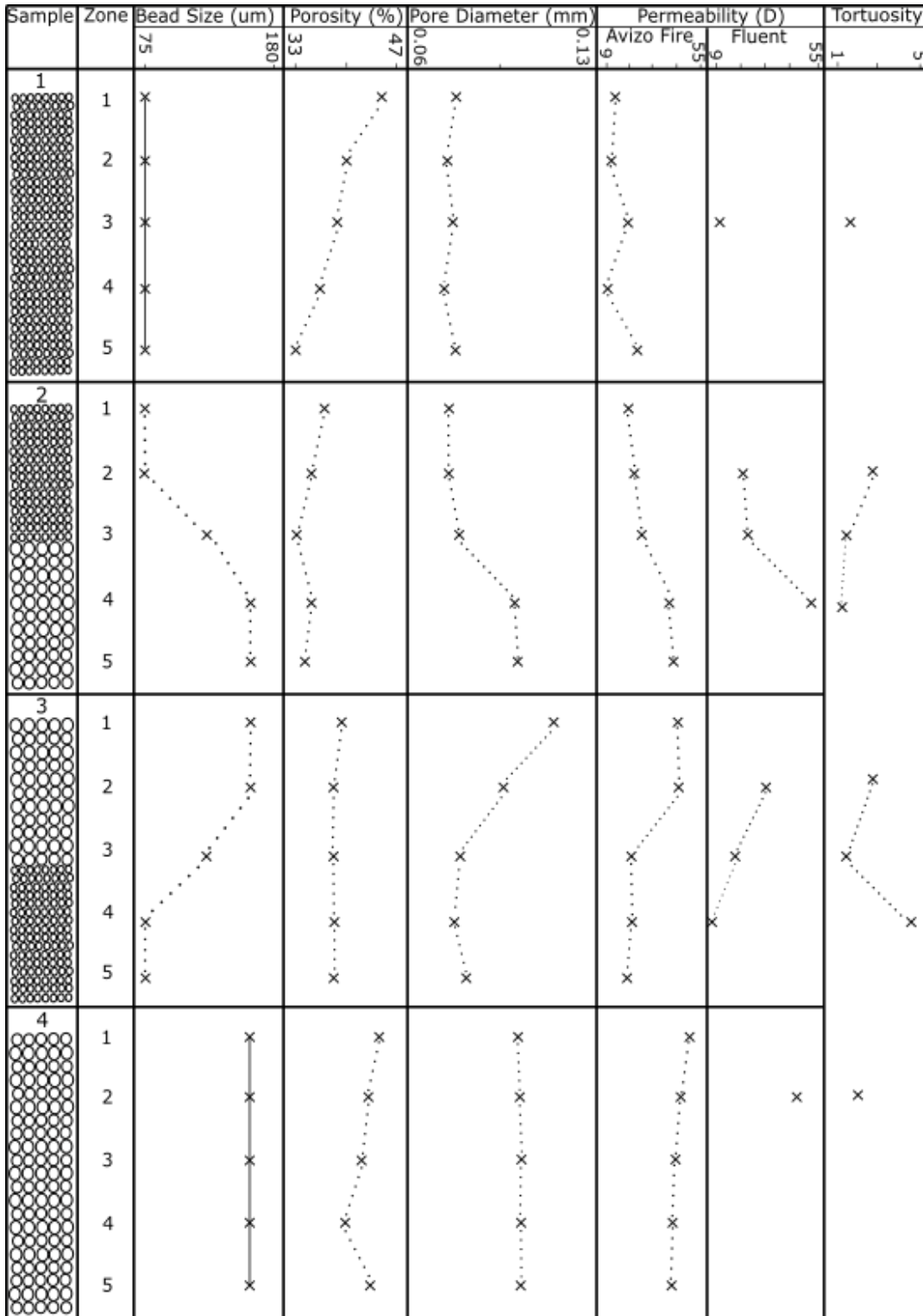


Figure 5.6: A log presenting the pore network properties of the bead pack samples and how they vary throughout the five zones of the sample. The properties were measured across a  $1 \times 1 \times 7$  mm scanned section of the bead pack samples and the porosity used in the log is the porosity measured in the Avizo®Fire software. Fluid flows in the  $z$  direction from zone 1 to zone 5.

Table 5.6: The average porosity results from the bead pack samples and meshes of the bead pack samples.

| Sample | Average Avizo®Fire Porosity (%) | Average ANSYS Fluent Porosity (%) |
|--------|---------------------------------|-----------------------------------|
| 1      | 38.86                           | 43.95                             |
| 2      | 35.25                           | 45.53                             |
| 3      | 37.59                           | 40.30                             |
| 4      | 42.33                           | 44.69                             |

Table 5.7: The comparable porosity results from the bead pack samples and meshes of the bead pack samples.

| Sample | Zone | Avizo®Fire Porosity (%) | ANSYS Fluent Porosity (%) |
|--------|------|-------------------------|---------------------------|
| 1      | 3    | 39.10                   | 43.95                     |
| 2      | 2    | 35.27                   | 50.32                     |
| 2      | 3    | 33.86                   | 40.05                     |
| 2      | 4    | 35.26                   | 46.21                     |
| 3      | 2    | 37.02                   | 40.30                     |
| 3      | 3    | 37.27                   | 38.78                     |
| 3      | 4    | 37.11                   | 41.81                     |
| 4      | 3    | 41.23                   | 44.69                     |

The different techniques used to measure porosity show some variation (5.29 - 22.57%) in the results and overall the porosity results from the Avizo®Fire software are lower than the porosity results from the ANSYS Fluent R2 software. Sample 2 shows the greatest difference in porosity (22.57%) and sample 4 shows the smallest difference in porosity (5.29%).

The porosity results from both techniques show that porosity varies throughout the samples with bead size contrasts, especially sample 2, where porosity ranges from 33.86 - 37.58% in the Avizo®Fire software and ranges from 40.30 - 50.32% in the ANSYS Fluent software. Both techniques show that sample 3 has more consistent porosity than sample 2, and in the Avizo®fire software porosity ranges from 37.02 - 39.06% and in the ANSYS Fluent software porosity ranges from 38.78 - 41.81%. The Avizo®Fire software also shows that there is a lot of variation in the porosity of sample 1 (33.10 - 45.00%).

The packing in the bead pack samples varies and in the samples with homogeneous bead size (samples 1 and 4) the samples present rhombohedral packing (Fig. 5.7). In samples 2 and 3 the packing was assessed in the transitional zone (zone 3) which showed that the packing was more random (Fig. 5.7). In sample 2 smaller beads were observed to fill the pore space and also wedge between larger beads (Fig. 5.8). Fewer beads were observed filling the pore space than wedging between the beads, for example, when smaller beads were observed to wedge in between the larger beads there would typically be 2-3 beads wedged however when smaller beads were observed to fill the pore space there would typically only be one bead filling the pore space. In sample 3 the transitional zone displays a clearer boundary between larger beads and smaller beads and the beads are more well sorted than the beads in the transitional zone of sample 2 (Fig. 5.9). Smaller beads were observed to fill the pore space between some larger beads and the amount of smaller beads which filled the pore space between the larger beads ranged from 1 - 5 (Fig. 5.9).



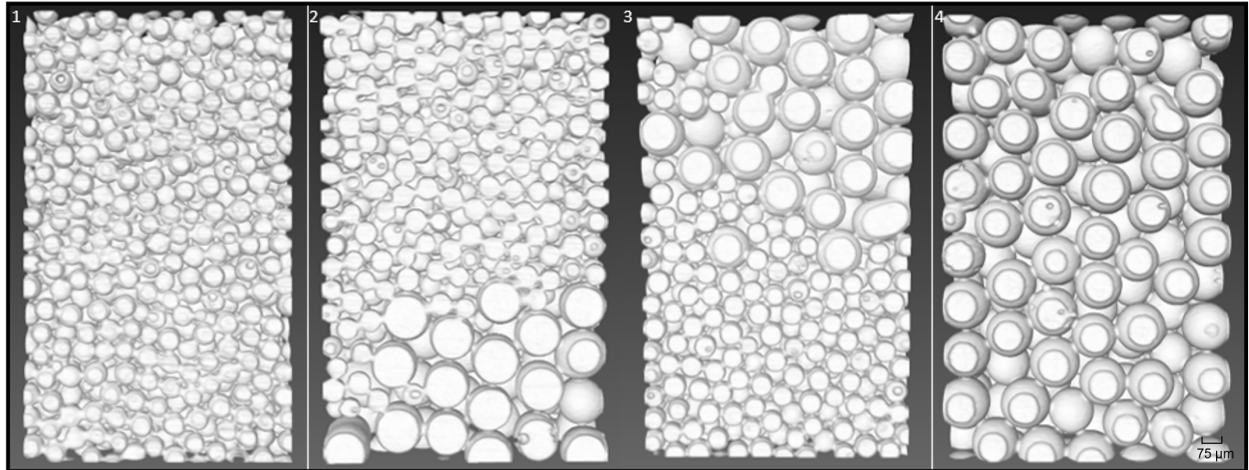


Figure 5.7: The central section (zone 3) of the four bead pack samples. The 3D image of each sample was taken in the Avizo®Fire software and is a 3D render of the image stack from the XCT scan.

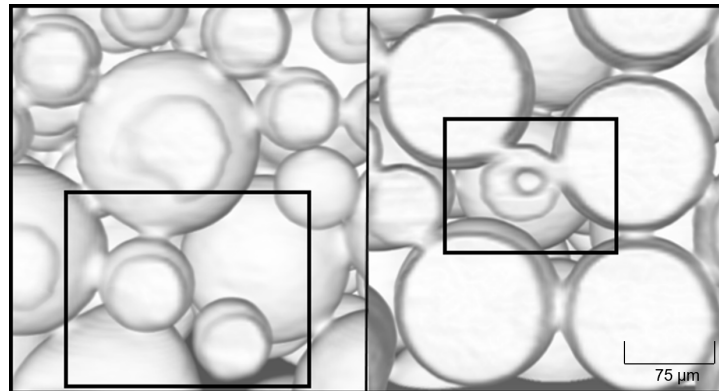


Figure 5.8: An example of smaller beads wedged between larger beads (panel on the left) and an example of a smaller bead infilling the pore space between larger beads (panel on the right).

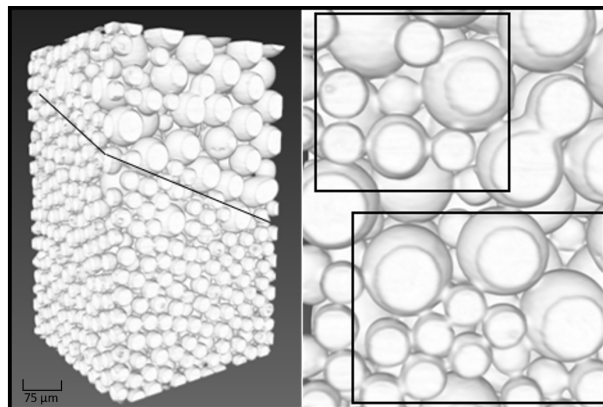


Figure 5.9: The boundary between larger beads and smaller beads in sample 3 (panel on the left) and an example of smaller beads infilling the pore space between larger beads in sample 3 (panel on the right).

Table 5.8: The experimental permeability results across the four bead pack samples.

| Sample | Average Permeability (D) | Average Permeability ( $\mu\text{m}^2$ ) |
|--------|--------------------------|--|
| 1      | 3.06                     | 3.10                                     |
| 2      | 3.77                     | 3.82                                     |
| 3      | 2.77                     | 2.81                                     |
| 4      | 6.50                     | 6.56                                     |

### 5.2.3 Permeability

The permeability results for the four samples with varying bead sizes were acquired from the pore-scale permeability experiments, the Kozeny-Carman model, permeability simulations conducted using the Avizo®Fire and ANSYS Fluent software.

#### Experimental Permeability

From the pore-scale permeability experiments the permeability was calculated using Darcy's Law,

$$K_D = \frac{\mu QL}{\Delta P A} \quad (5.1)$$

where  $\mu$  is the dynamic viscosity,  $Q$  is the volumetric flow rate,  $L$  is a length scale,  $\Delta P$  is the pressure difference and  $A$  is the cross-sectional area, and the results show that permeability ranges from 2.33 D ( $2.30 \mu\text{m}^2$ ) to 20.26 D ( $20.00 \mu\text{m}^2$ ). The average permeability values for each sample ranges from 2.81 D ( $2.77 \mu\text{m}^2$ ) to 6.56 D ( $6.50 \mu\text{m}^2$ ) (Table 5.8). Overall, sample 3 displays the lowest permeability and sample 4 shows the highest permeability.

The results from the experiments also show that the pressure difference increases linearly with increasing fluid flow rate across all samples (Fig. 5.10), however, the gradient of this relationship varies across the sample. The gradient is much steeper for sample 3 and the gradient is much gentler for sample 4. The error bars shown in Figure 5.10 were calculated from the standard deviation in the results for flow rate (horizontal error bars) and pressure difference (vertical error bars) after the system had stabilised for a minimum of 30 minutes. Results were recorded every 0.1 seconds.

#### Kozeny-Carman Permeability

The Kozeny-Carman permeability,

$$K_{KC} = \left( \frac{\phi^3}{(Sv)^2 K (1 - \phi)^2} \right) \quad (5.2)$$

where  $\phi$  = porosity,  $Sv = 6/D_P$  (where  $D_P$  = particle diameter),  $K$  = the Kozeny-Carman constant (which is 5 for spherical beads), was calculated using the porosity from the Avizo®Fire software (K1) and the ANSYS Fluent R2 software (K2). The Kozeny-Carman model was only applicable to the bead pack samples with homogeneous bead size (samples 1 and 4) and the zones which have homogeneous bead size (samples 2 and 3 zones 1,2,4,5).

The permeability results vary when different porosity values are used and permeability is predicted to be the greatest when the porosity results from ANSYS Fluent R2 (K2) are used and the permeability is predicted to be the lowest when the porosity results from Avizo®Fire (K1) are used (Fig. 5.6,

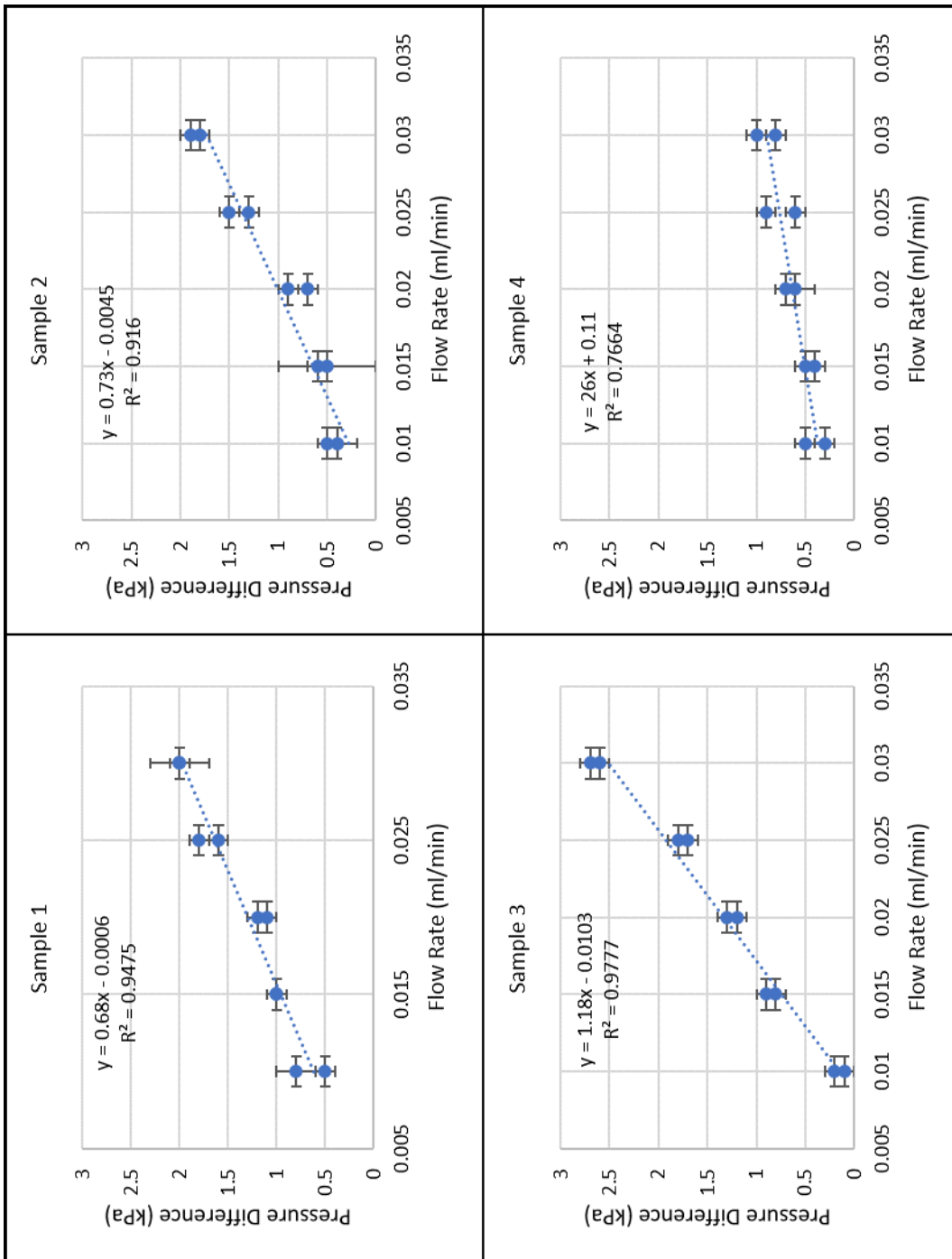


Figure 5.10: The results from the pore-scale permeability experiments for each sample.

Table 5.9: The average Kozeny-Carman permeability results across the four bead pack samples. Average K1 corresponds to the K-C permeability using the porosity results from Avizo®Fire and average K2 corresponds to the K-C permeability using the porosity results from ANSYS Fluent R2.

| Sample | Average K1 (D) | Average K2 (D) |
|--------|----------------|----------------|
| 1      | 4.42           | 8.48           |
| 2      | 5.93           | 24.59          |
| 3      | 6.93           | 10.85          |
| 4      | 9.26           | 45.56          |

Table 5.10: The Kozeny-Carman permeability results across the different zones of the four bead pack samples.

| Sample | Zone | K1 (D) | K2 (D) |
|--------|------|--------|--------|
| 1      | 3    | 5.04   | 8.48   |
| 2      | 2    | 3.27   | 16.14  |
| 2      | 4    | 15.83  | 51.58  |
| 3      | 2    | 19.34  | 27.78  |
| 3      | 4    | 4.04   | 6.74   |
| 4      | 3    | 30.71  | 45.56  |

Table 5.9). The porosity values vary as a result of using different techniques to measure porosity and due to the different scales that porosity was measured at. When porosity is measured at a smaller scale (ANSYS Fluent R2 porosity) the sample area is smaller and therefore the value of porosity may be less representative. Alternatively, when porosity is measured at a larger scale (Avizo®Fire porosity) the sample area may include areas which present lower or higher than average porosity. Due to this, multiple zones of the samples were analysed despite having the same bead size to ensure that the results were representative.

The permeability results from using the two different porosity values indicate that the average permeability is highest in bead pack sample 4 and lowest in bead pack sample 1. In the samples which have bead size contrasts the K1 results show that permeability is greater in sample 3 and the K2 results show that permeability is greater in sample 2.

The permeability results from the Kozeny-Carman model also vary throughout the bead pack samples and permeability is predicted to vary considerably throughout the zones of bead pack samples 2 and 3. The K1 results show that permeability varies more in sample 3 than in sample 2 and the K2 results show that permeability varies more in sample 2 than in sample 3. The permeability results also show that there is a large range in permeability values when zones with the same composition are compared (e.g. sample 2 zone 2 and sample 3 zone 4). The K1 results show that sample 2 zone 2 has 0.77 D (19.05%) lower permeability than sample 3 zone 4. Additionally, sample 2 zone 4 has 3.51 D (18.14%) lower permeability than sample 3. The K2 results show that sample 2 zone 2 has 9.40 D (58.24%) greater permeability than sample 3 zone 4. Furthermore, sample 2 zone 4 has 23.80 D (46.14%) greater permeability than sample 3 zone 2.

The K1 results show minimal variation throughout the zones in the samples with homogeneous bead size and permeability varies by 0.22 D in sample 1 and by 2.59 D in sample 4.

Table 5.11: The average absolute permeability results for each bead pack sample.

| Sample | Absolute Permeability (D) | Absolute Permeability ( $\mu\text{m}^2$ ) |
|--------|---------------------------|---|
| 1      | 10.38                     | 10.52                                     |
| 2      | 18.13                     | 17.90                                     |
| 3      | 18.02                     | 17.79                                     |
| 4      | 29.13                     | 28.75                                     |

### Simulated Permeability

The Absolute Permeability Experimental Simulations were conducted in the Avizo®Fire software and permeability was simulated for 5 zones of each sample and the zones are labelled 1 - 5, where zone 1 occurs at the top of the bead pack sample and zone 5 occurs at the bottom of the bead pack sample (Fig. 5.6). The average absolute permeability across the four samples ranges from 10.80 D ( $9.33 \mu\text{m}^2$ ) - 36.68 D ( $36.20 \mu\text{m}^2$ ) (Table 5.11).

The averaged permeability for the bead pack samples which have bead size contrasts was also compared to the transitional zone (zone 3) and the average permeability for sample 2 shows a 3.34 D difference in comparison to the transitional zone permeability and sample 3 shows a 5.58 D difference.

When permeability from the Absolute Permeability Experimental Simulations is plotted against porosity all samples show that permeability increases with increasing porosity (Fig. 5.11). The permeability also increases with increasing mean pore diameter (Fig. 5.11) and the linear relationship between permeability and mean pore diameter is more significant than the linear relationship between permeability and porosity. This is also demonstrated in Figure 5.6, which shows that permeability and mean pore diameter display similar trends throughout the samples, especially in samples 2 and 3. This indicates that porosity is less influential on permeability than pore diameter size and this is especially demonstrated by the results from sample 1, which show a small range in permeability yet a large range in porosity. Furthermore, this may also indicate that porosity is not a reliable property to use to predict permeability.

CFD simulations using ANSYS Fluent R2 2020 were conducted on ten tetrahedral meshes of selected zones of the bead pack samples. In the samples which have homogeneous bead size (samples 1 and 4) the CFD simulations were performed on one mesh from the central section (zone 3) of the sample. In samples which have heterogeneous bead size (samples 2 and 3) CFD simulations were performed on three meshes from three different zones of the samples (zones 2-4) to analyse fluid flow behaviour in zones which have different bead size or transitional bead size. The CFD simulations were also conducted on two scaled down homogeneous samples to analyse fluid flow in samples with smaller bead size (samples 5 and 6). The results from the CFD simulations include permeability, pressure and volumetric flow rate across the sample, velocity field, tortuosity and streamlines. Additionally, the CFD simulations were also used to determine the permeability at greater flow rates and pressures.

At the experimental scale (in this study), which is defined by a pressure difference of less than 100 kPa, the permeability varies between each of the samples and also varies across the different zones of the samples. The permeability is predicted to range from 0.69 D to 53.78 D (Table 5.12). Sample 2 shows the greatest range in permeability and ranges from 16.71 D - 53.78 D, which is a 37.07 D (68.92%) difference in permeability throughout the sample. Sample 3 also displays a range in permeability values from 8.94 D to 32.79 D, which is a 23.85 D (72.73%) difference in permeability throughout the sample. For the samples which present a bead size contrast the average permeability was also calculated from the zones either side of where the beads mixed (zone 3) and this is compared

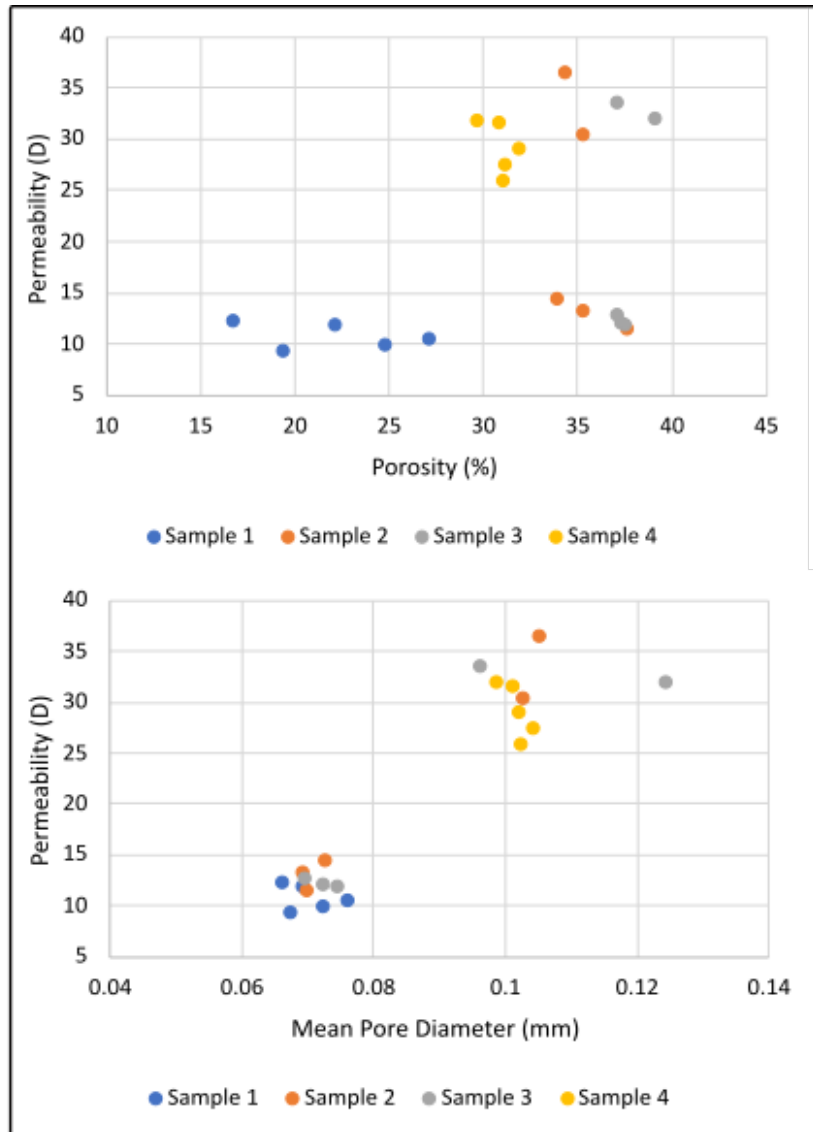


Figure 5.11: The permeability results from the Avizo Fire permeability simulations plotted against porosity (top panel) and pore diameter (bottom panel) which show that permeability increases with increasing porosity and mean pore diameter. The results show that mean pore diameter size has a greater impact on permeability than porosity, and this is especially demonstrated by sample 1, which shows a small range in permeability despite a large range in porosity. This may indicate that porosity is not a reliable property to use to predict permeability.

Table 5.12: The average permeability results from the CFD simulations conducted at the experimental scale in the Darcy flow regime.

| Sample | Zone | Bead Size ( $\mu\text{m}$ ) | Permeability (D) | Permeability ( $\mu\text{m}^2$ ) |
|--------|------|-----------------------------|------------------|----------------------------------|
| 1      | 3    | 75                          | 10.85            | 10.70                            |
| 2      | 2    | 75                          | 16.71            | 16.49                            |
| 2      | 3    | 75 - 180                    | 17.53            | 17.30                            |
| 2      | 4    | 150 - 180                   | 53.78            | 53.08                            |
| 3      | 2    | 150 - 180                   | 32.79            | 32.36                            |
| 3      | 3    | 75 - 180                    | 11.98            | 11.83                            |
| 3      | 4    | 150 - 180                   | 8.94             | 8.82                             |
| 4      | 3    | 150 - 180                   | 47.01            | 46.39                            |
| 5      | -    | 18                          | 0.69             | 0.68                             |
| 6      | -    | 40                          | 3.01             | 2.97                             |

with the predicted permeability from the CFD simulations. The average permeability for sample 2 is 25.50 D and the predicted permeability for the transitional zone is 17.53 D which shows a difference of 7.97 D (31.25%). The average permeability for sample 3 is 14.05 D and the prediction permeability for the transitional zone is 11.98 D which is a difference of 2.07 D (14.73%).

At the experimental scale in this study ( $> 100$  kPa) all six samples show a linear relationship between flow rate and pressure gradient. In samples 2 and 3 the different zones present obvious differences in the relationship between the flow rate and pressure gradient, for example, sample 2 zone 4 and sample 3 zone 2 demonstrate that pressure increases more steeply with increasing velocity than in the other zones. The average permeability was also predicted for the samples which were composed of two different bead sizes (samples 2 and 3) from the results of zones 2 and 4 and the results for the average permeability were compared to the permeability results from zone 3. The results for the predicted average permeability for sample 2 is 25.50 D and the permeability for sample 2 zone 3 is 17.53 D, which is a 7.97 D (31.26%) difference. For sample 3 the predicted average permeability is 14.05 D and the permeability for sample 3 zone 3 is 11.98 D, which is a 2.06 D (14.69%) difference.

In samples 2 and 3 the pressure and mass flow rate were also recorded at nine planes in the z direction across zone 3 to understand how the pressure and mass flow rate changes across the zones which have transitional bead size. The results for sample 2 show that when pressure is plotted against the z coordinate there is a significant change in the gradient of the data points indicating a change in pressure in sample 2. The results for sample 3 also show an obvious change in gradient in the data points displaying a change in pressure conditions. The mass flow rate remains constant across the pore network for sample 2, and remains largely constant across the pore network for sample 3 apart from at plane 1 ( $4.03 \times 10^{-5}$  m) where the mass flow rate increases slightly ( $+ 4.49 \times 10^{-8}$  m/s) (58.63%) which corresponds to a pressure value which is higher than the previous and following values ( $+ 1.54$  Pa) (23.18%) for pressure and does not follow the overall trend displayed by the other data points.

The permeability was also calculated between each of the planes and sample 2 shows that permeability increases throughout the sample and sample 3 shows that permeability decreases and then stabilises throughout the sample (Fig. 5.13).

The results from the CFD simulations performed at greater flow rates and pressures show that the relationship between pressure gradient and flow rate is not always linear (Fig. 5.14).

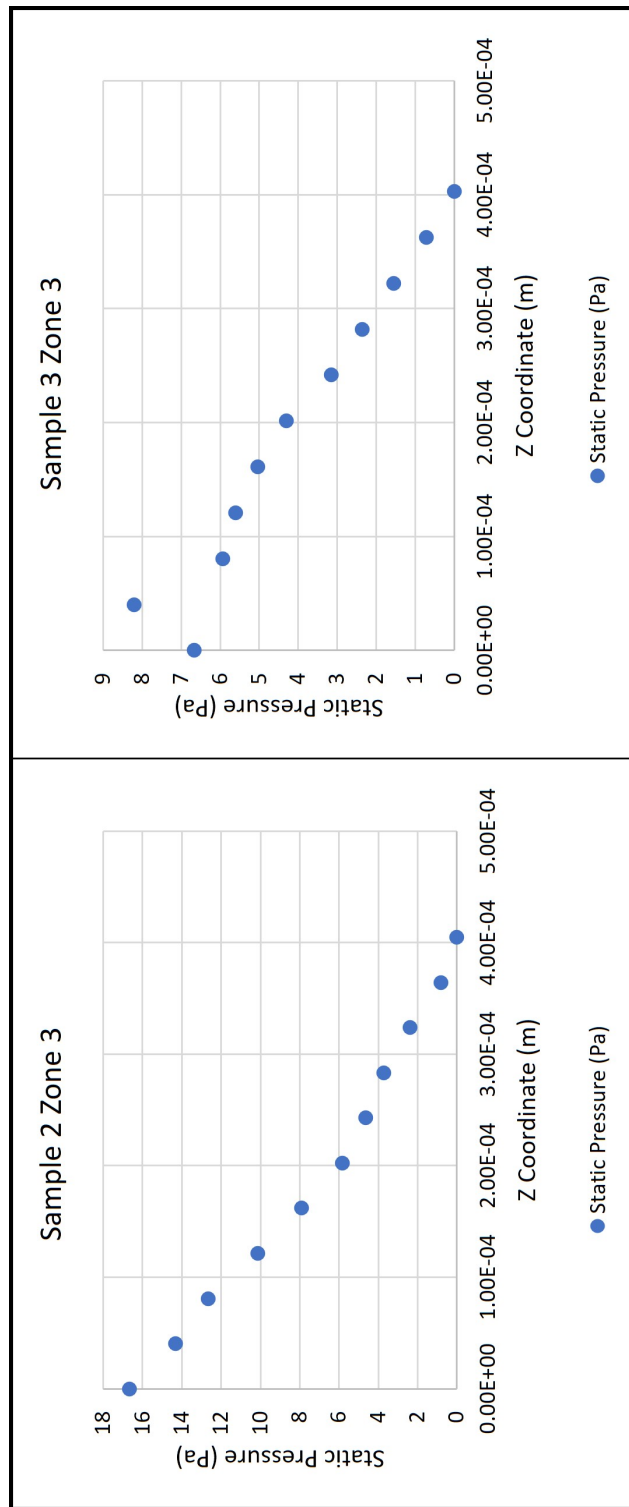


Figure 5.12: The pressure values across the tetrahedral meshes of the transitional zones in samples 2 and 3.



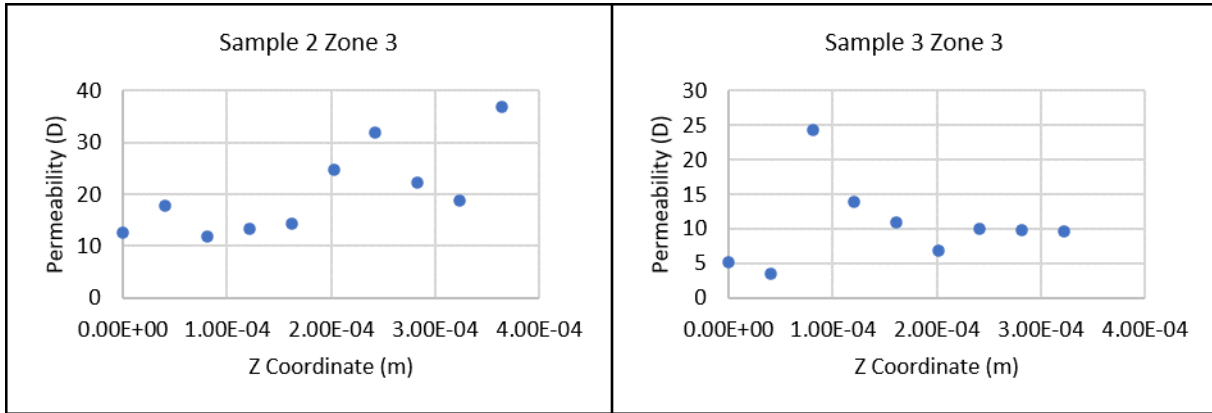


Figure 5.13: The permeability across the tetrahedral meshes of the transitional zones in samples 2 and 3.

Across the samples the linear relationship changes gradient and the point at which this gradient change occurs differs across the samples and sample zones (Fig. 5.14). Sample 1 presents a change in gradient at the lowest Darcian flow rate (0.02 m/s) and sample 4 presents a change in gradient at the lowest pressure difference (0.435 kPa). On the other hand, sample 6 shows a change in gradient at the highest Darcian flow rate (1.82 m/s) and pressure gradient (146.437 Pa). In samples 2 and 3 the gradient change does not occur synchronously across the zones of the same sample, for example, sample 2 zones 2 and 3 show that the change in gradient occurs at a lower flow rate than in zone 4 (approximately 0.05 m/s or 60.59% lower). This is also observed in sample 3 which shows that the change in gradient for zones 3 and 4 occurs at a higher flow rate (0.10 - 0.14 m/s or 57.02 - 64.16% greater) and at higher pressure differences (10.883 - 10.963 Pa or 90.15 - 90.22% greater).

The permeability from the four methods for the samples with homogeneous bead size is also plotted against bead size and overall indicates the permeability increases with increasing bead size (Fig. 5.15). The CFD results and the Kozeny-Carmen permeability using the CFD porosity values show a quadratic relationship between increasing permeability and increasing bead size whereas there are too few points from the experimental, Avizo®Fire and Kozeny-Carman permeability using the Avizo Fire results to draw a conclusion.

#### 5.2.4 Flow Regime and Reynold's Number

The Reynold's number,

$$\text{Re} = \frac{\rho v L}{\mu} \quad (5.3)$$

where  $\rho$  is the fluid density,  $\mu$  is the dynamics dynamic viscosity,  $v$  is the velocity and  $L$  is the average pore diameter, calculated from the experimental data is similar across all samples as flow rate was controlled and consistent during the experiments (Table 5.5). The experimental results range from  $9.58 \times 10^{-4} - 4.56 \times 10^{-3}$  and higher flow rate results in higher Re.

The CFD results show that the Re ranges from  $7.00 \times 10^{-4} - 211.53$  and sample 5 has the smallest Re at the lowest flow rate and sample 2 zone 4 has the highest Re at the highest flow rate and also displays the largest range in Re (211.51).

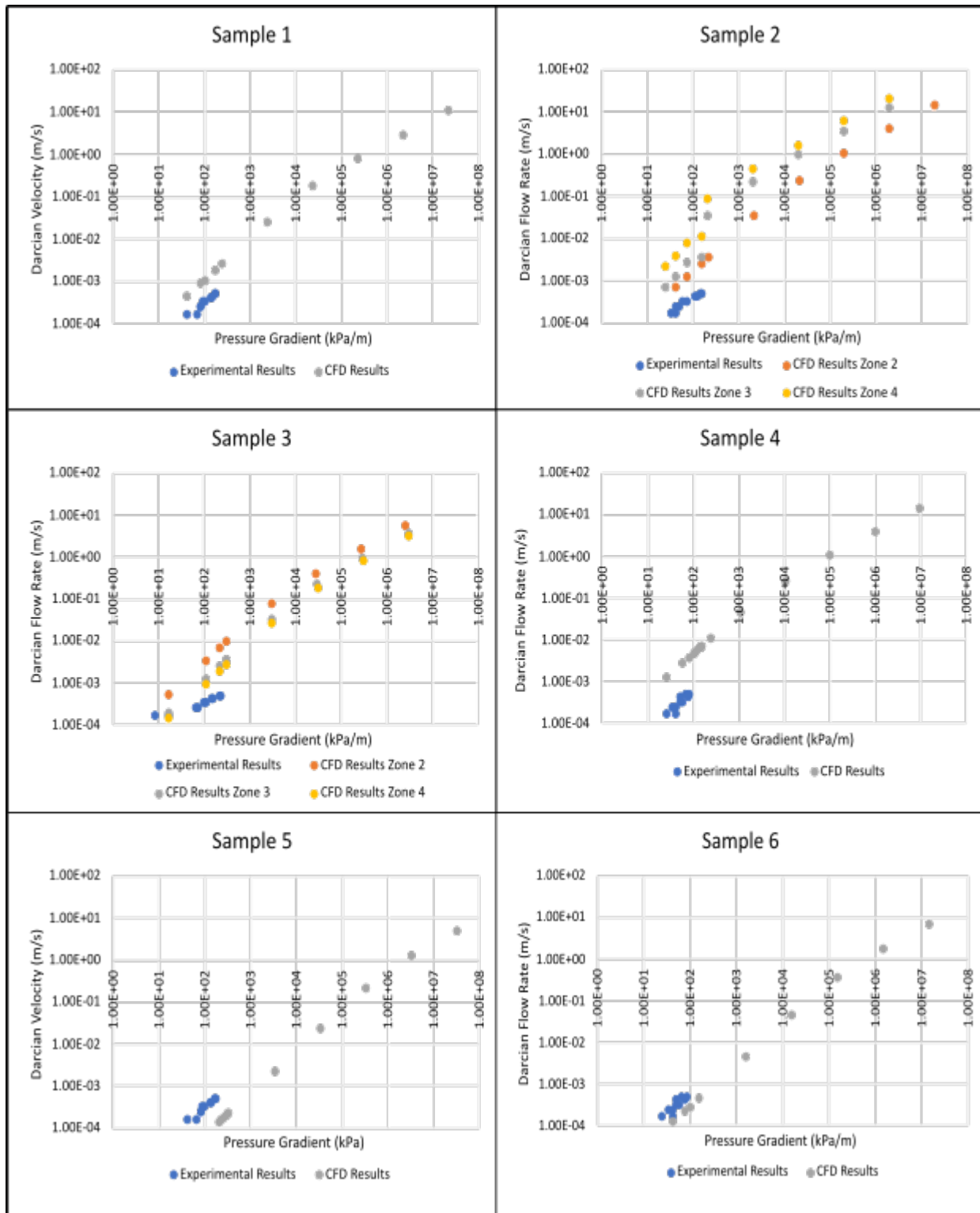


Figure 5.14: The results from the CFD simulations showing a gradient change in the linear trend line.

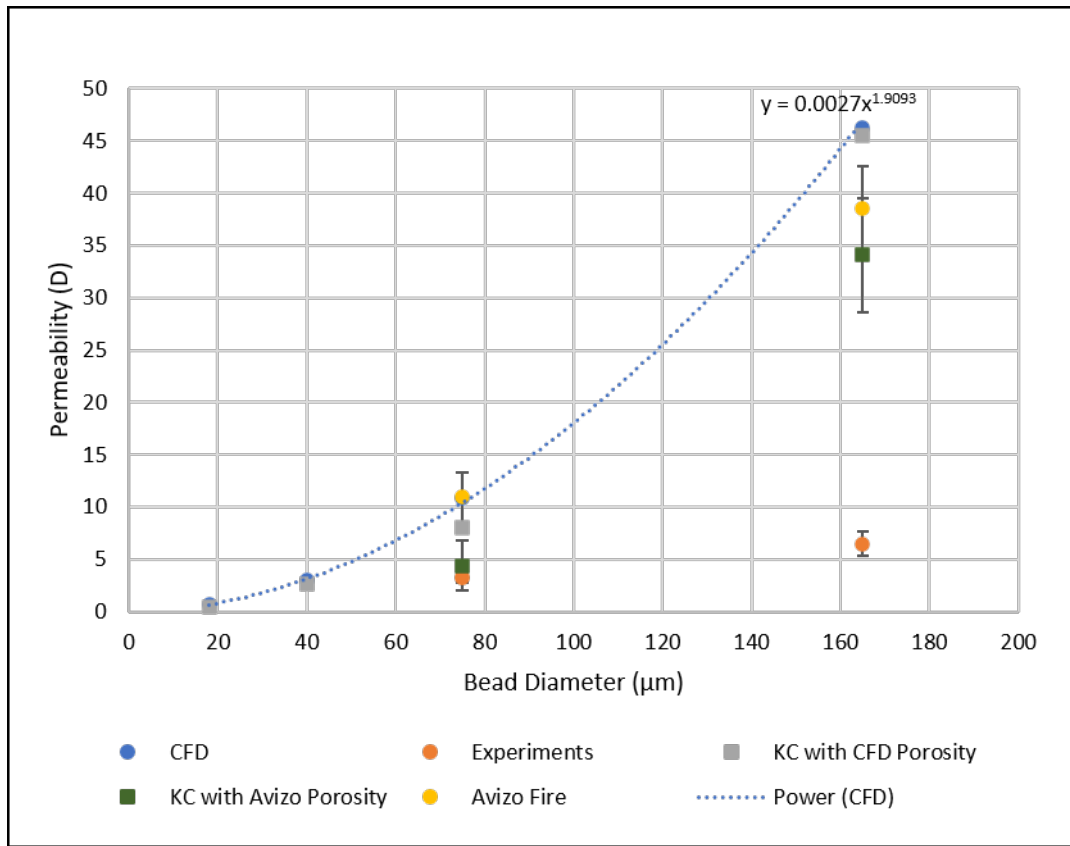


Figure 5.15: The permeability results compared to bead size indicating that permeability increases with increasing bead size in the samples.

Table 5.13: The Re at which permeability decreases for each sample.

| Sample | Zone | Bead Size ( $\mu\text{m}$ ) | Re    |
|--------|------|-----------------------------|-------|
| 1      | 3    | 75                          | 0.22  |
| 2      | 2    | 75                          | 0.29  |
| 2      | 3    | 75 - 180                    | 0.31  |
| 2      | 4    | 150 - 180                   | 0.08  |
| 3      | 2    | 150 - 180                   | 0.56  |
| 3      | 3    | 75 - 180                    | 0.17  |
| 3      | 4    | 150 - 180                   | 0.13  |
| 4      | 3    | 150 - 180                   | 37.18 |
| 5      | -    | 18                          | 1.87  |
| 6      | -    | 40                          | 0.09  |

When the experimental Re and CFD Re are compared the results show that overall the CFD results at the experimental scale ( $< 100$  kPa) are higher than the experimental results. However, the results show that there is some overlap in the results and some of the CFD Re results (1 - 2) occur in the same order of magnitude at similar flow rates, apart from sample 4, which shows no overlap between the experimental Re and the CFD Re and there is at least one order of magnitude difference in the Re results.

When the CFD Re results are plotted against permeability the permeability is stable at the experimental scale (approximately Re  $1.E-03$  -  $1.E-01$ ). Permeability is observed to decrease in all samples but the Re at which permeability decreases differs across the samples (Fig. 5.16, Table 5.13). The permeability decrease corresponds to the change in gradient of the linear relationship between Darcian flow rate and pressure difference (Fig. 5.14). Sample 2 zone 4 shows the lowest Re where permeability decreases and sample 4 shows the highest Re where permeability decreases. When the samples with bead size contrasts are compared the permeability decreases at a lower Re in sample 2 than in sample 3 in zones 2 and 4. In zone 3 sample 2 has a higher Re than sample 3 when permeability decreases. The Re at which permeability begins to decrease at is also compared against the pore diameter (Fig. 5.17) and the Re increases with increasing mean pore diameter size.

The inverse apparent permeability,  $1/K_{App}$ , was calculated and plotted as a function of  $\rho U/\mu$  (Forchheimer graph) (Fig. 5.18) and the slope of the graph reveals the value of the beta factor,  $\beta$ , also known as the non-Darcy coefficient, which is proportional to the additional term in the Forchheimer equation (Muljadi et al., 2016). The results show that  $\beta$  is the highest in sample 5 and  $\beta$  is lowest in sample 3 zone 2 (Table 5.14) and in the homogeneous samples  $\beta$  increases in samples with smaller bead size (Fig. 5.19).

### 5.2.5 Tortuosity and Fluid Flow Pathways

The tortuosity results vary between the samples and also throughout the samples and tortuosity ranges from 1.07 – 4.58. Tortuosity is lowest in sample 2 zone 4 and highest in sample 3 zone 4 (Table 5.15).

In the samples with homogeneous bead size (samples 1, 4, 5, 6) tortuosity increases with increasing bead size (Fig. 5.20). In the samples with heterogeneous bead size sample 3 shows greater tortuosity than sample 2 overall (Fig. 5.21) and the range in tortuosity is greater in sample 3, where the tortuosity varies by 3.21 (+ 55.18%) whereas in sample 2 the tortuosity only varies by 1.44. Sample

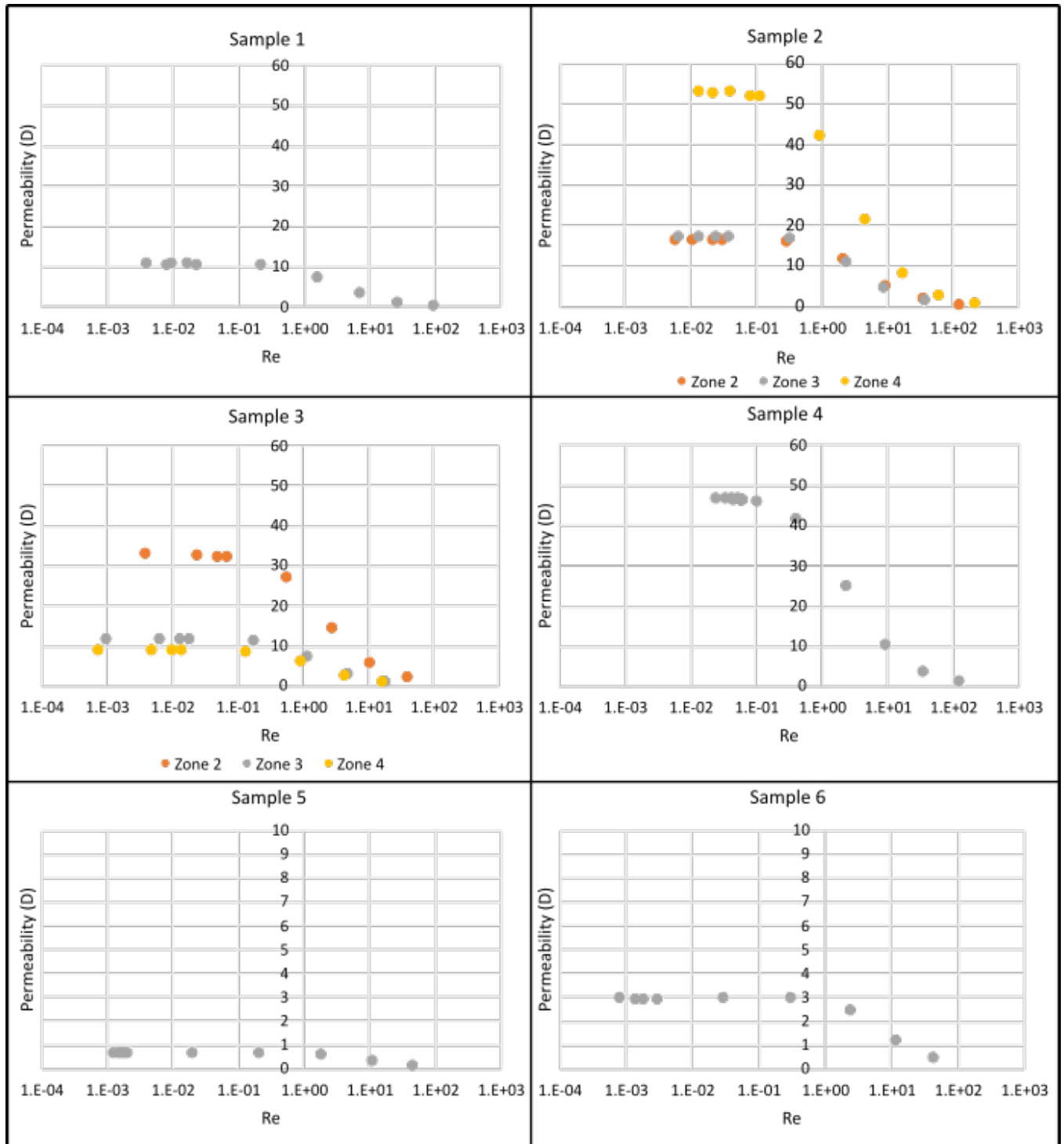


Figure 5.16: Permeability plotted against Re from the CFD simulations

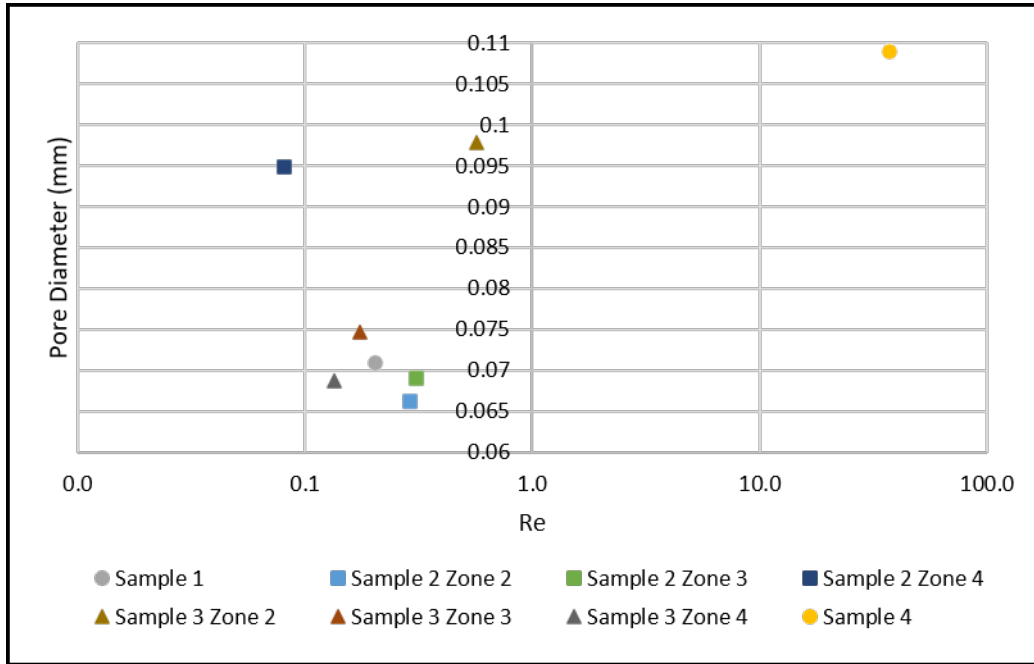


Figure 5.17: The mean pore diameter size plotted against the Re at which permeability begins to decrease in the samples. The results show that the permeability begins to decrease at lower Re when pore diameter is smaller.

Table 5.14: The  $\beta$  for each sample.

| Sample | Zone | Bead Size ( $\mu\text{m}$ ) | $\beta$ |
|--------|------|-----------------------------|---------|
| 1      | 3    | 75                          | 2.01    |
| 2      | 2    | 75                          | 1.50    |
| 2      | 3    | 75 - 180                    | 1.57    |
| 2      | 4    | 150 - 180                   | 1.23    |
| 3      | 2    | 150 - 180                   | 0.74    |
| 3      | 3    | 75 - 180                    | 2.09    |
| 3      | 4    | 150 - 180                   | 2.41    |
| 4      | 3    | 150 - 180                   | 1.25    |
| 5      | -    | 18                          | 96.70   |
| 6      | -    | 40                          | 25.85   |

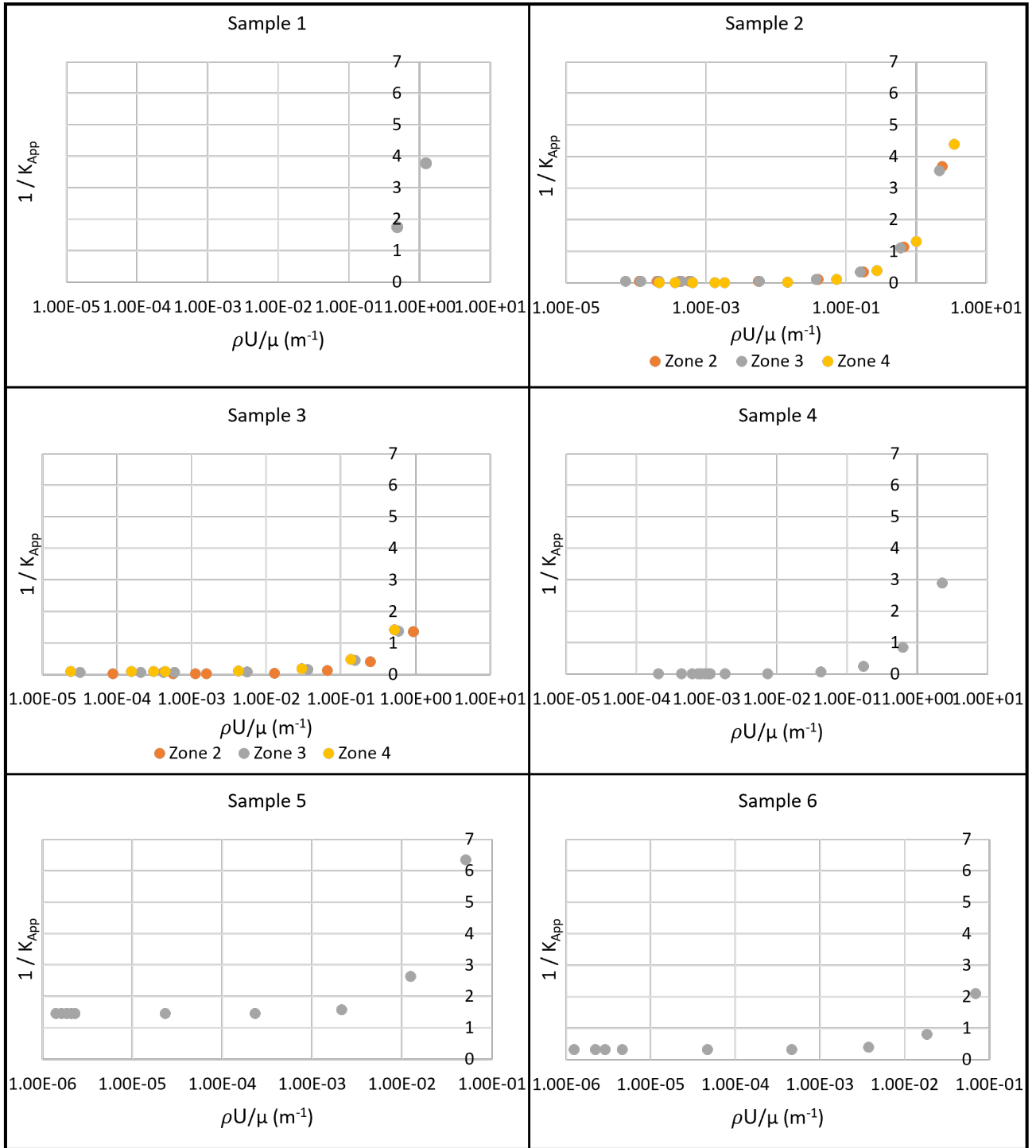


Figure 5.18: The Forchheimer graphs for each sample showing the inverse relationship between  $1/K_{App}$  and  $\rho U/\mu$ .

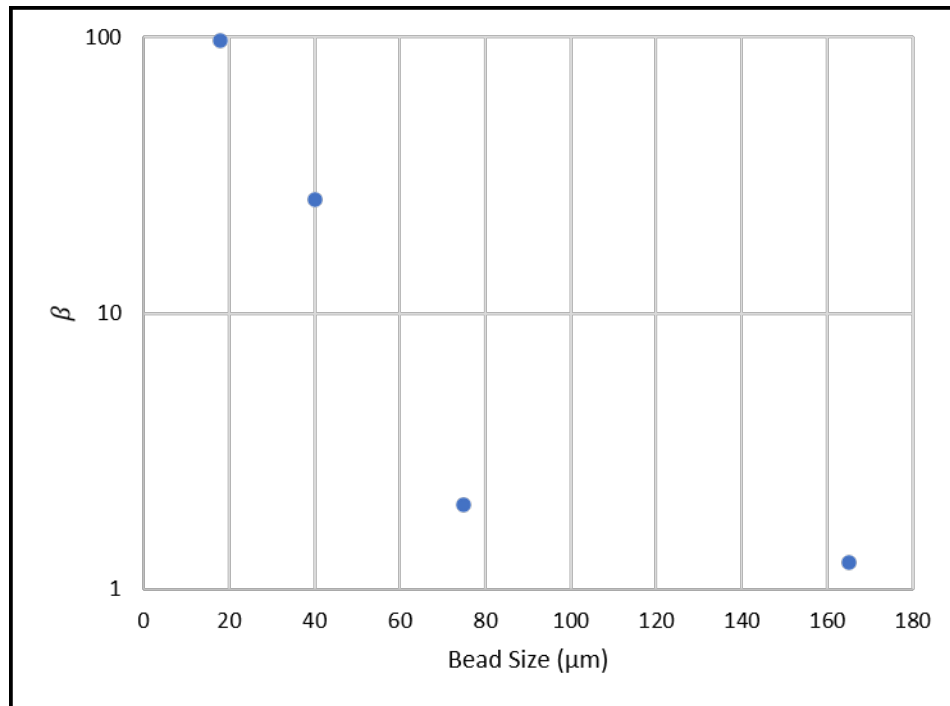


Figure 5.19:  $\beta$  compared to bead size showing that  $\beta$  decreases with decreasing bead size.

Table 5.15: The tortuosity results from the samples.

| Sample | Zone | Tortuosity |
|--------|------|------------|
| 1      | 3    | 1.47       |
| 2      | 2    | 2.51       |
| 2      | 3    | 1.73       |
| 2      | 4    | 1.07       |
| 3      | 2    | 2.79       |
| 3      | 3    | 1.37       |
| 3      | 4    | 4.58       |
| 4      | 2    | 1.51       |
| 5      | -    | 1.54       |
| 6      | -    | 1.21       |



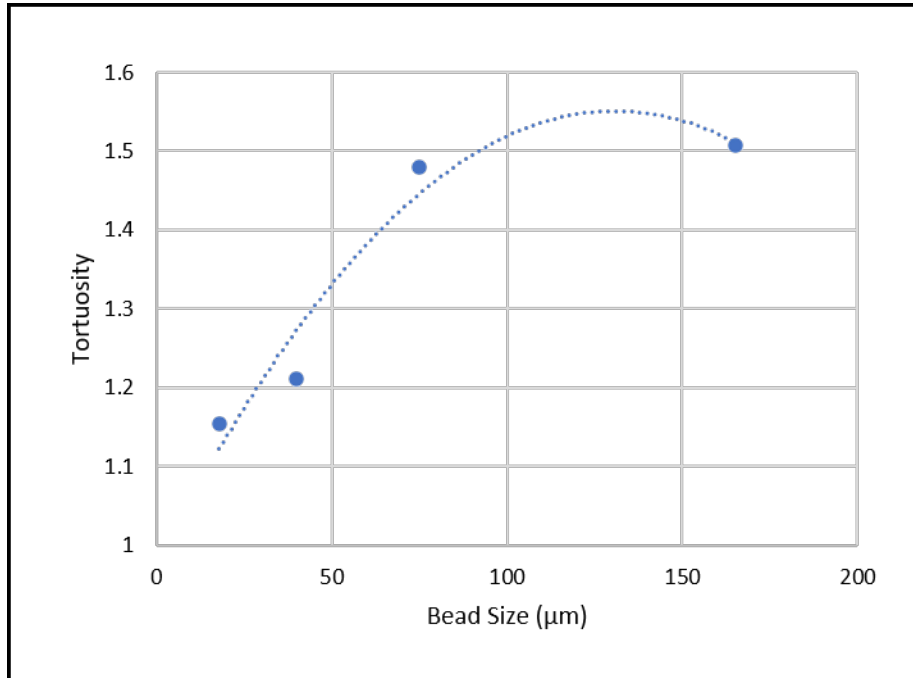


Figure 5.20: Tortuosity values plotted against the bead size from the samples with homogeneous bead size showing that the tortuosity value increases with increasing bead size.

2 shows that tortuosity decreases from zone 2 to zone 4 and sample 3 shows that tortuosity decreases from zone 2 to 3 and then increases from zone 3 to 4.

The flow pathline results display different velocities and flow patterns in the different samples and across the zones of the different samples (Figs. 5.22 - 5.31). Sample 1 presents the highest velocity flow, 2.10 m/s, and sample 5 shows the lowest velocity flow, 6.86E-05 m/s (Table 5.16). The samples which present a bead size contrast (samples 2 and 3) show that the average velocity varies throughout the samples and the average velocity in sample 2 decreases from zone 2 to zone 3 by 1.89E-03 (61.17%) and increases from zone 3 to zone 4 by 1.49E-03 (55.39%). The average velocity in sample 3 increases from zone 2 to zone 3 by 4.81E-02 (98.17%) and decreases from zone 3 to zone 4 by 4.59E-02 (93.71%).

Sample 1 shows less flow pathlines than the other five samples and both sample 1 and 6 present the most uniform flow velocity and flow pattern. Samples 4 and 5 show that flow is mostly uniform but some areas of high velocity flow occur and this is more significant in sample 4 where the areas of high velocity flow are larger than in sample 5. Samples 2 and 3 show that the flow velocity and flow pattern change throughout the sample.

In sample 2 zone 2 fluid flow and velocity is mostly uniform with some pathlines facilitating higher velocity flow (+ 3.09 × 10<sup>-3</sup> m/s (50%)). In sample 2 zones 3 and 4 the pathlines facilitating higher velocity flow increase in frequency and velocity and the velocity in the pathlines increases 2.90E-03 m/s (48.41%) in zone 3 and the velocity increases by 7.41E-03 m/s (55.30%) in zone 4. In sample 2 zone 3 some of the pathlines of high velocity flow form preferential channels across the sample and in sample 2 zone 4 most of the pathlines of high velocity flow form channels across the sample.

In sample 3 zone 2 multiple pathlines are observed to facilitate higher velocity flow (+ 3.59E-03 m/s (79.98%)) and most of which extend fully across the mesh and a lower number of pathlines are

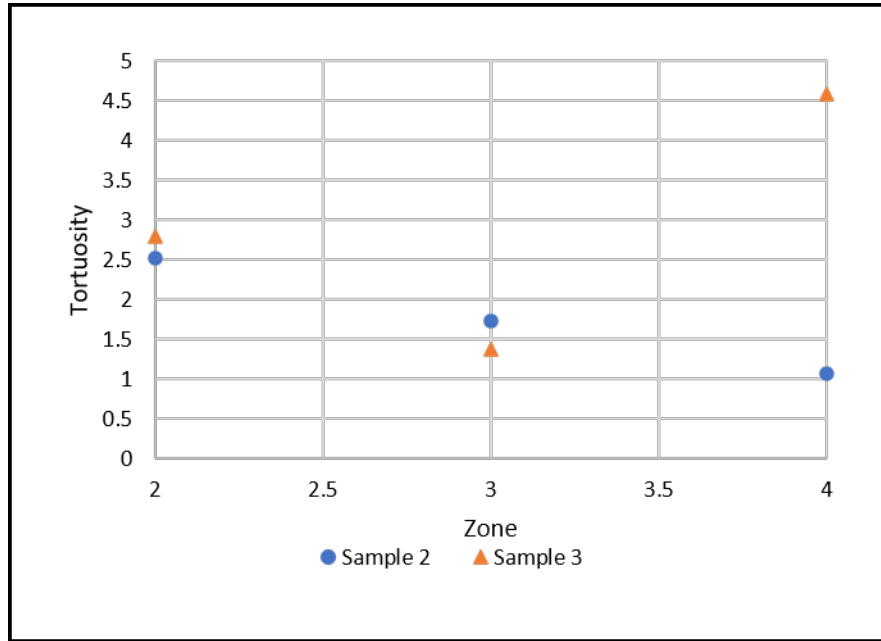


Figure 5.21: Tortuosity values from samples 2 and 3 showing that tortuosity differs between the different zones of the samples with heterogeneous bead size.

also observed to facilitate even higher velocity flow (+ 7.19E-03 m/s (88.89%)). In sample 3 zone 3 the flow velocity and flow pattern is uniform (4.90E-02 m/s). Sample 3 zone 4 displays pathlines of higher velocity flow (+ 1.54E-03m/s (83.35%)) but none extend fully across the mesh. The high velocity pathlines in sample 3 zone 2 are 2.64E-03m/s (58.80) higher than the high velocity pathlines in sample 3 zone 4.

In the zones which correspond to the same bead size (e.g. sample 2 zone 2 and sample 3 zone 4) the velocity of the pathlines which support high velocity flow differ. For example, the high velocity pathlines in sample 2 zone 2 are 1.24E-03 m/s (40.13%) greater than the high velocity pathlines in sample 3 zone 4. Additionally, the high velocity pathlines in sample 2 zone 4 are 8.91E-03 m/s (66.49%) greater than the high velocity pathlines in sample 3 zone 2.

### 5.3 Discussion

In this section the results of the sample characterisation, pore scale permeability experiments and permeability simulations will be discussed.

#### 5.3.1 How does heterogeneous bead size alter the pore network geometry?

The pore network geometry varies between each sample and this is demonstrated by the differing ranges of pore diameter size and porosity. Pore size in reservoir rocks is important to characterise as it is one of the key factors to consider when modelling fluid flow and chemical transport and it closely linked to other rock properties, such as permeability and diffusivity (Rijfkogel et al., 2019; Zhang et al., 2016). Furthermore, variable sizes of pores in pore networks can also influence thermodynamic behaviour and areas with small pore diameters can act as a semi-permeable membrane which filters transported molecules based on their size (Alfi et al., 2019). Additionally, the size of pores in

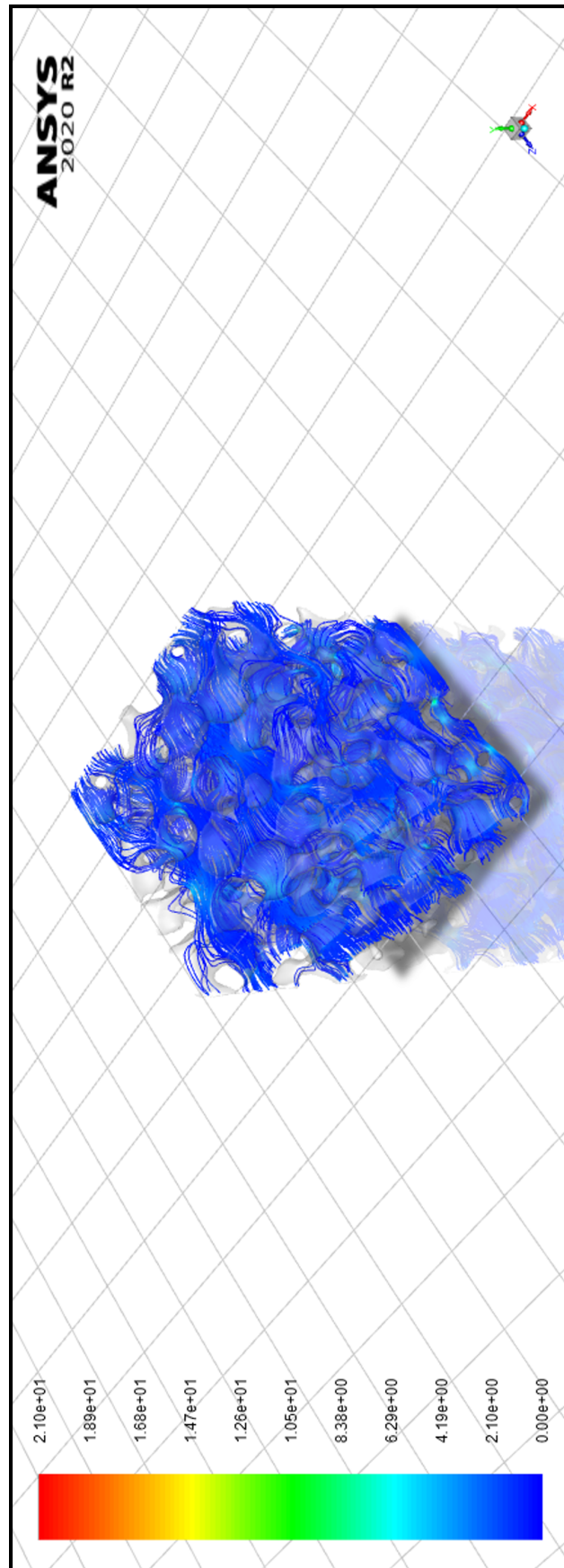


Figure 5.22: The pathlines for sample 1. The legend describes the velocity of the pathlines (m/s) and the size of the mesh is  $400 \mu\text{m}^3$ .

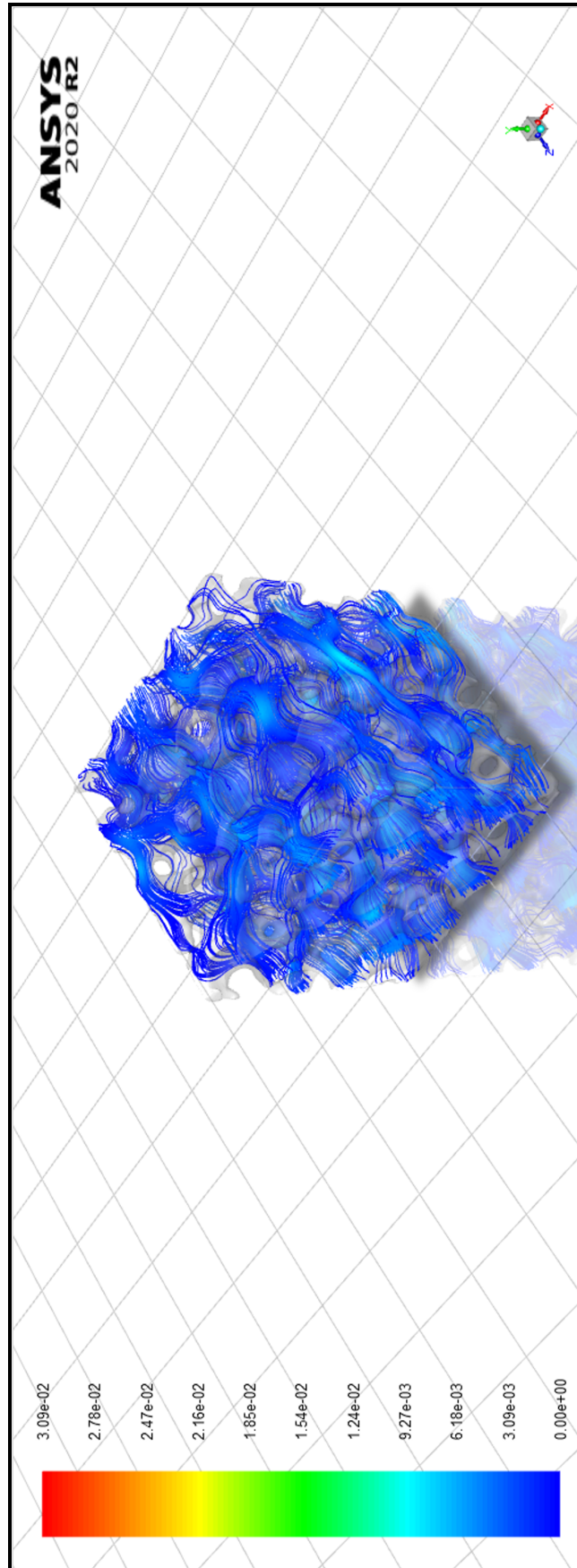


Figure 5.23: The pathlines for sample 2 zone 2. The legend describes the velocity of the pathlines (m/s) and the size of the mesh is  $400 \mu\text{m}^3$ .

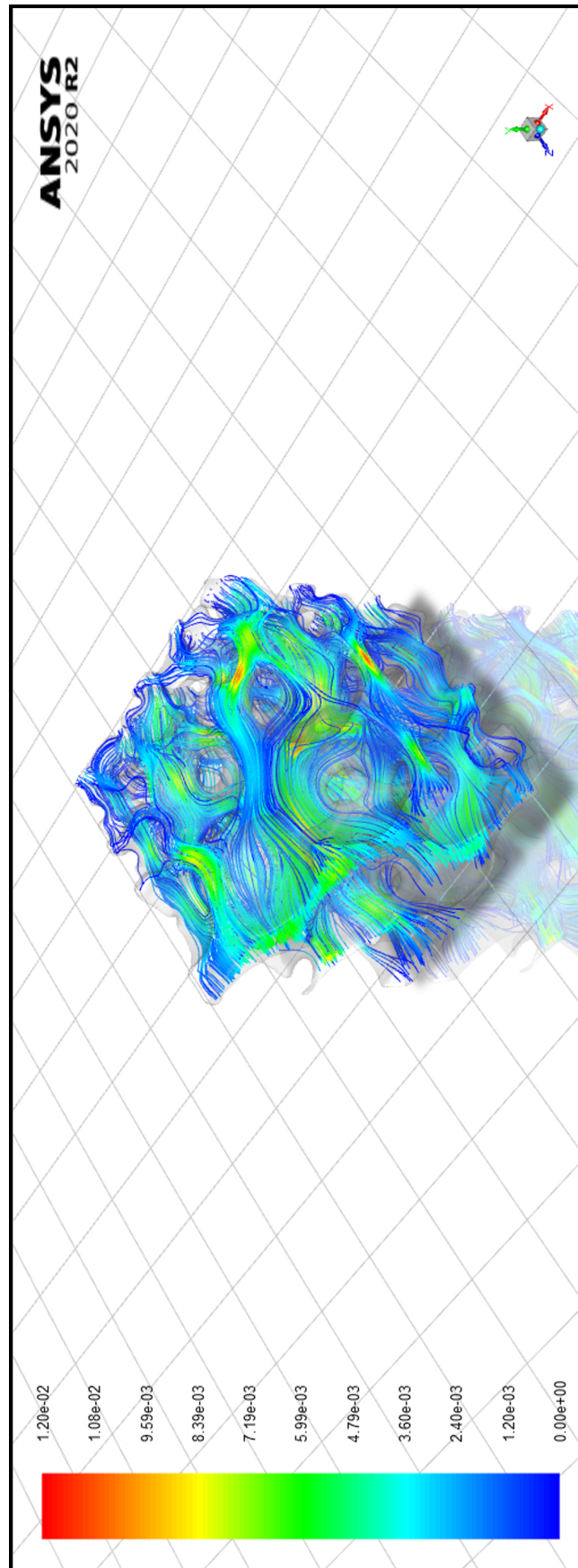


Figure 5.24: The pathlines for sample 2 zone 3. The legend describes the velocity of the pathlines (m/s) and the size of the mesh is  $400 \mu\text{m}^3$ .

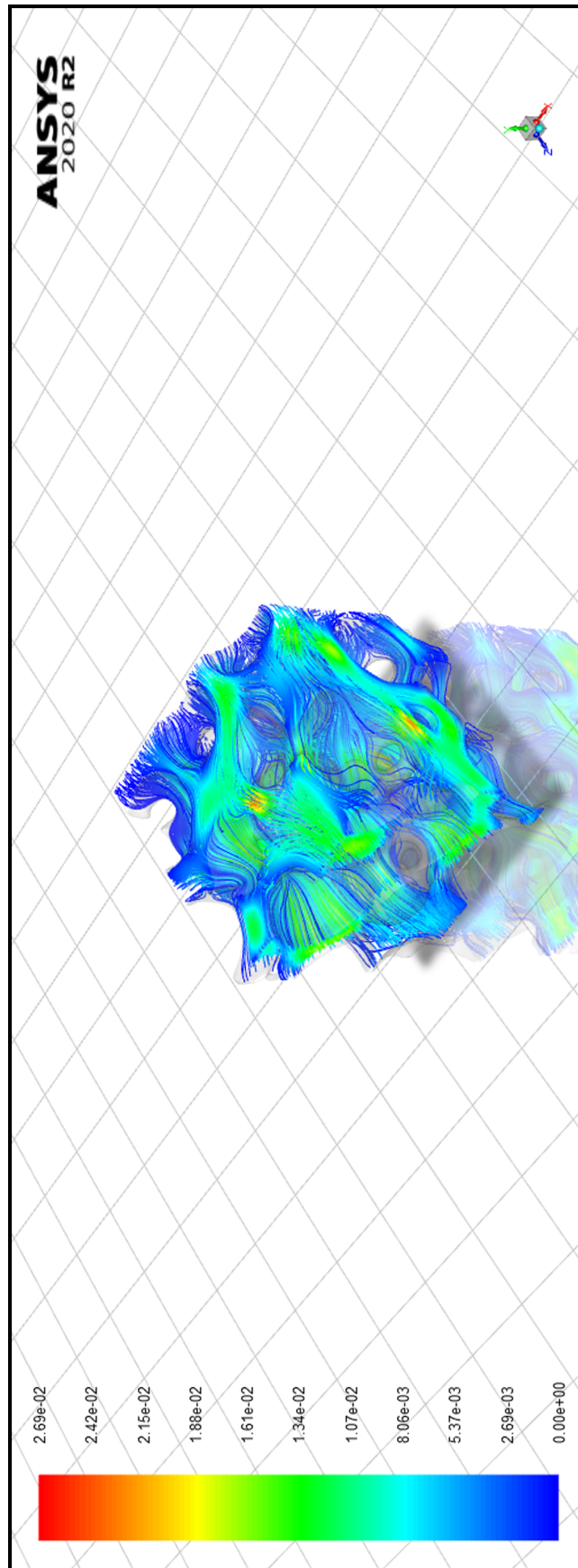


Figure 5.25: The pathlines for sample 2 zone 4. The legend describes the velocity of the pathlines (m/s) and the size of the mesh is  $400 \mu\text{m}^3$ .

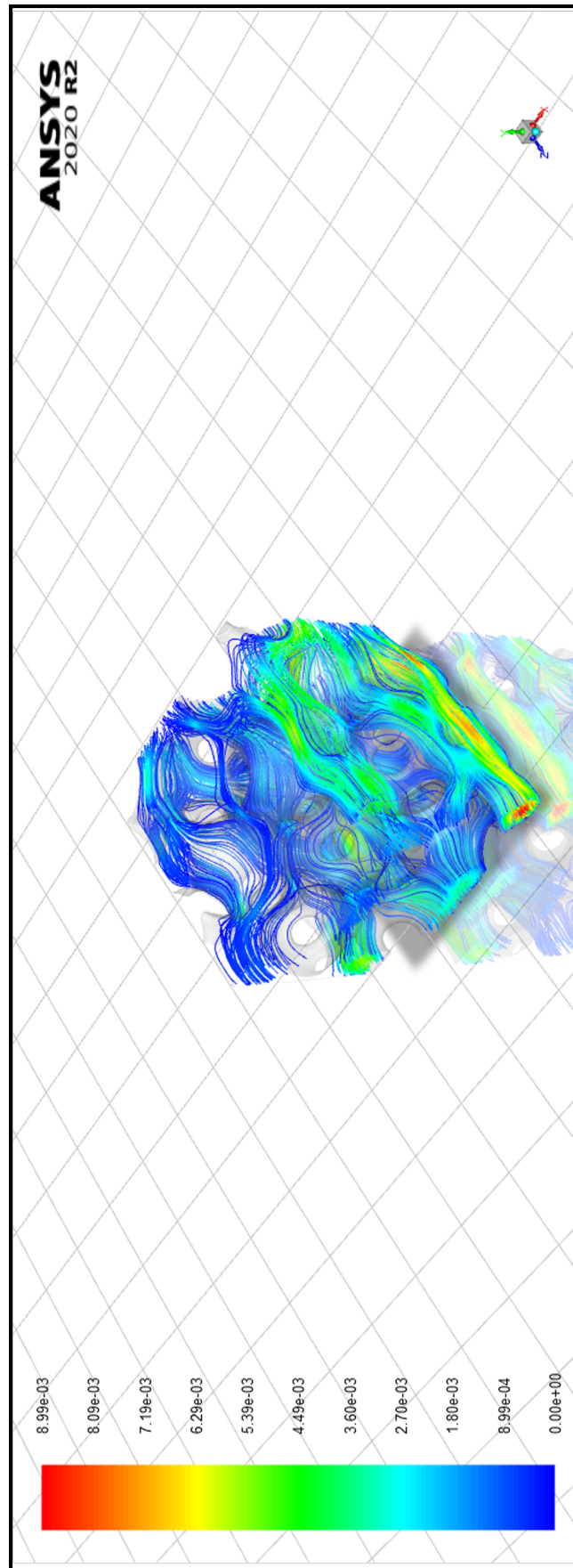


Figure 5.26: The pathlines for sample 3 zone 2. The legend describes the velocity of the pathlines (m/s) and the size of the mesh is  $400\ \mu\text{m}^3$ .

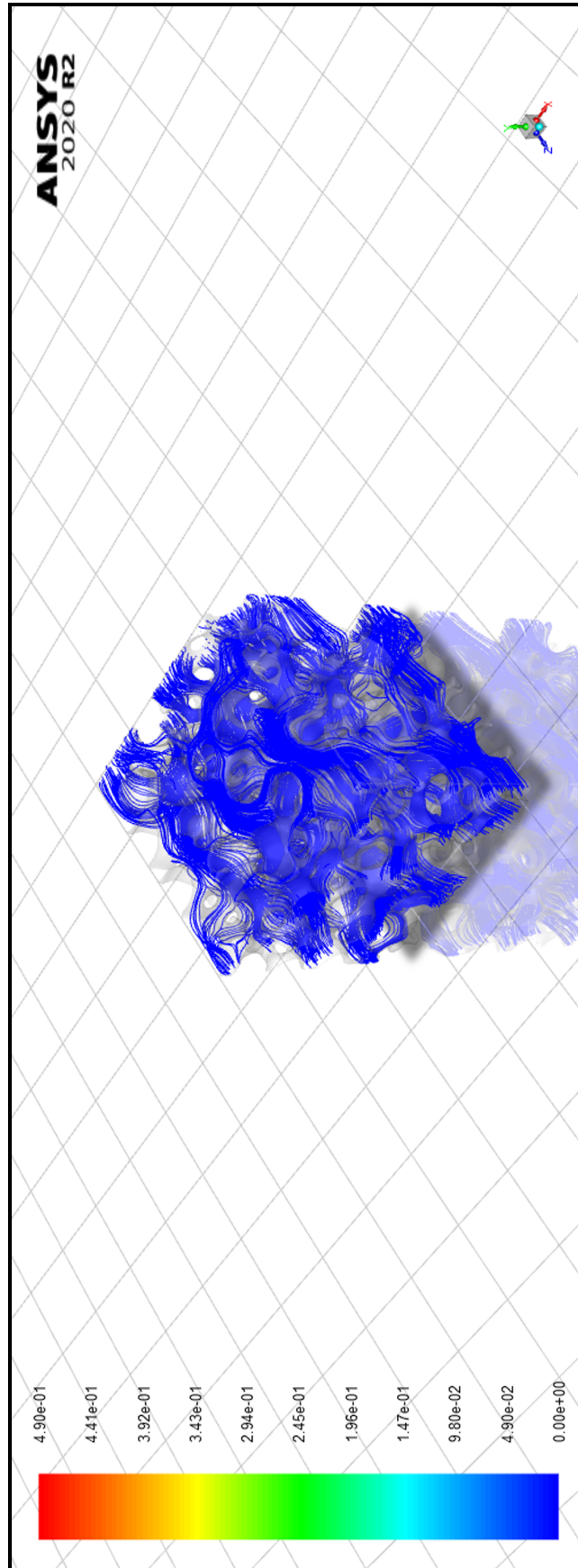


Figure 5.27: The pathlines for sample 3 zone 3. The legend describes the velocity of the pathlines (m/s) and the size of the mesh is  $400 \mu\text{m}^3$ .



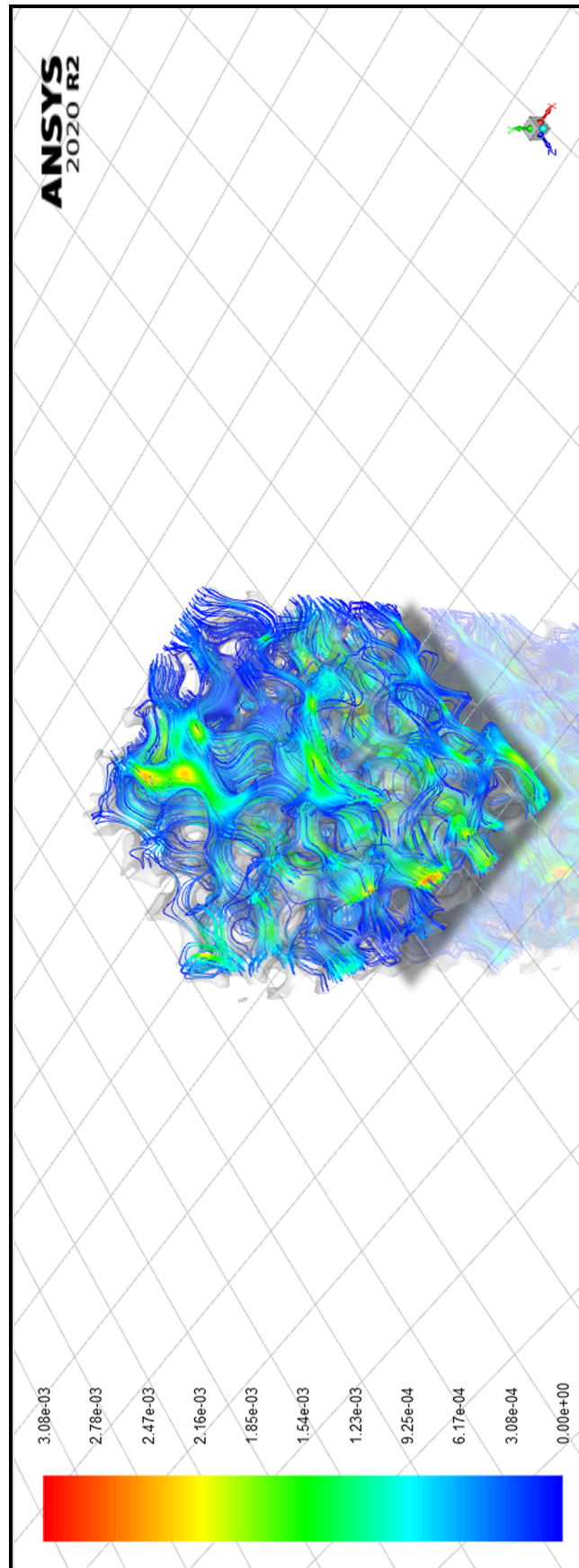


Figure 5.28: The pathlines for sample 3 zone 4. The legend describes the velocity of the pathlines (m/s) and the size of the mesh is  $400 \mu\text{m}^3$ .

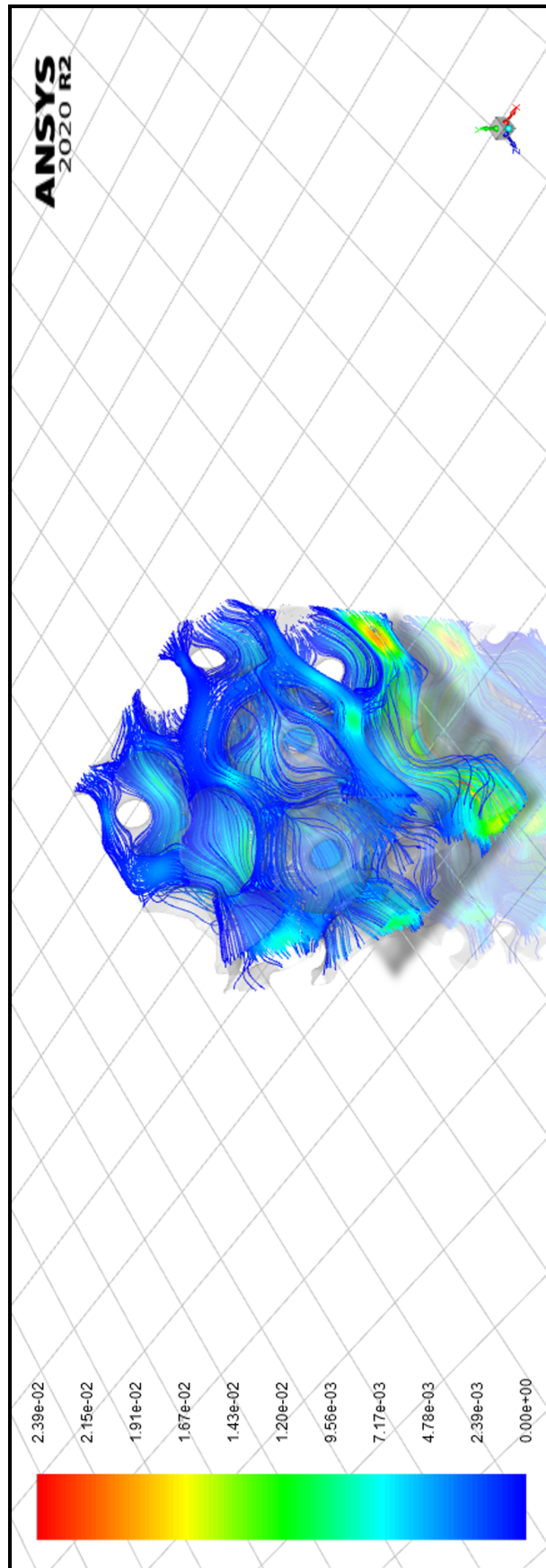


Figure 5.29: The pathlines for sample 4. The legend describes the velocity of the pathlines (m/s) and the size of the mesh is  $400 \mu\text{m}^3$ .

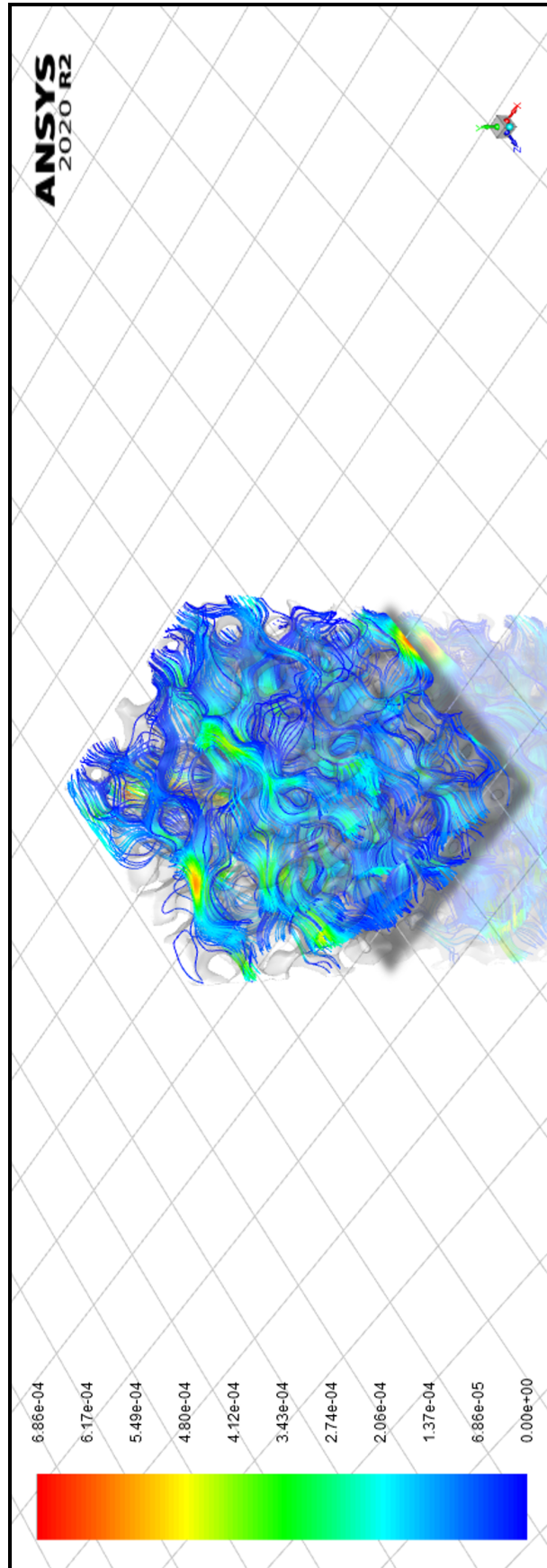


Figure 5.30: The pathlines for sample 5. The legend describes the velocity of the pathlines (m/s) and the size of the mesh is  $400 \mu\text{m}^3$ .

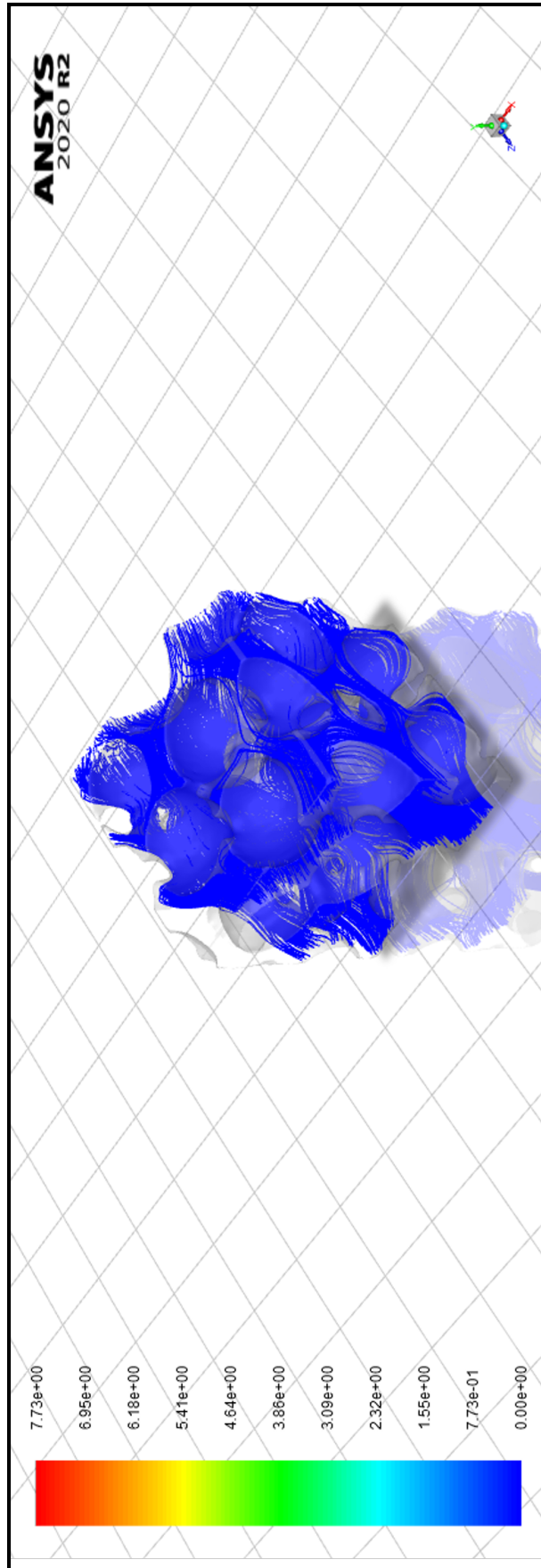


Figure 5.31: The pathlines for sample 6 The legend describes the velocity of the pathlines (m/s) and the size of the mesh is  $400 \mu\text{m}^3$ .

Table 5.16: The average flow velocity from the pathline results from the different meshes which have different pressure drops. The different pressure drops are based on the results from the pore-scale permeability experiments.

| Sample | Zone | Flow Velocity (m/s)   |
|--------|------|-----------------------|
| 1      | 3    | $2.10 \times 10^{-3}$ |
| 2      | 2    | $3.09 \times 10^{-3}$ |
| 2      | 3    | $1.20 \times 10^{-3}$ |
| 2      | 4    | $2.69 \times 10^{-3}$ |
| 3      | 2    | $8.99 \times 10^{-4}$ |
| 3      | 3    | $4.90 \times 10^{-2}$ |
| 3      | 4    | $3.08 \times 10^{-3}$ |
| 4      | 2    | $2.39 \times 10^{-3}$ |
| 5      | -    | $6.86 \times 10^{-5}$ |
| 6      | -    | $7.73 \times 10^{-1}$ |

a reservoir rock can also be associated with reservoir storage and productivity as pore size can determine the amount of hydrocarbon stored, for example, oil is more likely to be stored in pores  $> 20$  nm (Zhang et al., 2016; Alfi et al., 2019). From the core and bead pack characterisation results it is evident that grain/bead size significantly impacts the mean pore diameter and these results correspond well to other results in the literature, where the pore diameter is expected to roughly equate to grain size (Revil et al., 2012) and it is expected that the pore size increases with increasing bead size (Chung and Lin, 2017) and two geometrically similar pore geometries of different scales will see a scaling of pore size with grain diameter. The pore diameter distribution results from all four bead pack samples present a bimodal distribution, which is typical of fine grained sandstones (Zhang et al., 2018b), and the bimodal distribution is more pronounced in the sample with the largest bead size and less pronounced in the sample with the smallest bead size which implies that increasing bead size corresponds to increasing polarity in pore diameter size distribution.

The bead pack characterisation results also suggest that the arrangement of bead size (e.g. large beads to small beads or small beads to large beads) influences pore diameter and mean pore diameter and the range of mean pore diameter is larger overall when larger beads transition to smaller beads (Fig. 5.5 and 5.6). Furthermore, the results from the characterisation of the bead pack samples indicate that the bead size which occurs second in the samples which have two different bead sizes influences the distribution of pore diameter size more so than the bead size which occurs first in the sample. For example, samples 1 and 3 show comparable patterns where two distinct narrow peaks are observed when pore diameter size is plotted against frequency of pore diameter size (Fig. 5.5). On the other hand, the two peaks observed in samples 2 and 4 are much wider. The difference in pore diameter results in the samples which have bead size contrasts is a result of the different packing and bead sorting which creates different pore network geometries and this was demonstrated in Figures 5.7, 5.8 and 5.9. The packing and bead sorting in the samples is a gravity driven process and when smaller beads transition to larger beads the larger beads are below the smaller beads and the smaller beads are able to infill the pore space below when the sample is being made which subsequently leads to poorer sorting in the transitional zone, and a gradational boundary between the two bead sizes. This restricts the pore space and results in a smaller mean and range of pore diameter size and is in agreement with other results in the literature which indicate a mixture of small and large particle size reduce the size of pore openings (Porubcan and Xu, 2011). When larger beads transition to smaller beads the larger beads are above the smaller beads and the larger

beads are too big to infill the pore space below which produces better sorting and a sharp boundary between the two bead sizes. Due to the above reasons the pore space is less restricted than when larger beads transition to smaller beads which results in a larger mean and range of pore diameter size. Although the samples are synthetic this process can also be observed in natural rock samples at many scales, for example, gradational contacts and graded bedding can be observed due to a change in depositional conditions, such as increasing/decreasing energy in transport resulting in increasing/decreasing grain size in sedimentary deposits. Gradational contacts are defined by a gradual transition in the average size of deposited clasts and graded bedding is defined by vertical change in grain size (Onoja and Shariatipour, 2018). Graded bedding is observed in the Sherwood Sandstone Group and the particle size decreases upwards from coarse sandstones (750–1000  $\mu\text{m}$ ) to siltstones (8–63  $\mu\text{m}$ ) (Onoja and Shariatipour, 2018). Sharp contacts are commonly observed as a result of a sudden change in conditions, such as mass flow events (e.g. flash floods) (Rehrmann et al., 2012).

The porosity results from the homogeneous bead pack samples indicate that porosity increases with increasing bead size and this is in agreement with the results within the literature which associate smaller grain size with lower porosity (Kashif et al., 2019; Yusuf and Padmanabhan, 2019; Algive et al., 2012). The porosity increases with increasing bead size due to the differing packing in the samples and this is due the relative size of the beads in comparison to the diameter of the capillary tube. Additionally, the packing differs between the samples which have homogeneous bead size due to the sintering process which may have had a greater impact on the sample with smaller bead size as the surface area of the beads is greater therefore enhancing the amount of sintering (Fang et al., 2016) and result in a greater reduction of porosity. Furthermore, the degree of sintering may also be enhanced in the sample composed of smaller beads as temperature increases at bead contact points (Fang et al., 2016) and more of the smaller beads will be in contact than the larger beads. The sintering process may also alter the shape of the beads and the shape of particles strongly influences the packing density and the packing of non-spherical particles produces a greater range of porosities than the packing of spherical particles (Prior et al., 2013).

The porosity results also suggest that heterogeneity in bead size is a governing factor on porosity and both methods of estimating porosity demonstrate that the samples which present bead size contrasts have lower porosity than the samples which do not present bead size contrasts, however, the Avizo®Fire porosity indicates that porosity is lower in sample 2 whereas the ANSYS Fluent porosity indicates that porosity is lower in sample 3. Although the results from the two methods of estimating porosity differ, there are only three porosity results from ANSYS Fluent whereas there are five porosity results from Avizo®Fire. Furthermore, the five zones analysed in the Avizo®Fire software are much larger than the three tetrahedral meshes analysed in ANSYS Fluent and it is possible that an above average porous region was sampled when the meshes were created as the meshes were created from a smaller region of the same image stack which is analysed Avizo®Fire. Moreover, the porosity result for sample 2 zone 2 suggests that the porosity is the highest in an area of smaller beads than in an area of larger beads and the porosity results for sample 2 zone 2 is the highest result measured, which contradicts other results in this study and in the literature. The ANSYS Fluent porosity results for sample 2 are also higher than the results for sample 3 despite both samples sharing the same composition. When the ANSYS Fluent porosity results from sample 2 zone 2 are compared to the results from sample 3 zone 4 an 8.51% difference is observed in porosity despite both of the zones sharing the same bead size. Additionally, the pore diameter results show that sample 3 has a larger mean pore diameter and a larger range in pore diameter than sample 2 which is due to the different packing and sorting of the beads and this indicates that the pore space is greater in sample 3 than in sample 2. The sorting of the beads in sample 2 is poorer than the

sorting of beads in sample 3 as a consequence of smaller beads infilling the pore space between the larger beads below and poorer sorting is associated with reduced porosity (Al-hasani et al., 2018; Yusuf and Padmanabhan, 2019), further signifying that the porosity results from ANSYS Fluent for sample 2 are not representative. Due to this, it is expected that porosity is greater in sample 3 rather than sample 2, which implies that porosity is greater when larger beads transition to smaller beads than when smaller beads transition to larger beads.

In the core samples the porosity results from both the MIP and ImageJ analysis show that the porosity is highest in the sample with the largest overall grain size (core sample 4), however, the sample with the lowest porosity does not have the smallest overall grain size. During the ImageJ analysis two areas of the thin section sample were selected in samples which displayed contrasting properties (e.g. contrasting grain size, contrasting grain shape, contrasting mineralogy or cementation) due to features such as laminations or deformation bands. Core sample 3, which has the lowest porosity, exhibits clay sized laminations (Figs. 5.1 and 5.3) which provides a large grain size contrast between the rest of the sample. Clay particles are  $<62\ \mu\text{m}$  which means that at the least there is a  $438\ \mu\text{m}$  grain size contrast within the laminations which frequent this sample and there are regular zones of significantly lower porosity in core sample 3. This is also demonstrated by core sample 2, which features dolomite nodules and concretions. In the areas where dolomite nodules and concretions occur porosity is 10.16% lower which is expected as typically nodules and areas of cementation result in porosity reduction (Del Sole and Antonellini, 2019). These zones of lower porosity contribute to the reduction overall porosity of the sample, however, it is observed that the porosity is lower overall in core sample 3 due to the occurrence of clay sized laminations, so porosity is lower in samples which have laminations of finer material rather than in samples which have coarser material, such as core sample 1, which further supports the interpretation that grain size controls porosity. It is also important to consider the geometry of the minerals which occur in the core samples, and clay can occur in clasts, platy shapes, pore filling, sheet like, fibrous (e.g. illite), or as booklets (e.g. kaolinite) (Griffiths et al., 2019; Han et al., 2015; Gao et al., 2019) and clasts, pore filling, fibrous and booklet forms can be especially detrimental to porosity (Gao et al., 2019; Olivarius et al., 2015b), which may also account for the reduction in porosity in core sample 3 in addition to the large particle size contrast.

### 5.3.2 How does the pore network geometry influence tortuosity and flow pathways?

From the tortuosity results it is obvious that the variable pore network geometries, due to the differing bead sizes and bead size contrasts in the samples, influence the tortuosity of the pore network. Firstly, in the homogeneous samples it was observed that tortuosity increases with increasing bead size (Fig. 5.20), which is in agreement with other results in the literature (Ghassemi and Pak, 2011; Zakirov and Khrumchenkov, 2020), and this is interpreted to occur as a result of the increased range in pore diameter size and porosity resulting in greater disorder and heterogeneity in the pore network (Zhu et al., 2018; Zakirov and Khrumchenkov, 2020; Guo, 2012). A pore network with a greater range in pore diameter size distribution is expected to be more tortuous as fluid will naturally seek the easiest route through the medium which would be the route with the largest pores which enable the fastest fluid flow and in doing this fluid flow will bypass smaller pores which are not capable of supporting as fast fluid flow resulting in increased tortuosity (Salem, 1993; Nemati et al., 2020). The results from Nemati et al. (2020) also suggest that it is only pore throat radii which contributes to tortuosity and pore size does not influence tortuosity, which contradicts the results from this study. This disagreement could be a result of the different methodologies and samples used, as although Nemati et al. (2020) use a sample of the Berea sandstone to calculate tortuosity they then use a

pore network model (PNM) to study the effect of different pore and pore throat distributions. It is possible that the role of pores in fluid transport have been underestimated by [Nemati et al. \(2020\)](#) and the pore shape and sizes selected in this PNM are overly simplified, reducing their contribution to tortuosity. On the other hand, the samples in this study, despite presenting a more simplified pore network than those found in natural rock samples, have proven that they present a greater degree of complexity than a standard, homogeneous bead pack.

The results also show that the arrangement of bead size in the samples which have bead size contrasts influences tortuosity and this is evident in [Figure 5.21](#) and this is expected as variable particle arrangement can result in variation in tortuosity and flow pathways ([Ghanbarian et al., 2013](#)). When smaller beads transition to larger beads tortuosity gradually declines through the sample implying that tortuosity decreases with increasing bead size which contradicts the results from the homogeneous samples which suggest that tortuosity increases with increasing bead size. However, it is problematic to compare the results from the homogeneous samples to the results from the heterogeneous samples as the pore network properties (pore diameter, porosity) within the samples differ greatly due to the different degree of sorting and packing in the samples. The decline in tortuosity when smaller beads change to larger beads is likely a result of the gradual change from a more restricted pore network, due to the increased packing density as a result of poor sorting ([Desmond and Weeks, 2014](#)), to a more open pore network and the gradational nature of this change could prolong the effect that the smaller beads have on fluid flow throughout the sample. This could be due to the already established fluid flow pattern in the sample and fluid flow is expected to be controlled and uniform when the bead size is smaller because the mean pore diameter and range of pore diameter is smaller and porosity is lower so it is less common for pores to be bypassed in favour of larger pores which facilitate faster flow as expected in the homogeneous sample with the largest bead size and greatest tortuosity. When the fluid flow reaches zone 4, where the pore space increases significantly (29.39%), the fluid flow may still be influenced by the flow pattern in the previous zones and fluid may not be able to reach high velocities as the pore space in the previous zone does not enable this and therefore will not seek larger pores to facilitate faster transport and take a less tortuous path through the sample. Alternatively, zone 4 may be less tortuous as the pathways from zones 2 and 3 may enter zone 4 and create a confluence of flow through the rest of the sample, reducing tortuosity by concentrating several minor flow pathways into fewer, larger pathways. When larger beads transition to smaller beads tortuosity decreases from zone 2 to 3 and then increases from zone 3 to 4. The reduction in tortuosity between zone 2 and 3 is expected as the pore space is reduced and the mean pore diameter is observed to decrease by 0.02 mm (24.8%). The increase in tortuosity between zones 3 and 4 could be due to increased packing density in the lower half of the sample where larger beads change to smaller beads. When the sample was created the larger beads were packed on top of the smaller beads which meant that the smaller beads would become more densely packed as a result of the weight of the larger beads above. This may have increased the amount of sintering the smaller beads underwent causing them to compact further which would reduce the pore space and reduce the connections between the pore space, resulting in a more sintered, heterogeneous pore space which would increase tortuosity ([Nemati et al., 2020](#); [Attia, 2005](#); [Salem, 1993](#); [Muljadi et al., 2016](#)). The increased effect of sintering is comparable to the effect of cementation in sedimentary rocks and enhanced cementation can occur as a consequence of overburden pressure (from overlying sediment which increases with burial depth) which can flatten rounded particles resulting in greater angularity in particle shape and increasing cementation ([Salem, 1993](#)). This is not observed when smaller beads change to larger beads as the smaller beads do not have the same overburden pressure as when larger beads change to smaller beads and the pore space in the transitional zone is much less affected by enhanced sintering as much of the pore space between the larger beads is infilled with



smaller beads. The difference in the tortuosity results for the samples which have bead size contrasts can also be associated with the pore diameter size distribution and range of pore diameter size, as observed in the homogeneous samples, as greater variation in pore size creates more heterogeneous pore structure (Gao and Li, 2016). There is greater variation in pore diameter size when larger beads change to smaller bead so it is expected that the pore network will have greater heterogeneity which will increase tortuosity.

The tortuosity results are in agreement with the results in the literature which indicates that the bead pack samples created in this study have achieved the goal in increasing the complexity of a standard bead pack and have reduced the complexity of natural rock samples. In Muljadi et al. (2016) a homogeneous bead pack composed of 100  $\mu\text{m}$  glass beads has a tortuosity of 1.26, a sample of the Bentheimer sandstone has a tortuosity of 1.52 and a sample of the Estailades limestone has a tortuosity of 1.92. In comparison, the tortuosity of the bead packs in this study range from 1.07 - 4.58 and tortuosity is highest in the sample with the greatest amount of compaction and sintering. Furthermore, the tortuosity is lowest in the sample where large beads occur in the second half of the sample and flow is predicted to be able to confluence and form fewer, preferential flow pathways or flow is restricted by the reduced pore space in the zone with smaller beads and in the transitional zone. Laudone et al. (2015) report the tortuosity of two different limestone formations to range from 1.20 - 1.49 and a red bed sandstone to have a tortuosity of 1.52 which again signifies that tortuosity is generally greater in more complex samples. Furthermore, Zecca et al. (2018) show that tortuosity in three different sandstone formations (Berea, San Saba and Nugget sandstone) also fell within the range of 1 - 4 and Nemati et al. (2020) estimate tortuosity in a sample of the Berea sandstone to have a tortuosity of 2.07. Alongside the results from this study, the literature indicates that tortuosity increases with increasing heterogeneity in the pore network (Zakirov and Khramchenkov, 2020). Tortuosity is also related to porosity and the relationship between tortuosity and porosity varies depending on the study. For example, Ziarani and Aguilera (2012) and Laudone et al. (2015) indicate that tortuosity decreases with decreasing porosity, whereas Ghassemi and Pak (2011) and Zakirov and Khramchenkov (2020) suggest that tortuosity decreases with increasing porosity. In this study there is no clear relationship between tortuosity and porosity and the results indicate that other properties are important to consider when analysing tortuosity, such as the uniformity of pores and particle size and the tortuosity is only expected to be a function of porosity in simple, isotropic porous media (Guo, 2012).

The fluid flow pathways displayed in Figures 5.22 - 5.31 are consistent with the tortuosity results. In the homogeneous samples (Figs. 5.22, 5.29, 5.30 and 5.31) the sample with the largest bead size, and therefore the pore network with the largest mean pore diameter, range in pore diameter and porosity, displays areas of preferential, high velocity flow which occur sporadically throughout the sample. This supports the tortuosity results which suggest that samples which have larger bead size are more tortuous due to the fluid flow bypassing smaller pores to reach larger pores which facilitate high velocity flow (Salem, 1993; Nemati et al., 2020). The sample with smaller bead size presents much more uniform flow velocity throughout the sample which again supports the tortuosity results which indicate that tortuosity is reduced when bead size is smaller due to the limited pore space available for fluid flow and the limited range in pore diameter size. In the samples which present bead size contrasts it is evident that the flow pathways are influenced by the arrangement of bead size (Figs. 5.23 - 5.28). When smaller beads transition to larger beads, the flow pathways transition from uniform fluid flow to less uniform fluid flow. The flow pathways, to an extent, confirm the tortuosity results, which suggest that fluid flow became less tortuous downstream due to two reasons:

1. higher velocity tortuous flows were not supported in the pore network as the previous zones

restricted flow

2. multiple flow pathways merge into fewer, larger, high velocity flow pathways.

It is clear from the results that when smaller beads have changed to larger beads fluid flow becomes concentrated into fewer, preferential high velocity flow paths as fluid flow favours the wider pores (Li et al., 2018). When larger beads transition to smaller beads the flow pathways present three different flow patterns which are also agreeable with the tortuosity results. Tortuosity decreases from zone 2 to zone 3 due to the reduced pore space and this is displayed by the pathlines which show a less uniform flow field with preferential high velocity pathways in zone 2 and a very uniform flow pattern and low velocity flow in zone 3, indicating that zone 3 may act as a baffle to fluid flow or even a barrier to high velocity flow as it does not have the available pore space (or large enough pores) to enable high velocity flow. High velocity flow requires larger pores as larger pores have a greater capacity (Li et al., 2018). In zone 4 tortuosity increases due to increased bead packing and compaction and this is demonstrated by the flow pathways which show a non-uniform flow pattern which displays small isolated areas of higher velocity. This pattern is also observed in sample 5, which has the smallest bead size (18  $\mu\text{m}$ ), and suggests that the increased effect of packing and compaction in the smaller beads in the lower half of this sample has a similar impact on fluid flow pathways and tortuosity as reduced bead size does.

### 5.3.3 How does the pore network geometry, tortuosity and fluid flow pathways control pore scale flow phenomena?

The permeability throughout each of the four bead pack samples varies depending on the technique used to measure / estimate permeability.

The experimental permeability results present the lowest permeability from the four methods used to estimate permeability and suggest that permeability increases with increasing average bead size (Table 5.8). This is supported by the bead pack characterisation, tortuosity and flow pathway results which indicate that the pore diameter size and range in pore diameter size increases with increasing bead size which enables a greater amount of fluid flow in the samples with larger bead size. This corresponds well with results in the literature which also conclude that permeability increases with increasing particle size (Yoneda et al., 2019; Oliveira and Nicolodi, 2017; Ghassemi and Pak, 2011) and pore size (Pape et al., 2000) and resistance to flow is expected to increase with decreasing pore size and smaller pores are also less able to permit high velocity fluid flow (Nemati et al., 2020; Salem, 1993). The samples which present bead size contrasts indicate that the arrangement of bead size influences the permeability and suggest that permeability is greater when smaller beads have changed to larger beads.

The results from the Kozeny-Carman model further indicate that permeability increases with increasing bead size (Table 5.9). This trend is also reflected throughout the different zones of the samples which have bead size contrasts. It is expected that the Kozeny-Carman permeability in this study will increase with increasing bead size as porosity also increases with increasing bead size and the model directly relates porosity to permeability (Zhang et al., 2016; Ghanizadeh et al., 2015; Wang et al., 2017; Sun et al., 2007; Urumović, 2016; Szabó et al., 2015). Due to this two sets of porosity values (from the Avizo®Fire and ANSYS Fluent software) were inputted into the model to assess the reliability of the results. The results from the homogeneous samples show good agreement (Fig. 5.15) and the results from the Avizo®Fire porosity show minimal deviation from the experimental results, however, in the sample with the largest bead size the permeability is predicted to be much higher (+ 36.30D) when using the porosity results from ANSYS Fluent despite the

average porosity only increasing by 2.36%, suggesting that the model overestimates the influence of increasing particle size on permeability. The model's reliance on porosity is well documented in the literature and if porosity is slightly overestimated then the permeability predicted by the Kozeny-Carman model will also be overestimated (Urumović, 2016). Similarly, if porosity is underestimated then the permeability predicted by the Kozeny-Carman model will also be underestimated (Urumović, 2016). On the other hand, some studies in the literature conclude that the Kozeny-Carman model carries an error of up to one order of magnitude (Szabó et al., 2015), however, in this study the difference between the overall permeability from the experiments and from the model is much less. The permeability results for the samples which present bead size contrasts show opposing results determined by the porosity values used, for example, when the Avizo Fire porosity is used it is suggested that permeability is greater when smaller beads transition to larger beads also support the experimental results which show that permeability is greater when smaller beads transition to larger beads. On the other hand, when the porosity from ANSYS Fluent is used the results indicate that permeability is greater when larger beads transition to smaller beads, which supports the results from the pore-scale permeability experiments.

The range of permeability values from the Avizo®Fire software are in agreement with the results from the pore-scale permeability experiments and the Kozeny-Carman model and the results from the homogeneous samples indicate that permeability increases with increasing bead size. The average permeability result for the sample with the smallest beads shows a small difference of 6.78 D when compared to the results from the experiments and a difference of 1.9-5.96 D when compared to the Kozeny-Carman results. However, the permeability results for the sample with the largest beads shows greater variation and the average permeability differs by 22.63 D when compared to the experimental results and by 16.43 – 19.87 D when compared to the Kozeny-Carman results. This suggests that like the Kozeny-Carman model, the Absolute Permeability Experimental Simulations in the Avizo®Fire software may also overestimate permeability in samples which have larger bead size. Alternatively, as the results from the Kozeny-Carman model and Avizo Fire simulations are in agreement it may suggest that the experimental permeability for the sample with larger bead size is underestimated. The experimental equipment or experimental procedure could have restricted the fluid flow during the experiments which in turn could have reduced the permeability. For example, the size of the bead pack and the connecting pipes could have reduced the amount of fluid flow into the sample. Additionally, the flow meter may have also reduced fluid flow as fluid flowed from a pipe with a larger diameter into the flow metre where the pipe diameter was reduced and to exit the flow metre fluid flowed into a pipe with a larger diameter. The reduction in pipe diameter may have influenced the pressure gradient in the experimental system and a reduction in pipe diameter can result in an enhanced pressure gradient due to increased friction inside the pipe which would decrease permeability (Al-Wahaibi et al., 2014). On the other hand the permeability results from the Kozeny-Carman model and Avizo®Fire simulations may have been overestimated due to image processing errors as image segmentation and image filtering varied between the different image stacks of the samples. Over-processing may increased the porosity and permeability of the pore network and under-processing may have decreased the porosity and permeability of the pore network. Due to this, some variation in the results is to be expected due to the differences in then techniques used to measure and predict permeability and the permeability is still within one order of magnitude and permeability in soft sediments and reservoir rock can often vary by at least one order of magnitude due to variable conditions such as petrophysical properties and temperature (Oliveira and Nicolodi, 2017; Cheng and Milsch, 2020). The permeability results from the samples which display bead size contrasts are in agreement with the results from the experiments and the Kozeny-Carman model and demonstrate that permeability is greater when smaller beads transition to larger beads.

Additionally, when the permeability for the samples is averaged the permeability is comparable with the permeability from the transitional zone for both samples (3 - 6 D).

The CFD simulations conducted in ANSYS Fluent are in accordance with the other permeability results and the literature. In comparison with the other permeability results the CFD results predict permeability to be higher and this is especially evident in the zones/sample with larger bead size. The tetrahedral meshes of the bead pack samples are created in the Avizo®Fire software so any over-processing which could have influenced the permeability results in the Avizo®Fire simulations may also influence the permeability results in the CFD simulations. Additionally, the CFD simulations use a smaller sample area ( $0.4 \text{ mm} \times 0.4 \text{ mm}$ ) to increase resolution and reduce computational time and it is possible that some of the areas which were sampled exhibited above average permeability, such as sample 2 zone 4. In the samples which present bead size contrasts the CFD results suggest that permeability is greater when smaller beads transition to larger beads and the CFD results also provide an insight into how the pressure difference and permeability varies throughout the transitional zones (Figs. 5.12, 5.13). In both samples the pressure difference displays a distinct change in gradient where the bead size changes and in sample 2 this shows that the pressure difference decreases throughout the zone whereas in sample 3 the pressure difference increases throughout the zone. This is in agreement with the previous analysis on the pore network geometry, tortuosity and flow pathways which demonstrate that when smaller beads transition to larger beads the pore diameter size and range in pore diameter sizes increases throughout the sample resulting in a more open pore network which has greater capacity for fluid flow, which is further demonstrated by the increase in tortuosity as there are more routes through the sample fluid can take. Additionally, the experimental results (Fig. 5.10) show that pressure difference is the lowest in the sample with the largest bead size so it is expected that the pressure difference would decrease when bead size is increased. This corresponds with the literature which predicts that the effect of capillary pressure decreases with increasing grain size (Tsai et al., 2018). When larger beads transition to smaller beads the inverse is observed and the previously discussed results indicate that the pore space becomes more restricted and heterogeneous and the pressure difference increases when the bead size is reduced which is expected due to the established relationship between bead size and pressure difference aforementioned (Tsai et al., 2018). The permeability throughout the transitional zones presents a less distinct trend but in sample 2, when smaller beads change to larger beads, the overall permeability increases throughout the sample (Fig. 5.13). This again is to be expected due to the change in pore network properties, tortuosity, flow pathways and pressure difference as outlined previously. In sample 3, where larger beads change to smaller beads, the permeability appears to decrease then stabilise throughout the sample. Again, this is to be expected and reinforces the pore network geometry, tortuosity, flow pathways and pressure difference results discussed earlier. The average permeability for the samples also corresponds well to the permeability values from the transitional zones and shows a 2-8 D difference.

The CFD simulations were also used to analyse the transition from Darcy flow in the samples and the transition from Darcy flow was observed when permeability begins to decrease (Fig. 5.16). Additionally, the transition from Darcy flow may also be observed when flow rate is plotted against pressure difference and the transition is expected when then gradient becomes less than 95% (Comiti et al., 2000; Muljadi et al., 2016) where inertial forces begin to increase and eventually become dominant (Li et al., 2017a). The onset of non-Darcy flow is often related with high velocities and is expected to occur near pumping wells, near or in the wellbore region or in fractured reservoirs (Wen et al., 2011; Chukwudozie et al., 2012; Li and Engler, 2001). When the critical Re is compared to mean pore diameter (Fig. 5.17) it suggests that the critical Re increases with increasing mean pore diameter size, and mean pore diameter size increases with increasing bead size, indicating that the

critical  $Re$  increases with increasing bead size. In this study increasing mean pore diameter size corresponds to a greater range in pore diameter sizes, higher tortuosity, lower resistance to fluid flow and high velocity preferential pathways which increases permeability. Due to this, it is interpreted that the onset on non-Darcy flow occurs at lower  $Re$  in the samples with smaller mean pore diameter as the flow is more restricted by the pore network geometry and due to this the pore networks are not capable of reaching the higher  $Re$  before the transition from non-Darcy flow occurs. This is supported by the experimental and CFD  $Re$  results which show that the samples with the lowest bead size (and lowest mean pore diameter size) also have the lowest  $Re$  under the same conditions and it is also noted in the literature that  $Re$  and critical  $Re$  increases with increasing particle diameter size (Li et al., 2017b) and this is due to larger pores facilitating turbulent flow (Bordier and Zimmer, 2000). Furthermore, the variation in  $Re$  at which the onset of non-Darcy flow occurs is to be expected as it is well documented that non-Darcy flow characteristics and flow regimes differ throughout porous media with different structures and this is enhanced at higher  $Re$  (Li et al., 2017b; Tosco et al., 2013). In the samples which have bead size contrasts the onset of non-Darcy flow occurs asynchronously throughout the sample and this is expected as the transition from laminar flow is gradual and non-linear (Venkataraman and Rao, 1998). Both samples show that the critical  $Re$  decreases throughout the sample regardless of the bead size in the lower half of the sample which suggests that bead size is not the only factor which influences the critical  $Re$ . When smaller beads change to larger beads the tortuosity results show that tortuosity also decreases throughout the zones (Fig. 5.21) and this suggests that tortuosity also plays a key role in influencing the critical  $Re$ . On the other hand, when larger beads change to smaller beads the tortuosity doesn't decrease throughout the zones which suggests that tortuosity may not play as vital role in the determining the critical  $Re$ . Alternatively, heterogeneity in the pore space increases downstream in both samples, due to heterogeneous bead size and enhanced packing and sintering, signifying that increased heterogeneity in the pore space results in increased heterogeneity in the critical  $Re$ . From this analysis it is evident that there is no single control on the critical  $Re$  and many variables must be considered in samples which are more complex.

The  $\beta$  results from the Forchheimer graphs indicate that, alike the critical  $Re$ ,  $\beta$  also varies across the samples. In the homogeneous samples the results indicate that  $\beta$  increases with decreasing bead size. In the samples which present bead size contrasts  $\beta$  increases when larger beads transition to smaller beads which further supports the results from the homogeneous samples which indicate that  $\beta$  is related to bead size. When smaller beads transition to larger beads there is an overall reduction in  $\beta$  if the transitional zone is discounted. The transitional zone when smaller beads change to larger beads is more poorly sorted than the transitional zone when larger beads change to smaller beads and it may be that the beads in the sampled area are predominantly small, which is likely as smaller beads are able to infill the pore space between the larger beads. Due to this it is accepted that  $\beta$  increases with decreasing bead size and this is in good agreement with the results from the literature as it is reported that  $\beta$  is dependent on the properties of porous media (Sidiropoulou et al., 2007; Venkataraman and Rao, 1998) and Arbhahirama and Dinoy (1973), Ahmed and Sunada (1969), Venkataraman and Rao (1998), Bordier and Zimmer (2000) and Sidiropoulou et al. (2007) also report that  $\beta$  decreases with increasing grain size in glass beads, sands, gravels and crushed rock. Furthermore, Sidiropoulou et al. (2007) suggest that in glass bead samples  $\beta$  is inversely proportional to porosity and this is also observed from the results from the homogeneous samples in this study. In the homogeneous samples permeability increases with increasing bead size and given that  $\beta$  decreases with increasing bead size it is implied that  $\beta$  decreases with increasing permeability too. This contradicts with the results from Venkataraman and Rao (1998) who suggest that  $\beta$  increases with increasing permeability despite also finding that  $\beta$  decreases with increasing grain size. Given

that it is widely considered that permeability increases with increasing bead size (Yoneda et al., 2019; Oliveira and Nicolodi, 2017) and  $\beta$  decreases with increases with increasing grain size (Arbhabhirama and Dinoy, 1973; Bordier and Zimmer, 2000; Sidiropoulou et al., 2007) it is accepted that it is more likely that  $\beta$  decreases with increasing permeability.

In the literature the  $\beta$  values are variable and the  $\beta$  is also referred to as the turbulence factor, the coefficient of inertial resistance, the velocity coefficient, the non-Darcy flow coefficient, the Forchheimer coefficient, the inertial coefficient and the non-linear parameter in the literature, and ranges from 3.00E+00 - 2.09E+06 (Li and Engler, 2001; Chukwudozie et al., 2012; Tosco et al., 2013; Arbhabhirama and Dinoy, 1973; Venkataraman and Rao, 1998; Muljadi et al., 2016) (Ranganadha et al., 1970). The large range in the  $\beta$  is expected to occur as a result of the limitations in using empirical formulas to model flow parameters (Chukwudozie et al., 2012) and computed results which are validated by experimental data, the root mean square error and normalised objective function are expected to present more reliable results (Sidiropoulou et al., 2007).

## 5.4 Conclusions

The results from this chapter confirm the widely held view that bead size and the arrangement of bead size significantly influences the pore network geometry which in turn controls how fluid flow moves throughout the pore space and determines the permeability of the sample.

In the homogeneous samples bead size influences mean pore diameter size, the range of pore diameter size and porosity, and larger bead size corresponds to larger mean pore diameter size, a larger range in pore diameter size, a less uniform distribution of pore diameter size and greater porosity. The arrangement of bead size (e.g. when smaller beads transition to larger beads or larger beads transition to smaller beads) also influences the mean and range of pore diameter size and when smaller beads transition to larger beads the mean pore diameter and range of pore diameter sizes is lower but the distribution of pore diameter size is more uniform than when larger beads transition to smaller beads. This is due to the different packing and sorting which is facilitated by the available pore space and when smaller beads transition to larger beads the pore space is more restricted as the degree of sorting is poorer and the beads are more densely packed and this is due to the smaller beads being able to invade the pore space between the larger beads below, which is not possible when the bead sizes are arranged the opposite way.

In the homogeneous samples it is observed that larger bead size results in higher tortuosity because of the reduced uniformity in pore diameter size, range and distribution. Reduced uniformity in pore diameter size, range and distribution presents a greater resistance to fluid flow as fluid flow will bypass smaller pores in favour of larger pores which have a greater capacity for high velocity flow resulting in more tortuous flow paths. In the samples which have bead size contrasts it is evident that fluid flow is more consistent throughout the pore network (multiple, smaller, low velocity flow pathways) when smaller beads transition to larger beads than when larger beads transition to smaller beads and this is due to a more heterogeneous pore network in the lower half of the sample which is a consequence of increased packing density and compaction due to overburden of the larger beads.

The permeability results from the samples with homogeneous bead size are in agreement with the literature and show that permeability increases with increasing bead size and this is a consequence of a large ranging non-uniform pore diameter distribution which encourages high velocity preferential flow pathways. In the samples with heterogeneous bead size permeability is higher when smaller beads transition to larger beads as the pore network geometry is more homogeneous due to less

bead compaction and a lesser amount of sintering in comparison to when larger beads transition to smaller beads.

The CFD simulations present the highest permeability and the experiments present the lowest permeability. Some variation is expected due to the different techniques used to measure and predict permeability and the variation is predicted to have been influenced by some human error during image processing and the possibility that the pressure difference in the experiments was artificially increased by experimental instruments with very narrow pipes. Despite this, the permeability results are still within the same order of magnitude which is comparable as permeability can often vary over one order of magnitude.

In the samples with homogeneous bead size the onset of non-Darcy flow is determined by the size of pores and the critical  $Re$  is higher when pores are larger as larger pores have the capacity for high velocity flow and are less resistant to flow in comparison to smaller pores. In the samples which present bead size contrasts the onset of non-Darcy flow appears to be influenced by different properties and when smaller beads transition to larger beads the critical  $Re$  decreases with decreasing tortuosity throughout the sample as a result of fluid flow being funneled from multiple smaller pores into fewer, larger pores which restricts the velocity of the flow and reduces the critical  $Re$ . When larger beads transition to smaller beads the critical  $Re$  also decreases throughout the sample due to increasing heterogeneity and decreasing permeability of the pore space. From the samples with heterogeneous bead size it is evident that many variables must be considered when assessing the influence on the critical  $Re$ .

In the non-Darcian regime the  $\beta$  results show that  $\beta$  increases with decreasing bead size and this is displayed by all of the samples. The homogeneous samples further indicate that  $\beta$  increases with decreasing permeability.

## Chapter 6

# How does heterogeneity in mineralogy impact mineral dissolution and transport properties in the pore network?

### 6.1 Introduction

The mineralogy in sandstones can vary greatly and the dominant minerals include quartz, feldspars, clay minerals and carbonate minerals. The mineralogy is dependent on the provenance, transport mechanisms, weathering, tectonic setting, climate, the environmental conditions at the time of sediment deposition and diagenetic processes (Wang et al., 2020c; Mahmud et al., 2018). A change in mineralogy may be gradual or abrupt and this is determined by the type of contact with the over/underlying facies, the diagenetic history of the rock (e.g. cementation/dissolution patterns) and any structural features, such as faults or folds. The minerals which occur in sandstones can influence reservoir quality, for example, clay minerals are associated with reduced intragranular porosity and pore size (Qiao et al., 2020). Furthermore, the form in which minerals occur also plays a large role in reservoir quality and pore network geometry. For example, quartz and carbonate minerals (e.g. calcite, dolomite) can occur as grains, cement or overgrowths and clay minerals can occur in the form of fibres, booklets, platelets, dendritic shapes and coatings on other grains, which in some cases is beneficial as it can prevent mineral overgrowths during diagenesis and preserve original porosity (Olivarius et al., 2015b; Arribas et al., 2012).

The mineralogy of sandstones can also determine wettability and quartz rich sandstones are typically water wet but when clay minerals occur it changes the wettability to mixed wet or CO<sub>2</sub> wet media (Chaudhary et al., 2013b). The dissolution of minerals is a geochemical process where fluids react with reactive minerals (e.g. calcite, dolomite, feldspars) which can result in the reactive mineral partially or fully dissolving or parts of the reactive mineral becoming broken off. Dissolution can occur due to various reasons, for example, diagenesis, acid injection, CO<sub>2</sub> injection, and can result in secondary porosity or alternatively the dissolution of feldspars can create secondary minerals such as illite, kaolinite and smectite which can reduce porosity and permeability as clay minerals are often associated with reducing porosity and blocking pore throats, especially when the occurrence of clay minerals is significant (>3%) (Wang et al., 2020a; Arribas et al., 2012; Olivarius et al., 2015b; Xiao et al., 2018) and dissolved carbonate minerals in solution may later precipitate as new carbonate (Liu et al., 2011). Furthermore, this may lead to spatial differences in porosity and permeability (Sabo



and Beckingham, 2021) and dissolution may occur close to the injection site and precipitation may occur further away. The rate of dissolution is determined by mineralogical reaction rates which are controlled by the surface area of the mineral, heterogeneity in mineralogy, fluid flow rate, reaction time, fluid chemistry and temperature (Liu et al., 2018).

Currently, it is not well understood how different minerals and the dissolution of different minerals influences fluid transport phenomena in sandstone pore networks but it is expected that variable mineralogy may result in varying pore network properties, such as porosity and permeability, which will influence mineral reactions which may further alter the pore network geometry and transport phenomena. In order to gain insight into these processes, this chapter analyses and discusses the results from the pore scale permeability experiments across bead pack samples with different mineralogy before and after an acidic fluid flow to assess how different minerals alter pore diameter distribution, porosity, permeability and reaction rate.

## 6.2 Results

The results presented and discussed in this chapter include core characterisation, pore network geometry, permeability from the pore-scale permeability experiments before and after acidic flow, Avizo®Fire absolute permeability simulations and the amount of mineral dissolution after acidic flow.

### 6.2.1 Core Characterisation

The four reservoir sandstone core samples, which were previously analysed for grain size in Chapter 5, were studied to determine the mineralogy of sandstone and how the mineralogy of a sandstone may vary throughout the cores. The mineralogy was studied at the core scale, thin section scale and using powdered X-ray diffraction (PXRD). Core scale analysis showed that, as expected, quartz occurred in abundance in all samples and plagioclase feldspar was also identified. Thin section analysis provided further insight into the mineralogy of the sandstone samples and showed that plagioclase feldspar also occurs in core samples 2 (1%) and 3 (1%) and dolomite occurs in all samples and sample 4 has the greatest dolomite content (10%), where it occurs as pore filling cement (Fig. 6.1), and sample 1 has the lowest dolomite content (3%), where it mostly occurs as isolated, sporadic rhombic crystals. Muscovite and biotite were also identified in sample 3 (Fig. 6.1).

PXRD was performed twice on the samples, first of all to determine the bulk mineralogy and secondly to determine the clay mineralogy of each sample (described in Chapter 3). The four bulk composition diffraction patterns are similar, and indicate quartz, dolomite and clay mineral content (Fig. 6.2). The diffraction pattern for sample 1 suggests a quartz rich composition, indicated by the large peak at  $26.6\ 2\theta$ , and lack of other diffraction patterns. Samples 2-4 show slightly more variation in composition, and indicate quartz and dolomite content. Quartz is identified in the samples by the large peak at  $26.6\ 2\theta$ , and dolomite is identified by the very small peaks at  $30.9\ 2\theta$ ,  $41.1\ 2\theta$  and  $50.9\ 2\theta$ . Sample 4 also suggests the occurrence of chlorite in addition to quartz and dolomite and chlorite has been recognised by the small peak at  $12.4\ 2\theta$  and  $25.2\ 2\theta$ .

To determine the clay mineralogy of the samples clay minerals were separated from the denser particles in the sample (e.g. quartz) and this process was described in Chapter 3. Clay minerals are typically harder to identify in bulk PXRD analysis as different clay minerals can accumulate as multiple layers (Hubert et al., 2009) which generate ambiguous diffraction patterns. Additionally, clay particles are very small ( $< 2\ \mu\text{m}$ ) and it is difficult to generate pronounced diffraction patterns

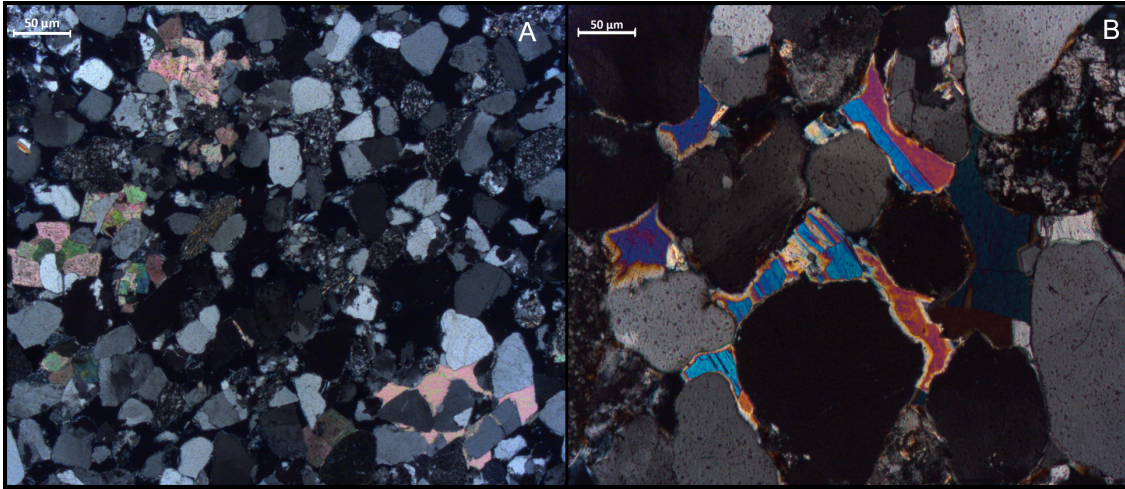


Figure 6.1: Thin section images under cross polarisation (XPL) showing the mineralogy in the sandstone samples; A: clusters of pore filling dolomite in sample 4 which are recognisable as the pale pink and green grains; B: Muscovite in sample 3 which recognisable as the brightly coloured and sometimes striped grains. The darker grey grains in both images are quartz.

so the clay minerals are separated to produce a well-oriented mount instead of natural, disoriented, random bulk sample (Sokolova et al., 2017). Once the layers are separated, from different sample preparation methods, accurate mineral identification can take place. All samples show the occurrence of illite/micas and kaolinite/chlorite and peaks at  $8.5$ ,  $18.5$  and  $26.5$   $2\theta$  are typical of illite and micas and peaks at  $12.1$  and  $25.1$   $2\theta$  are indicative kaolinite and chlorite (Fig. 6.3). Illite and micas show very similar diffraction patterns and were not able to be distinguished from this analysis alone. The occurrence of kaolinite/chlorite can be determined from further sample analysis where the sample was added to a HCl solution and heated which dissolves chlorite. Any peaks remaining during XRD analysis occur from kaolinite content. Samples 1, 3 and 4 show that kaolinite is present rather than chlorite (Fig. 6.4). Sample 2 shows that chlorite is present rather than kaolinite (Fig. 6.4).

### 6.2.2 Bead Pack Characterisation

Four additional bead pack samples were designed and created based on the mineralogy identified in the core characterisation (Figs. 3.3, 6.5). Sample 7 is a homogeneous bead pack composed of solely  $75\ \mu\text{m}$  glass acid-washed beads and the other three samples present mineralogy contrasts, where the top half of the sample is composed solely of  $75\ \mu\text{m}$  glass acid-washed beads and the bottom half also contains specified minerals (Fig. 6.5). Sample 8 contains 5% of crushed dolomite ( $63\ \mu\text{m}$ ), sample 9 contains 5% kaolinite and sample 10 contains both 5% of crushed dolomite and 5% of kaolinite. The glass beads are expected to mimic the behaviour of quartz as they are water-wet and will not undergo chemical alterations unlike dolomite and kaolinite. Furthermore, the bead pack samples in this chapter were not sintered to ensure the minerals did not undergo any physical or chemical alterations. Instead the sample is held firmly in place by extra fine steel wool at either end of the sample.

The bead pack samples discussed in this chapter were each split into five zones, where zone 1 occurs at the top of the scanned section of the sample and zone 5 occurs at the bottom and fluid flows from zone 1 to zone 5 in the  $z$  direction (Fig. 6.6). The mean pore diameter size was measured in the Avizo®Fire software and varies from  $0.026\ \text{mm}$  -  $0.081\ \text{mm}$  and sample 9 has the smallest mean

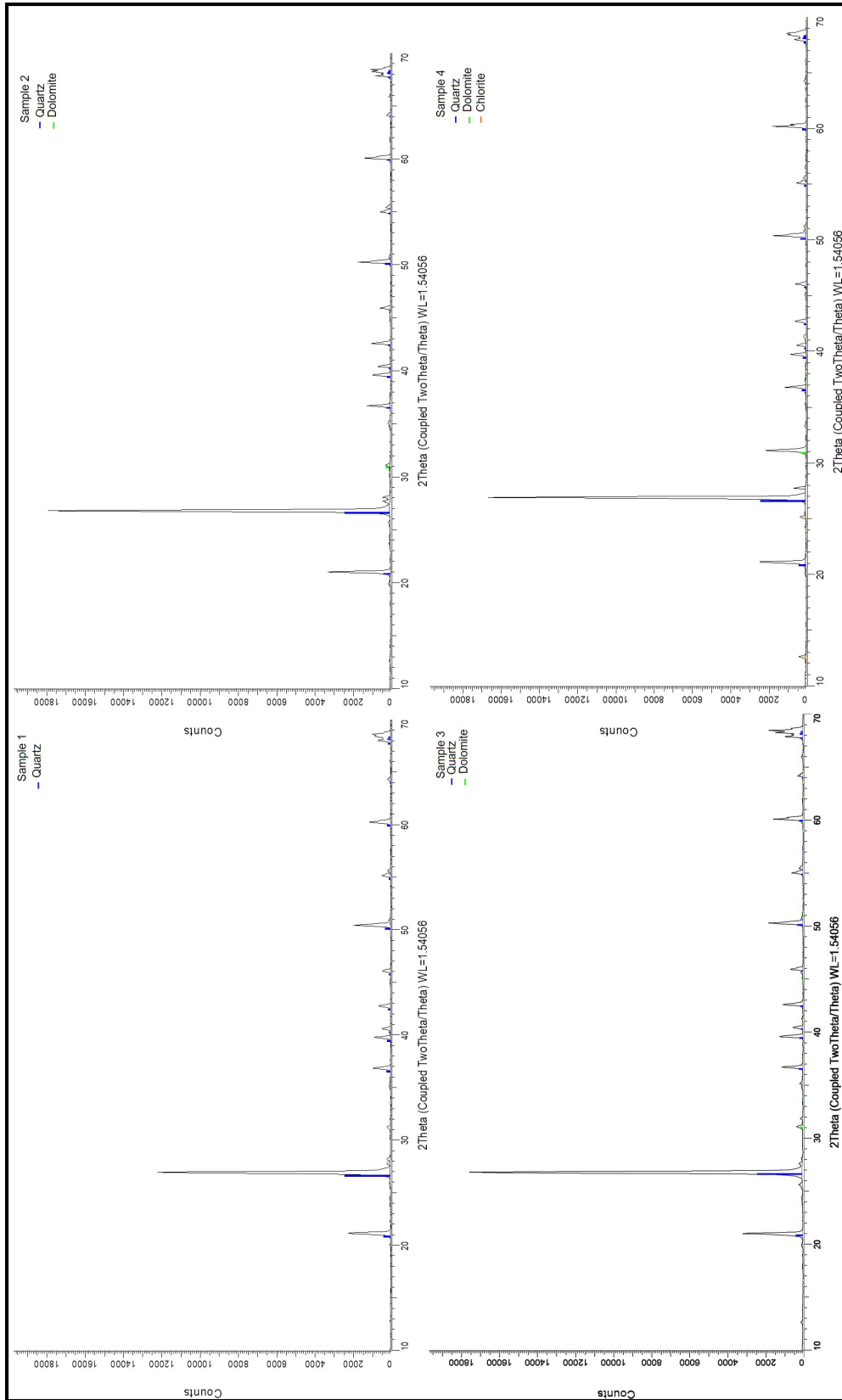


Figure 6.2: PXRd diffraction patterns indicative of quartz, dolomite and chlorite in the sandstone samples.

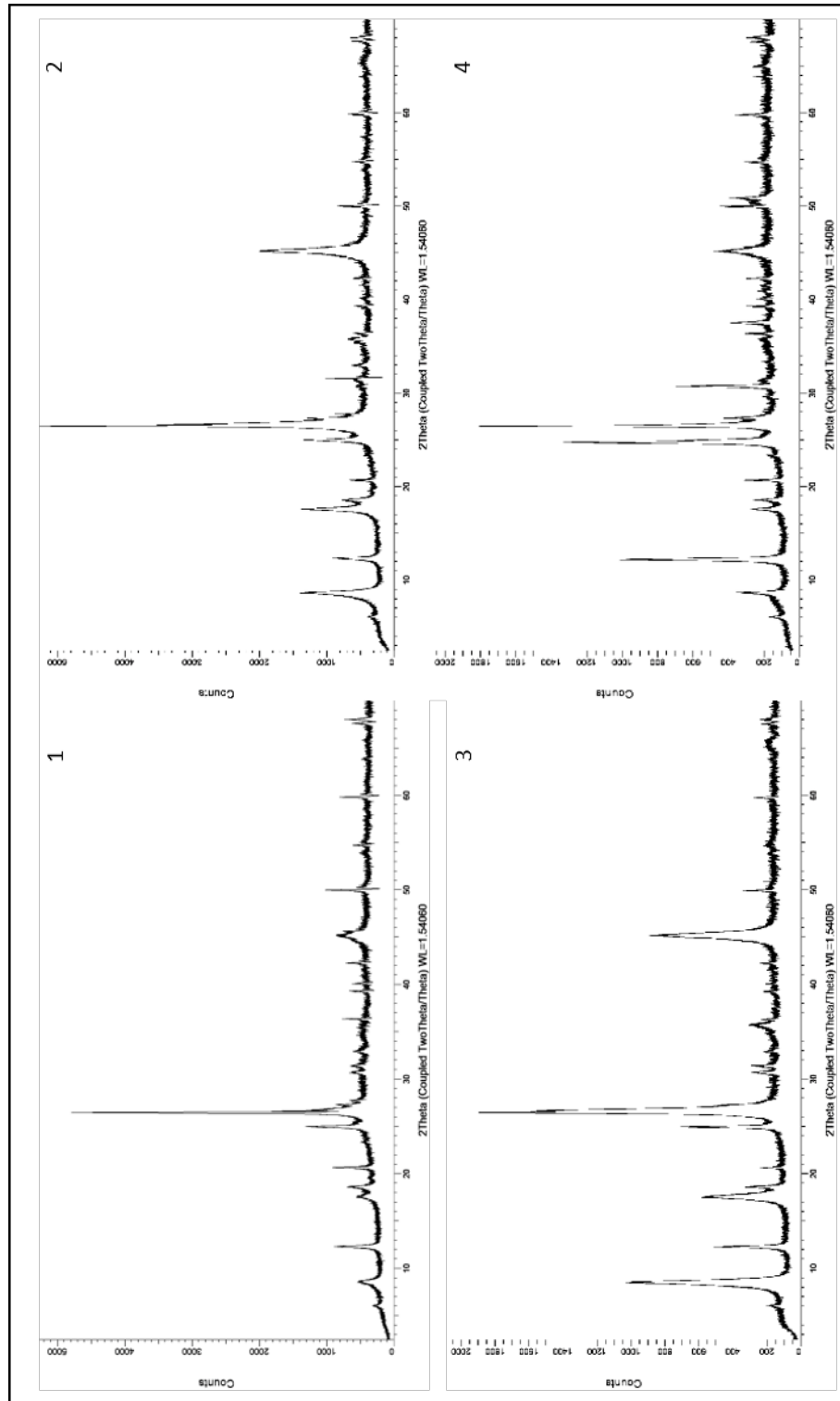


Figure 6.3: PXRD diffraction patterns from the clay minerals which occur in the four samples.

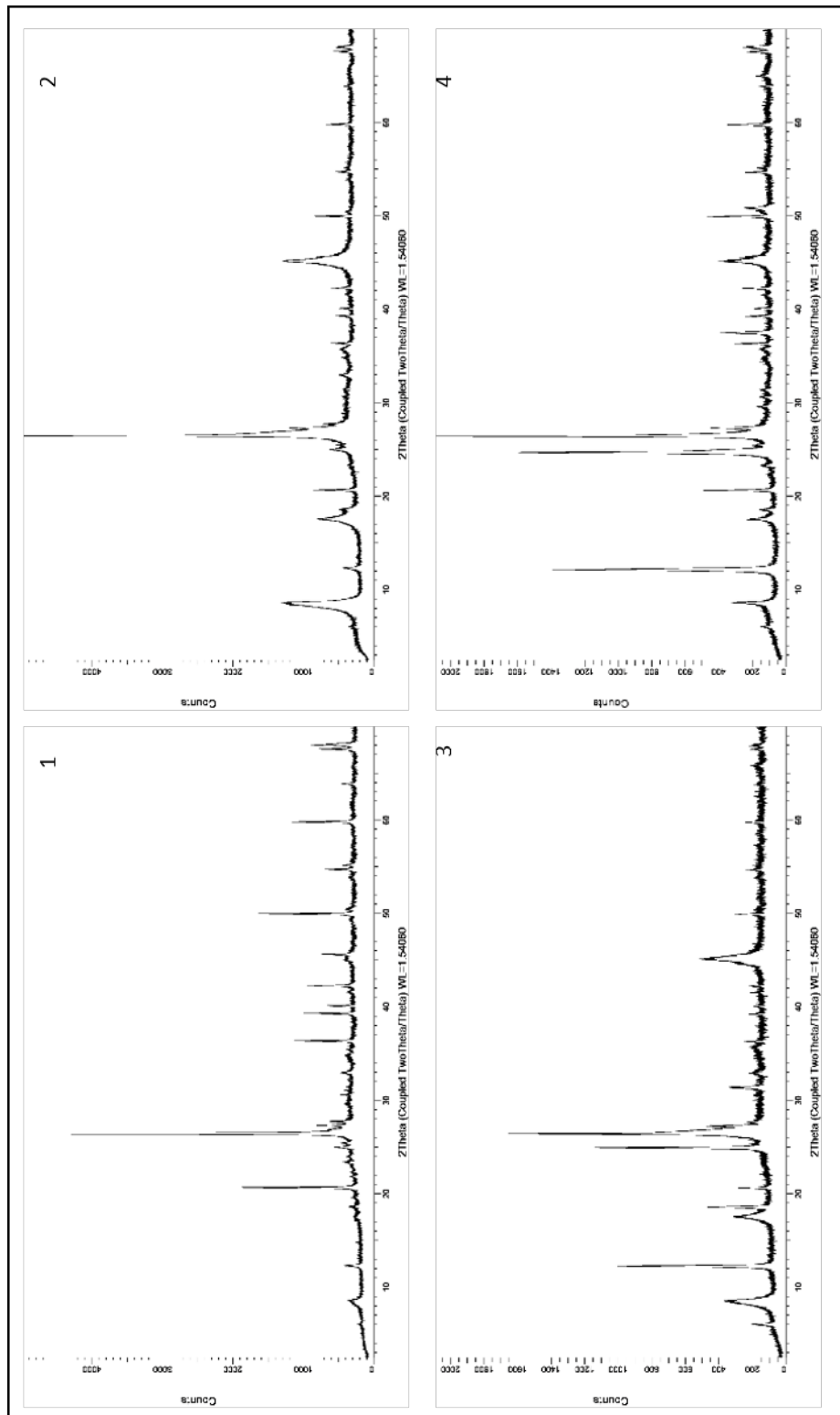


Figure 6.4: PXRD diffraction patterns from the samples after chlorite was removed.

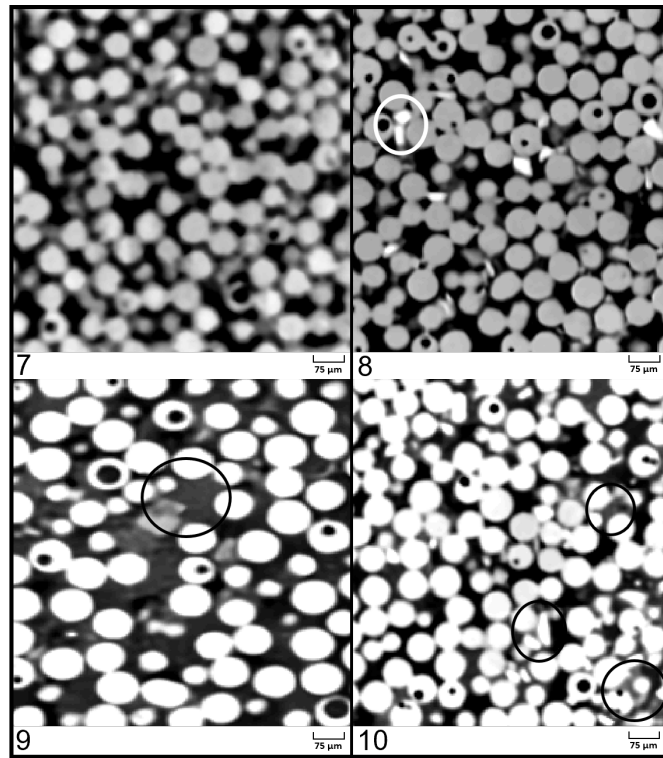


Figure 6.5: 2D images of the four bead pack samples discussed in this chapter showing the different mineralogical compositions. Sample 7 is composed of 75  $\mu\text{m}$  glass acid washed beads, sample 8 is composed of 75  $\mu\text{m}$  glass acid washed beads and 5% dolomite, sample 9 is composed of 75  $\mu\text{m}$  glass acid washed beads and 5% kaolinite and sample 10 is composed of 75  $\mu\text{m}$  glass acid washed beads, 5% dolomite and 5% kaolinite. Dolomite is identifiable as the white, angular or acicular grains and kaolinite is identifiable as the dark grey pore filling material. Note: the resolution differs across the samples due to the differing particle sizes (dolomite particle size: 63  $\mu\text{m}$ , kaolinite particle size: 0 - 63  $\mu\text{m}$ ). The colour of the glass beads also varies due to the varying contrast settings used for each sample and different contrast settings were used to more easily identify the minerals.

Table 6.1: The mean pore diameter and porosity of the bead pack samples.

| Sample | Mean Pore Diameter (mm) | Mean Porosity (%) |
|--------|-------------------------|-------------------|
| 7      | 0.081                   | 19.76             |
| 8      | 0.035                   | 15.98             |
| 9      | 0.026                   | 17.56             |
| 10     | 0.029                   | 16.47             |

pore diameter size and sample 7 has the largest mean pore diameter size (Table 6.1). The mean pore diameter size also varies throughout the zones within the different samples and sample 10 shows the greatest variation (0.03 mm) and sample 7 shows the smallest variation (0.01 mm) (Fig. 6.6). The porosity varies throughout the four samples and the average porosity is greatest in sample 7 and lowest in sample 10 (Table 6.1).

The range of pore diameter sizes in the samples varies and sample 7 shows the smallest range in mean pore diameter (0.13 mm) and sample 9 shows the greatest range in the mean pore diameter (0.72 mm) (Table 6.2).

### 6.2.3 Permeability

#### Experimental Permeability

The results from the pore-scale permeability experiments show that sample 7 has the highest permeability (4.08 D) and sample 9 has the lowest permeability (0.49 D) (Table 6.3). The results from the experiments also show that pressure difference increases linearly with increasing fluid flow rate across all samples and the increase in pressure difference is greatest in sample 9 and lowest in sample 7 (Fig. 6.7). The  $R^2$  value is above 0.9 for all samples and the  $R^2$  is 0.99 for sample 7, 0.98 for sample 8, 0.94 for sample 9 and 0.98 for sample 10. The error bars shown in Figure 6.7 were calculated from the standard deviation in the results for flow rate (horizontal error bars) and pressure difference (vertical error bars) after the system had stabilised for a minimum of 30 minutes. Results were recorded every 0.1 seconds.

The linear relationship between pressure difference and fluid flow rate in all samples is typical of Darcy flow (Fig. 6.7). As in previous chapters, the Reynolds number is

$$\text{Re} = \frac{\rho v L}{\mu}, \quad (6.1)$$

where  $\rho$  is the fluid density,  $\mu$  is the dynamics dynamic viscosity,  $v$  is the velocity ( $Q/A$ ), and  $L$  is the average pore diameter, with  $Q$  and  $A$  being the flow rate and cross-sectional area of the sample respectively. The Re for all samples ranges from  $4.34 \times 10^{-7}$  -  $4.05 \times 10^{-6}$  (Fig. 6.8).

The results also show that in sample 9 permeability decreases with increasing experiments (Fig. 6.8), which may suggest that the sample configuration is altered by the experiments. The decrease in permeability indicates that material is not leaving the sample as if kaolinite was being flushed out of the sample permeability would increase due to the increased pore space. Despite the sample being held in place by steel wool there may still be some movement between the glass beads and kaolinite in sample 9, and the sample may be reconfigured during episodes of purging and fluid flow. Additionally, the kaolinite particles may become transported with fluid flow until they are no

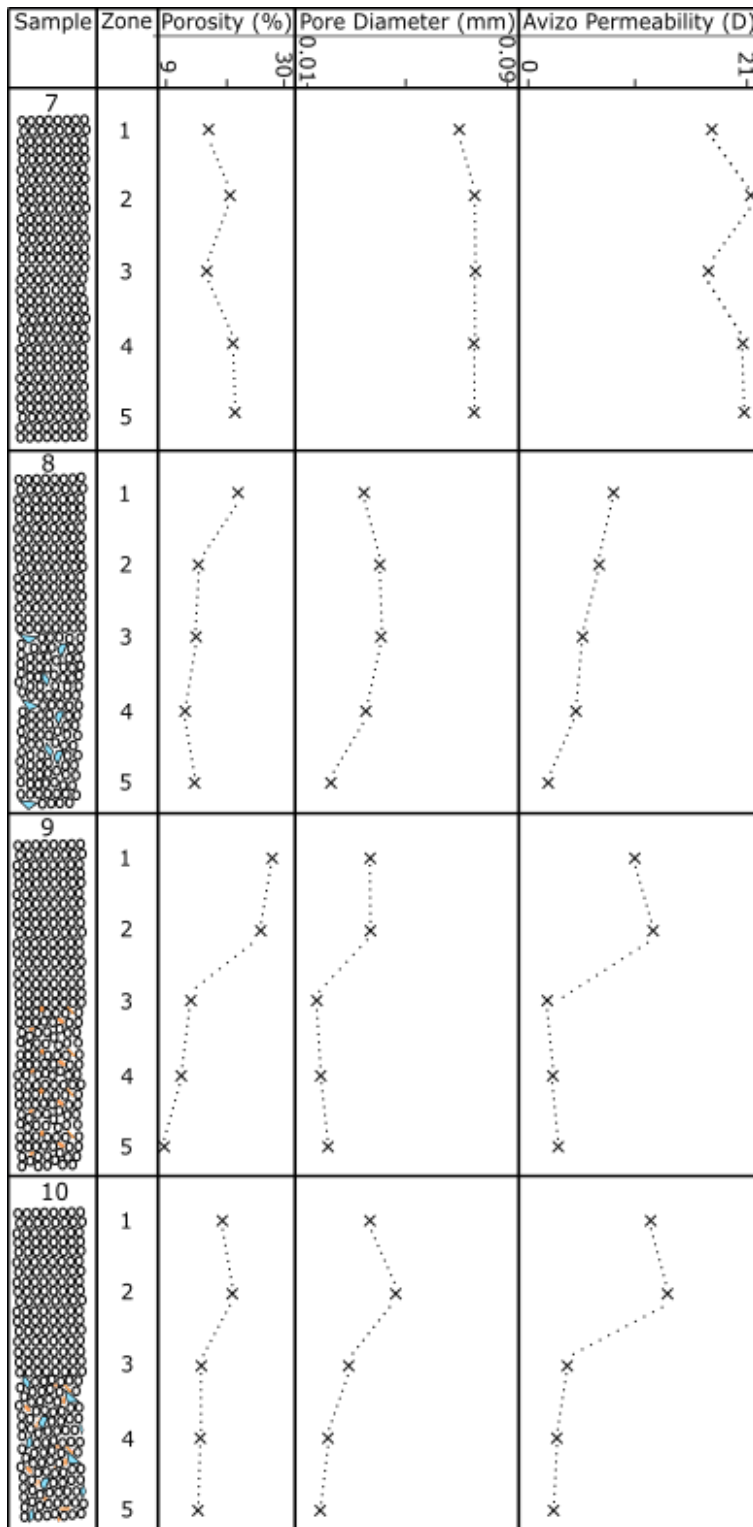


Figure 6.6: A log presenting the pore network properties of the bead pack samples discussed in this chapter and how they vary throughout the five zones of the samples. The properties were measured across a  $1 \times 1 \times 7$  mm scanned section of the samples. Fluid flows from zone 1 to zone 5.



Table 6.2: The range of mean pore diameter results across the five zones in the bead pack samples. There is not much variation between the minimum values and the lowest value measured for samples 7 and 8 is 0.004 963 07 mm and the lowest value measured for samples 9 and 10 is 0.004 962 86 mm.

| Sample | Zone | Range in Pore Diameter Size (mm) |
|--------|------|----------------------------------|
| 7      | 1    | 0.005 - 0.147                    |
|        | 2    | 0.005 - 0.140                    |
|        | 3    | 0.005 - 0.153                    |
|        | 4    | 0.005 - 0.152                    |
|        | 5    | 0.005 - 0.170                    |
| 8      | 1    | 0.005 - 0.439                    |
|        | 2    | 0.005 - 0.435                    |
|        | 3    | 0.005 - 0.439                    |
|        | 4    | 0.005 - 0.437                    |
|        | 5    | 0.005 - 0.472                    |
| 9      | 1    | 0.005 - 0.549                    |
|        | 2    | 0.005 - 0.561                    |
|        | 3    | 0.005 - 0.550                    |
|        | 4    | 0.005 - 0.408                    |
|        | 5    | 0.005 - 0.728                    |
| 10     | 1    | 0.005 - 0.430                    |
|        | 2    | 0.005 - 0.482                    |
|        | 3    | 0.005 - 0.426                    |
|        | 4    | 0.005 - 0.511                    |
|        | 5    | 0.005 - 0.370                    |

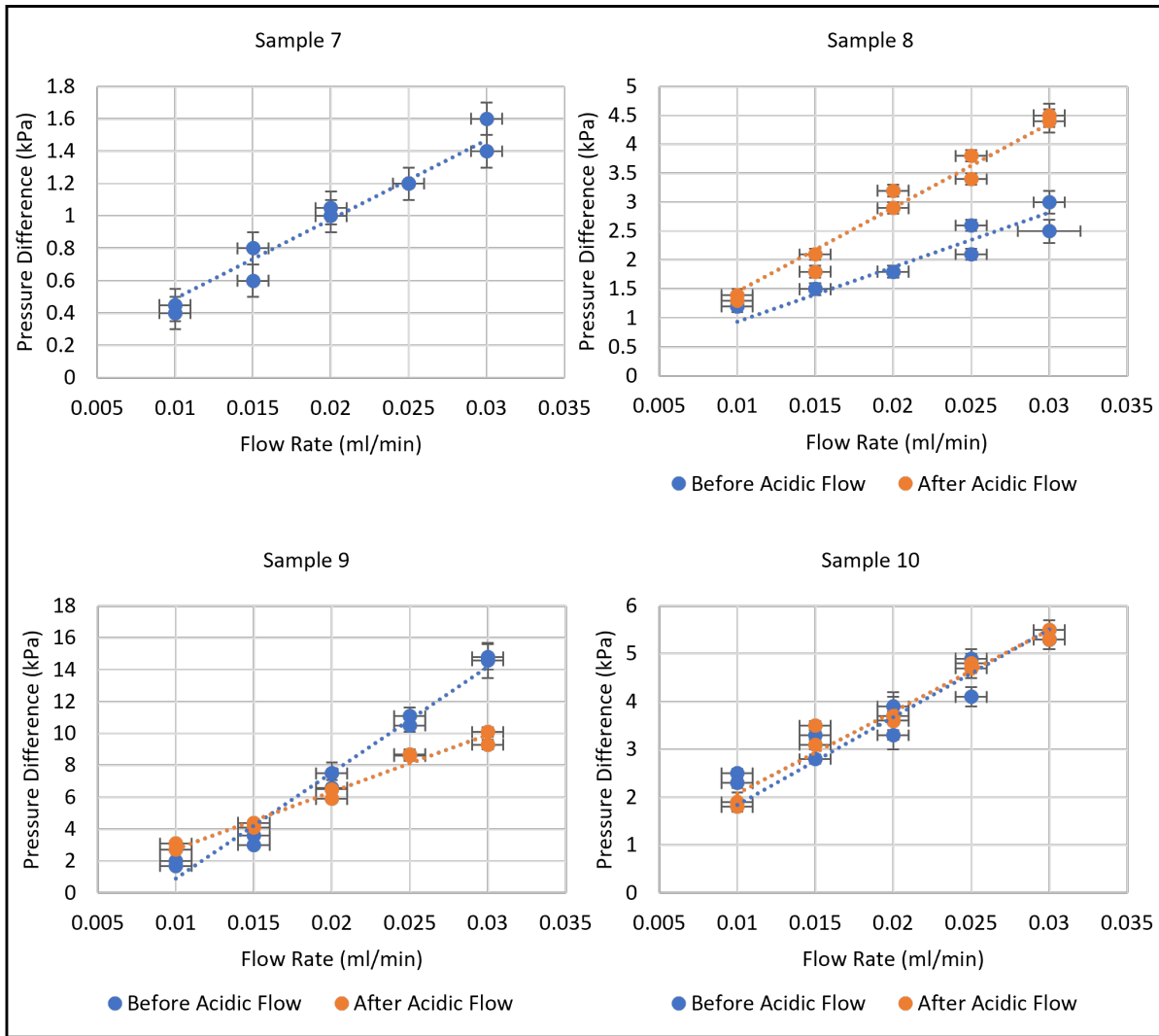


Figure 6.7: Plots of pressure difference against flow rate for the four samples before and after acidic flow.

longer able to be transported and become deposited in pores and pore throats (Sameni et al., 2015; Zhang et al., 2020a; Rosenbrand et al., 2012). The more experiments which are performed increases the amount of kaolinite which can be transported and deposited and may result in accumulations of kaolinite clogging regions of the sample and reducing permeability. The permeability does not decrease throughout the experiments in sample 10 which indicates that the kaolinite is perhaps more restricted and is not as easily transported throughout the sample.

Additional pore-scale permeability experiments were conducted on the samples which contain dolomite and kaolinite after acidic fluid (pH 3.1) was flushed through at 0.03 ml/min for 3 hours. The permeability of the samples was altered after the acidic flow and sample 8 shows that permeability has decreased by 0.73 D (34.43%), sample 9 shows that permeability has increased by 0.05 D (9.63%) and sample 10 shows that permeability has decreased by 0.01 D (1.48%). The relationship between pressure difference and flow rate was also altered after the acidic flow (Fig. 6.7) and for sample 10 the pressure difference increases between 0.1 - 1.9 kPa. In samples 9 and 10 the pressure difference results are more variable and for sample 9 the pressure difference mostly decreases between 1 -

Table 6.3: The results from the pore-scale permeability experiments for the bead pack samples.

| Sample | Permeability (D) |
|--------|------------------|
| 7      | 4.13             |
| 8      | 2.15             |
| 9      | 0.50             |
| 10     | 1.10             |

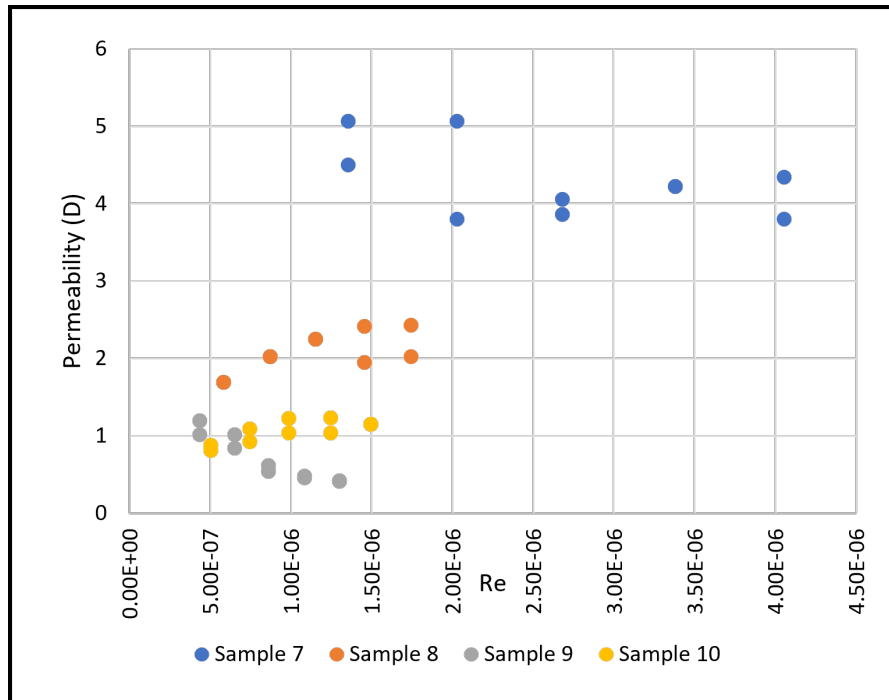


Figure 6.8: The Re results plotted against the experimental permeability results.

Table 6.4: The averaged permeability results from the Avizo Fire simulations.

| Sample | Permeability (D) |
|--------|------------------|
| 7      | 20.29            |
| 8      | 4.34             |
| 9      | 4.41             |
| 10     | 4.20             |

Table 6.5: The averaged permeability results compared to the permeability results from the transitional zone (zone 3).

| Sample | Averaged Permeability (D) | Zone 3 Permeability (D) |
|--------|---------------------------|-------------------------|
| 8      | 4.34                      | 5.63                    |
| 9      | 4.41                      | 2.24                    |
| 10     | 4.20                      | 3.84                    |

5.3 kPa and for sample 10 mostly decreases between 0.1 - 0.6 kPa. All samples still present a linear relationship between flow rate and pressure difference indicating Darcy flow. The  $R^2$  value is above 0.9 for all samples and is 0.99 for sample 8, 0.97 for sample 9 and 0.96 for sample 10.

### Simulated Permeability

Permeability simulations were performed in Avizo Fire across the five zones of each sample before acidic flow and the averaged permeability is greatest in sample 7 (20.29 D) and the lowest in sample 10 (4.20 D) (Table 6.4). The permeability simulations were used to compare permeability at different scales and to analyse how permeability may be impacted by a change in mineralogy at a greater resolution. The permeability in the samples varies across the different zones and sample 8 shows that permeability decreases by 6.92 D (77.36%) from zone 1 to zone 5. Sample 9 shows greater variation in permeability throughout the zones and from zone 2 to zone 3 permeability decreases by 9.81 D (81.40%) and overall the permeability decreases throughout the sample in the Z direction. Sample 10 shows more variation in permeability than sample 8 but less variation than sample 9 and permeability mostly decreases downstream and permeability decreases by 11.74 D (84.06%) from zone 2 to zone 5.

The averaged permeability from the permeability simulations was also compared to the permeability prediction for the transitional zone (zone 3) of the bead pack samples which contain dolomite and kaolinite. The transitional zone is the centre of the sample where the sample changes from solely 75  $\mu\text{m}$  glass beads to 75  $\mu\text{m}$  glass beads mixed with 5% dolomite (sample 8), 5% kaolinite (sample 9) and 5% dolomite and 5% kaolinite (sample 10). The averaged permeability in samples 8, 9 and 10 is compared to the permeability in zone 3 (Table 6.5) and there is a difference of 1.28 D (22.87%) between the results in sample 8, a difference of 2.17 D (49.24%) in sample 9 and a difference of 0.36 D (8.56%) in sample 10.

### 6.2.4 Fluid Chemistry Analysis

The drained fluid from the acidic flow for each sample (8-10) was collected and analysed using inductively coupled plasma - optical emission spectrometry (ICP-OES). Sample 8 shows that 0.103 mg (5.15%) of dolomite was dissolved from the sample, sample 9 shows that 0.008 mg (0.44%) of kaolin-

ite was dissolved and sample 10 shows that 0.113 mg (5.64%) of dolomite was dissolved and 0.04 mg (2.36%) of kaolinite was dissolved.

The reaction rate for the samples can be calculated, where

$$R = \frac{Q\Delta C}{S_A} \quad (6.2)$$

where  $Q$  = flow rate of acid (L/s),  $\Delta C$  = change in concentration (mol/L) and  $S_A$  is the surface area of the mineral ( $\text{cm}^2$ )

however, the drained fluid from the experiments was sampled at the end of the reactive flow instead of at regular sampling intervals and this may have resulted in a diluted sample and also it would be unknown as to whether the reaction rate had reached a steady state. Due to this the reaction rate was not calculated.

## 6.3 Discussion

### 6.3.1 How does heterogeneous mineralogy impact the pore network geometry?

As discussed in the results section the pore network geometry varies between each sample and this is demonstrated by the different mean pore diameter size and porosity values. The results show that the occurrence of minerals in the bead pack samples reduces the mean pore diameter and increases the range in mean pore diameter. This is especially evident as sample 7 has the largest mean pore diameter (0.081 mm) and smallest range in pore diameter size (0.13 mm) and the samples which contain dolomite and/or kaolinite have significantly smaller mean pore diameter size (up to 0.046mm (56%) smaller) and significantly larger ranges in pore diameter size (up to 0.59 mm (81.9%)). Out of the three samples which contain minerals sample 9 shows the smallest mean pore diameter and the largest range in mean pore diameter sizes (Table 6.1 and 6.2) and this may be due to the difference in particle size in this sample which ranges from 15 - 75  $\mu\text{m}$ . Based on the results presented in the previous chapter and in the literature review it is expected that pore diameter is roughly equal to grain diameter and therefore pore diameter will decrease with decreasing particle size (Revil et al., 2012; Chung and Lin, 2017). This is often related to grains which are spherical however the results from this study suggest that it may also be applicable to non-spherical particles and this is supported by other studies which observe that pore size increases with decreasing kaolinite surface area (Zhang et al., 2018a). Moreover, increasing kaolinite content can result in the reduction in the volume of larger pores (5-50 nm) and an increase in the volume of micropores (Qi et al., 2019). Additionally, clay minerals are associated with wider pore size distributions (Scott et al., 2019) and this may be enhanced due to the large size difference between the glass beads and kaolinite and kaolinite is able to infill the pore space between the beads more easily, as demonstrated in Figure 6.5, which will further reduce the size of the mean pore diameter and this is commonly associated with clay minerals (Wang et al., 2020c; Zahid et al., 2019; Qiao et al., 2020; Schmitt et al., 2015a; Wilson et al., 2014). The shape of the different particles (e.g. glass beads, kaolinite) in the bead pack samples is also expected to influence the size and range of pore diameter (Sperry and Peirce, 1995; Xu et al., 2020). Kaolinite platelets have large aspect ratios (ratio of diameter of the planar platelet to the laminar thickness) which results in high variation in particle dimensions (Vora and Dugan, 2019; Cheng et al., 2014) and increasing width is expected to have a greater influence on the pore size, where increasing width corresponds to a reduction in pore size (Björk et al., 2013). Furthermore, due to the design of the sample the kaolinite in the sample is not uniformly distributed and is

mostly concentrated in the lower half of the sample which will increase variation in the range of pore diameter size throughout the sample and this is demonstrated in Figure 6.6 where the mean pore diameter decreases downstream as the kaolinite content increases downstream. This results in a greater contrast between particle size upstream and downstream and as demonstrated in the previous chapter (Chapter 5) the transition between larger particles to smaller particles increases the range in pore diameter size which increases heterogeneity in the pore network. Sample 10 also contains kaolinite and also shows a much lower mean pore diameter size and higher range of pore diameter sizes than the samples which do not contain kaolinite (samples 7 and 8), however, the mean pore diameter size in sample 10 is 10% greater than the mean pore diameter size in sample 9. This is due to the dolomite content in the sample and the dolomite grains are observed as angular (Fig. 6.5) and occur between the glass beads which restricts high concentrations of kaolinite from infilling pore space and therefore preserves some of the open pore space.

The occurrence of minerals within the bead pack samples also reduces porosity and sample 8 presents the lowest average porosity value (15.98%). This is due to the size of the dolomite crystals in sample 8, which are much larger than the grains of kaolinite (+ 48  $\mu\text{m}$  or 76.19%) and occupy larger pores which largely reduces intergranular porosity, demonstrated in Figures 6.5 and 6.1. The grains of dolomite in the bead pack sample are angular which allows the grains to fit alongside beads as well as in open pore space (Fig. 6.5) which enhances porosity reduction. The form in which kaolinite occurs also largely influences porosity and in the bead pack samples the kaolinite is pore filling which reduces porosity and pore filling kaolinite is associated with micropores (< 10  $\mu\text{m}$  which are not as favourable for porosity as intergranular macropores (> 10  $\mu\text{m}$  (Lai et al., 2015; Zhou et al., 2019) and pore filling clays are often regarded as the key contributing factor to porosity reduction in sandstones (Scott et al., 2019; Lai et al., 2015). Sample 9 which contains kaolinite has the largest range in porosity out of all the samples (19.22%) and alike the large range in pore diameter size this could be due to the large range in kaolinite particle size. A greater range in particle size will enhance the distribution of kaolinite throughout the second half of the sample as the smaller particles of kaolinite will be able to infill smaller pores as well as larger pores in the sample. The impact of kaolinite will be greater in smaller pores than in larger pores which results in the wide range of porosity. Additionally, the occurrence of kaolinite can increase interparticle and interlayer porosity at the nanoscale (Asaad et al., 2021; Zhou et al., 2019; Cao et al., 2016) which will also contribute towards the large range in porosity. The wide range in porosity is also likely to be influenced by the design of the sample as the upper half of the sample has a more uniform composition and therefore the pore space is also expected to be more uniform which contrasts with the lower half of the sample where kaolinite predominantly occurs. The porosity contrast could have also been enhanced when the sample was made, as the addition of extra beads in zones 1 - 3 may have encouraged the kaolinite to migrate into lower zones and accumulate at the bottom of the sample. Although this is possible, the porosity contrast is very sharp at zone 3 and after zone 3 the porosity results are relatively stable and only vary by 3% so it is expected that the kaolinite is well distributed throughout zones 3 - 5 and does not solely accumulate in the bottom of the sample. This is also observed in samples 8 and 10 which demonstrate a significant porosity reduction in zone 3 which then stabilises throughout zones 4 and 5.

### 6.3.2 How does heterogeneous mineralogy impact mineral dissolution at the pore scale?

It is evident that the differing mineralogy across the samples influences the amount of mineral dissolution which occurs within the samples. Dissolution is greatest in sample 10 which is the only sample which contains two minerals, dolomite and kaolinite, and the amount of dolomite dissolved

increases by 0.5% and the amount of kaolinite dissolved increases by 1.9%. This could be due to the pore network geometry and sample 10 has a lower mean pore diameter size than sample 8 and shows the greatest range in pore diameter size out of all of the samples, which is due to the pore occupying dolomite grains and pore filling kaolinite. Greater variation in pore diameter size leads to a less uniform pore network which will result in a higher frequency of flow pathways (David, 1993) and greater tortuosity in fluid flow (Salem, 1993; Datta et al., 2013; Cai et al., 2019) as the fluid flow will bypass smaller pores in favour of larger pores (Li et al., 2018) which was demonstrated in the previous chapter (Chapter 5). Larger pores are capable of facilitating higher velocity flow (Salem, 1993; Nemati et al., 2020) which may lead to heterogeneous mineral dissolution focused along preferential flow paths in the pore network and higher flow rate is associated with a more uniform reactions and lower flow rate is associated with less uniform reactions (Sabo and Beckingham, 2021). Additionally, tortuosity is largely influenced by the shape of grains/particles in the pore network and tortuosity is expected to increase with increasing height-to-width ratio (Ghassemi and Pak, 2011). The dolomite grains in samples 8 and 10 (Fig. 6.5) are angular and have a greater height-to-width ratio than the glass beads or kaolinite accumulations so it is expected that tortuosity is greater in samples 8 and 10 than in samples 7 and 9. An increase in tortuosity results in a longer fluid flow pathway (Habisreuther et al., 2009) and a longer fluid flow pathway is likely to have access to more reactive minerals which therefore increases the rate of reaction and dissolution of reactive minerals in samples which have higher tortuosity (samples 8 and 10) (Zhang et al., 2020b; Ma et al., 2019; Jung and Navarre-Sitchler, 2018).

### 6.3.3 How does heterogeneous mineralogy impact permeability and transport phenomena?

The permeability results show that heterogeneous mineralogy impacts permeability and permeability is reduced when dolomite and kaolinite occur (Fig. 6.6, Table 6.3 and 6.4) which is due to the reduced pore space in the samples which contain minerals as the additional minerals occupy the pore space between the glass beads, which reduces the mean pore diameter size and increases the range of mean pore diameter size, resulting in a more heterogeneous pore network. The permeability results from the experiments indicate that permeability is lowest in sample 9, which contains kaolinite, whereas the simulated permeability results show that permeability is the lowest in sample 10, which contains both kaolinite and dolomite. The simulated average permeability results show very little difference between the samples which contain minerals (0.07 - 0.21 D or 1.5 - 4.7%) yet the experimental results show that the samples vary quite significantly (1.03 - 1.38 D or 49.7 - 66.6%). Some variation is expected between the two different methodologies used to assess permeability and the difference may be due to the sampled area as the experiments produce results for the entire sample ( $1 \times 1 \times 12$  mm) whereas the simulations produce results from the central section of the sample ( $1 \times 1 \times 7$  mm). In addition to this, the results from the simulations show that permeability consistently decreases from zone 1 to zone 5 and permeability may continue to decrease throughout the sample which would reduce the averaged permeability. Overall, both sets of permeability results show that the occurrence of kaolinite is detrimental to permeability which is agreeable throughout the literature and clay minerals are typically associated with reduced permeability and porosity as they infill pores, clog pore throats and increase pore throat heterogeneity (Wang et al., 2020c; Qiao et al., 2020; Schmitt et al., 2015a; Wilson et al., 2014; Li et al., 2020; Fox et al., 2018).

When the simulated permeability throughout the sample zones is analysed sample 8 (containing dolomite) shows the smallest range in permeability throughout the sample and permeability decreases steadily (Fig. 6.6) whereas the sample which contains kaolinite shows a larger range in permeability (+ 4 to 6%). This indicates that although the addition of dolomite to the bead pack sample reduces

permeability it reduces permeability in a more predictable way and increased dolomite content results in a steady decrease in permeability 2 - 3D from zone 1 to zone 5. On the other hand, the permeability reduction as a result of kaolinite content is more unpredictable and the permeability initially decreases by 9.8D and then slightly increases by 0.3 - 0.4D. This is likely due to the greater range of mean pore diameter size and porosity in the sample which creates a more heterogeneous pore network. In the literature clay minerals are associated with a large variation in permeability and this is interpreted to be a result of clay mineral dimensions and the large aspect ratio of clay minerals (Vora and Dugan, 2019). Additionally, kaolinite is able to accumulate in pore throats which reduces the connectivity of the pore network (Wang et al., 2020c; Wilson et al., 2014) and therefore reduces permeability (Zhou et al., 2016). When dolomite and kaolinite occur together the permeability results show characteristics of the sample which solely contains dolomite and the sample which solely contains kaolinite. Permeability steadily decreases throughout the sample, similarly to the sample which only contains dolomite, and the sample also displays a large range of permeability, similarly to the sample which only contains kaolinite. The occurrence of both minerals in the same sample has a lesser effect on permeability than when the minerals occur independently and this could be due to the average particle size in the sample. The sample which contains glass beads (75  $\mu\text{m}$ ), dolomite (63  $\mu\text{m}$ ) and kaolinite (15  $\mu\text{m}$ ) will have a larger average particle size than the sample which only contains kaolinite and a smaller average particle size than the sample which only contains dolomite and therefore it is expected that the sample will have an average pore size which is larger than the average pore size in the sample which contains kaolinite and smaller than the average pore size in the sample which contains dolomite (Revil et al., 2012). In the literature and in the previous chapter it was noted that permeability increases with increasing bead size (Yoneda et al., 2019; Oliveira and Nicolodi, 2017; Ghassemi and Pak, 2011) and this is because larger bead size corresponds to higher porosity and a larger mean pore diameter size which encourages high velocity preferential fluid pathways. Furthermore, the permeability may be less impacted in the sample which contains both kaolinite and dolomite than in the sample which solely contains kaolinite as the distribution of kaolinite may be restricted by the occurrence of dolomite. As mentioned previously dolomite occupies the larger pores and wedges alongside beads which limits the amount of pore space where kaolinite can accumulate which may result in a more uniform distribution of kaolinite and therefore a more uniform distribution of pore sizes.

The permeability of the samples containing dolomite and dolomite and kaolinite was reduced after acidic flow and the sample containing dolomite only showed the greatest reduction in permeability (32.54%). The permeability was reduced despite the ICP-OES results showing that dissolution had occurred (2.36-5.64%). The permeability reduction is greatest in the sample which has the largest reactive mineral surface (63  $\mu\text{m}$ ) and the largest average particle size (sample 8) and it is interpreted that during the dissolution process smaller fragments (< 63  $\mu\text{m}$ ) of the dolomite crystals became detached and transported with the acidic flow (Ma et al., 2019; Liu et al., 2020b; Israeli and Emmanuel, 2018; Singurindy and Berkowitz, 2003; Wang et al., 2021). Some of the smaller fragments of dolomite may then be transported out of the sample, however, other fragments may become trapped in pores and pore throats and clog fluid pathways and reduce the permeability of the sample (Ma et al., 2019; Liu et al., 2020a). The impact of this process may have been enhanced by the average particle size as samples with larger particle size are associated with increased permeability and high velocity preferential pathways and it would be more detrimental to permeability and fluid flow in the pore network if a high velocity preferential pathway became blocked. The permeability may have also been reduced by increased surface roughness on the grains of dolomite during the acidic flow (Shiraki and Dunn, 2000). The permeability in the sample which contains both dolomite and kaolinite was less affected by this as it is expected that dolomite and kaolinite in the sample



were exposed to acidic flow for longer because the pore network in this sample is more restricted by the smaller pore diameter size (Table 6.1) and larger range in pore diameter size increases tortuosity in the flow which enables the fluid to access more reactive minerals in the pore network (Nemati et al., 2020; Salem, 1993; Habisreuther et al., 2009; Zhang et al., 2020b). As a result of this any fragments which detached from the dolomite grains are expected to be smaller and more able to be transported out of the sample and less likely to clog pores and pore throats. Additionally, a more restrictive pore network would limit how far particles could be transported and therefore reduces the amount of fragments which block pores/pore throats and in the literature it is widely accepted that the solutes released by dissolution need to be removed from the area of dissolution and that requires favourable fluid flow conduits (Yuan et al., 2019). The decrease in permeability may have also been reduced due to the dissolution of kaolinite and the sample which only contains kaolinite shows that permeability increases (9.6%) as a result of kaolinite dissolution. Additionally, the permeability before acidic flow in the sample which solely contains kaolinite decreased throughout the experiments and this is interpreted to have occurred due to migrating particles of kaolinite blocking pores and pore throats (Sameni et al., 2015; Zhang et al., 2020a; Rosenbrand et al., 2012). Particle migration is not uncommon in sandstone reservoirs (Zhang et al., 2020a; Rosenbrand et al., 2012) and may result in localised regions of high reaction rates when accumulations of reactive minerals occur. Accumulations of kaolinite particles blocking pores and pore throats may result in concentrated regions of kaolinite accumulations which will further reduce permeability and consequently increase tortuosity which as mentioned previously, can promote access to more reactive minerals (Mangane et al., 2013; Nemati et al., 2020; Salem, 1993; Habisreuther et al., 2009; Zhang et al., 2020b). Moreover, the size of pores prior to mineral dissolution may impact the effect of mineral dissolution on permeability and dissolution which occurs in smaller pores may contribute more to permeability than mineral dissolution in larger pores (Sabo and Beckingham, 2021). The samples which contain kaolinite have a smaller mean pore diameter than the samples which do not contain kaolinite which suggests that dissolution in the samples which contain kaolinite will contribute more to permeability than dissolution in the samples which do not contain kaolinite.

In contrast to the results from this study carbonate cement dissolution in sandstone reservoirs is associated with increased reservoir quality (porosity and permeability) (Cui et al., 2018; Claes et al., 2018). However, many studies only record an increase of porosity after dissolution (Cui et al., 2018; Wei et al., 2015; Yang et al., 2017). There are studies in the literature which present large, abnormal porosity and permeability contrasts in deeply buried sandstones (> 2000 - 4000 m depending on the study) however this may be a consequence of grain coating clays preventing cementation, lack of quartz cement, grain composition, early emplacement (shallow depths) of hydrocarbons or development of fluid overpressure at shallow depths rather than a direct consequence of mineral dissolution (Ehrenberg, 1993; Warren and Pulham, 2002; Freiburg et al., 2016; Li et al., 2020). Furthermore, the impact of increased porosity as a consequence of dissolution (commonly referred to as secondary porosity) on reservoir quality isn't well established and it is not definite that secondary porosity directly results in a net increase of porosity and permeability (Bloch, 1994; Li et al., 2020; Giles and de Boer, 1990) and permeability evolution as a result of mineral dissolution is more complex and more difficult to predict than porosity evolution (Sabo and Beckingham, 2021). Moreover, some studies also indicate that secondary porosity is a re-distributional process where the porosity increase from mineral dissolution is offset by mineral precipitation, which can occur as a by-product of mineral dissolution (Bloch, 1994), and some studies suggest that by-products cannot be fully exported which limits the effect of mineral dissolution (Li et al., 2020). Permeability increases after acidic flow and mineral dissolution have been recorded and Ma et al. (2020) report that permeability significantly increases as a result of dolomite cement dissolution, however, the experiments were

conducted over 455 hours, in contrast to the 3 hour acidic flow in this study, and under reservoir conditions. This suggests that the acidic flow experiments conducted in this study may have been successful at achieving mineral dissolution but unsuccessful in the aim to recreate realistic mineral dissolution. The difference in permeability and dissolved volume of dolomite may be due to the type of sample used and the composition of the sample and [Ma et al. \(2020\)](#) use a sandstone sample which exhibits dolomite cement, rather than grains of dolomite. Alternatively, [Ma et al. \(2019\)](#) also use a sandstone sample which exhibits dolomite cement and perform flow through reactive experiments at reservoir conditions and observe an increase in porosity and a decrease in permeability. The two sandstone samples used in [Ma et al. \(2020\)](#) and [Ma et al. \(2019\)](#) present different porosities and the sandstone sample used in [Ma et al. \(2020\)](#) has a porosity of 8.76% whereas the sandstone sample in ([Ma et al., 2019](#)) has a porosity of 21.9%, which suggests that the original porosity of the sandstone samples influences the effect of dolomite dissolution. The samples used in this study also have greater porosity (+ 7.22 - 8.80%) than the sample used in [Ma et al. \(2020\)](#) which indicates that samples which have relatively high original porosity to begin with may be less impacted by dolomite dissolution. This is also supported by the experimental results from [Bertier et al. \(2006\)](#) which show greater dissolution of carbonates (dolomite, ankerite) in sandstone cores with lower porosity (13.1%) than in sandstone cores with greater porosity (17.0%). The size of pores may also influence how permeability is impacted by mineral dissolution and [Sabo and Beckingham \(2021\)](#) suggest that dissolution in larger pores contributes less to permeability than dissolution in smaller pores. This is also reflected by the results in this study where permeability increases after mineral dissolution in the sample which has the lowest mean pore diameter and permeability decreases after mineral dissolution in the sample which has the largest mean pore diameter. Permeability is also observed to reduce after CO<sub>2</sub> injection and dolomite dissolution in sandstone samples by [Wang et al. \(2019b\)](#), [Sayegh et al. \(1990\)](#), [Shiraki and Dunn \(2000\)](#) and [Mohamed et al. \(2012\)](#). The effect of acidic flow and mineral dissolution on permeability may also be influenced by the form in which the reactive minerals occur in. In this study dolomite occurs as unattached grains, however, this is rarely observed in sandstone reservoir rocks. Loose, unattached dolomite grains enable circumgranular dissolution which may increase the possibility of clogging during transport. It is unlikely that this type of dissolution would occur in sandstone reservoir rocks so it is also less likely that clogging would occur.

## 6.4 Conclusions

The addition of kaolinite and dolomite into the bead pack samples reduces the mean pore diameter size and increases the range of mean pore diameter sizes. Kaolinite content reduces the mean pore diameter size more than dolomite content and increases the range of mean pore diameter sizes more than dolomite content. This is due to the size and distribution of kaolinite and kaolinite is more randomly distributed throughout the sample as it is much finer than the dolomite grains.

When both kaolinite and dolomite occur within a sample the effect of kaolinite on the pore diameter size and range is reduced as dolomite grains occupy larger pores which restricts large accumulations of kaolinite in the pores and encourages a more uniform distribution of kaolinite throughout the sample.

The addition of kaolinite and dolomite also reduces the porosity of the bead pack samples and porosity is reduced the most when only dolomite occurs and this is due to the size and shape of the dolomite grains. The dolomite grains are large (63-75  $\mu\text{m}$ ) and occupy most of the pore space between the grains and are angular so they are able to fit alongside the glass beads too which

further enhances porosity reduction. Kaolinite content in the sample increases the range in porosity throughout the sample and this is due to the different types of porosity kaolinite can provide at different scales, such as interparticle and interlayer porosity.

The amount of dissolution is the greatest in the sample which contains both kaolinite and dolomite as this sample has the greatest variation in pore diameter sizes which results in a more tortuous pore network. Increased tortuosity results in longer fluid flow pathways so more reactive minerals are exposed to the acidic flow.

The permeability is lower in the samples which contain minerals and the results suggest that permeability is lowest in the samples which contain kaolinite and this is due to the reduced pore space and greater range in pore diameter size which creates a more heterogeneous pore network.

When kaolinite and dolomite occur in the same sample the effect of each mineral on permeability is reduced and this is due the influence of particle size and distribution on permeability. The distribution of kaolinite is restricted by the occurrence of dolomite and limits the amount of pores kaolinite infills which increases uniformity in the pore network and increases the size of accumulations of kaolinite which increases particle size overall. Permeability increases with increasing particle size and the average particle size in this sample is greater than the sample which solely contains kaolinite but lower than the sample which contains solely dolomite. As a result of this the permeability for the sample which contains both kaolinite and dolomite is greater than in the sample which contains kaolinite but lesser than the sample which contains dolomite.

Permeability was reduced in all samples after acidic flow despite evidence of mineral dissolution. The permeability was reduced the most in the sample which contains dolomite and this was interpreted due to small detached mineral fragments blocking pores and pore throats. The other samples were less affected and this was due to greater reaction rates and more restrictive pore networks which limited the size of particles which may become blocked and the distance which they could be transported.

## Chapter 7

# How does heterogeneity in grain size and mineralogy impact pore network reactive transport properties?

### 7.1 Introduction

As outlined in the previous chapters variable particle size and mineralogy are strong influences on how fluid flow behaves in the pore network and heterogeneity in particle size results in a change in pore network geometry which alters the permeability and alters how the fluid navigates through the pore network (e.g. preferential fluid pathways or uniformly). Additionally, different mineralogy also influences the pore network geometry which in turn determines the permeability, reaction rates and dissolution in the pore network. It is not well studied how the combination of heterogeneous mineralogy and heterogeneous particle size influences the pore network and it has been observed in this study that different variations of minerals and particle sizes independently produce different pore network geometries and fluid flow behaviour. Variable mineralogy, grain shape and grain size is expected to change the packing density, the degree of sorting and the availability of the pore space (Adepehin et al., 2019) but it is not yet understood how this will impact the pore network geometry and reactive fluid flow behaviour. Due to this, this chapter focuses on how fluid flow behaviour is impacted by heterogeneity in particle size and mineralogy before and after acidic flow. The sample analysed in this chapter is more complex than the previous samples and the top half of the sample is composed of 75  $\mu\text{m}$  glass beads and the bottom half of the sample is composed of randomly mixed 75-180  $\mu\text{m}$  glass beads, 2 mg (5% of sample weight) dolomite and 2 mg (5% of sample weight) kaolinite. The permeability of the sample will be assessed from the pore-scale permeability experiments, before and after acidic flow, and in the Avizo®Fire software. The pore network geometry of the sample will also be analysed in the Avizo®Fire software and the rate of reaction and amount of dissolution from the acidic flow will be calculated from ICP-OES analysis of the drained acidic fluid.

### 7.2 Results

The results in this chapter include core characterisation, bead pack characterisation, permeability from the pore-scale permeability experiments before and after acidic flow, Avizo®Fire absolute permeability simulations and the amount of mineral dissolution from the acidic flow.

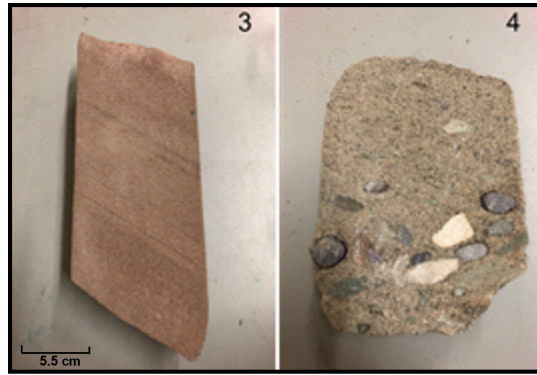


Figure 7.1: Core sample 3 (left) shows high angle cross laminations of silt which present both a change in mineralogy and a change in grain size. Core sample 4 (right) shows significant grain size heterogeneity and shows the addition of detrital clasts which may have contrasting mineralogy and or provenance.

### 7.2.1 Core Characterisation

The four reservoir sandstone core samples previously analysed in Chapters 5 and 6 were also studied to identify areas which showed strong heterogeneity. At the core scale significant heterogeneity in grain size was identified in cores 3 and 4 (Fig. 7.1) which show the occurrence of silt high angle cross laminations which present a grain size contrast (250-400  $\mu\text{m}$ ) and mineralogy contrast (sudden increase in clay mineral content) and the addition of large detrital clasts which also show a grain size contrast (3.6-38.5 mm) and may also present a different mineralogy as a result of different provenance, however, the mineralogy of the detrital clasts was not studied. At the thin section scale heterogeneity in the core samples was also observed (Fig. 7.2) and grain size heterogeneity was observed in samples 1, 3 and 4. In core samples 1 and 3 bands of finer grains and material infill the pore space between larger grains and in core sample 4 much larger clast occupy large portions of the sample. Heterogeneous mineralogy was also observed in core sample 3 and dolomite grains and cement occur sporadically and muscovite occurs within and local to the bands of finer material.

### 7.2.2 Bead Pack Characterisation

Two bead pack samples were designed and created to incorporate grain size and mineralogical heterogeneity (Fig. 7.3 and 7.4). Sample 11, similar to the bead pack samples in the previous chapters, is composed of 75  $\mu\text{m}$  glass beads in the top half of the sample and 75-180  $\mu\text{m}$  glass beads, 5% dolomite (2 mg) and 5% kaolinite (2 mg) in the second half of the sample. The second sample in this chapter, sample 12, is composed of rock powder from core sample 3, which showed significant heterogeneity at the core and thin section scale, and the top half of the sample is composed of rock powder which is 0-75  $\mu\text{m}$ , and the bottom half of the sample is composed of rock powder which is 75-180  $\mu\text{m}$ . In sample 11 five consecutive zones (zones 1 - 5; zone 1 occurs at the top and zone 5 occurs at the bottom) (Fig. 7.3) were analysed and in sample 12 three consecutive zones (zone 1: 0-75  $\mu\text{m}$  grains, zone 2: transition zone between zone 1 and 3 0-180  $\mu\text{m}$  grains and zone 3: 75-180  $\mu\text{m}$  grains) (Fig. 7.4), were analysed in the Avizo®Fire software.

The analysis shows that the mean pore diameter ranges from 0.009-0.083 mm and overall the mean pore diameter is larger in sample 11 (Table 7.1). In sample 11 the mean pore diameter ranges from 0.0104-0.0831 mm and generally decreases from zone 1 to zone 5 (Fig. 7.5). In sample 12 the

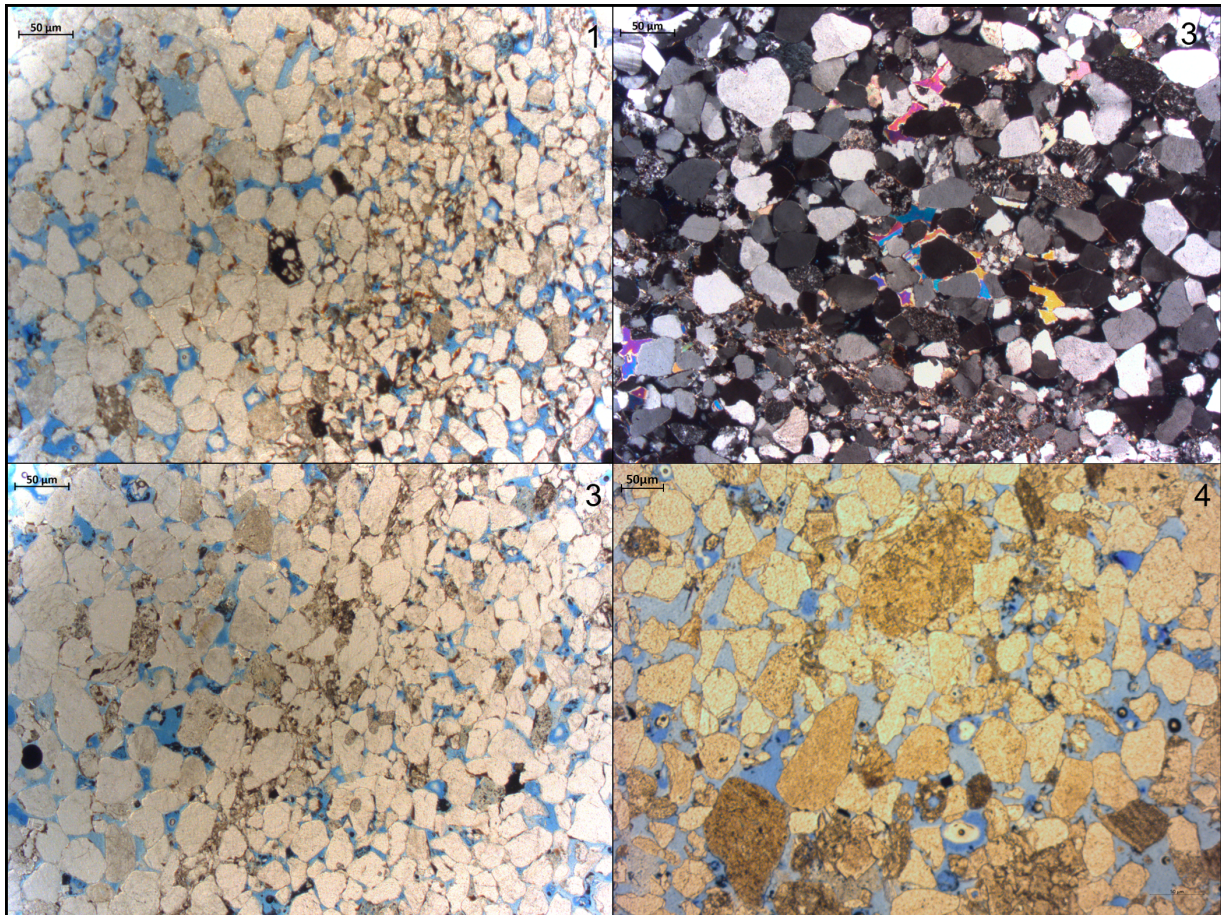


Figure 7.2: The thin section images of core samples 1, 3 and 4; core sample 1 shows grain size heterogeneity and shows a band of finer material; core sample 3 displays heterogeneity in mineralogy (XPL) and grain size (PPL) and shows sporadic dolomite grains/cement and muscovite mica occurring in clusters local to the band of finer material which infills the pore space between larger grains; core sample 4 shows grain size heterogeneity and various areas of pore space which are cemented.

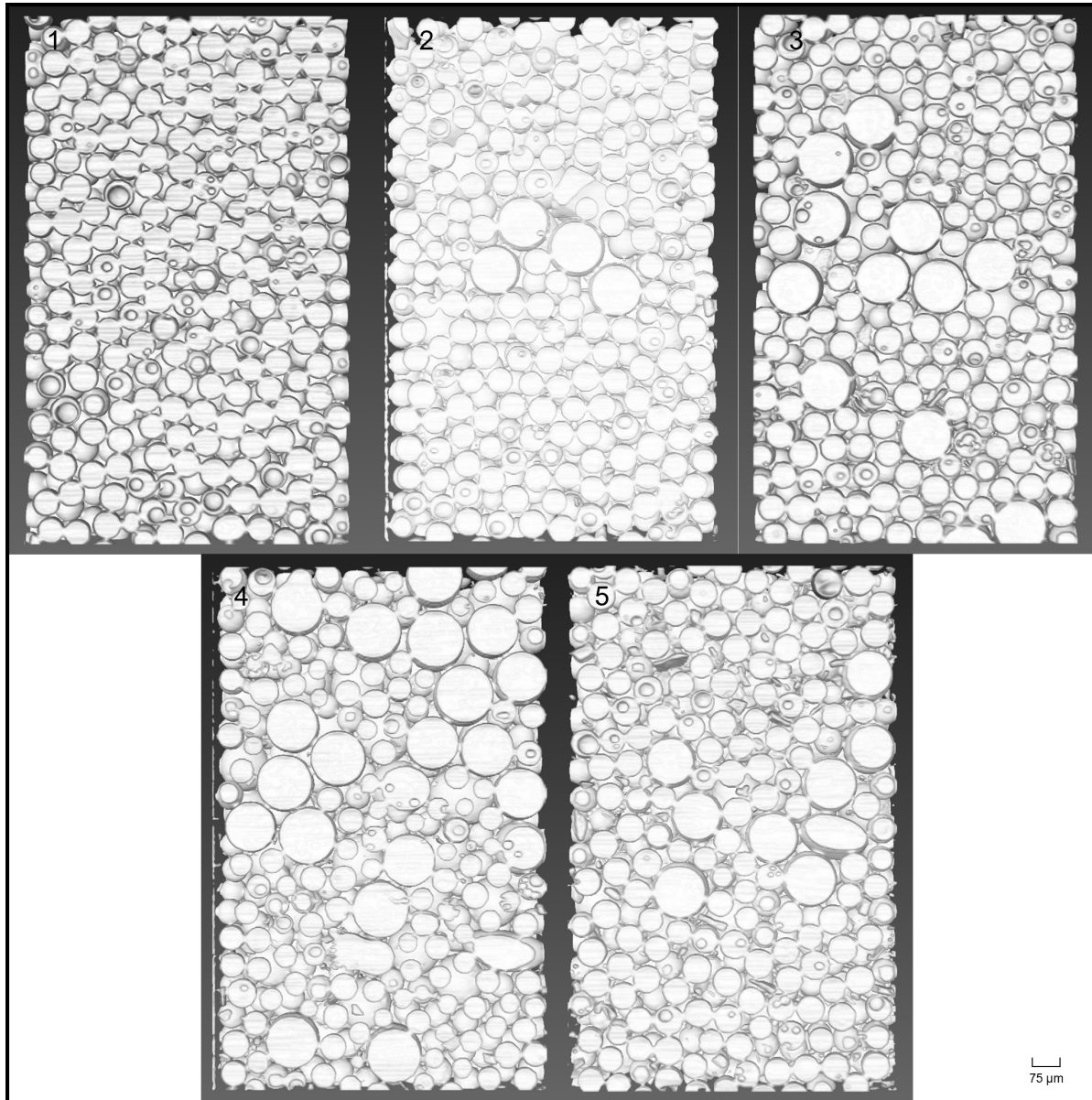


Figure 7.3: The five zones of sample 11 showing the transition from homogeneous bead size ( $75\ \mu\text{m}$ ) (zones 1-2) to mixed bead size ( $75\text{-}180\ \mu\text{m}$ ), 2 mg of dolomite and 2 mg of kaolinite (zones 3-5). Zone 3 is the transitional zone between the homogeneous bead size and heterogeneous bead size with the addition of dolomite and kaolinite.



Figure 7.4: The three zones analysed in sample 12; zone 1 is composed of 75-180  $\mu\text{m}$  grains, zone 2 is composed of 0-180  $\mu\text{m}$  grains and zone 3 is composed of 0-75  $\mu\text{m}$  grains.

mean pore diameter shows a smaller range across the different zones and only differs by 0.0005 mm (5.80%). The range of mean pore diameter in the different zones of the samples also varies and sample 12, zone 3 shows the greatest range and sample 11, zone 1 shows the smallest range (Table 7.1). The porosity also differs between the samples and overall sample 11 has higher porosity than sample 12 (Table 7.1). Overall the porosity decreases from zone 1 to zone 5 in sample 11 and sample 12 shows a significant reduction in porosity in zone 3.

### 7.2.3 Permeability

#### Experimental Permeability

The pore-scale permeability experiments were performed on sample 11 before and after acidic flow. The permeability before acidic flow was 0.47 D and was reduced to 0.11 D after acidic flow which is a reduction of 0.36 D (76.6%). The results show that pressure difference increases with increasing flow rate both before and after acidic flow which suggests Darcian flow (Fig. 7.6). The error bars shown in Figure 7.6 were calculated from the standard deviation in the results for flow rate (horizontal error bars) and pressure difference (vertical error bars) after the system had stabilised for a minimum of 30 minutes. Results were recorded every 0.1 seconds.

The pore-scale permeability experiments were not conducted on sample 10 as pressure in the system exceeded the pressure limit ( $> 3$  bar) before the pressure stabilised.

#### Simulated Permeability

The Absolute Permeability Experimental Simulations were conducted in Avizo<sup>®</sup>Fire on both samples and show that overall permeability is greater in sample 11 than in sample 12 (Table 7.2). The averaged permeability for sample 11 is 4.72 D and the average permeability for sample 12 is 1.42 D. Overall, the permeability decreases through sample 11 from zone 1 to zone 5 (Fig. 7.5) and both samples show that permeability is lowest in the transitional zone.



Table 7.1: The mean pore diameter and porosity results from the samples. The minimum pore diameter for both samples was 0.00496307 mm. The same value for the minimum pore diameter was also observed in the bead pack samples from the previous chapter (Chapter 6) which contained kaolinite. This suggests one of two things; 1) the mineralogical composition determines the minimum pore size in the sample, or, 2) the Avizo Fire software has a limited resolution where pores below 0.00496307 mm are not detectable. The limited resolution could be due to how the image stack was processed and the bead pack samples which contained minerals proved more difficult to convert into binary images due to the different shades of colour each image contained which was due to the different minerals. For example, the glass beads and dolomite are white and the kaolinite is dark grey which makes it difficult to distinguish the kaolinite from the pore space.

| Sample | Zone | Mean Pore Diameter (mm) | Range in Pore Diameter (mm) | Porosity (%) |
|--------|------|-------------------------|-----------------------------|--------------|
| 11     | 1    | 0.082                   | 0.005 - 0.182               | 37.18        |
|        | 2    | 0.083                   | 0.005 - 0.207               | 37.25        |
|        | 3    | 0.009                   | 0.005 - 0.646               | 8.49         |
|        | 4    | 0.013                   | 0.005 - 0.580               | 9.96         |
|        | 5    | 0.010                   | 0.005 - 0.602               | 7.64         |
| 12     | 1    | 0.0097                  | 0.005 - 0.557               | 11.04        |
|        | 2    | 0.0093                  | 0.005 - 0.717               | 12.43        |
|        | 3    | 0.0099                  | 0.005 - 0.556               | 8.43         |

Table 7.2: The simulated permeability results from the samples.

| Sample | Zone | Permeability (D) |
|--------|------|------------------|
| 11     | 1    | 15.40            |
|        | 2    | 7.97             |
|        | 3    | 0.89             |
|        | 4    | 1.73             |
|        | 5    | 1.32             |
| 12     | 1    | 1.54             |
|        | 2    | 1.00             |
|        | 3    | 1.32             |

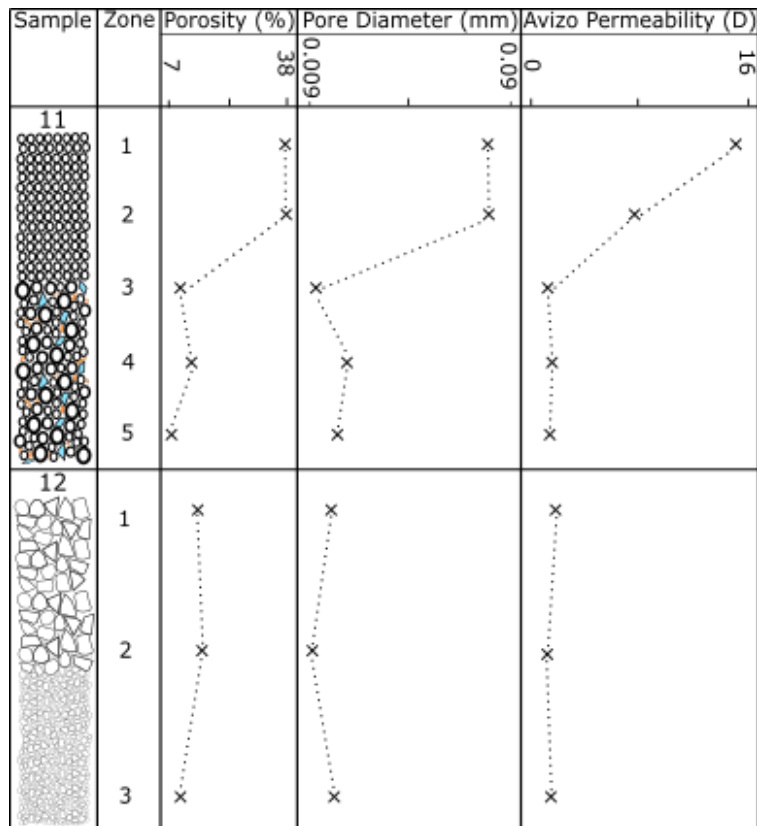


Figure 7.5: A log presenting the pore network properties of the bead pack samples discussed in this chapter and how they vary throughout the different zones of the samples. The properties were measured across a  $1 \times 1 \times 7$  mm scanned section of the samples. Fluid flows in the  $z$  direction from zones 1 to zone 5 in sample 11 and from zone 1 to zone 3 in sample 12.

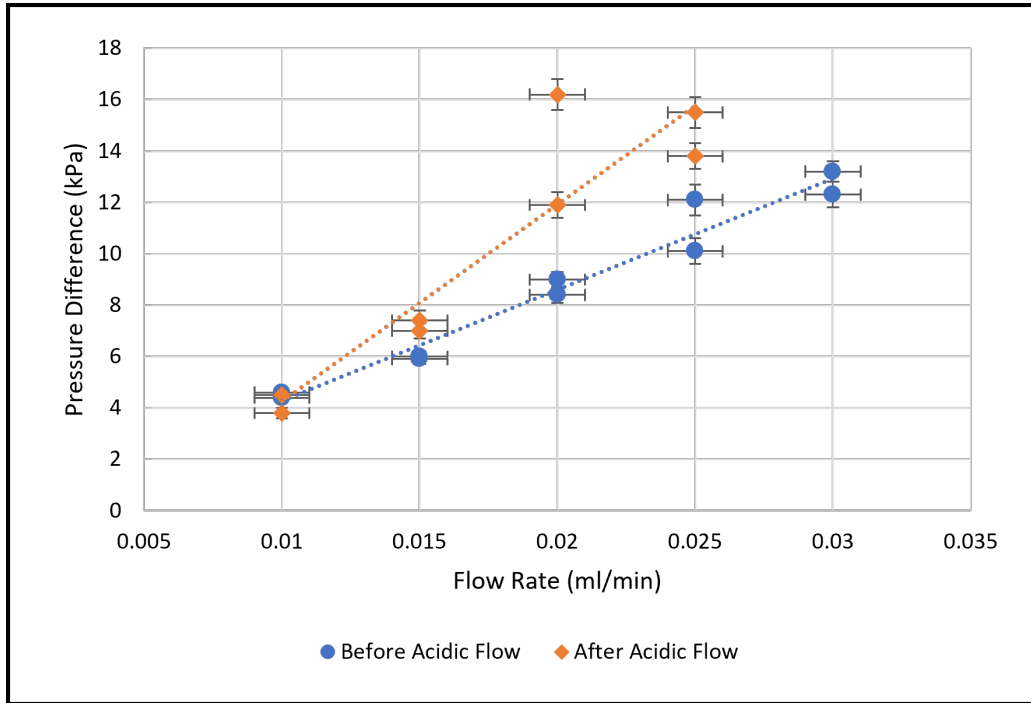


Figure 7.6: The results from the pore-scale permeability experiments before and after acidic flow.

## 7.2.4 Fluid Chemistry Analysis

Acid was flushed through sample 11 and a replica of sample 11 to demonstrate reliability of the results and the drained fluid from the acidic flow was collected and analysed using inductively coupled plasma - optical emission spectrometry (ICP-OES). In sample 11, 0.142 mg (7.10%) of dolomite was dissolved from the sample and in the replica sample 0.151 mg (7.55%) of dolomite was dissolved. Further analysis showed that 0.047 mg (2.36%) of kaolinite was dissolved in sample 11 and in the replica sample.

## 7.3 Discussion

### 7.3.1 How does heterogeneous grain size and mineralogy influence pore network geometry?

The results show that mean pore diameter and porosity are smaller in the natural rock sample (sample 12) in comparison to the bead pack sample (sample 11), however, the results are more comparable in the lower half of the bead pack sample, where the mean pore diameter size differs by 4.9 - 10.4%, the range in mean pore diameter size differs by 4.1 - 9.9% and the porosity differs by 0.8 - 4.8%. This indicates that the lower half of the bead pack sample is a better analogue for a natural sample. In comparison to the results from the previous chapter (Chapter 6) sample 11 shows that increasing heterogeneity (heterogeneous bead size, addition of dolomite and kaolinite) results in reduced pore diameter size (31.6 - 65.4%) and porosity (3.7 - 5.7%) and increases the range in mean pore diameter size (20.3 - 26.0%) and this is likely to be due to the heterogeneous bead size as the smaller beads are able to infill the pore space between the larger beads, as demonstrated in Chapter 5, in Figure 5.8 and in the literature (Quasim et al., 2021), as well as kaolinite and dolomite. Kaolinite is much smaller than the glass beads (ranging from 0 - 63  $\mu\text{m}$ ) and can easily

fit alongside the beads and accumulate in pores and clay minerals can often be observed to narrow or fill pores in sandstones which reduces pore connectivity (Zhao et al., 2017) and increases small pore volume ( $< 0.01 \mu\text{m}$ ) (Jiao et al., 2021; Lei et al., 2020). Dolomite is also slightly smaller than the glass beads (ranging from 63 - 75  $\mu\text{m}$ ) and is observed to occur as angular grains which are able to occupy the pore space as they have a large height-width ratio which enables the narrower part of the grain to fit alongside beads and enables a higher frequency of dolomite grains, or kaolinite, to occupy the pore space. In addition to infilling the pore space this will also result in a more irregular pore space which results in the wider range in pore diameter sizes and angular grains are often associated with a wider range of pore size distribution (Chaudhary et al., 2013a). This is enhanced in the transitional zone of both samples and both samples show that mean pore diameter is lowest in the transitional zone. The reduction in mean pore diameter size and porosity throughout the bead pack sample may have also been influenced by how the sample was created as the bottom half of the sample may have become more densely packed as the top half of the sample was added gradually creating an overburden stress on the sample. As a result of this it is expected that the packing density increases from zone 1 to zone 5. This process is also observed in natural rock samples when sediments become compacted during burial and lithification and this also results in reduced pore space. However, the packing density is limited in the bottom half of the sample as angular grains are more resistant to packing than spherical grains (Lehocki and Avseth, 2021) and this may further account for the greater variation in pore diameter sizes in the lower half of the sample as the packing will be heterogeneous and this is due to the smaller particles in the sample (e.g. kaolinite) as smaller grains tend to resist compaction more than larger grains (e.g. glass beads) (Lehocki and Avseth, 2021) as they occupy less of the pore space.

The agreement in the results from the bead pack sample and the sample which contains crushed rock signifies that the bead pack sample is a good analogue for a natural sample and is able to emulate realistic conditions found in rock samples which is significant for the applicability of results in this study and an important finding for future work.

### 7.3.2 How does heterogeneous mineralogy and grain size control mineral dissolution at the pore scale?

The amount of dissolution of dolomite in the sample discussed in this chapter suggest that dissolution is increased when particle size is heterogeneous and the amount of dolomite dissolution increases by 1.5 - 2.4% in comparison to the bead pack with homogeneous bead size which contains dolomite and kaolinite discussed in the previous chapter (Chapter 6). The amount of dissolution may increase due to the heterogeneous distribution of pores in the pore network and from the bead pack characterisation it is evident that the combination of heterogeneous mineralogy and bead size in the sample results in a greater range of pore diameter sizes. A heterogeneous distribution of pores in the pore network increases the tortuosity of fluid flow as it increases resistance to fluid flow and fluid will by-pass smaller pores in favour for larger pores (Nemati et al., 2020; Salem, 1993) and increasing tortuosity increases the length of the fluid pathway (Habisreuther et al., 2009). Fluid pathways with greater lengths will have greater access to reactive minerals in the pore network which may progress reactions (Zhang et al., 2020b; Ma et al., 2019). Fluid pathways within the pore network will differ and this may affect the contact time between acidic fluid and reactive mineral and therefore influence the reaction rate (Zhang et al., 2020b; Ma et al., 2019). Due to this, it is expected that increased heterogeneity in pore network geometry leads to increased tortuosity and longer fluid pathways which progress geochemical reactions and increase mineral dissolution.

### 7.3.3 How does heterogeneous mineralogy and grain size affect permeability and fluid flow behaviour?

The experimental permeability shows that the combination of minerals and mixed bead size further reduces permeability when compared to the results from the previous chapter (Chapter 6). The results show that the addition of dolomite and kaolinite to a bead pack with homogeneous bead size reduces permeability by 3.2D (75.7%) and also suggest that when mixed bead size is combined with dolomite and kaolinite permeability further decreases by 0.5D (54.8%). The experimental permeability discussed in this chapter was also compared to the experimental permeability of the two samples which present bead size contrasts in Chapter 5 and this shows that permeability decreases by 3.9-4.9D (89.4-91.4%) when dolomite and kaolinite occur alongside heterogeneous bead size. Heterogeneous grain size distribution in sandstone reservoirs is predicted to be less favourable for fluid flow as it is related to variable production rates (Ogbe, 2021) and sandstones with poorly sorted grain size with clay content are commonly associated with poor reservoir quality (low porosity and permeability) (He et al., 2019; Al-hasani et al., 2018). The comparisons between the bead pack samples which were discussed in the previous two chapters (Chapters 5 and 6) indicate that the addition of dolomite and kaolinite have a stronger influence over permeability than heterogeneous bead size. Adding dolomite and kaolinite into the bead pack sample introduces particles with different shapes and also increases the heterogeneity in particle size and the size of particles in the sample varies from 0-180  $\mu\text{m}$  whereas in the previous samples the particle size has only varied by 0-75  $\mu\text{m}$  or 75-180  $\mu\text{m}$ . Furthermore, the impact of kaolinite on pores may also be heterogeneous and Matmon and Hayden (2003) record that kaolinite has a greater impact in larger pores than in smaller pores. The reduction in permeability is a result of the reduced pore space and the increased range in pore diameter which results in increased heterogeneity in the pore network geometry. Increased heterogeneity in the pore network geometry results in a heterogeneous distribution of permeability and the pores with a larger diameter are able to contribute more to permeability (Meng et al., 2021; Apostolopoulou et al., 2019) whereas the pores with smaller diameter contribute less to permeability, and higher amounts of pores with smaller diameters result in lower permeability overall due to the connectivity of smaller pores as the connectivity of smaller pores is expected to be less than the connectivity of larger pores (Apostolopoulou et al., 2019). Heterogeneous connectivity in the pore network will also reduce permeability (Sato et al., 2019) and the connectivity of pores is also reduced by the kaolinite content which narrows and fills pores and this can increase tortuosity in the pore network (Zhao et al., 2017; Carcione et al., 2019), and clay minerals are typically associated with blocking pores and pore throats which reduces permeability (Zhao et al., 2017; Neasham, 1977; Qiao et al., 2020; Schmitt et al., 2015b; Wilson et al., 2014; Li et al., 2020; Fox et al., 2018). Additionally, the occurrence of smaller pores in the pore network can also influence permeability and zones which are dominated by smaller pores may create zones of reduced permeability or baffles for fluid flow (Apostolopoulou et al., 2019). Permeability decreases in the lower half of the sample and the lower half of the sample may act as a baffle for fluid flow and reduce the permeability of the sample overall, as observed in Chapter 6, where the addition of dolomite and kaolinite to the samples reduced permeability up to 87.9% in the experimental results and 79.3% in the simulation results. In the crushed rock sample permeability shows less variation and the decrease in permeability throughout the sample is less significant when compared to the permeability in the bead pack sample (Fig. 7.5). This may suggest that the effect of heterogeneity in sedimentary properties in natural rock samples is less severe on permeability. Alternatively, this may also be due to the low overall permeability of the sample to begin with and permeability may not vary as much since permeability is more restricted by the properties of the sample, such as poor sorting due to mixed grain size and shape, which reduce the pore space and therefore reduce permeability (Meng et al., 2021; Apostolopoulou

et al., 2019). In comparison, in the bead pack sample the change in properties is much more severe and the sample changes from well sorted homogeneous bead size to poorly sorted beads with pore-filling kaolinite and dolomite which significantly reduces the permeability. When the permeability of the bead pack sample and the crushed rock sample are compared to permeabilities of samples of well studied homogeneous, sandstones (e.g. Bentheimer, Berea sandstones) the permeability of the bead pack and crushed rock sample have lower permeability or sit within the lower permeability range, which indicates that the samples created in this study have been successful in achieving the goal of increasing the complexity and heterogeneity of a simple bead pack and homogeneous sandstone sample. The Bentheimer sandstone is regarded as a well sorted sandstone with a constant mineralogy (Peksa et al., 2015) and the permeability of a sample of the Bentheimer sandstone ranges from 0.52-3.54 D (Peksa et al., 2015; Lin et al., 2019; Muljadi et al., 2016; Jacquy et al., 2015). The Berea sandstone is also described as a well sorted sandstone and a homogeneous, well connected porous medium (Sato et al., 2019; Peng et al., 2014) and permeability varies much more than the Bentheimer sandstone and is recorded to range from 0.01 - 1 D (Sato et al., 2019; Peng et al., 2014; Baizhanov et al., 2019; Kareem et al., 2017) and Kareem et al. (2017) observe four ranges of permeability within four separate samples ranging from  $< 0.05$  - 1 D. Despite both the Bentheimer and Berea sandstones commonly being described as homogeneous the literature also records areas of heterogeneity (e.g. local cements, variable clay content (Baraka-Lokmane et al., 2009; Kareem et al., 2017)) which accounts for the range in recorded values.

The permeability of the bead pack sample was reduced after acidic flow despite mineral dissolution (7.1-7.5% dolomite dissolution, 2.4% kaolinite dissolution) occurring and this was also observed in the experimental results from the previous chapter (Chapter 6). The reduction in permeability is interpreted to occur as a result of smaller particles breaking off during the dissolution process and becoming lodged in pores and pore throats, blocking or partially blocking flow pathways and therefore reducing permeability (Ma et al., 2019; Liu et al., 2020b; Israeli and Emmanuel, 2018; Singurindy and Berkowitz, 2003; Wang et al., 2021). As well as reducing the permeability the clogging of pores and pore throats and blocking or partially blocking flow pathways may also result in increasing variation in permeability and increasing tortuosity (Mangane et al., 2013). Additionally, the reduction in volume and size of the minerals will allow the bead pack sample to become more compacted (Ma et al., 2019) which further reduces the pore space and permeability which will increase the possibility of smaller particles clogging pores and pore throats. The permeability reduction is greater in the sample which contains dolomite and kaolinite as well as heterogeneous bead size when compared to the sample which contains dolomite and kaolinite which has homogeneous bead size and this indicates that the amount of smaller particles becoming lodged in pores and pore throats is increased when bead size is heterogeneous. More particles may become lodged in pores and pore throats when bead size is heterogeneous as heterogeneous bead size increases the range of mean pore diameter and porosity which is associated with increasing disorder and heterogeneity in the pore network (Zakirov and Khrumchenkov, 2020; Zhu et al., 2018; Guo, 2012) and increased heterogeneity typically leads to reduced permeability which may restrict particle transport. Additionally, heterogeneity in the pore structure may influence carbonate dissolution (She et al., 2016; You and Lee, 2021) as the pore structure can determine acid concentrations, transport limitations and mineral accessibility (You and Lee, 2021; Molins et al., 2017) and heterogeneity in pore size can influence the effective solubility of reactive minerals and dissolution (Emmanuel and Berkowitz, 2007). For example, Steinwinder and Beckingham (2019) show that the effect of mineralogical reactions varies due to pore size and reactions in smaller pores can increase permeability whereas reactions in larger pores increases porosity. Additionally, Roded et al. (2020) indicate that the width of flow channels, which is determined by pore network geometry, and heterogeneous flow fields influence the

permeability evolution in the pore network after dissolution and narrow fluid pathways increase the permeability enhancement. Furthermore, [You and Lee \(2021\)](#) state that larger grain size results in a reduction in cross sectional area of micro-channels and smaller grain size increased the length of fluid pathways and velocity resistance. Moreover, [Liu et al. \(2020b\)](#) also suggest that smaller grains have a higher rate of reaction and [Saldi et al. \(2017\)](#) indicate that variation in grain size influences surface reactivity. From this it is understood that a pore network with heterogeneous pore diameter and porosity will have heterogeneous permeability and dissolution and heterogeneous dissolution may lead to a greater contrast between pore sizes which may increase the occurrence of trapped particles in the pore network as different pores will be able to facilitate a different degree of transport. This reasoning is supported by the results from the previous chapter (Chapter 5) which shows that fluid flow is favoured by larger pores ([Salem, 1993](#); [Nemati et al., 2020](#)) so acidic fluid will be preferentially distributed throughout the pore network which may also contribute towards heterogeneous dissolution. Additionally, larger pores can enable higher velocity flow ([Li et al., 2018](#)) which may result in heterogeneous velocity locally which may also contribute towards heterogeneous dissolution.

The amount of dolomite dissolution in the bead pack sample discussed in this chapter is greater than the amount of dolomite dissolution in the bead pack samples discussed in the previous chapter (Chapter 6) and this is understood to have occurred as a result of increased heterogeneity in the pore network geometry which increases resistance to flow and tortuosity and lengthened fluid pathways, which increases access to reactive minerals in the pore network and increases the rate of reactions ([Nemati et al., 2020](#); [Salem, 1993](#); [Habisreuther et al., 2009](#); [Zhang et al., 2020b](#)). In addition to increased mineral dissolution the bead pack sample analysed in this chapter also shows the greatest permeability reduction, 72.7%, which is significantly greater than the other 3 samples where permeability reduction ranges from 1.8-35.5%. This could be due to the increased amount of finer particles released during the acidic flow and also due to the smaller and more heterogeneous pore space in the sample and pores, pore throats and flow pathways may be more easily blocked than in the other samples which have a greater content of larger pores and less heterogeneity in pores. Furthermore, the bead pack sample analysed in this chapter also shows the greatest variation in permeability throughout the different zones of the sample (Fig. 7.5) and permeability in zone 3 is 48.5% lower than zone 4, which has 23.6% greater permeability than the following zone (zone 5). It is recorded in the literature that permeability influences the rate of reactions ([Zhang et al., 2020b](#)) and the fluctuations in permeability throughout the sample may correspond to localised fluctuations in reaction rate and amount of dissolution. The fluctuation in permeability, and potentially reaction rate and dissolution throughout the sample may create localised baffles and barriers to fluid flow and also localised preferential flow pathways and a consecutive sequence of fluid flow barriers/baffles and preferential flow pathways not only increases heterogeneity but may enhance the effect of barriers/baffles after acidic flow and dissolution. For example, a zone of greater permeability, greater rates of reaction and dissolution will be able to transport increased amounts of solutes and finer particles to a zone of lower permeability, lower reaction rates and dissolution. The zone which has lower permeability will not only be less able to facilitate fluid flow, solute transport and particle transport but the pores, pore throats and fluid pathways within the zone will be more easily blocked and this may result in localised regions of the sample becoming blocked more readily and creating enhanced permeability contrasts throughout the sample and in some cases blocking flow completely. Localised dissolution features which alter permeability are more commonly associated with limestone dissolution ([Luquot et al., 2014](#)), rather than dissolution of carbonates in sandstones, and this is due to the increased heterogeneity typically observed in carbonate rocks in comparison to siliciclastic rocks. However, analysis of carbonate dissolution in sandstones is often studied in samples with limited heterogeneity

so this is perhaps why such dissolution features are not commonly observed. [Ma et al. \(2019\)](#) do not fully describe the properties of the sandstone used in the dissolution experiments conducted in their research however the permeability before acidic flow was 0.36 D and the porosity was 21.9%, which is comparable to recorded values of porosity and permeability for the Bentheimer and Berea sandstones, which are regarded as having good reservoir quality and are relatively homogeneous below the cm scale ([Baraka-Lokmane et al., 2009](#); [Kareem et al., 2017](#); [Peksa et al., 2015](#); [Muljadi et al., 2016](#)). Additionally, [Liu et al. \(2018\)](#) also use a sandstone sample with porosity (23.8%) and permeability (0.64 D) values comparable to the Berea and Bentheimer sandstones, [Dawson et al. \(2015\)](#) use a sample of the Berea sandstone and [Weibel et al. \(2011\)](#) use samples from the Bunter sandstone and the Skaggerak formation, which are again both regarded as having strong reservoir quality and the Skaggerak formation is observed to exhibit exceptional reservoir quality in fluvial channel reservoirs due to the anomalously high porosity and permeability values ([Stricker et al., 2016](#); [Olivarius et al., 2015a](#)).

## 7.4 Conclusions

Increasing heterogeneity in mineralogy and particle size resulted in a reduction in mean pore diameter size (31.6-65.4%) and porosity (3.7-5.7%) and an increase in the range of mean pore diameter size (20.3-26.0%). The lower half of the bead pack sample showed good agreement with the results from the natural rock sample showing that bead pack samples are capable of presenting realistic pore network geometries.

Increased heterogeneity in the pore network geometry is expected to result in greater tortuosity and fluid pathway length which promotes geochemical reactions and increases mineral dissolution.

Permeability is reduced (75.7%) by increased heterogeneity in the pore network geometry and a higher content of smaller pores. Permeability is further reduced (76.6) by dissolution which occurred during acidic flow and this is due to small particles becoming removed from the minerals and becoming lodged in pores and pore throats, blocking fluid pathways and reducing permeability. The reduction in permeability after acidic flow is increased (44.1%) when bead size is heterogeneous in comparison to bead pack samples with homogeneous bead size.

Permeability reduction is enhanced by fluctuations in local permeability which is expected to correspond to fluctuations in geochemical reactions and dissolution. Consecutive zones of low permeability and high permeability produce permeability contrasts which may become enhanced after acidic flow as the higher permeability regions enable an increased rate of reaction and dissolution and the low permeability regions are less able to facilitate transport of fluid, solutes and finer particles and the pore space becomes more readily clogged and permeability is reduced further.



## Chapter 8

# Conclusions

The aim of this study was to quantify the effect of heterogeneity in grain size and mineralogy on the pore network geometry and fluid flow behaviour in the pore network before and after reactive flow. To achieve this the project was divided into two approaches; experimental and computational. The experimental approach enabled realistic design of the synthetic bead pack samples used in the experiments which validated the results from the visualisation software and CFD simulations. The visualisation software and CFD simulations offered a greater insight into the samples with differing properties and also enabled analysis at greater scales not achievable using the experimental system. Ten synthetic bead pack samples were designed based on naturally occurring sedimentological heterogeneities and four samples were designed to analyse grain size heterogeneity, four samples were designed to analyse mineralogical heterogeneity and two samples were designed to analyse the combination of grain size and heterogeneity. The naturally occurring sedimentological heterogeneities were identified in four reservoir sandstone cores originating from the southern North Sea gas fields through core scale analysis, thin section analysis and powdered X-ray diffraction analysis. The analysis of the bead pack samples was approached using experimental methods to determine permeability, 3D visualisation and analysis software (Avizo®Fire) to determine pore diameter size, porosity and permeability and computational modelling techniques (ANSYS Fluent R2) to determine permeability and study the onset of non-Darcy flow.

The experimental methodology was designed and developed prior to the experiments to enable reliable and accurate measurement of flow rate and pressure drop over a 3D customised bead pack sample. During the development of the experimental methodology it was observed that trapped air bubbles occurred within the bead pack sample which continuously increased pressure within the system. It was observed that a combination of two different types of degassing techniques were required to ensure pressure stabilised within the system. The trial experiments produced reliable and repeatable data and were in agreement with Kozeny-Carman permeability results produced for the same sample. The methodology was also designed to incorporate additional techniques, such as fluid flow visualisation and inductively coupled plasma optical emission spectrometry, and is able to accommodate samples with varying sizes (1- 6 mm diameter).

The results from the analysis of the samples which exhibit different bead sizes and bead size heterogeneity confirm the widely held view that bead size and the arrangement of bead size (e.g. smaller beads transitioning to larger beads) influences the pore network geometry, how fluid flow moves throughout the pore space and the permeability of the sample. In the homogeneous samples increasing bead size (+ 54.5%) corresponds to larger mean pore diameter size (35.2%), larger range in mean

pore diameter, less uniform distribution in pore diameter size and greater porosity (0.74-3.47%). A less uniform distribution in pore diameter size results in higher tortuosity (2.65%) and a greater resistance to fluid flow as fluid flow will bypass smaller pores in favour of larger pores which have greater capacity for high velocity flow which encourages high velocity preferential pathways. Due to this, permeability is greater when bead size is larger (52.2-98.5% across all homogeneous samples and techniques) and this is in agreement with the literature. In the samples which have heterogeneous bead size the mean pore diameter size and range of pore diameter size is lower (7.7%) and the distribution of pore diameter size is more uniform when smaller beads transition to larger beads. This is due to the reduction in pore space due to a poorer degree of sorting and increased packing density when smaller beads transition to larger beads as the smaller beads are able to invade the pore space between the larger beads below. The pore network is more uniform when smaller beads transition to larger beads and this results in more consistent fluid flow (e.g. multiple, smaller, low velocity flow pathways). The pore network is less uniform when larger beads transition to smaller beads because the lower half of the sample has greater packing density and compaction due to the overburden of the larger beads and this also enhances the effect of sintering. Due to this permeability is greater (0.60-55.9% across all techniques) in the sample where smaller beads transition to larger beads. The different techniques of measuring/predicting permeability show some variation, especially between the experimental and the CFD results. Some variation is expected due to the differing approaches and human error and the results are within one order of magnitude which is comparable as permeability can often vary over one order of magnitude. The CFD results also suggest that the onset of non-Darcy flow is determined by pore size and the critical  $Re$  is larger when pores are larger as larger pores have greater capacity for high velocity flow and are less resistant to flow. The samples which have heterogeneous bead size indicate that the properties which influence the onset of non-Darcy flow vary depending on the properties of the sample. When smaller beads transition to larger beads the critical  $Re$  decreases with decreasing tortuosity whereas when larger beads transition to smaller beads the critical  $Re$  decreases due to increasing heterogeneity and decreasing permeability. In the non-Darcian regime the  $\beta$  results show that  $\beta$  increases with decreasing bead size and the results from the homogeneous samples suggest that  $\beta$  increases with decreasing permeability.

The analysis of the samples which have variable mineralogy show that the addition of kaolinite and dolomite influence the geometry of the pore network and the addition of kaolinite and dolomite reduces the mean pore diameter size (56.8-68.0%), the range of mean pore diameter sizes and porosity (2.2-3.8%). Kaolinite content is observed to result in a greater reduction in mean pore diameter size (68.0%) and increases the range of mean pore diameter size and this is due to the size and distribution of the minerals. Kaolinite is more randomly distributed throughout the sample due to the greater range in particle size (0-63  $\mu\text{m}$ ) which allows kaolinite to occur within a greater number of pores. When kaolinite occurs in addition to dolomite the distribution of kaolinite is limited as dolomite mostly occupies larger pores (> 63  $\mu\text{m}$ ) due to the size of dolomite grains. Dolomite also occurs alongside beads as well as in the pore cavities due to the angular shape of the grains and as a result of this dolomite is more destructive to porosity. The pore network geometry is interpreted to influence the rate of reactions and amount of dissolution and the rate of reaction and amount of dissolution is greatest in the sample which contains both kaolinite and dolomite, which has the greatest variation in pore diameter size. A greater variation in pore diameter size corresponds to a more tortuous pore network which in turn results in longer fluid flow pathways which increases access to reactive minerals. The results further indicate that the pore network geometry influences permeability and the permeability is lowest in the samples which contain kaolinite (- 73.4-88.0%) as kaolinite content corresponds to reduced pore space and a greater range in pore diameter size which creates a more heterogeneous pore network. The permeability is less affected by kaolinite content

when kaolinite occurs with dolomite and this is due to the influence of particle size on permeability and both the literature and the results from the analysis on bead size and bead size heterogeneity show that permeability increases with increasing particle size. The average particle size in the sample which contains dolomite and kaolinite is greater than in the sample which only contains kaolinite and this is again due to dolomite occupying more of the pore space which restricts the distribution of kaolinite in the sample and in some cases the kaolinite is observed to accumulate in the remaining available pore space. The permeability of the samples which contain dolomite was reduced after acidic flow despite evidence of mineral dissolution and this is interpreted to be a result of small particles becoming detached during the dissolution process and becoming lodged in pores and pore throats. The permeability of the sample which contains solely kaolinite increased by 9.6% and this is understood to have occurred due to the influence of pore size in this sample. The sample which solely contains kaolinite has the lowest mean pore diameter and mineral dissolution in smaller pores contributes more to permeability than dissolution in larger pores.

The sample which displays both grain size and mineralogical heterogeneity presents a reduced mean pore diameter (31.6-65.4%) and porosity (3.7-5.7%) and increased range in pore diameter size (20.3-26.0%) in comparison to the bead pack samples discussed previously and the lower half of the sample (mixed bead size and mineralogy) showed comparable pore diameter, porosity and permeability results to the crushed rock sample which indicates that bead pack samples are capable of presenting realistic pore network geometries and are a good analogue for natural samples. Increased heterogeneity is expected to result in greater tortuosity and fluid pathway length which increases access to reactive minerals which promotes geochemical reactions and increases mineral dissolution (1.46-2.40%). As a result of the increased heterogeneity in the pore space and greater volume of smaller pores the permeability is lower (57.3%) when compared to the previous bead pack samples and permeability is further reduced after acidic flow (75.1%) and the reduction in permeability is greater (44.1%) when the bead size is heterogeneous. Permeability is interpreted to be reduced as a consequence of small detached particles becoming lodged in pores and pore throats which may partially or completely block fluid pathways. The reduction in permeability may also be enhanced by the observed local fluctuations in permeability which in turn may result in local fluctuations in geochemical reactions and dissolution. Local fluctuations in geochemical reactions and dissolution may enhance the variation in permeability after acidic flow or create a series of permeability contrasts where the regions of higher permeability enable an increased rate of reaction and dissolution and the regions of low permeability are less able to facilitate transport of fluid, solutes and finer particles and become more readily clogged, reducing permeability further.

The results from this study show that sedimentary heterogeneity identified in sandstone rocks can be introduced into controlled, simplified samples for the analysis of fluid flow behaviour. This study has been successful in understanding how complex pore network geometries influence single phase fluid flow behaviour which provides a foundation for analysis on more complex processes, such as multiphase flow or fluid flow in the transitional or turbulent flow regime.

## 8.1 Future Work

Future experimental work of interest includes conducting pore-scale permeability experiments on the crushed rock sample before and after acidic flow to further assess how the results from the bead pack samples correspond to natural rock samples. Additional samples, such as small consolidated cores ( $1 \times 1 \times 7$  mm), are also of interest and the next step in increasing heterogeneity in samples. Another area of interest is incorporating particle imaging velocimetry into the experimental system,

which would allow further comparison between the experimental and computational results. Further future work could include acidic flow experiments which ran for longer periods of time (10 hours +) and incorporated multiple sampling intervals to enable accurate calculation of reaction rates which can be compared to mineral dissolution results.

Future computational work of interest includes analysis of the pore networks from the samples with variable mineralogy and variable mineralogy and grain size after acidic flow. Analysis could provide a greater insight into the permeability reduction in some of the samples and also provide an insight into how mineralogy influences the critical  $Re$  and  $\beta$ .

# References

- Adam R. Abate, Julian Thiele, Marie Weinhart, and David A. Weitz. Patterning microfluidic device wettability using flow confinement. *Lab on a Chip*, 2010. ISSN 14730189. doi: 10.1039/c004124f.
- Jassem Abbasi, Mojtaba Ghaedi, and Masoud Riazi. A new numerical approach for investigation of the effects of dynamic capillary pressure in imbibition process. *Journal of Petroleum Science and Engineering*, 162(November 2017):44–54, 2018. ISSN 09204105. doi: 10.1016/j.petrol.2017.12.035. URL <https://doi.org/10.1016/j.petrol.2017.12.035>.
- Mohsen Abbaszadeh and Seyed M. Shariatipour. Investigating the impact of reservoir properties and injection parameters on carbon dioxide dissolution in saline aquifers. *Fluids*, 3(4):1–16, 2018. ISSN 23115521. doi: 10.3390/fluids3040076.
- Wael Abdallah, Jill S. Buckley, Andrew Carnegie, John Edwards, Bernd Herold, Edmund Fordham, Arne Graue, Tarek Habashy, Nikita Seleznev, Claude Signer, Hassan Hussain, Bernard Montaron, and Murtaza Ziauddin. Fundamentals of wettability. *Oilfield Review*, 19(2):44–61, 2007. ISSN 09231730.
- Aderonke O. Adegbule and Tohren C.G. Kibbey. Exploring the impact of long-term evaporation on the relationship between capillary pressure and water saturation in unsaturated porous media. *Journal of Hydrology*, 582(December 2019):124557, 2020. ISSN 00221694. doi: 10.1016/j.jhydrol.2020.124557. URL <https://doi.org/10.1016/j.jhydrol.2020.124557>.
- Joseph Adepehin, Che Aziz Ali, and A. A. Zakaria. Textural and petrological characteristics of possible reservoir sandstones in the onshore Balingian province, NW Borneo. *AIP Conference Proceedings*, 2111(June), 2019. ISSN 15517616. doi: 10.1063/1.5111264.
- Hadi Adloo, Ivan L’Heureux, and Abdolreza Kharaghani. Effects of correlated morphological and topological heterogeneity of pore network on effective transport and reaction parameters. *Chemical Engineering Science*, 207:280–304, 2019. ISSN 00092509. doi: 10.1016/j.ces.2019.05.029. URL <https://doi.org/10.1016/j.ces.2019.05.029>.
- Nazeer Ahmed and Daniel K. Sunada. Nonlinear Flow in Porous Media. *Journal of the Hydraulics Division*, 95(6):1847–1858, 11 1969. ISSN 0044-796X. doi: 10.1061/JYCEAJ.0002193. URL <http://ascelibrary.org/doi/10.1061/JYCEAJ.0002193>.
- Ahmed Al-Futaisi and Tad W. Patzek. Secondary imbibition in NAPL-invaded mixed-wet sediments. *Journal of Contaminant Hydrology*, 74(1-4):61–81, 2004. ISSN 01697722. doi: 10.1016/j.jconhyd.2004.02.005.
- Abdullah Al-hasani, Mohammed Hail Hakimi, Ismail M. Saaid, Ahmed M.A. Salim, Siti Qurratu Aini Mahat, Abdelazim A. Ahmed, and Abubakar Abu Bakar Umar. Reservoir characteristics of

- the Kuhlan sandstones from Habban oilfield in the Sabatayn Basin, Yemen and their relevance to reservoir rock quality and petroleum accumulation. *Journal of African Earth Sciences*, 145 (March):131–147, 2018. ISSN 18791956. doi: 10.1016/j.jafrearsci.2018.05.013. URL <https://doi.org/10.1016/j.jafrearsci.2018.05.013>.
- Yousef Al-Khulaifi, Qingyang Lin, Martin J. Blunt, and Branko Bijeljic. Reaction Rates in Chemically Heterogeneous Rock: Coupled Impact of Structure and Flow Properties Studied by X-ray Microtomography. *Environmental Science and Technology*, 51(7):4108–4116, 2017. ISSN 15205851. doi: 10.1021/acs.est.6b06224.
- T. Al-Wahaibi, Y. Al-Wahaibi, A. Al-Ajmi, R. Al-Hajri, N. Yusuf, A. S. Olawale, and I. A. Mohammed. Experimental investigation on flow patterns and pressure gradient through two pipe diameters in horizontal oil-water flows. *Journal of Petroleum Science and Engineering*, 122:266–273, 2014. ISSN 09204105. doi: 10.1016/j.petrol.2014.07.019. URL <http://dx.doi.org/10.1016/j.petrol.2014.07.019>.
- Masoud Alfi, Maria Barrufet, and John Killough. Effect of pore sizes on composition distribution and enhance recovery from liquid shale—Molecular sieving in low permeability reservoirs. *Fuel*, 235(February 2018):1555–1564, 2019. ISSN 00162361. doi: 10.1016/j.fuel.2018.08.063. URL <https://doi.org/10.1016/j.fuel.2018.08.063>.
- L. Algive, S. Békri, F.H. Nader, O. Lerat, and O. Vizika. Impact of Diagenetic Alterations on the Petrophysical and Multiphase Flow Properties of Carbonate Rocks Using a Reactive Pore Network Modeling Approach. *Oil & Gas Science and Technology – Revue d’IFP Energies nouvelles*, 67(1):147–160, 1 2012. ISSN 1294-4475. doi: 10.2516/ogst/2011171. URL <http://ogst.ifpenergiesnouvelles.fr/10.2516/ogst/2011171>.
- Nayef Alyafei and Martin J. Blunt. Estimation of relative permeability and capillary pressure from mass imbibition experiments. *Advances in Water Resources*, 115:88–94, 2018. ISSN 03091708. doi: 10.1016/j.advwatres.2018.03.003. URL <https://doi.org/10.1016/j.advwatres.2018.03.003>.
- Ali Aminian and Bahman ZareNezhad. Wettability alteration in carbonate and sandstone rocks due to low salinity surfactant flooding. *Journal of Molecular Liquids*, 275:265–280, 2019. ISSN 01677322. doi: 10.1016/j.molliq.2018.11.080. URL <https://doi.org/10.1016/j.molliq.2018.11.080>.
- Aijun An and Zhihong Nie. Quantification of Shape Properties and Their Effects on Particle Packing of Coarse-Grain Soil. *Indian Geotechnical Journal*, 51(2):405–413, 2021. ISSN 22773347. doi: 10.1007/s40098-020-00454-y. URL <https://doi.org/10.1007/s40098-020-00454-y>.
- Chris Y. Anani, Daniel Kwayisi, Naa A. Agra, and Daniel K. Asiedu. Provenance of shales and sandstones from the Devonian Accraian Group, southern Ghana. *Geosciences Journal*, 22(3): 393–405, 2018. ISSN 15987477. doi: 10.1007/s12303-017-0066-9.
- Matthew Andrew, Branko Bijeljic, and Martin Blunt. Reservoir condition pore scale imaging of the capillary trapping of CO<sub>2</sub>. *Energy Procedia*, 63:5427–5434, 2014. ISSN 18766102. doi: 10.1016/j.egypro.2014.11.573. URL <http://dx.doi.org/10.1016/j.egypro.2014.11.573>.
- Lawrence M. Anovitz, David R. Cole, Andrew J. Jackson, Gernot Rother, Kenneth C. Littrell, Lawrence F. Allard, Anthony D. Pollington, and David J. Wesolowski. Effect of quartz overgrowth

- precipitation on the multiscale porosity of sandstone: A (U)SANS and imaging analysis. *Geochimica et Cosmochimica Acta*, 158:199–222, 2015. ISSN 00167037. doi: 10.1016/j.gca.2015.01.028. URL <http://dx.doi.org/10.1016/j.gca.2015.01.028>.
- Marco A. Antonellini, Atilla Aydin, and David D. Pollard. Microstructure of deformation bands in porous sandstones at Arches National Park, Utah. *Journal of Structural Geology*, 16(7):941–959, 1994. ISSN 01918141. doi: 10.1016/0191-8141(94)90077-9.
- Maria Apostolopoulou, Ron Dusterhoft, Richard Day, Michail Stamatakis, Marc Olivier Coppens, and Alberto Striolo. Estimating permeability in shales and other heterogeneous porous media: Deterministic vs. stochastic investigations. *International Journal of Coal Geology*, 205(October 2018):140–154, 2019. ISSN 01665162. doi: 10.1016/j.coal.2019.02.009. URL <https://doi.org/10.1016/j.coal.2019.02.009>.
- Anat Arbhahirama and Antonio A. Dinoy. Friction Factor and Reynolds Number in Porous Media Flow. *Journal of the Hydraulics Division*, 99(6):901–911, 6 1973. ISSN 0044-796X. doi: 10.1061/JYCEAJ.0003663. URL <http://ascelibrary.org/doi/10.1061/JYCEAJ.0003663>.
- Maria Eugenia Arribas, Juan Pedro Rodríguez-López, Nieves Meléndez, Ana Rosa Soria, and Poppe L. de Boer. Giant calcite concretions in aeolian dune sandstones; sedimentological and architectural controls on diagenetic heterogeneity, mid-Cretaceous Iberian Desert System, Spain. *Sedimentary Geology*, 243-244:130–147, 2012. ISSN 00370738. doi: 10.1016/j.sedgeo.2011.10.011. URL <http://dx.doi.org/10.1016/j.sedgeo.2011.10.011>.
- Maziar Arshadi, Masakazu Gesho, Tianzhu Qin, Lamia Goual, and Mohammad Piri. Impact of mineralogy and wettability on pore-scale displacement of NAPLs in heterogeneous porous media. *Journal of Contaminant Hydrology*, 230(December 2019):103599, 2020. ISSN 18736009. doi: 10.1016/j.jconhyd.2020.103599. URL <https://doi.org/10.1016/j.jconhyd.2020.103599>.
- A. Asaad, F. Hubert, E. Ferrage, T. Dabat, E. Paineau, P. Porion, S. Savoye, B. Gregoire, B. Dazas, A. Delville, and E. Tertre. Role of interlayer porosity and particle organization in the diffusion of water in swelling clays. *Applied Clay Science*, 207(April):106089, 2021. ISSN 01691317. doi: 10.1016/j.clay.2021.106089. URL <https://doi.org/10.1016/j.clay.2021.106089>.
- Shabina Ashraf, Ganesh Visavale, and Jyoti Phirani. Spontaneous imbibition in randomly arranged interacting capillaries. *Chemical Engineering Science*, 192:218–234, 2018. ISSN 00092509. doi: 10.1016/j.ces.2018.07.036. URL <https://doi.org/10.1016/j.ces.2018.07.036>.
- Attia M. Attia. Effects of petrophysical rock properties on tortuosity factor. *Journal of Petroleum Science and Engineering*, 48(3-4):185–198, 2005. ISSN 09204105. doi: 10.1016/j.petrol.2005.06.012.
- Bin Bai, Rukai Zhu, Songtao Wu, Wenjing Yang, Jeff Gelb, Allen Gu, Xiangxiang Zhang, and Ling Su. Multi-scale method of Nano(Micro)-CT study on microscopic pore structure of tight sandstone of Yanchang Formation, Ordos Basin. *Petroleum Exploration and Development*, 40(3):354–358, 2013. ISSN 18763804. doi: 10.1016/S1876-3804(13)60042-7. URL [http://dx.doi.org/10.1016/S1876-3804\(13\)60042-7](http://dx.doi.org/10.1016/S1876-3804(13)60042-7).
- Christopher Baiyegunhi, Kuiwu Liu, and Oswald Gwavava. Grain size statistics and depositional pattern of the Ecca Group sandstones, Karoo Supergroup in the Eastern Cape Province, South Africa. *Open Geosciences*, 9(1):554–576, 2017. ISSN 23915447. doi: 10.1515/geo-2017-0042.

- Bekdar Baizhanov, Daisuke Katsuki, Azra N. Tutuncu, and Ali I. Mese. Experimental Investigation of Coupled Geomechanical, Acoustic, and Permeability Characterization of Berea Sandstone Using a Novel True Triaxial Assembly. *Rock Mechanics and Rock Engineering*, 52(8):2491–2503, 2019. ISSN 1434453X. doi: 10.1007/s00603-019-01816-6. URL <https://doi.org/10.1007/s00603-019-01816-6>.
- Sahar Bakhshian, Seyyed A. Hosseini, and Nima Shokri. Pore-scale characteristics of multiphase flow in heterogeneous porous media using the lattice Boltzmann method. *Scientific Reports*, 9(1): 1–13, 2019. ISSN 20452322. doi: 10.1038/s41598-019-39741-x.
- Gregory Ballas, Haakon Fossen, and Roger Soliva. Factors controlling permeability of cataclastic deformation bands and faults in porous sandstone reservoirs. *Journal of Structural Geology*, 76: 1–21, 2015. ISSN 01918141. doi: 10.1016/j.jsg.2015.03.013. URL <http://dx.doi.org/10.1016/j.jsg.2015.03.013>.
- S Baraka-Lokmane, I.G. Main, B.T. Ngwenya, and S.C. Elphick. Application of complementary methods for more robust characterization of sandstone cores. *Marine and Petroleum Geology*, 26(1):39–56, 1 2009. ISSN 02648172. doi: 10.1016/j.marpetgeo.2007.11.003. URL <https://linkinghub.elsevier.com/retrieve/pii/S0264817207001298>.
- Kaplan S. Basniev, Nikolay M Dmitriev, and George V Chilingar. *Mechanics of Fluid Flow*. Wiley, 2012.
- Jacob Bear. *Dynamics of Fluids in Porous Media*. Dover Publications, New York, 1972. ISBN : 0-186-65675-6.
- Dhruvit S. Berawala and Pål Andersen. Numerical investigation of Non-Darcy flow regime transitions in shale gas production. *Journal of Petroleum Science and Engineering*, 190(February):107114, 2020. ISSN 09204105. doi: 10.1016/j.petrol.2020.107114. URL <https://doi.org/10.1016/j.petrol.2020.107114>.
- Y. Bernabé, M. Li, and A. Maineult. Permeability and pore connectivity: A new model based on network simulations. *Journal of Geophysical Research: Solid Earth*, 115(10):1–14, 2010. ISSN 21699356. doi: 10.1029/2010JB007444.
- Yves Bernabé, Min Li, Yan-Bing Tang, and Brian Evans. Pore Space Connectivity and the Transport Properties of Rocks. *Oil & Gas Science and Technology – Revue d’IFP Energies nouvelles*, 71(4):50, 7 2016. ISSN 1294-4475. doi: 10.2516/ogst/2015037. URL <http://ogst.ifpenergiesnouvelles.fr/10.2516/ogst/2015037>.
- P. Bertier, R. Swennen, B. Laenen, D. Lagrou, and R. Dreesen. Experimental identification of CO<sub>2</sub>-water-rock interactions caused by sequestration of CO<sub>2</sub> in Westphalian and Buntsandstein sandstones of the Campine Basin (NE-Belgium). *Journal of Geochemical Exploration*, 89(1-3 SPEC. ISS.):10–14, 2006. ISSN 03756742. doi: 10.1016/j.gexplo.2005.11.005.
- Branko Bijeljic, Ali Raeini, Peyman Mostaghimi, and Martin J. Blunt. Predictions of non-Fickian solute transport in different classes of porous media using direct simulation on pore-scale images. *Physical Review E - Statistical, Nonlinear, and Soft Matter Physics*, 87(1):1–9, 2013. ISSN 15393755. doi: 10.1103/PhysRevE.87.013011.
- Emma M. Björk, Fredrik Söderlind, and Magnus Odén. Tuning the shape of mesoporous silica particles by alterations in parameter space: From rods to platelets. *Langmuir*, 29(44):13551–13561, 2013. ISSN 07437463. doi: 10.1021/la403201v.



- Salman Bloch. Secondary Porosity in Sandstones: Significance, Origin, Relationship to Subaerial Unconformities, and Effect on Pre-drill Reservoir Quality Prediction. In *Reservoir Quality Assessment and Prediction in Clastic Rocks*, pages 137–159. SEPM (Society for Sedimentary Geology), 1994. doi: 10.2110/scn.94.30.0137. URL <https://pubs.geoscienceworld.org/books/book/1200/chapter/10589252/>.
- J. P. Bloomfield, D. C. Gooddy, M. I. Bright, and P. J. Williams. Pore-throat size distributions in Permo-Triassic sandstones from the United Kingdom and some implications for contaminant hydrogeology. *Hydrogeology Journal*, 9(3):219–230, 2001. ISSN 14312174. doi: 10.1007/s100400100135.
- Martin J. Blunt. Flow in porous media - Pore-network models and multiphase flow. *Current Opinion in Colloid and Interface Science*, 6(3):197–207, 2001. ISSN 13590294. doi: 10.1016/S1359-0294(01)00084-X.
- Martin J. Blunt. *Multiphase Flow in Permeable Media A Pore-Scale Perspective*. Cambridge University Press, Cambridge, 2017.
- Gianluca Boccardo, Eleonora Crevacore, Rajandrea Sethi, and Matteo Icardi. A robust upscaling of the effective particle deposition rate in porous media. *Journal of Contaminant Hydrology*, 212: 3–13, 2018. ISSN 18736009. doi: 10.1016/j.jconhyd.2017.09.002.
- C. Bordier and D. Zimmer. Drainage equations and non-Darcian modelling in coarse porous media or geosynthetic materials. *Journal of Hydrology*, 228(3-4):174–187, 2000. ISSN 00221694. doi: 10.1016/S0022-1694(00)00151-7.
- Florent Brondolo. *Experimental and numerical investigations of geomechanical controls on petrophysical changes of carbonates during fluid flow*. PhD thesis, University of Edinburgh, 2019.
- M. Buchgraber, M. Al-Dossary, C. M. Ross, and A. R. Kovscek. Creation of a dual-porosity micro-model for pore-level visualization of multiphase flow. *Journal of Petroleum Science and Engineering*, 2012. ISSN 09204105. doi: 10.1016/j.petrol.2012.03.012.
- Tom Bultreys, Luc Van Hoorebeke, and Veerle Cnudde. Simulating secondary waterflooding in heterogeneous rocks with variable wettability using an image-based, multiscale pore network model. *Water Resources Research*, 52(9):6833–6850, 9 2016. ISSN 00431397. doi: 10.1002/2016WR018950. URL <http://doi.wiley.com/10.1002/2016WR018950>.
- Jianchao Cai, Zhien Zhang, Wei Wei, Dongming Guo, Shuai Li, and Peiqiang Zhao. The critical factors for permeability-formation factor relation in reservoir rocks: Pore-throat ratio, tortuosity and connectivity. *Energy*, 188:116051, 2019. ISSN 03605442. doi: 10.1016/j.energy.2019.116051. URL <https://doi.org/10.1016/j.energy.2019.116051>.
- Zhe Cao, Guangdi Liu, Hongbin Zhan, Chaozheng Li, Yuan You, Chengyu Yang, and Hang Jiang. Pore structure characterization of Chang-7 tight sandstone using MICP combined with N 2 GA techniques and its geological control factors. *Scientific Reports*, 6(November):1–14, 2016. ISSN 20452322. doi: 10.1038/srep36919. URL <http://dx.doi.org/10.1038/srep36919>.
- José M. Carcione, Davide Gei, Ting Yu, and Jing Ba. Effect of Clay and Mineralogy on Permeability. *Pure and Applied Geophysics*, 176(6):2581–2594, 2019. ISSN 14209136. doi: 10.1007/s00024-019-02117-3.

- Nick J. Carroll, Kaare H. Jensen, Shima Parsa, N. Michele Holbrook, and David A. Weitz. Measurement of flow velocity and inference of liquid viscosity in a microfluidic channel by fluorescence photobleaching. *Langmuir*, 2014. ISSN 15205827. doi: 10.1021/la404891g.
- Victor Chang, Alexander Zambrano, Melcris Mena, and Agustin Millan. A sensor for on-line measurement of the viscosity of non-Newtonian fluids using a neural network approach, 1995. ISSN 09244247.
- Elli Maria Charalampidou, Stephen A. Hall, Sergei Stanchits, Helen Lewis, and Gioacchino Viggiani. Characterization of shear and compaction bands in a porous sandstone deformed under triaxial compression. *Tectonophysics*, 503(1-2):8–17, 2011. ISSN 00401951. doi: 10.1016/j.tecto.2010.09.032. URL <http://dx.doi.org/10.1016/j.tecto.2010.09.032>.
- Kuldeep Chaudhary, M. Bayani Cardenas, Wen Deng, and Philip C. Bennett. The role of eddies inside pores in the transition from Darcy to Forchheimer flows. *Geophysical Research Letters*, 38(24):1–6, 2011. ISSN 00948276. doi: 10.1029/2011GL050214.
- Kuldeep Chaudhary, M. Bayani Cardenas, Wen Deng, and Philip C. Bennett. Pore geometry effects on intrapore viscous to inertial flows and on effective hydraulic parameters. *Water Resources Research*, 49(2):1149–1162, 2013a. ISSN 00431397. doi: 10.1002/wrcr.20099.
- Kuldeep Chaudhary, M. Bayani Cardenas, William W. Wolfe, Jessica A. Maisano, Richard A. Ketcham, and Philip C. Bennett. Pore-scale trapping of supercritical CO<sub>2</sub> and the role of grain wettability and shape. *Geophysical Research Letters*, 40(15):3878–3882, 2013b. ISSN 00948276. doi: 10.1002/grl.50658.
- Li Chen, Qinjun Kang, Hari S. Viswanathan, and Wen-Quan Tao. Pore-scale study of dissolution-induced changes in hydrologic properties of rocks with binary minerals. *Water Resources Research*, 50(12):9343–9365, 12 2014. ISSN 00431397. doi: 10.1002/2014WR015646. URL <http://doi.wiley.com/10.1002/2014WR015646>.
- Quan Chen and Y. Q. Song. What is the shape of pores in natural rocks? *Journal of Chemical Physics*, 116(19):8247–8250, 3 2002. ISSN 00219606. doi: 10.1063/1.1477183.
- Chaojie Cheng and Harald Milsch. Permeability Variations in Illite-Bearing Sandstone: Effects of Temperature and NaCl Fluid Salinity. *Journal of Geophysical Research: Solid Earth*, 125(9), 2020. ISSN 21699356. doi: 10.1029/2020JB020122.
- Hongfei Cheng, Zhiliang Zhang, Qinfu Liu, and Joseph Leung. A new method for determining platy particle aspect ratio: A kaolinite case study. *Applied Clay Science*, 97-98:125–131, 2014. ISSN 01691317. doi: 10.1016/j.clay.2014.05.018. URL <http://dx.doi.org/10.1016/j.clay.2014.05.018>.
- Bm Chentnik. Characterizing Fractures and Deformation Bands: Implications for Long-Term CO<sub>2</sub> Storage within the Cambrian Mount Simon Sandstone. *The Journal of Purdue Undergraduate Research*, 2(3):8–15, 2012. ISSN 21584044. doi: 10.5703/jpur.02.1.02. URL <http://docs.lib.purdue.edu/jpur/vol2/iss1/3/>.
- Cheema Chomsurin and Charles J. Werth. Analysis of pore-scale nonaqueous phase liquid dissolution in etched silicon pore networks. *Water Resources Research*, 39(9), 2003. ISSN 00431397. doi: 10.1029/2002WR001643.

- C. P. Chukwudozie, M. Tyagi, S. O. Sears, and C. D. White. Prediction of Non-Darcy Coefficients for Inertial Flows Through the Castlegate Sandstone Using Image-Based Modeling. *Transport in Porous Media*, 95(3):563–580, 12 2012. ISSN 0169-3913. doi: 10.1007/s11242-012-0062-5. URL <http://link.springer.com/10.1007/s11242-012-0062-5>.
- C. A. Chung and Hung Yu Lin. Enhancing Immiscible Fluid Displacement in Porous Media by Capillary Pressure Discontinuities. *Transport in Porous Media*, 2017. ISSN 15731634. doi: 10.1007/s11242-017-0922-0.
- Steven Claes, Fadi H. Nader, and Souhail Youssef. Coupled experimental/numerical workflow for assessing quantitative diagenesis and dynamic porosity/permeability evolution in calcite-cemented sandstone reservoir rocks. *Oil and Gas Science and Technology*, 73, 2018. ISSN 19538189. doi: 10.2516/ogst/2018027.
- J. Comiti, N. E. Sabiri, and A. Montillet. Experimental characterization of flow regimes in various porous media - III: Limit of Darcy's or creeping flow regime for Newtonian and purely viscous non-Newtonian fluids. *Chemical Engineering Science*, 55(15):3057–3061, 2000. ISSN 00092509. doi: 10.1016/S0009-2509(99)00556-4.
- Christophe Cottin, Hugues Bodiguel, and Annie Colin. Drainage in two-dimensional porous media: From capillary fingering to viscous flow. *Physical Review E - Statistical, Nonlinear, and Soft Matter Physics*, 82(4), 10 2010. ISSN 15393755. doi: 10.1103/PhysRevE.82.046315.
- A. A. Cronin, J. A.C. Barth, T. Elliot, and R. M. Kalin. Recharge velocity and geochemical evolution for the Permo-Triassic Sherwood Sandstone, Northern Ireland. *Journal of Hydrology*, 315(1-4): 308–324, 2005. ISSN 00221694. doi: 10.1016/j.jhydrol.2005.04.016.
- Luis Cueto-Felgueroso and Ruben Juanes. A discrete-domain description of multiphase flow in porous media: Rugged energy landscapes and the origin of hysteresis. *Geophysical Research Letters*, 43(4):1615–1622, 2016. ISSN 19448007. doi: 10.1002/2015GL067015.
- Guodong Cui, Yi Wang, Zhenhua Rui, Bailian Chen, Shaoran Ren, and Liang Zhang. Assessing the combined influence of fluid-rock interactions on reservoir properties and injectivity during CO<sub>2</sub> storage in saline aquifers. *Energy*, 155:281–296, 2018. ISSN 03605442. doi: 10.1016/j.energy.2018.05.024. URL <https://doi.org/10.1016/j.energy.2018.05.024>.
- K. A. Culligan, D. Wildenschild, B. S.B. Christensen, W. G. Gray, and M. L. Rivers. Pore-scale characteristics of multiphase flow in porous media: A comparison of air-water and oil-water experiments. *Advances in Water Resources*, 29(2):227–238, 2 2006. ISSN 03091708. doi: 10.1016/j.advwatres.2005.03.021.
- Ali Danesh. *PVT and Phase Behaviour of Petroleum Reservoir Fluids*. Elsevier B.V, Amsterdam, 3 edition, 2003. ISBN 0444821961.
- Sujit S. Datta, H. Chiang, T. S. Ramakrishnan, and David A. Weitz. Spatial fluctuations of fluid velocities in flow through a three-dimensional porous medium. *Physical Review Letters*, 111(6): 1–5, 2013. ISSN 00319007. doi: 10.1103/PhysRevLett.111.064501.
- Sujit S. Datta, T. S. Ramakrishnan, and David A. Weitz. Mobilization of a trapped non-wetting fluid from a three-dimensional porous medium. *Physics of Fluids*, 26(2):022002, 2 2014. ISSN 1070-6631. doi: 10.1063/1.4866641. URL <http://aip.scitation.org/doi/10.1063/1.4866641>.

- Christian David. Geometry of flow paths for fluid transport in rocks. *Journal of Geophysical Research: Solid Earth*, 98(B7):12267–12278, 7 1993. ISSN 01480227. doi: 10.1029/93JB00522. URL <http://doi.wiley.com/10.1029/93JB00522>.
- Richard A. Dawe, Albert Caruana, and Carlos A. Grattoni. Microscale Visual Study of End Effects at Permeability Discontinuities. *Transport in Porous Media*, 86(2):601–616, 1 2011. ISSN 0169-3913. doi: 10.1007/s11242-010-9642-4. URL <http://link.springer.com/10.1007/s11242-010-9642-4>.
- G. K.W. Dawson, J. K. Pearce, D. Biddle, and S. D. Golding. Experimental mineral dissolution in Berea Sandstone reacted with CO<sub>2</sub> or SO<sub>2</sub>-CO<sub>2</sub> in NaCl brine under CO<sub>2</sub> sequestration conditions. *Chemical Geology*, 399:87–97, 2015. ISSN 00092541. doi: 10.1016/j.chemgeo.2014.10.005. URL <http://dx.doi.org/10.1016/j.chemgeo.2014.10.005>.
- E. De Boever, C. Varloteaux, F.H. Nader, A. Foubert, S. Békri, S. Youssef, and E. Rosenberg. Quantification and Prediction of the 3D Pore Network Evolution in Carbonate Reservoir Rocks. *Oil & Gas Science and Technology – Revue d'IFP Energies nouvelles*, 67(1):161–178, 1 2012. ISSN 1294-4475. doi: 10.2516/ogst/2011170. URL <http://ogst.ifpenergiesnouvelles.fr/10.2516/ogst/2011170>.
- Leonardo Del Sole and Marco Antonellini. Microstructural, petrophysical, and mechanical properties of compactive shear bands associated to calcite cement concretions in arkose sandstone. *Journal of Structural Geology*, 126(January):51–68, 2019. ISSN 01918141. doi: 10.1016/j.jsg.2019.05.007. URL <https://doi.org/10.1016/j.jsg.2019.05.007>.
- Wen Deng, M. Bayani Cardenas, and Philip C. Bennett. Extended Roof snap-off for a continuous nonwetting fluid and an example case for supercritical CO<sub>2</sub>. *Advances in Water Resources*, 64: 34–46, 2014. ISSN 03091708. doi: 10.1016/j.advwatres.2013.12.001. URL <http://dx.doi.org/10.1016/j.advwatres.2013.12.001>.
- Wen Deng, Matthew Balhoff, and M. Bayani Cardenas. Influence of dynamic factors on non-wetting fluid snap-off in pores. *Water Resources Research*, 51(11):9182–9189, 11 2015. ISSN 0043-1397. doi: 10.1002/2015WR017261. URL <https://onlinelibrary.wiley.com/doi/abs/10.1002/2015WR017261>.
- M. Dentz, M. Icardi, and J. J. Hidalgo. Mechanisms of dispersion in a porous medium. *Journal of Fluid Mechanics*, 841:851–882, 2018. ISSN 14697645. doi: 10.1017/jfm.2018.120.
- Kenneth W. Desmond and Eric R. Weeks. Influence of particle size distribution on random close packing of spheres. *Physical Review E - Statistical, Nonlinear, and Soft Matter Physics*, 90(2), 8 2014. ISSN 15502376. doi: 10.1103/PhysRevE.90.022204.
- Hongna Ding and Sheik Rahman. Experimental and theoretical study of wettability alteration during low salinity water flooding—an state of the art review. *Colloids and Surfaces A: Physicochemical and Engineering Aspects*, 520(January):622–639, 2017. ISSN 18734359. doi: 10.1016/j.colsurfa.2017.02.006. URL <http://dx.doi.org/10.1016/j.colsurfa.2017.02.006>.
- E.C Donaldson, G.V Chilingarian, and T.F Yen. *Enhanced Oil Recovery, I: Fundamentals and Analyses*. Elsevier Science Publishers B.V, Amsterdam, 1 edition, 1985. ISBN 0444422064.
- Erle C Donaldson and Waqi Alam. *Wettability and Production*. Gulf Publishing Company, Houston, 2008. ISBN 978-1-60119-631-6.

- Wenchao Dou, Luofu Liu, Kangjun Wu, Zhengjian Xu, Xiaoxiang Liu, and Xu Feng. Diagenetic heterogeneity, pore throats characteristic and their effects on reservoir quality of the Upper Triassic tight sandstones of Yanchang Formation in Ordos Basin, China. *Marine and Petroleum Geology*, 98:243–257, 12 2018. ISSN 02648172. doi: 10.1016/j.marpetgeo.2018.08.019.
- S. N Ehrenberg. Preservation of Anomalously High Porosity in Deeply Buried Sandstones by Grain-Coating Chlorite: Examples from the Norwegian Continental Shelf. *AAPG Bulletin*, 77, 1993. ISSN 0149-1423. doi: 10.1306/BDF8E5C-1718-11D7-8645000102C1865D. URL <http://search.datapages.com/data/doi/10.1306/BDF8E5C-1718-11D7-8645000102C1865D>.
- A. A. El-Zehairy, M. Mousavi Nezhad, V. Joekar-Niasar, I. Guymmer, N. Kourra, and M. A. Williams. Pore-network modelling of non-Darcy flow through heterogeneous porous media. *Advances in Water Resources*, 131(January):103378, 2019. ISSN 03091708. doi: 10.1016/j.advwatres.2019.103378. URL <https://doi.org/10.1016/j.advwatres.2019.103378>.
- Jonathan S. Ellis and Aimy Bazylak. Dynamic pore network model of surface heterogeneity in brine-filled porous media for carbon sequestration. *Physical Chemistry Chemical Physics*, 14(23): 8382–8390, 2012. ISSN 14639076. doi: 10.1039/c2cp40812k.
- Simon Emmanuel and Brian Berkowitz. Effects of pore-size controlled solubility on reactive transport in heterogeneous rock. *Geophysical Research Letters*, 34(6):1–5, 2007. ISSN 00948276. doi: 10.1029/2006GL028962.
- Anthony L Endres, British Columbia, and Rosemary Knight. The effects of pore-scale fluid distribution of partially saturated tight sandstones on the physical properties. *Simulation*, 1091: 1091–1098, 1991.
- R. Enouy, M. Li, M. A. Ioannidis, and A. J.A. Unger. Gas exsolution and flow during supersaturated water injection in porous media: II. Column experiments and continuum modeling. *Advances in Water Resources*, 34(1):15–25, 2011. ISSN 03091708. doi: 10.1016/j.advwatres.2010.09.013.
- Ulrike Exner, Jasmin Kaiser, and Susanne Gier. Deformation bands evolving from dilation to cementation bands in a hydrocarbon reservoir (Vienna Basin, Austria). *Marine and Petroleum Geology*, 43:504–515, 2013. ISSN 02648172. doi: 10.1016/j.marpetgeo.2012.10.001. URL <http://dx.doi.org/10.1016/j.marpetgeo.2012.10.001>.
- Chung Fang, Wei Wu, Yung Jung Lin, Yen Hung Chen, and Thiep Doanh. On sintering of tiny glass beads in oscillating diametric compressions. *Granular Matter*, 18(4):1–18, 2016. ISSN 14347636. doi: 10.1007/s10035-016-0669-2.
- Saeed Farrokhpay, Bulelwa Ndlovu, and Dee Bradshaw. Behaviour of swelling clays versus non-swelling clays in flotation. *Minerals Engineering*, 96-97:59–66, 2016. ISSN 08926875. doi: 10.1016/j.mineng.2016.04.011. URL <http://dx.doi.org/10.1016/j.mineng.2016.04.011>.
- Faruk Civan. *Porous Media Transport Phenomena*. John Wiley & Sons, Incorporated, New Jersey, 1 edition, 2011. ISBN 9781118086438.
- Hassan E. Fayed, Nadeem A. Sheikh, and Oleg Iliev. On Laminar Flow of Non-Newtonian Fluids in Porous Media. *Transport in Porous Media*, 111(1):253–264, 2016. ISSN 15731634. doi: 10.1007/s11242-015-0592-8.

- M. Ferer, Chuang Ji, Grant S. Bromhal, Joshua Cook, Goodarz Ahmadi, and Duane H. Smith. Crossover from capillary fingering to viscous fingering for immiscible unstable flow: Experiment and modeling. *Physical Review E - Statistical Physics, Plasmas, Fluids, and Related Interdisciplinary Topics*, 70(1):7, 2004. ISSN 1063651X. doi: 10.1103/PhysRevE.70.016303.
- Quentin J. Fisher, Martin Casey, M. Ben Clennell, and Robert J. Knipe. Mechanical compaction of deeply buried sandstones of the North Sea. *Marine and Petroleum Geology*, 16(7):605–618, 1999. ISSN 02648172. doi: 10.1016/S0264-8172(99)00044-6.
- H. Fossen, R.A. Schultz, Z.K. Shipton, and K. Mair. Deformation bands in sandstone: a review. *Journal of the Geological Society*, 164:1–15, 2007. ISSN 0016-7649. doi: 10.1144/0016-76492006-036.
- Aryeh Fox, Aaron I. Packman, Fulvio Boano, Colin B. Phillips, and Shai Arnon. Interactions Between Suspended Kaolinite Deposition and Hyporheic Exchange Flux Under Losing and Gaining Flow Conditions. *Geophysical Research Letters*, 45(9):4077–4085, 2018. ISSN 19448007. doi: 10.1029/2018GL077951.
- Christopher N. Fredd and H. Scott Fogler. Influence of transport and reaction on wormhole formation in porous media. *AIChE Journal*, 44(9):1933–1949, 1998. ISSN 00011541. doi: 10.1002/aic.690440902.
- Jared T. Freiburg, Robert W. Ritzi, and Kelsey S. Kehoe. Depositional and diagenetic controls on anomalously high porosity within a deeply buried CO<sub>2</sub> storage reservoir - The Cambrian Mt. Simon Sandstone, Illinois Basin, USA. *International Journal of Greenhouse Gas Control*, 55:42–54, 2016. ISSN 17505836. doi: 10.1016/j.ijggc.2016.11.005. URL <http://dx.doi.org/10.1016/j.ijggc.2016.11.005>.
- Bruce K. Gale, Alexander R. Jafek, Christopher J. Lambert, Brady L. Goenner, Hossein Moghimi-fam, Ugochukwu C. Nze, and Suraj Kumar Kamarapu. A review of current methods in microfluidic device fabrication and future commercialization prospects. *Inventions*, 3(3), 2018. ISSN 24115134. doi: 10.3390/inventions3030060.
- F. J. Galindo-Rosales, F. J. Rubio-Hernández, and A. Sevilla. An apparent viscosity function for shear thickening fluids. *Journal of Non-Newtonian Fluid Mechanics*, 166(5-6):321–325, 2011. ISSN 03770257. doi: 10.1016/j.jnnfm.2011.01.001. URL <http://dx.doi.org/10.1016/j.jnnfm.2011.01.001>.
- S. Gambino, E. Fazio, R. Maniscalco, R. Punturo, G. Lanzafame, G. Barreca, and R. W.H. Butler. Fold-related deformation bands in a weakly buried sandstone reservoir analogue: A multi-disciplinary case study from the Numidian (Miocene) of Sicily (Italy). *Journal of Structural Geology*, 118(April 2018):150–164, 2019. ISSN 01918141. doi: 10.1016/j.jsg.2018.10.005. URL <https://doi.org/10.1016/j.jsg.2018.10.005>.
- Leonhard Ganzer, Viktor Reitenbach, Dieter Pudlo, Daniel Albrecht, Arron Tchouka Singhe, Kilian Nhungong Awemo, Joachim Wienand, and Reinhard Gaupp. Experimental and numerical investigations on CO<sub>2</sub> injection and enhanced gas recovery effects in Altmark gas field (Central Germany). *Acta Geotechnica*, 9(1):39–47, 2014. ISSN 18611125. doi: 10.1007/s11440-013-0226-7.
- Hui Gao and Huazhou Andy Li. Pore structure characterization, permeability evaluation and enhanced gas recovery techniques of tight gas sandstones. *Journal of Natural Gas Science and Engineering*, 28:536–547, 2016. ISSN 18755100. doi: 10.1016/j.jngse.2015.12.018. URL <http://dx.doi.org/10.1016/j.jngse.2015.12.018>.

- Xiangdong Gao, Yanbin Wang, L. I. Yong, Hui Guo, N. I. Xiaoming, W. U. Xiang, and Shihu Zhao. Characteristics of Tight Sandstone Reservoirs and Controls of Reservoir Quality: A Case Study of He 8 Sandstones in the Linxing Area, Eastern Ordos Basin, China. *Acta Geologica Sinica*, 93(3):637–659, 2019. ISSN 17556724. doi: 10.1111/1755-6724.13862.
- Thomas Gervais and Klavs F. Jensen. Mass transport and surface reactions in microfluidic systems. *Chemical Engineering Science*, 61(4):1102–1121, 2006. ISSN 00092509. doi: 10.1016/j.ces.2005.06.024.
- Behzad Ghanbarian, Allen G. Hunt, Robert P. Ewing, and Muhammad Sahimi. Tortuosity in Porous Media: A Critical Review. *Soil Science Society of America Journal*, 77(5):1461–1477, 2013. ISSN 0361-5995. doi: 10.2136/sssaj2012.0435.
- A. Ghanizadeh, C. R. Clarkson, S. Aquino, O. H. Ardakani, and H. Sanei. Petrophysical and geomechanical characteristics of Canadian tight oil and liquid-rich gas reservoirs: I. Pore network and permeability characterization. *Fuel*, 153:664–681, 2015. ISSN 00162361. doi: 10.1016/j.fuel.2015.03.020. URL <http://dx.doi.org/10.1016/j.fuel.2015.03.020>.
- Ali Ghassemi and Ali Pak. Pore scale study of permeability and tortuosity for flow through particulate media using Lattice Boltzmann method. *International Journal for Numerical and Analytical Methods in Geomechanics*, 35(8):886–901, 2011. ISSN 03639061. doi: 10.1002/nag.932.
- M. R. Giles and R. B. de Boer. Origin and significance of redistributive secondary porosity. *Marine and Petroleum Geology*, 7(4):378–397, 1990. ISSN 02648172. doi: 10.1016/0264-8172(90)90016-A.
- Jon Gluyas and Andy Leonard. Diagenesis of the Rotliegend sandstone: the answer ain’t blowin’ in the wind. *Marine and Petroleum Geology*, 12(5):491–497, 1995. ISSN 02648172. doi: 10.1016/0264-8172(95)91504-I.
- Robert Granger. *Fluid Mechanics*, volume 2. Dover Publications, New York, 2 edition, 1995. ISBN 978-0-486-68356-0.
- Jay W. Grate, Changyong Zhang, Thomas W. Wietsma, Marvin G. Warner, Norman C. Anheier, Bruce E. Bernacki, Galya Orr, and Mart Oostrom. A note on the visualization of wetting film structures and a nonwetting immiscible fluid in a pore network micromodel using a solvatochromic dye. *Water Resources Research*, 46(11), 2010. ISSN 00431397. doi: 10.1029/2010WR009419.
- Joshua Griffiths, Richard H. Worden, Luke J. Wooldridge, James E.P. Utley, Robert A. Duller, and Rhiannon L. Edge. Estuarine clay mineral distribution: Modern analogue for ancient sandstone reservoir quality prediction. *Sedimentology*, 66(6):2011–2047, 2019. ISSN 13653091. doi: 10.1111/sed.12571.
- Zongyu Gu and Martin Z. Bazant. Microscopic theory of capillary pressure hysteresis based on pore-space accessivity and radius-resolved saturation. *Chemical Engineering Science*, 196:225–246, 2019. ISSN 00092509. doi: 10.1016/j.ces.2018.10.054. URL <https://doi.org/10.1016/j.ces.2018.10.054>.
- Boyun Guo, Kai Sun, and Ali Ghalambor. *Properties of Lipids Properties of Lipids*. Gulf Publishing Company, Houston, 2008. ISBN 1-933762-32-2.
- Peijun Guo. Dependency of Tortuosity and Permeability of Porous Media on Directional Distribution of Pore Voids. *Transport in Porous Media*, 95(2):285–303, 2012. ISSN 01693913. doi: 10.1007/s11242-012-0043-8.

- P. Habisreuther, N. Djordjevic, and N. Zarzalis. Statistical distribution of residence time and tortuosity of flow through open-cell foams. *Chemical Engineering Science*, 64(23):4943–4954, 2009. ISSN 00092509. doi: 10.1016/j.ces.2009.07.033. URL <http://dx.doi.org/10.1016/j.ces.2009.07.033>.
- Sébastien Haffen, Yves Géraud, Michel Rosener, and Marc Diraison. Thermal conductivity and porosity maps for different materials: A combined case study of granite and sandstone. *Geothermics*, 66:143–150, 3 2017. ISSN 03756505. doi: 10.1016/j.geothermics.2016.12.005.
- M. R. Hall, S. P. Rigby, P. Dim, K. Bateman, S. J. Mackintosh, and C. A. Rochelle. Post-CO<sub>2</sub> injection alteration of the pore network and intrinsic permeability tensor for a Permo-Triassic sandstone. *Geofluids*, 16(2):249–263, 2016. ISSN 14688123. doi: 10.1111/gfl.12146.
- Paul S. Hammond and Evren Unsal. A Dynamic Pore Network Model for Oil Displacement by Wettability-Altering Surfactant Solution. *Transport in Porous Media*, 92(3):789–817, 2012. ISSN 01693913. doi: 10.1007/s11242-011-9933-4.
- Tongcheng Han, Angus I. Best, Jeremy Sothcott, Laurence J. North, and Lucy M. MacGregor. Relationships among low frequency (2Hz) electrical resistivity, porosity, clay content and permeability in reservoir sandstones. *Journal of Applied Geophysics*, 112:279–289, 2015. ISSN 09269851. doi: 10.1016/j.jappgeo.2014.12.006. URL <http://dx.doi.org/10.1016/j.jappgeo.2014.12.006>.
- S Hannis. Reservoir evaluation of 3 wells in the Palaeozoic of the Orcadian Basin ( UK North Sea ): Petrophysical interpretations of clay volume , porosity and Energy and Marine Geoscience Programme. *British Geological Survey Commissioned Report*, 2016.
- T. Hassenkam, C. S. Pedersen, K. Dalby, T. Austad, and S. L.S. Stipp. Pore scale observation of low salinity effects on outcrop and oil reservoir sandstone. *Colloids and Surfaces A: Physicochemical and Engineering Aspects*, 390(1-3):179–188, 2011. ISSN 18734359. doi: 10.1016/j.colsurfa.2011.09.025. URL <http://dx.doi.org/10.1016/j.colsurfa.2011.09.025>.
- Jie He, Hua Wang, Chengcheng Zhang, Xiangrong Yang, Yunfei Shangguan, Rui Zhao, Yin Gong, and Zhixiong Wu. A comprehensive analysis of the sedimentology, petrography, diagenesis and reservoir quality of sandstones from the Oligocene Xiaganchaigou (E 3 ) Formation in the Lengdong area, Qaidam Basin, China. *Journal of Petroleum Exploration and Production Technology*, 9(2): 953–969, 2019. ISSN 21900566. doi: 10.1007/s13202-018-0571-z. URL <http://dx.doi.org/10.1007/s13202-018-0571-z>.
- Johan Olav Helland, Helmer André Friis, Espen Jettestuen, and Svein M. Skjæveland. Footprints of spontaneous fluid redistribution on capillary pressure in porous rock. *Geophysical Research Letters*, 44(10):4933–4943, 2017. ISSN 19448007. doi: 10.1002/2017GL073442.
- Nasim Heydari, Mahdi Asgari, Narjes Shojai Kaveh, and Zahra Fakhroueian. Novel application of PEG/SDS interaction as a wettability modifier of hydrophobic carbonate surfaces. *Petroleum Science*, 16(2):318–327, 2019. ISSN 19958226. doi: 10.1007/s12182-018-0260-z. URL <https://doi.org/10.1007/s12182-018-0260-z>.
- Hai Hoang and Guillaume Galliero. Local viscosity of a fluid confined in a narrow pore. *Physical Review E - Statistical, Nonlinear, and Soft Matter Physics*, 86(2):1–10, 2012. ISSN 15393755. doi: 10.1103/PhysRevE.86.021202.



- Ran Holtzman. Effects of Pore-Scale Disorder on Fluid Displacement in Partially-Wettable Porous Media. *Scientific Reports*, 6(July):1–10, 2016. ISSN 20452322. doi: 10.1038/srep36221.
- F. Hubert, L. Caner, A. Meunier, and B. Lanson. Advances in characterization of soil clay mineralogy using X-ray diffraction: From decomposition to profile fitting. *European Journal of Soil Science*, 60(6):1093–1105, 2009. ISSN 13510754. doi: 10.1111/j.1365-2389.2009.01194.x.
- Katherine J. Humphry, Armand Ajdari, Alberto Fernández-Nieves, Howard A. Stone, and David A. Weitz. Suppression of instabilities in multiphase flow by geometric confinement. *Physical Review E - Statistical, Nonlinear, and Soft Matter Physics*, 79(5):1–5, 2009. ISSN 15393755. doi: 10.1103/PhysRevE.79.056310.
- Paul T. Imhoff, Geoffrey P. Thyrum, and Cass T. Miller. Dissolution fingering during the solubilization of nonaqueous phase liquids in saturated porous media 2. Experimental observations. *Water Resources Research*, 32(7):1929–1942, 7 1996. ISSN 00431397. doi: 10.1029/96WR00601.
- Yoni Israeli and Simon Emmanuel. Impact of grain size and rock composition on simulated rock weathering. *Earth Surface Dynamics*, 6(2):319–327, 2018. ISSN 2196632X. doi: 10.5194/esurf-6-319-2018.
- Antoine B. Jacquy, Mauro Cacace, Guido Blöcher, Norihiro Watanabe, and Magdalena Scheck-Wenderoth. Hydro-Mechanical Evolution of Transport Properties in Porous Media: Constraints for Numerical Simulations. *Transport in Porous Media*, 110(3):409–428, 2015. ISSN 15731634. doi: 10.1007/s11242-015-0564-z.
- Madjid Jalilavi, Mansoor Zoveidavianpoor, Farshid Attarhamed, Radzuan Junin, and Rahmat Mohsin. Artificial weathering as a function of co2 injection in pahang sandstone malaysia: Investigation of dissolution rate in surficial condition. *Scientific Reports*, 4:1–10, 2014. ISSN 20452322. doi: 10.1038/srep03645.
- Ali Javaheri, Ali Habibi, Hassan Dehghanpour, and James M. Wood. Imbibition oil recovery from tight rocks with dual-wettability behavior. *Journal of Petroleum Science and Engineering*, 167 (January):180–191, 2018. ISSN 09204105. doi: 10.1016/j.petrol.2018.01.046. URL <https://doi.org/10.1016/j.petrol.2018.01.046>.
- Z. Jiang, M. I.J. Van Dijke, K. S. Sorbie, and G. D. Couples. Representation of multiscale heterogeneity via multiscale pore networks. *Water Resources Research*, 49(9):5437–5449, 2013. ISSN 00431397. doi: 10.1002/wrcr.20304.
- Wencan Jiao, Dong Zhou, and Yetian Wang. Effects of clay content on pore structure characteristics of marine soft soil. *Water (Switzerland)*, 13(9):1–19, 2021. ISSN 20734441. doi: 10.3390/w13091160.
- V. Joekar Joekar-Niasar, S. M. Hassanizadeh, L. J. Pyrak-Nolte, and C. Berentsen. Simulating drainage and imbibition experiments in a high-porosity micromodel using an unstructured pore network model. *Water Resources Research*, 45(2):1–15, 2009. ISSN 00431397. doi: 10.1029/2007WR006641.
- Vahid Joekar-Niasar and S. Majid Hassanizadeh. Effect of fluids properties on non-equilibrium capillarity effects: Dynamic pore-network modeling. *International Journal of Multiphase Flow*, 37(2):198–214, 2011. ISSN 03019322. doi: 10.1016/j.ijmultiphaseflow.2010.09.007. URL <http://dx.doi.org/10.1016/j.ijmultiphaseflow.2010.09.007>.

- Yang Ju, Peng Liu, Dong Shuang Zhang, Jia Bin Dong, P. G. Ranjith, and Chun Chang. Prediction of preferential fluid flow in porous structures based on topological network models: Algorithm and experimental validation. *Science China Technological Sciences*, 61(8):1217–1227, 2018. ISSN 1862281X. doi: 10.1007/s11431-017-9171-x.
- Heewon Jung and Alexis Navarre-Sitchler. Physical heterogeneity control on effective mineral dissolution rates. *Geochimica et Cosmochimica Acta*, 227:246–263, 4 2018. ISSN 00167037. doi: 10.1016/j.gca.2018.02.028. URL <https://doi.org/10.1016/j.gca.2018.02.028><https://linkinghub.elsevier.com/retrieve/pii/S0016703718301108>.
- I. Kalashnikova, R. Tezaur, and C. Farhat. A discontinuous enrichment method for variable-coefficient advection-diffusion at high Péclet number. *International Journal for Numerical Methods in Engineering*, 87(1-5):309–335, 7 2011. ISSN 00295981. doi: 10.1002/nme.3058. URL <http://onlinelibrary.wiley.com/doi/10.1002/nme.3279/full><http://doi.wiley.com/10.1002/nme.3058>.
- W. Kallel, M. I. J. van Dijke, K. S. Sorbie, and R. Wood. Pore-scale modeling of wettability alteration during primary drainage. *Water Resources Research*, 53(3):1891–1907, 3 2017. ISSN 00431397. doi: 10.1002/2016WR018703. URL <http://doi.wiley.com/10.1002/2016WR018703>.
- Qinjun Kang, Li Chen, Albert J. Valocchi, and Hari S. Viswanathan. Pore-scale study of dissolution-induced changes in permeability and porosity of porous media. *Journal of Hydrology*, 517:1049–1055, 2014. ISSN 00221694. doi: 10.1016/j.jhydrol.2014.06.045. URL <http://dx.doi.org/10.1016/j.jhydrol.2014.06.045>.
- Rikan Kareem, Pablo Cubillas, Jon Gluyas, Leon Bowen, Stephen Hillier, and H. Christopher Greenwell. Multi-technique approach to the petrophysical characterization of Berea sandstone core plugs (Cleveland Quarries, USA). *Journal of Petroleum Science and Engineering*, 149(May 2016):436–455, 2017. ISSN 09204105. doi: 10.1016/j.petrol.2016.09.029.
- Muhammad Kashif, Yingchang Cao, Guanghui Yuan, Muhammad Asif, Wang Jian, Wang Zhukhun, Saif Ur Rehman, Atif Zafar, Muhammad Kamran, Orkhan Isgandarov, and Asim Falak Naz. Correction to: Sedimentological impact on reservoir quality of Es1 sandstone of Shahejie formation, Nanpu Sag, East China (Arabian Journal of Geosciences, (2019), 12, 17, (545), 10.1007/s12517-019-4671-y). *Arabian Journal of Geosciences*, 12(18), 2019. ISSN 18667538. doi: 10.1007/s12517-019-4770-9.
- Daesang Kim and W Brent Lindquist. Effects of network dissolution changes on pore-to-core upscaled reaction rates for kaolinite and anorthite reactions under acidic conditions. 49(October):7575–7586, 2013. doi: 10.1002/2013WR013667.
- Hyungsoo Kim, Zhong Zheng, and Howard A. Stone. Noncircular stable displacement patterns in a meshed porous layer. *Langmuir*, 31(20):5684–5688, 2015. ISSN 15205827. doi: 10.1021/acs.langmuir.5b00958.
- Jin Seok Kim, Ho Young Jo, and Seong Taek Yun. Visualization of gaseous and dissolved CO<sub>2</sub> migration in porous media. *Environmental Earth Sciences*, 77(8):1–14, 2018. ISSN 18666299. doi: 10.1007/s12665-018-7484-5. URL <https://doi.org/10.1007/s12665-018-7484-5>.
- Yongman Kim, Jiamin Wan, Timothy J. Kneafsey, and Tetsu K. Tokunaga. Dewetting of silica surfaces upon reactions with supercritical CO<sub>2</sub> and brine: Pore-scale studies in micromodels. *Environmental Science and Technology*, 2012. ISSN 0013936X. doi: 10.1021/es204096w.

- Brian Kirby. Passive Scalar Transport: Dispersion, Patterning, and Mixing. In *Micro- and Nanoscale Fluid Mechanics*, pages 79–96. Cambridge University Press, Cambridge, 2012. doi: 10.1017/CBO9780511760723.006. URL [https://www.cambridge.org/core/product/identifier/CBO9780511760723A034/type/book\\_part](https://www.cambridge.org/core/product/identifier/CBO9780511760723A034/type/book_part).
- Karen Kirk. Potential for storage of carbon dioxide in the rocks beneath the East Irish Sea. 2006.
- Amir H. Kohanpur, Mahsa Rahromostaqim, Albert J. Valocchi, and Muhammad Sahimi. Two-phase flow of CO<sub>2</sub>-brine in a heterogeneous sandstone: Characterization of the rock and comparison of the lattice-Boltzmann, pore-network, and direct numerical simulation methods. *Advances in Water Resources*, 135(August 2019), 2020. ISSN 03091708. doi: 10.1016/j.advwatres.2019.103469.
- Samuel Krevor, Martin J. Blunt, Sally M. Benson, Christopher H. Pentland, Catriona Reynolds, Ali Al-Menhali, and Ben Niu. Capillary trapping for geologic carbon dioxide storage - From pore scale physics to field scale implications. *International Journal of Greenhouse Gas Control*, 40: 221–237, 2015. ISSN 17505836. doi: 10.1016/j.ijggc.2015.04.006. URL <http://dx.doi.org/10.1016/j.ijggc.2015.04.006>.
- Amber T. Krummel, Sujit S. Datta, Stefan Münster, and David A. Weitz. Visualizing multiphase flow and trapped fluid configurations in a model three-dimensional porous medium. *AIChE Journal*, 59(3):1022–1029, 2013. ISSN 00011541. doi: 10.1002/aic.14005.
- Vimal Kumar, Marius Paraschivoiu, and K. D.P. Nigam. Single-phase fluid flow and mixing in microchannels. *Chemical Engineering Science*, 66(7):1329–1373, 2011. ISSN 00092509. doi: 10.1016/j.ces.2010.08.016. URL <http://dx.doi.org/10.1016/j.ces.2010.08.016>.
- Takeshi Kurotori, Christopher Zahasky, Sayed Alireza Hosseinzadeh Hejazi, Saurabh M. Shah, Sally M. Benson, and Ronny Pini. Measuring, imaging and modelling solute transport in a microporous limestone. *Chemical Engineering Science*, 196:366–383, 3 2019. ISSN 00092509. doi: 10.1016/j.ces.2018.11.001.
- Y. Kuwata and K. Suga. Large eddy simulations of pore-scale turbulent flows in porous media by the lattice Boltzmann method. *International Journal of Heat and Fluid Flow*, 55:143–157, 2015. ISSN 0142727X. doi: 10.1016/j.ijheatfluidflow.2015.05.015. URL <http://dx.doi.org/10.1016/j.ijheatfluidflow.2015.05.015>.
- J. L. Lage and B. V. Antohe. Darcy’s Experiments and the Deviation to Nonlinear Flow Regime. *Journal of Fluids Engineering*, 122(3):619–625, 9 2000. ISSN 0098-2202. doi: 10.1115/1.1287722. URL <https://doi.org/10.1115/1.1287722https://asmedigitalcollection.asme.org/fluidsengineering/article/122/3/619/447402/Darcys-Experiments-and-the-Deviation-to-Nonlinear>.
- Jin Lai, Guiwen Wang, Yu Chai, Ye Ran, and Xiaotao Zhang. Depositional and diagenetic controls on pore structure of tight gas sandstone reservoirs: Evidence from lower cretaceous bashijiqike formation in kelasu thrust belts, kuqa depression in tarim basin of West China. *Resource Geology*, 65(2):55–75, 2015. ISSN 17513928. doi: 10.1111/rge.12061.
- Giuliano M. Laudone, Christopher M. Gribble, Katie L. Jones, Hannah J. Collier, and G. Peter Matthews. Validated a priori calculation of tortuosity in porous materials including sandstone and limestone. *Chemical Engineering Science*, 131:109–117, 2015. ISSN 00092509. doi: 10.1016/j.ces.2015.03.043. URL <http://dx.doi.org/10.1016/j.ces.2015.03.043>.

- C. H. Lee and Z. T. Karpyn. Numerical Analysis of Imbibition Front Evolution in Fractured Sandstone under Capillary-Dominated Conditions. *Transport in Porous Media*, 94(1):359–383, 2012. ISSN 01693913. doi: 10.1007/s11242-012-0009-x.
- Ivan Lehoccki and Per Avseth. From cradle to grave: how burial history controls the rock-physics properties of quartzose sandstones. *Geophysical Prospecting*, 69(3):629–649, 2021. ISSN 13652478. doi: 10.1111/1365-2478.13039.
- Qiang Lei, Liehui Zhang, Hongming Tang, Yulong Zhao, Man Chen, and Chunyu Xie. Describing the Full Pore Size Distribution of Tight Sandstone and Analyzing the Impact of Clay Type on Pore Size Distribution. *Geofluids*, 2020, 2020. ISSN 14688123. doi: 10.1155/2020/5208129.
- Dacun Li and Thomas W. Engler. Literature Review on Correlations of the Non-Darcy Coefficient. In *All Days*. SPE, 5 2001. doi: 10.2118/70015-MS. URL <https://onepetro.org/SPEPBOGR/proceedings/010GR/All-010GR/Midland,Texas/133633>.
- Huan Li, Xiaofeng Du, Qingbin Wang, Xianghua Yang, Hongtao Zhu, and Feilong Wang. Formation of abnormally high porosity/permeability in deltaic sandstones (Oligocene), Bozhong depression, offshore Bohai Bay Basin, China. *Marine and Petroleum Geology*, 121(July), 2020. ISSN 02648172. doi: 10.1016/j.marpetgeo.2020.104616.
- Huigui Li, Huamin Li, Baobin Gao, Wen Wang, and Chuang Liu. Study on pore characteristics and microstructure of sandstones with different grain sizes. *Journal of Applied Geophysics*, 136: 364–371, 1 2017a. ISSN 09269851. doi: 10.1016/j.jappgeo.2016.11.015.
- Huina Li, Chongxun Pan, and Cass T. Miller. Pore-scale investigation of viscous coupling effects for two-phase flow in porous media. *Physical Review E - Statistical, Nonlinear, and Soft Matter Physics*, 72(2):1–14, 2005. ISSN 15393755. doi: 10.1103/PhysRevE.72.026705.
- J. Li, S. R. McDougall, and K. S. Sorbie. Dynamic pore-scale network model (PNM) of water imbibition in porous media. *Advances in Water Resources*, 107:191–211, 2017b. ISSN 03091708. doi: 10.1016/j.advwatres.2017.06.017.
- Z. Li, X. Sun, F. Wang, and Y. Liang. Microscopic Flow Characteristics of Fluids in Porous Medium and Its Relationship with Remaining Oil Distribution: A Case Study in Saertu Oilfield of Daqing in China. *Geofluids*, 2018, 2018. ISSN 14688123. doi: 10.1155/2018/7549831.
- Teo Lay Lian. The multiscale pore connectivity network via scaling relationship derived from a sandstone Image. *Discrete Dynamics in Nature and Society*, 2011, 2011. ISSN 10260226. doi: 10.1155/2011/487839.
- Qingyang Lin, Branko Bijeljic, Steffen Berg, Ronny Pini, Martin J. Blunt, and Samuel Krevor. Minimal surfaces in porous media: Pore-scale imaging of multiphase flow in an altered-wettability Bentheimer sandstone. *Physical Review E*, 99(6):1–13, 2019. ISSN 24700053. doi: 10.1103/PhysRevE.99.063105.
- Jiang Linsong, Liu Hongsheng, Suo Shaoyi, Xie Maozhao, Wu Dan, and Bai Minli. Pore-scale simulation of flow and turbulence characteristics in three-dimensional randomly packed beds. *Powder Technology*, 338:197–210, 2018. ISSN 1873328X. doi: 10.1016/j.powtec.2018.06.013. URL <http://dx.doi.org/10.1016/j.powtec.2018.06.013>.

- Faye Liu, Peng Lu, Chen Zhu, and Yitian Xiao. Coupled reactive flow and transport modeling of CO<sub>2</sub> sequestration in the Mt. Simon sandstone formation, Midwest U.S.A. *International Journal of Greenhouse Gas Control*, 5(2):294–307, 2011. ISSN 17505836. doi: 10.1016/j.ijggc.2010.08.008. URL <http://dx.doi.org/10.1016/j.ijggc.2010.08.008>.
- Guangfeng Liu, Hang Yin, Yifei Lan, Shixiang Fei, and Daoyong Yang. Experimental determination of dynamic pore-throat structure characteristics in a tight gas sandstone formation with consideration of effective stress. *Marine and Petroleum Geology*, 113(September 2019):104170, 2020a. ISSN 02648172. doi: 10.1016/j.marpetgeo.2019.104170. URL <https://doi.org/10.1016/j.marpetgeo.2019.104170>.
- Haihu Liu, Yonghao Zhang, and Albert J. Valocchi. Lattice boltzmann simulation of immiscible fluid displacement in porous media: Homogeneous versus heterogeneous pore network. *Physics of Fluids*, 27(5), 2015. ISSN 10897666. doi: 10.1063/1.4921611. URL <http://dx.doi.org/10.1063/1.4921611>.
- Jianliang Liu, Keyu Liu, and Xiu Huang. Effect of sedimentary heterogeneities on hydrocarbon accumulations in the Permian Shanxi Formation, Ordos Basin, China: Insight from an integrated stratigraphic forward and petroleum system modelling. *Marine and Petroleum Geology*, 76:412–431, 9 2016. ISSN 02648172. doi: 10.1016/j.marpetgeo.2016.05.028.
- Min Liu, Mehdi Shabaninejad, and Peyman Mostaghimi. Predictions of permeability, surface area and average dissolution rate during reactive transport in multi-mineral rocks. *Journal of Petroleum Science and Engineering*, 170(June):130–138, 2018. ISSN 09204105. doi: 10.1016/j.petrol.2018.06.010. URL <https://doi.org/10.1016/j.petrol.2018.06.010>.
- Min Liu, Vitalii Starchenko, Lawrence M. Anovitz, and Andrew G. Stack. Grain detachment and transport clogging during mineral dissolution in carbonate rocks with permeable grain boundaries. *Geochimica et Cosmochimica Acta*, 280:202–220, 2020b. ISSN 00167037. doi: 10.1016/j.gca.2020.04.022. URL <https://doi.org/10.1016/j.gca.2020.04.022>.
- Xuefeng Liu, Jianfu Wang, Lin Ge, Falong Hu, Chaoliu Li, Xia Li, Jun Yu, Hongjun Xu, Shuangfang Lu, and Qingzhong Xue. Pore-scale characterization of tight sandstone in Yanchang Formation Ordos Basin China using micro-CT and SEM imaging from nm- to cm-scale. *Fuel*, 209:254–264, 2017. ISSN 00162361. doi: 10.1016/j.fuel.2017.07.068. URL <http://dx.doi.org/10.1016/j.fuel.2017.07.068>.
- Zhida Liu and Yonghe Sun. Characteristics and formation process of contractional deformation bands in oil-bearing sandstones in the hinge of a fold: A case study of the Youshashan anticline, western Qaidam Basin, China. *Journal of Petroleum Science and Engineering*, 189(June 2019):106994, 2020. ISSN 09204105. doi: 10.1016/j.petrol.2020.106994. URL <https://doi.org/10.1016/j.petrol.2020.106994>.
- Marco Lommatzsch, Ulrike Exner, Susanne Gier, and Bernhard Grasemann. Dilatant shear band formation and diagenesis in calcareous, arkosic sandstones, Vienna Basin (Austria). *Marine and Petroleum Geology*, 62:144–160, 2015. ISSN 02648172. doi: 10.1016/j.marpetgeo.2015.02.002. URL <http://dx.doi.org/10.1016/j.marpetgeo.2015.02.002>.
- Xavier Lopez, Per H. Valvatne, and Martin J. Blunt. Predictive network modeling of single-phase non-Newtonian flow in porous media. *Journal of Colloid and Interface Science*, 264(1):256–265, 8 2003. ISSN 00219797. doi: 10.1016/S0021-9797(03)00310-2. URL <https://linkinghub.elsevier.com/retrieve/pii/S0021979703003102>.

- L. Luquot, O. Rodriguez, and P. Gouze. Experimental Characterization of Porosity Structure and Transport Property Changes in Limestone Undergoing Different Dissolution Regimes. *Transport in Porous Media*, 101(3):507–532, 2014. ISSN 01693913. doi: 10.1007/s11242-013-0257-4.
- Benben Ma, Yingchang Cao, and Yancong Jia. Feldspar dissolution with implications for reservoir quality in tight gas sandstones: evidence from the Eocene Es4 interval, Dongying Depression, Bohai Bay Basin, China. *Journal of Petroleum Science and Engineering*, 150(January 2016):74–84, 2017. ISSN 09204105. doi: 10.1016/j.petrol.2016.11.026. URL <http://linkinghub.elsevier.com/retrieve/pii/S092041051631049X>.
- Jin Ma, Lorenzo Querci, Bodo Hattendorf, Martin O. Saar, and Xiang Zhao Kong. Toward a Spatiotemporal Understanding of Dolomite Dissolution in Sandstone by CO<sub>2</sub>-Enriched Brine Circulation. *Environmental Science and Technology*, 53(21):12458–12466, 2019. ISSN 15205851. doi: 10.1021/acs.est.9b04441.
- Jin Ma, Lorenzo Querci, Bodo Hattendorf, Martin O. Saar, and Xiang Zhao Kong. The Effect of Mineral Dissolution on the Effective Stress Law for Permeability in a Tight Sandstone. *Geophysical Research Letters*, 47(15):1–9, 2020. ISSN 19448007. doi: 10.1029/2020GL088346.
- P. Macini, E. Mesini, and R. Viola. Laboratory measurements of non-Darcy flow coefficients in natural and artificial unconsolidated porous media. *Journal of Petroleum Science and Engineering*, 77(3-4):365–374, 2011. ISSN 09204105. doi: 10.1016/j.petrol.2011.04.016.
- Nariman Mahabadi, Leon Van Paassen, Ilenia Battiato, Tae Sup Yun, Hyunwook Choo, and Jaewon Jang. Impact of Pore-Scale Characteristics on Immiscible Fluid Displacement. *Geofluids*, 2020: 1–10, 2020. ISSN 14688123. doi: 10.1155/2020/5759023.
- Syed A. Mahmud, Mike W. Hall, and Khalid A. Almalki. Mineralogy and spectroscopy of Owen Group sandstones, Australia: implications for the provenance, diagenesis, and origin of coloration. *Geosciences Journal*, 22(5):765–776, 2018. ISSN 15987477. doi: 10.1007/s12303-017-0079-4.
- Papa O. Mangane, Philippe Gouze, and Linda Luquot. Permeability impairment of a limestone reservoir triggered by heterogeneous dissolution and particles migration during CO<sub>2</sub>-rich injection. *Geophysical Research Letters*, 40(17):4614–4619, 2013. ISSN 19448007. doi: 10.1002/grl.50595.
- L. Martinelli, S. Talvy, S. Liégeois, A. Vanden Berghe, Eric Chauveheid, and B. Haut. Single-phase flow model development for macroscopic liquid flow evaluation in gas-liquid reactors, by computational fluid dynamics. *Chemical Engineering Science*, 66(14):3369–3376, 2011. ISSN 00092509. doi: 10.1016/j.ces.2011.01.031.
- Edgar G. Martínez-Mendoza, Martín A. Díaz-Viera, Manuel Coronado, and Ana T. Mendoza-Rosas. Capillary pressure and relative permeability estimation for low salinity waterflooding processes using pore network models. *Journal of Petroleum Science and Engineering*, 182(April):106253, 2019. ISSN 09204105. doi: 10.1016/j.petrol.2019.106253. URL <https://doi.org/10.1016/j.petrol.2019.106253>.
- D. Matmon and N. J. Hayden. Pore space analysis of NAPL distribution in sand-clay media. *Advances in Water Resources*, 26(7):773–785, 2003. ISSN 03091708. doi: 10.1016/S0309-1708(03)00032-0.
- S. R. McDougall, A. B. Dixit, and K. S. Sorbie. Network analogues of wettability at the pore scale. *Geological Society Special Publication*, 122(122):19–35, 1997. ISSN 03058719. doi: 10.1144/GSL.SP.1997.122.01.03.

- Neil S. Meadows. The correlation and sequence architecture of the Ormskirk Sandstone Formation in the Triassic Sherwood Sandstone Group of the East Irish Sea Basin, NW England. *Geological Journal*, 41(1):93–122, 2006. ISSN 00721050. doi: 10.1002/gj.1034.
- E. F. Medici and J. S. Allen. Existence of the phase drainage diagram in proton exchange membrane fuel cell fibrous diffusion media. *Journal of Power Sources*, 191(2):417–427, 2009. ISSN 03787753. doi: 10.1016/j.jpowsour.2009.02.050.
- G. Medici, K. Boulesteix, N. P. Mountney, L. J. West, and N. E. Odling. Palaeoenvironment of braided fluvial systems in different tectonic realms of the Triassic Sherwood Sandstone Group, UK. *Sedimentary Geology*, 329:188–210, 2015. ISSN 00370738. doi: 10.1016/j.sedgeo.2015.09.012. URL <http://dx.doi.org/10.1016/j.sedgeo.2015.09.012>.
- G. Medici, L. J. West, and N. P. Mountney. Characterizing flow pathways in a sandstone aquifer: Tectonic vs sedimentary heterogeneities. *Journal of Contaminant Hydrology*, 194:36–58, 11 2016. ISSN 18736009. doi: 10.1016/j.jconhyd.2016.09.008.
- Giacomo Medici, L. Jared West, Nigel P. Mountney, and Michael Welch. Permeability of rock discontinuities and faults in the Triassic Sherwood Sandstone Group (UK): insights for management of fluvio-aeolian aquifers worldwide. *Hydrogeology Journal*, 27(8):2835–2855, 2019. ISSN 14350157. doi: 10.1007/s10040-019-02035-7.
- A. H. Meghdadi Isfahani and Masoud Afrand. Experiment and Lattice Boltzmann numerical study on nanofluids flow in a micromodel as porous medium. *Physica E: Low-Dimensional Systems and Nanostructures*, 2017. ISSN 13869477. doi: 10.1016/j.physe.2017.07.008.
- Yashar Mehmani and Hamdi A. Tchelepi. Multiscale computation of pore-scale fluid dynamics: Single-phase flow. *Journal of Computational Physics*, 375:1469–1487, 2018. ISSN 10902716. doi: 10.1016/j.jcp.2018.08.045. URL <https://doi.org/10.1016/j.jcp.2018.08.045>.
- Ziyuan Meng, Wei Sun, Yiqun Liu, Bin Luo, and Minru Zhao. Effect of pore networks on the properties of movable fluids in tight sandstones from the perspective of multi-techniques. *Journal of Petroleum Science and Engineering*, 201(December 2020):108449, 2021. ISSN 09204105. doi: 10.1016/j.petrol.2021.108449. URL <https://doi.org/10.1016/j.petrol.2021.108449>.
- Hannah Menke, Branko Bijeljic, Matthew Andrew, and Martin J. Blunt. Dynamic pore-scale imaging of reactive transport in heterogeneous carbonates at reservoir conditions. *Energy Procedia*, 63: 5503–5511, 2014. ISSN 18766102. doi: 10.1016/j.egypro.2014.11.583. URL <http://dx.doi.org/10.1016/j.egypro.2014.11.583>.
- L. I. Mi, Yinghai Guo, L. I. Zhuangfu, Huaichang Wang, and Jingxia Zhang. Pore-Throat Combination Types and Gas-Water Relative Permeability Responses of Tight Gas Sandstone Reservoirs in the Zizhou Area of East Ordos Basin, China. *Acta Geologica Sinica*, 93(3):622–636, 2019. ISSN 17556724. doi: 10.1111/1755-6724.13872.
- Purna Chandra Mishra, Sayantan Mukherjee, Santosh Kumar Nayak, and Arabind Panda. A brief review on viscosity of nanofluids. *International Nano Letters*, 4(4):109–120, 2014. ISSN 2008-9295. doi: 10.1007/s40089-014-0126-3.
- Ibrahim Mohamed Mohamed, Jia He, and Hisham A. Nasr-El-Din. Carbon Dioxide Sequestration in Sandstone Aquifers: How Does It Affect the Permeability? In *Carbon Management Technology Conference*. Carbon Management Technology Conference, 4 2012. doi: 10.7122/149958-MS. URL <http://www.onepetro.org/doi/10.7122/149958-MS>.

- Nicolaas Molenaar, Marita Felder, Kristian Bär, and Annette E. Götz. What classic greywacke (litharenite) can reveal about feldspar diagenesis: An example from Permian Rotliegend sandstone in Hessen, Germany. *Sedimentary Geology*, 326:79–93, 2015. ISSN 00370738. doi: 10.1016/j.sedgeo.2015.07.002. URL <http://dx.doi.org/10.1016/j.sedgeo.2015.07.002>.
- Sergi Molins, David Trebotich, Gregory H. Miller, and Carl I. Steefel. Mineralogical and transport controls on the evolution of porous media texture using direct numerical simulation. *Water Resources Research*, 53(5):3645–3661, 5 2017. ISSN 00431397. doi: 10.1002/2016WR020323. URL <https://onlinelibrary.wiley.com/doi/10.1111/j.1752-1688.1969.tb04897.xhttps://doi.wiley.com/10.1002/2016WR020323>.
- Mai Britt E. Mørk and Kari Moen. Compaction microstructures in quartz grains and quartz cement in deeply buried reservoir sandstones using combined petrography and EBSD analysis. *Journal of Structural Geology*, 29(11):1843–1854, 2007. ISSN 01918141. doi: 10.1016/j.jsg.2007.08.004.
- Jianye Mou, Lei Wang, Shicheng Zhang, Xinfang Ma, and Boyang Li. A Research on the Effect of Heterogeneities on Sandstone Matrix Acidizing Performance. *Geofluids*, 2019, 2019. ISSN 14688123. doi: 10.1155/2019/6328909.
- Bagus P. Muljadi, Martin J. Blunt, Ali Q. Raeini, and Branko Bijeljic. The impact of porous media heterogeneity on non-Darcy flow behaviour from pore-scale simulation. *Advances in Water Resources*, 95:329–340, 9 2016. ISSN 03091708. doi: 10.1016/j.advwatres.2015.05.019.
- Meiheriayi Mutailipu, Yu Liu, Lanlan Jiang, and Yi Zhang. Measurement and estimation of CO<sub>2</sub>-brine interfacial tension and rock wettability under CO<sub>2</sub> sub- and super-critical conditions. *Journal of Colloid and Interface Science*, 534:605–617, 2019. ISSN 10957103. doi: 10.1016/j.jcis.2018.09.031. URL <https://doi.org/10.1016/j.jcis.2018.09.031>.
- Bassem S. Nabawy, Pierre Rochette, and Yves Géraud. Petrophysical and magnetic pore network anisotropy of some cretaceous sandstone from Tushka Basin, Egypt. *Geophysical Journal International*, 177(1):43–61, 2009. ISSN 0956540X. doi: 10.1111/j.1365-246X.2008.04061.x.
- Fadi H. Nader, France Champenois, Mickaël Barbier, Mathilde Adelinet, Elisabeth Rosenberg, Pascal Houel, Jocelyne Delmas, and Rudy Swennen. Diagenetic effects of compaction on reservoir properties: The case of early callovian “Dalle Nacrée” formation (Paris basin, France). *Journal of Geodynamics*, 101:5–29, 2016. ISSN 02643707. doi: 10.1016/j.jog.2016.05.010. URL <http://dx.doi.org/10.1016/j.jog.2016.05.010>.
- John W. Neasham. The Morphology Of Dispersed Clay In Sandstone Reservoirs And Its Effect On Sandstone Shaliness, Pore Space And Fluid Flow Properties. In *All Days*. SPE, 10 1977. doi: 10.2118/6858-MS. URL <https://onepetro.org/SPEATCE/proceedings/77SPE/All-77SPE/Denver,Colorado/138627>.
- Philip H. Nelson. Pore-throat sizes in sandstones, tight sandstones, and shales. *AAPG Bulletin*, 93(3):329–340, 2009. ISSN 01491423. doi: 10.1306/10240808059.
- Ramin Nemati, Javad Rahbar Shahrouzi, and Reza Alizadeh. A stochastic approach for predicting tortuosity in porous media via pore network modeling. *Computers and Geotechnics*, 120 (September 2019):103406, 2020. ISSN 18737633. doi: 10.1016/j.compgeo.2019.103406. URL <https://doi.org/10.1016/j.compgeo.2019.103406>.



- Catherine Noiriél and Damien Daval. Pore-Scale Geochemical Reactivity Associated with CO<sub>2</sub> Storage: New Frontiers at the Fluid-Solid Interface. *Accounts of Chemical Research*, 50(4):759–768, 2017. ISSN 15204898. doi: 10.1021/acs.accounts.7b00019.
- Denis M. O’Carroll, Kevin G. Mumford, Linda M. Abriola, and Jason I. Gerhard. Influence of wettability variations on dynamic effects in capillary pressure. *Water Resources Research*, 46(8): 1–13, 2010. ISSN 00431397. doi: 10.1029/2009WR008712.
- Ovie B. Ogbe. Reservoir sandstone grain-size distributions: Implications for sequence stratigraphic and reservoir depositional modelling in Otovwe field, onshore Niger Delta Basin, Nigeria. *Journal of Petroleum Science and Engineering*, 203(March):108639, 8 2021. ISSN 09204105. doi: 10.1016/j.petrol.2021.108639. URL <https://doi.org/10.1016/j.petrol.2021.108639><https://linkinghub.elsevier.com/retrieve/pii/S0920410521002990>.
- S. R. Ogilvie, J. M. Orribo, and P. W.J. Glover. The influence of deformation bands upon fluid flow using profile permeametry and positron emission tomography. *Geophysical Research Letters*, 28(1):61–64, 2001. ISSN 00948276. doi: 10.1029/2000GL008507.
- Mette Olivarius, Rikke Weibel, Henrik Friis, Lars Ole Boldreel, Morten Leth Hjuler, Lars Kristensen, Claus Kjøller, and Lars H. Mathiesen, Anders Nielsen. Diagenesis, provenance and depositional environments of the Bunter Sandstone Formation: Detailed interpretation of reservoir quality using a combined approach. In *31st IAS Meeting of Sedimentology*, 2015a.
- Mette Olivarius, Rikke Weibel, Morten L. Hjuler, Lars Kristensen, Anders Mathiesen, Lars H. Nielsen, and Claus Kjøller. Diagenetic effects on porosity-permeability relationships in red beds of the Lower Triassic Bunter Sandstone Formation in the North German Basin. *Sedimentary Geology*, 321:139–153, 2015b. ISSN 00370738. doi: 10.1016/j.sedgeo.2015.03.003. URL <http://dx.doi.org/10.1016/j.sedgeo.2015.03.003>.
- Elaine Baroni Oliveira and João Luiz Nicolodi. Oil permeability variations on lagoon sand beaches in the Patos-Guaíba system in Rio Grande do Sul, Brazil. *Marine Pollution Bulletin*, 115(1-2): 154–163, 2017. ISSN 18793363. doi: 10.1016/j.marpolbul.2016.12.020. URL <http://dx.doi.org/10.1016/j.marpolbul.2016.12.020>.
- Michael U. Onoja and Seyed M. Shariatipour. The impact of gradational contact at the reservoir-seal interface on geological CO<sub>2</sub> storage capacity and security. *International Journal of Greenhouse Gas Control*, 72(March):1–13, 2018. ISSN 17505836. doi: 10.1016/j.ijggc.2018.03.007. URL <https://doi.org/10.1016/j.ijggc.2018.03.007>.
- M. Oostrom, Y. Mehmani, P. Romero-Gomez, Y. Tang, H. Liu, H. Yoon, Q. Kang, V. Joekar-Niasar, M. T. Balhoff, T. Dewers, G. D. Tartakovsky, E. A. Leist, N. J. Hess, W. A. Perkins, C. L. Rakowski, M. C. Richmond, J. A. Serkowski, C. J. Werth, A. J. Valocchi, T. W. Wietsma, and C. Zhang. Pore-scale and continuum simulations of solute transport micromodel benchmark experiments. *Computational Geosciences*, 20(4):857–879, 2016. ISSN 15731499. doi: 10.1007/s10596-014-9424-0.
- L. Orgéas, Z. Idris, C. Geindreau, J. F. Bloch, and J. L. Auriault. Modelling the flow of power-law fluids through anisotropic porous media at low-pore Reynolds number. *Chemical Engineering Science*, 61(14):4490–4502, 2006. ISSN 00092509. doi: 10.1016/j.ces.2006.01.046.

- Holger Ott and Sjaam Oedai. Wormhole formation and compact dissolution in single- and two-phase CO<sub>2</sub>-brine injections. *Geophysical Research Letters*, 42(7):2270–2276, 2015. ISSN 19448007. doi: 10.1002/2015GL063582.
- Arnab Kumat Pal, Siddharth Garia, Ravi Karangat, and Archana M Nair. Influence of packing grain particles on porosity. 2018.
- Nikhil Kumar Palakurthi, Santosh Konangi, Aravind Kishore, Ken Comer, and Urmila Ghia. Prediction of capillary pressure-saturation relationship for primary drainage in a 3D fibrous porous medium using volume-of-fluid method. *European Journal of Mechanics, B/Fluids*, 67:357–365, 2018. ISSN 09977546. doi: 10.1016/j.euromechflu.2017.10.008. URL <https://doi.org/10.1016/j.euromechflu.2017.10.008>.
- Hapnsgeorg Pape, Christoph Clauser, and Joachim Iffland. Variation of permeability with porosity in sandstone diagenesis interpreted with a fractal pore space model. *Pure and Applied Geophysics*, 157(4):603–619, 2000. ISSN 00334553. doi: 10.1007/978-3-0348-8430-3{\\_}8.
- A. Parmigiani, C. Huber, O. Bachmann, and B. Chopard. Pore-scale mass and reactant transport in multiphase porous media flows. *Journal of Fluid Mechanics*, 686:40–76, 2011. ISSN 0022-1120. doi: 10.1017/jfm.2011.268. URL [http://www.journals.cambridge.org/abstract\\_S0022112011002680](http://www.journals.cambridge.org/abstract_S0022112011002680).
- Anna E. Peksa, Karl Heinz A.A. Wolf, and Pacelli L.J. Zitha. Bentheimer sandstone revisited for experimental purposes. *Marine and Petroleum Geology*, 67:701–719, 2015. ISSN 02648172. doi: 10.1016/j.marpetgeo.2015.06.001. URL <http://dx.doi.org/10.1016/j.marpetgeo.2015.06.001>.
- Sheng Peng, Qinhong Hu, Stefan Dultz, and Ming Zhang. Using X-ray computed tomography in pore structure characterization for a Berea sandstone: Resolution effect. *Journal of Hydrology*, 472-473:254–261, 2012. ISSN 00221694. doi: 10.1016/j.jhydrol.2012.09.034. URL <http://dx.doi.org/10.1016/j.jhydrol.2012.09.034>.
- Sheng Peng, Federica Marone, and Stefan Dultz. Resolution effect in X-ray microcomputed tomography imaging and small pore’s contribution to permeability for a Berea sandstone. *Journal of Hydrology*, 510:403–411, 2014. ISSN 00221694. doi: 10.1016/j.jhydrol.2013.12.028. URL <http://dx.doi.org/10.1016/j.jhydrol.2013.12.028>.
- Renee J. Perez and James R. Boles. Interpreting fracture development from diagenetic mineralogy and thermoelastic contraction modeling. *Tectonophysics*, 400(1-4):179–207, 2005. ISSN 00401951. doi: 10.1016/j.tecto.2005.03.002.
- Christian L. Perrin, Philippe M.J. Tardy, Ken S. Sorbie, and John C. Crawshaw. Experimental and modeling study of Newtonian and non-Newtonian fluid flow in pore network micromodels. *Journal of Colloid and Interface Science*, 2006. ISSN 00219797. doi: 10.1016/j.jcis.2005.09.012.
- D. Petrak and H. Rauh. Micro-flow metering and viscosity measurement of low viscosity Newtonian fluids using a fibreoptical spatial filter technique. *Flow Measurement and Instrumentation*, 20(2): 49–56, 2009. ISSN 09555986. doi: 10.1016/j.flowmeasinst.2008.12.005. URL <http://dx.doi.org/10.1016/j.flowmeasinst.2008.12.005>.
- Sven Philit, Roger Soliva, Gregory Ballas, and Haakon Fossen. Grain Deformation Processes in Porous Quartz Sandstones - Insight from the Clusters of Cataclastic Deformation Bands. *EPJ Web of Conferences*, 140(1):3–6, 2017. ISSN 2100014X. doi: 10.1051/epjconf/201714007002.

- Ronny Pini and Sally M. Benson. Characterization and scaling of mesoscale heterogeneities in sandstones. *Geophysical Research Letters*, 40(15):3903–3908, 8 2013. ISSN 00948276. doi: 10.1002/grl.50756.
- Ronny Pini, Nicholas T. Vandehey, Jennifer Druhan, James P. O’Neil, and Sally M. Benson. Quantifying solute spreading and mixing in reservoir rocks using 3-D PET imaging. *Journal of Fluid Mechanics*, 796:558–587, 6 2016. ISSN 14697645. doi: 10.1017/jfm.2016.262.
- Alexis A. Porubcan and Shangping Xu. Colloid straining within saturated heterogeneous porous media. *Water Research*, 45(4):1796–1806, 2011. ISSN 00431354. doi: 10.1016/j.watres.2010.11.037. URL <http://dx.doi.org/10.1016/j.watres.2010.11.037>.
- Jorge M.V. Prior, Iolanda Almeida, and José M. Loureiro. Prediction of the packing porosity of mixtures of spherical and non-spherical particles with a geometric model. *Powder Technology*, 249:482–496, 2013. ISSN 00325910. doi: 10.1016/j.powtec.2013.09.006. URL <http://dx.doi.org/10.1016/j.powtec.2013.09.006>.
- Dieter Pudlo, Daniel Albrecht, Leonhard Ganzer, Reinhard Gaupp, Bernd Kohlhepp, Robert Meyer, Viktor Reitenbach, and Joachim Wienand. Petrophysical, facies and mineralogical-geochemical investigations of rotliegend sandstones from the Altmark natural gas field in central Germany. *Energy Procedia*, 4:4648–4655, 2011. ISSN 18766102. doi: 10.1016/j.egypro.2011.02.425. URL <http://dx.doi.org/10.1016/j.egypro.2011.02.425>.
- Dieter Pudlo, Viktor Reitenbach, Daniel Albrecht, Leonhard Ganzer, Ulrich Gernert, Joachim Wienand, Bernd Kohlhepp, and Reinhard Gaupp. The impact of diagenetic fluid-rock reactions on Rotliegend sandstone composition and petrophysical properties (Altmark area, central Germany). *Environmental Earth Sciences*, 67(2):369–384, 9 2012. ISSN 18666280. doi: 10.1007/s12665-012-1723-y.
- Yu Qi, Yiwen Ju, Cheng Huang, Hongjian Zhu, Yuan Bao, Jianguang Wu, Shangzhi Meng, and Wangang Chen. Influences of organic matter and kaolinite on pore structures of transitional organic-rich mudstone with an emphasis on S2 controlling specific surface area. *Fuel*, 237(August 2018):860–873, 2019. ISSN 00162361. doi: 10.1016/j.fuel.2018.10.048.
- Juncheng Qiao, Jianhui Zeng, Shu Jiang, and Yanu Wang. Impacts of sedimentology and diagenesis on pore structure and reservoir quality in tight oil sandstone reservoirs: Implications for macroscopic and microscopic heterogeneities. *Marine and Petroleum Geology*, 111:279–300, 1 2020. ISSN 02648172. doi: 10.1016/j.marpetgeo.2019.08.008.
- Y. Qiao, P. Andersen, S. Evje, and D. C. Standnes. A mixture theory approach to model co- and counter-current two-phase flow in porous media accounting for viscous coupling. *Advances in Water Resources*, 112(July 2017):170–188, 2018. ISSN 03091708. doi: 10.1016/j.advwatres.2017.12.016. URL <https://doi.org/10.1016/j.advwatres.2017.12.016>.
- Chao Zhong Qin, Bo Guo, Michael Celia, and Rui Wu. Dynamic pore-network modeling of air-water flow through thin porous layers. *Chemical Engineering Science*, 202:194–207, 2019. ISSN 00092509. doi: 10.1016/j.ces.2019.03.038. URL <https://doi.org/10.1016/j.ces.2019.03.038>.
- Mohammad Adnan Quasim, Shaista Khan, Vineet Kumar Srivastava, Asma Amjad Ghaznavi, and Abul Hasnat Masood Ahmad. Role of cementation and compaction in controlling the reservoir quality of the Middle to Late Jurassic Sandstones, Jara dome, Kachchh Basin, western India. *Geological Journal*, 56(2):976–994, 2021. ISSN 10991034. doi: 10.1002/gj.3989.

- Harris Sajjad Rabbani, Benzhong Zhao, Ruben Juanes, and Nima Shokri. Pore geometry control of apparent wetting in porous media. *Scientific Reports*, 8(1):1–8, 2018. ISSN 20452322. doi: 10.1038/s41598-018-34146-8. URL <http://dx.doi.org/10.1038/s41598-018-34146-8>.
- Ali Q. Raeini, Branko Bijeljic, and Martin J. Blunt. Modelling capillary trapping using finite-volume simulation of two-phase flow directly on micro-CT images. *Advances in Water Resources*, 83:102–110, 2015. ISSN 03091708. doi: 10.1016/j.advwatres.2015.05.008. URL <http://dx.doi.org/10.1016/j.advwatres.2015.05.008>.
- A Raoof, H M Nick, S M Hassanizadeh, and C J Spiers. Computers & Geosciences PoreFlow : A complex pore-network model for simulation of reactive transport in variably saturated porous media. *Computers and Geosciences*, 61:160–174, 2013. ISSN 0098-3004. doi: 10.1016/j.cageo.2013.08.005. URL <http://dx.doi.org/10.1016/j.cageo.2013.08.005>.
- Seyed Omid Rastegar and Tingyue Gu. Empirical correlations for axial dispersion coefficient and Peclet number in fixed-bed columns. *Journal of Chromatography A*, 1490:133–137, 2017. ISSN 18733778. doi: 10.1016/j.chroma.2017.02.026. URL <http://dx.doi.org/10.1016/j.chroma.2017.02.026>.
- T. D. Rathnaweera, P. G. Ranjith, and M. S.A. Perera. Effect of Salinity on Effective CO<sub>2</sub> Permeability in Reservoir Rock Determined by Pressure Transient Methods: an Experimental Study on Hawkesbury Sandstone. *Rock Mechanics and Rock Engineering*, 48(5):2093–2110, 9 2015. ISSN 07232632. doi: 10.1007/s00603-014-0671-0.
- T. D. Rathnaweera, P. G. Ranjith, and M. S.A. Perera. Experimental investigation of geochemical and mineralogical effects of CO<sub>2</sub> sequestration on flow characteristics of reservoir rock in deep saline aquifers. *Scientific Reports*, 6(December 2015):1–12, 2016. ISSN 20452322. doi: 10.1038/srep19362.
- Simona Regenspurg, Elvira Feldbusch, Ben Norden, and Marion Tichomirowa. Fluid-rock interactions in a geothermal Rotliegend/Permo-Carboniferous reservoir (North German Basin). *Applied Geochemistry*, 69:12–27, 2016. ISSN 18729134. doi: 10.1016/j.apgeochem.2016.03.010. URL <http://dx.doi.org/10.1016/j.apgeochem.2016.03.010>.
- Stephanie Rehrmann, Carita Augustsson, Rocio Nereyda Izaguirre Valdez, Uwe Jenchen, and Peter Schulte. Provenance and depositional conditions of Cretaceous-Paleogene boundary sandstones from northeastern Mexico. *Sedimentary Geology*, 282:321–335, 2012. ISSN 00370738. doi: 10.1016/j.sedgeo.2012.10.002. URL <http://dx.doi.org/10.1016/j.sedgeo.2012.10.002>.
- André Revil, Kristof Koch, and Klaus Holliger. Is it the grain size or the characteristic pore size that controls the induced polarization relaxation time of clean sands and sandstones? *Water Resources Research*, 48(5), 5 2012. ISSN 00431397. doi: 10.1029/2011WR011561. URL <http://doi.wiley.com/10.1029/2011WR011561>.
- Catriona Reynolds, Martin Blunt, and Sam Krevor. Impact of reservoir conditions on CO<sub>2</sub>-brine relative permeability in sandstones. *Energy Procedia*, 63:5577–5585, 2014. ISSN 18766102. doi: 10.1016/j.egypro.2014.11.591. URL <http://dx.doi.org/10.1016/j.egypro.2014.11.591>.
- Catriona A. Reynolds, Hannah Menke, Matthew Andrew, Martin J. Blunt, and Samuel Krevor. Dynamic fluid connectivity during steady-state multiphase flow in a sandstone. *Proceedings of the National Academy of Sciences*, 114(31):8187–8192, 2017. ISSN 0027-8424. doi: 10.1073/pnas.1702834114. URL <http://www.pnas.org/lookup/doi/10.1073/pnas.1702834114>.

- Luke S. Rijfkoogel, Behzad Ghanbarian, Qinhong Hu, and Hui Hai Liu. Clarifying pore diameter, pore width, and their relationship through pressure measurements: A critical study. *Marine and Petroleum Geology*, 107(May):142–148, 2019. ISSN 02648172. doi: 10.1016/j.marpetgeo.2019.05.019. URL <https://doi.org/10.1016/j.marpetgeo.2019.05.019>.
- Béatrice Rivière. *Discontinuous Galerkin Methods for Solving Elliptic and Parabolic Equations*. Society for Industrial and Applied Mathematics, 1 2008. ISBN 978-0-89871-656-6. doi: 10.1137/1.9780898717440. URL <http://epubs.siam.org/doi/book/10.1137/1.9780898717440>.
- R. Roded, E. Aharonov, R. Holtzman, and P. Szymczak. Reactive Flow and Homogenization in Anisotropic Media. *Water Resources Research*, 56(12):1–22, 2020. ISSN 19447973. doi: 10.1029/2020WR027518.
- Antonio Rodríguez de Castro, Mehrez Agnaou, Azita Ahmadi-Sénichault, and Abdelaziz Omari. Application of Non-toxic Yield Stress Fluids Porosimetry Method and Pore-Network Modelling to Characterize the Pore Size Distribution of Packs of Spherical Beads. *Transport in Porous Media*, 130(3):799–818, 2019. ISSN 15731634. doi: 10.1007/s11242-019-01339-2. URL <https://doi.org/10.1007/s11242-019-01339-2>.
- Antonio Rodríguez de Castro, Mehrez Agnaou, Azita Ahmadi-Sénichault, and Abdelaziz Omari. Numerical porosimetry: Evaluation and comparison of yield stress fluids method, mercury intrusion porosimetry and pore network modelling approaches. *Computers and Chemical Engineering*, 133, 2020. ISSN 00981354. doi: 10.1016/j.compchemeng.2019.106662.
- Esther Rosenbrand, Ida Lykke Fabricius, and Hao Yuan. Thermally induced permeability reduction due to particle migration in sandstones: the effect of temperature on kaolinite mobilisation and aggregation. *Thirty-Seventh Workshop on Geothermal Reservoir Engineering*, (January):9, 2012.
- Esther Rosenbrand, Ida Lykke Fabricius, Quentin Fisher, and Carlos Grattoni. Permeability in Rotliegendes gas sandstones to gas and brine as predicted from NMR, mercury injection and image analysis. *Marine and Petroleum Geology*, 64:189–202, 2015. ISSN 02648172. doi: 10.1016/j.marpetgeo.2015.02.009.
- William R. Rossen. A critical review of Roof snap-off as a mechanism of steady-state foam generation in homogeneous porous media. *Colloids and Surfaces A: Physicochemical and Engineering Aspects*, 225(1-3):1–24, 2003. ISSN 09277757. doi: 10.1016/S0927-7757(03)00309-1.
- M. Rücker, W. B. Bartels, G. Garfi, M. Shams, T. Bultreys, M. Boone, S. Pieterse, G. C. Maitland, S. Krevor, V. Cnudde, H. Mahani, S. Berg, A. Georgiadis, and P. F. Luckham. Relationship between wetting and capillary pressure in a crude oil/brine/rock system: From nano-scale to core-scale. *Journal of Colloid and Interface Science*, 562:159–169, 2020. ISSN 10957103. doi: 10.1016/j.jcis.2019.11.086.
- L. C. Ruspini, R. Farokhpoor, and P. E. Øren. Pore-scale modeling of capillary trapping in water-wet porous media: A new cooperative pore-body filling model. *Advances in Water Resources*, 108: 1–14, 2017. ISSN 03091708. doi: 10.1016/j.advwatres.2017.07.008. URL <https://doi.org/10.1016/j.advwatres.2017.07.008>.
- Mollie S. Sabo and Lauren E. Beckingham. Porosity-Permeability Evolution During Simultaneous Mineral Dissolution and Precipitation. *Water Resources Research*, 57(6):1–15, 2021. ISSN 19447973. doi: 10.1029/2020WR029072.

- Mohammad Amin Sadeghi, Mehrez Agnaou, Jake Barralet, and Jeff Gostick. Dispersion modeling in pore networks: A comparison of common pore-scale models and alternative approaches. *Journal of Contaminant Hydrology*, 228(August 2019):103578, 2020. ISSN 18736009. doi: 10.1016/j.jconhyd.2019.103578. URL <https://doi.org/10.1016/j.jconhyd.2019.103578>.
- Giuseppe D. Saldi, Marco Voltolini, and Kevin G. Knauss. Effects of surface orientation, fluid chemistry and mechanical polishing on the variability of dolomite dissolution rates. *Geochimica et Cosmochimica Acta*, 206:94–111, 6 2017. ISSN 00167037. doi: 10.1016/j.gca.2017.02.007.
- Hilmi S Salem. Derivation of the Cementation Factor (Archie’s Exponents) and the Kozeney–Carman Constant from Well Log Data and Dependence on Lithology and Other Physical Parameters. *SPE Paper*, 26309, 1993.
- Abdolhamid Sameni, Peyman Pourafshary, Milad Ghanbarzadeh, and Shahab Ayatollahi. Effect of nanoparticles on clay swelling and migration. *Egyptian Journal of Petroleum*, 24(4):429–437, 2015. ISSN 20902468. doi: 10.1016/j.ejpe.2015.10.006. URL <http://dx.doi.org/10.1016/j.ejpe.2015.10.006>.
- Xavier Sanchez-Vila, Marco Dentz, and Leonardo David Donado. Transport-controlled reaction rates under local non-equilibrium conditions. *Geophysical Research Letters*, 34(10):1–5, 2007. ISSN 00948276. doi: 10.1029/2007GL029410.
- Soheil Saraji, Lamia Goual, Mohammad Piri, and Henry Plancher. Wettability of supercritical carbon dioxide/water/quartz systems: Simultaneous measurement of contact angle and interfacial tension at reservoir conditions. *Langmuir*, 29(23):6856–6866, 2013. ISSN 07437463. doi: 10.1021/la3050863.
- Minoru Sato, Kamran Panaghi, Naoki Takada, and Mikio Takeda. Effect of Bedding Planes on the Permeability and Diffusivity Anisotropies of Berea Sandstone. *Transport in Porous Media*, 127(3):587–603, 2019. ISSN 1573-1634. doi: 10.1007/s11242-018-1214-z. URL <https://doi.org/10.1007/s11242-018-1214-z>.
- S. G. Sayegh, F. F. Krause, Marcel Girard, and Cornelius DeBree. Rock/fluid interactions of carbonated brines in a sandstone reservoir Pembina Cardium, Alberta, Canada. *SPE Formation Evaluation*, 5(4):399–405, 1990. ISSN 0885923X. doi: 10.2118/19392-PA.
- S. Schmid, R. H. Worden, and Q. J. Fisher. Diagenesis and reservoir quality of the Sherwood Sandstone (Triassic), Corrib Field, Slyne Basin, west of Ireland. *Marine and Petroleum Geology*, 21(3):299–315, 2004. ISSN 02648172. doi: 10.1016/j.marpetgeo.2003.11.015.
- Susanne Schmid, Richard H. Worden, and Quentin J. Fisher. Sedimentary facies and the context of dolocrete in the Lower Triassic Sherwood Sandstone group: Corrib Field west of Ireland. *Sedimentary Geology*, 187(3-4):205–227, 2006. ISSN 00370738. doi: 10.1016/j.sedgeo.2005.12.028.
- Mayka Schmitt, Celso Peres Fernandes, Fabiano G. Wolf, José A. Bellini da Cunha Neto, Christoffer P. Rahner, and Viviane Sampaio Santiago dos Santos. Characterization of Brazilian tight gas sandstones relating permeability and Angstrom-to micron-scale pore structures. *Journal of Natural Gas Science and Engineering*, 27:785–807, 2015a. ISSN 18755100. doi: 10.1016/j.jngse.2015.09.027.
- Mayka Schmitt, Celso Peres Fernandes, Fabiano G. Wolf, José A. Bellini da Cunha Neto, Christoffer P. Rahner, and Viviane Sampaio Santiago dos Santos. Characterization of Brazilian tight

- gas sandstones relating permeability and Angstrom-to micron-scale pore structures, 2015b. ISSN 18755100.
- Gilbert Scott, Kejian Wu, and Yingfang Zhou. Multi-scale Image-Based Pore Space Characterisation and Pore Network Generation: Case Study of a North Sea Sandstone Reservoir. *Transport in Porous Media*, 129(3):855–884, 2019. ISSN 15731634. doi: 10.1007/s11242-019-01309-8. URL <https://doi.org/10.1007/s11242-019-01309-8>.
- M. Sharifipour, A. Nakhaee, and P. Pourafshary. Model development of permeability impairment due to clay swelling in porous media using micromodels. *Journal of Petroleum Science and Engineering*, 175(May 2018):728–742, 2019. ISSN 09204105. doi: 10.1016/j.petrol.2018.12.082.
- Milad Sharifipour, Peyman Pourafshary, and Ali Nakhaee. Study of the effect of clay swelling on the oil recovery factor in porous media using a glass micromodel. *Applied Clay Science*, 2017. ISSN 01691317. doi: 10.1016/j.clay.2017.02.020.
- Mostafa H. Sharqawy. Construction of pore network models for Berea and Fontainebleau sandstones using non-linear programming and optimization techniques. *Advances in Water Resources*, 98:198–210, 2016. ISSN 03091708. doi: 10.1016/j.advwatres.2016.10.023. URL <http://dx.doi.org/10.1016/j.advwatres.2016.10.023>.
- Edward Shaughnessy, Ira Katz, and James Schaffer. *Fluid Mechanics*. Oxford University Press, New York, 2005. ISBN 978-0-195154-51-1.
- Min She, Jianfeng Shou, Anjiang Shen, Liyin Pan, Anping Hu, and Yuanyuan Hu. Experimental simulation of dissolution law and porosity evolution of carbonate rock. *Petroleum Exploration and Development*, 43(4):616–625, 2016. ISSN 18763804. doi: 10.1016/S1876-3804(16)30072-6. URL [http://dx.doi.org/10.1016/S1876-3804\(16\)30072-6](http://dx.doi.org/10.1016/S1876-3804(16)30072-6).
- Yue Shi, Mahmood Reza Yassin, and Hassan Dehghanpour. A modified model for spontaneous imbibition of wetting phase into fractal porous media. *Colloids and Surfaces A: Physicochemical and Engineering Aspects*, 543(November 2017):64–75, 2018. ISSN 18734359. doi: 10.1016/j.colsurfa.2017.12.052. URL <https://doi.org/10.1016/j.colsurfa.2017.12.052>.
- Ryoji Shiraki and Thomas L. Dunn. Experimental study on water-rock interactions during CO<sub>2</sub> flooding in the Tensleep formation, Wyoming, USA. *Applied Geochemistry*, 15(3):265–279, 2000. ISSN 08832927. doi: 10.1016/S0883-2927(99)00048-7.
- N. Shojai Kaveh, A. Barnhoorn, and K. H. Wolf. Wettability evaluation of silty shale caprocks for CO<sub>2</sub> storage. *International Journal of Greenhouse Gas Control*, 49:425–435, 2016. ISSN 17505836. doi: 10.1016/j.ijggc.2016.04.003. URL <http://dx.doi.org/10.1016/j.ijggc.2016.04.003>.
- Melina G. Sidiropoulou, Konstadinos N. Moutsopoulos, and Vassilios A. Tsihrintzis. Determination of Forchheimer equation coefficients a and b. *Hydrological Processes*, 21(4):534–554, 2 2007. ISSN 08856087. doi: 10.1002/hyp.6264. URL <http://jamsb.austms.org.au/courses/CSC2408/semester3/resources/ldp/abs-guide.pdf><http://doi.wiley.com/10.1002/hyp.6264>.
- Kamaljit Singh, Hannah Menke, Matthew Andrew, Qingyang Lin, Christoph Rau, Martin J. Blunt, and Branko Bijeljic. Dynamics of snap-off and pore-filling events during two-phase fluid flow in permeable media. *Scientific Reports*, 7(1):1–13, 2017. ISSN 20452322. doi: 10.1038/s41598-017-05204-4.

- Kamaljit Singh, Benaiah U. Anabaraonye, Martin J. Blunt, and John Crawshaw. Partial dissolution of carbonate rock grains during reactive CO<sub>2</sub>-saturated brine injection under reservoir conditions. *Advances in Water Resources*, 122(June):27–36, 2018. ISSN 03091708. doi: 10.1016/j.advwatres.2018.09.005. URL <https://doi.org/10.1016/j.advwatres.2018.09.005>.
- Olga Singurindy and Brian Berkowitz. Flow, dissolution, and precipitation in dolomite. *Water Resources Research*, 39(6):1–13, 2003. ISSN 00431397. doi: 10.1029/2002WR001624.
- Rakulan Sivanesapillai and Holger Steeb. Fluid interfaces during viscous-dominated primary drainage in 2D micromodels using pore-scale SPH simulations. *Geofluids*, 2018:27–29, 2018. ISSN 14688123. doi: 10.1155/2018/8269645.
- P. L. Smedley, P. Shand, and A. S. Butcher. Age and quality stratification of groundwater in the Triassic Sherwood Sandstone aquifer of South Yorkshire and the East Midlands, UK. *Applied Geochemistry*, 97(March):109–122, 2018. ISSN 18729134. doi: 10.1016/j.apgeochem.2018.08.002. URL <https://doi.org/10.1016/j.apgeochem.2018.08.002>.
- Taha Sochi. Flow of non-Newtonian fluids in converging-diverging rigid tubes. *Asia-Pacific Journal of Chemical Engineering*, 10(3):387–399, 2015. ISSN 19322143. doi: 10.1002/apj.1882.
- T. A. Sokolova, I. I. Tolpeshta, Yu G. Izosimova, V. A. Umnova, and P. V. Lashukov. The Effect of Treatment with Hydrogen Peroxide and the Mehra–Jackson Reagent on X-ray Diffraction Patterns of Clay Fractions. *Eurasian Soil Science*, 50(12):1386–1394, 2017. ISSN 10642293. doi: 10.1134/S1064229317120092.
- Rui Song, Jianjun Liu, and Mengmeng Cui. Single- and two-phase flow simulation based on equivalent pore network extracted from micro-CT images of sandstone core. *SpringerPlus*, 5(1):817, 2016. ISSN 2193-1801. doi: 10.1186/s40064-016-2424-x. URL <http://springerplus.springeropen.com/articles/10.1186/s40064-016-2424-x>.
- Cyprien Soulaire, Sophie Roman, Anthony Kovscek, and Hamdi A. Tchelepi. Mineral dissolution and wormholing from a pore-scale perspective. *Journal of Fluid Mechanics*, 827:457–483, 2017. ISSN 14697645. doi: 10.1017/jfm.2017.499.
- James M. Sperry and J. Jeffrey Peirce. A Model for Estimating the Hydraulic Conductivity of Granular Material Based on Grain Shape, Grain Size, and Porosity. *Groundwater*, 33(6):892–898, 1995. ISSN 17456584. doi: 10.1111/j.1745-6584.1995.tb00033.x.
- Jeffrey Steinwinder and Lauren E. Beckingham. Role of Pore and Pore-Throat Distributions in Controlling Permeability in Heterogeneous Mineral Dissolution and Precipitation Scenarios. *Water Resources Research*, 55(7):5502–5517, 2019. ISSN 19447973. doi: 10.1029/2019WR024793.
- Stephan Stricker, Stuart J. Jones, Shanvas Sathar, Leon Bowen, and Norman Oxtoby. Exceptional reservoir quality in HPHT reservoir settings: Examples from the Skagerrak Formation of the Heron Cluster, North Sea, UK. *Marine and Petroleum Geology*, 77:198–215, 2016. ISSN 02648172. doi: 10.1016/j.marpetgeo.2016.02.003. URL <http://dx.doi.org/10.1016/j.marpetgeo.2016.02.003>.
- Adnan Sufian, Adrian R Russell, Andrew J Whittle, and Mohammad Saadatfar. Pore shapes, volume distribution and orientations in monodisperse granular assemblies. *Granular Matter*, 17(6):727–742, 2015. ISSN 14347636. doi: 10.1007/s10035-015-0590-0.



- Adnan Sufian, Christopher Knight, Catherine O'Sullivan, Berend van Wachem, and Daniele Dini. Ability of a pore network model to predict fluid flow and drag in saturated granular materials. *Computers and Geotechnics*, 110(February):344–366, 2019. ISSN 18737633. doi: 10.1016/j.compgeo.2019.02.007. URL <https://doi.org/10.1016/j.compgeo.2019.02.007>.
- Hyoung Suk Suh, Dong Hun Kang, Jaewon Jang, Kwang Yeom Kim, and Tae Sup Yun. Capillary pressure at irregularly shaped pore throats: Implications for water retention characteristics. *Advances in Water Resources*, 110(September):51–58, 2017. ISSN 03091708. doi: 10.1016/j.advwatres.2017.09.025. URL <https://doi.org/10.1016/j.advwatres.2017.09.025>.
- Hai Sun, Lian Duan, Lei Liu, Weipeng Fan, Dongyan Fan, Jun Yao, Lei Zhang, Yongfei Yang, and Jianlin Zhao. The influence of micro-fractures on the flow in tight oil reservoirs based on pore-network models. *Energies*, 12(21), 2019. ISSN 19961073. doi: 10.3390/en12214104.
- Shuwen Sun, Liangshu Shu, Yanwei Zeng, Jian Cao, and Zhiqiang Feng. Porosity-permeability and textural heterogeneity of reservoir sandstones from the Lower Cretaceous Putaohua Member Of Yaojia Formation, Weixing Oilfield, Songliao Basin, Northeast China. *Marine and Petroleum Geology*, 24(2):109–127, 2007. ISSN 02648172. doi: 10.1016/j.marpetgeo.2006.10.006.
- N. P. Szabó, K. Kormos, and M. Dobróka. Evaluation of hydraulic conductivity in shallow groundwater formations: a comparative study of the Csókás' and Kozeny–Carman model. *Acta Geodaetica et Geophysica*, 50(4):461–477, 2015. ISSN 22135820. doi: 10.1007/s40328-015-0105-9.
- Y. B. Tang, M. Li, X. J. Liu, W. S. Zhang, T. Qi, and M. J. Wei. Pore-scale heterogeneity, flow channeling and permeability: Network simulation and comparison to experimental data. *Physica A: Statistical Mechanics and its Applications*, 535, 2019. ISSN 03784371. doi: 10.1016/j.physa.2019.122533.
- Yongqiang Tang, Chengyuan Lv, Rui Wang, and Maolei Cui. Mineral dissolution and mobilization during CO<sub>2</sub> injection into the water-flooded layer of the Pucheng Oilfield, China. *Journal of Natural Gas Science and Engineering*, 33:1364–1373, 2016. ISSN 18755100. doi: 10.1016/j.jngse.2016.06.073. URL <http://dx.doi.org/10.1016/j.jngse.2016.06.073>.
- Y. Tanino and Martin J. Blunt. Capillary trapping in sandstones and carbonates: Dependence on pore structure. *Water Resources Research*, 48(8):1–13, 2012. ISSN 00431397. doi: 10.1029/2011WR011712.
- Paul Ross Thomson, Aizhan Aituar-Zhakupova, and Saswata Hier-Majumder. Image segmentation and analysis of pore network geometry in two natural sandstones. *Frontiers in Earth Science*, 6 (June):1–14, 2018. ISSN 22966463. doi: 10.3389/feart.2018.00058.
- Paul Ross Thomson, Alexander Hazel, and Saswata Hier-Majumder. The influence of microporous cements on the pore network geometry of natural sedimentary rocks. *Frontiers in Earth Science*, 7(March):1–14, 2019. ISSN 22966463. doi: 10.3389/feart.2019.00048.
- Djebbar Tiab and Erle C Donaldson. *Petrophysics - Theory and Practice of Measuring Reservoir Rock and Fluid Transport Properties*. Gulf Professional Publishing, Oxford, 3 edition, 2012. ISBN 978-0-12-383848-3.
- V. A. Torrealba, Z. T. Karpyn, H Yoon, K. A. Klise, and D Crandall. Pore-scale investigation on stress-dependent characteristics of granular packs and the impact of pore deformation on fluid distribution. *Geofluids*, 16(1):198–207, 2016. ISSN 14688115. doi: 10.1111/gfl.12143. URL <http://doi.wiley.com/10.1111/gfl.12143>.

- Tiziana Tosco, Daniele L. Marchisio, Federica Lince, and Rajandrea Sethi. Extension of the Darcy–Forchheimer Law for Shear-Thinning Fluids and Validation via Pore-Scale Flow Simulations. *Transport in Porous Media*, 96(1):1–20, 1 2013. ISSN 0169-3913. doi: 10.1007/s11242-012-0070-5. URL <http://link.springer.com/10.1007/s11242-012-0070-5>.
- Yi Zhih Tsai, Yu Tung Liu, Yung Li Wang, Liang Cheng Chang, and Shao Yiu Hsu. Effects of the Grain Size on Dynamic Capillary Pressure and the Modified Green-Ampt Model for Infiltration. *Geofluids*, 2018, 2018. ISSN 14688123. doi: 10.1155/2018/8946948.
- C. D. Tsakiroglou, M. Theodoropoulou, V. Karoutsos, D. Papanicolaou, and V. Sygouni. Experimental study of the immiscible displacement of shear-thinning fluids in pore networks. *Journal of Colloid and Interface Science*, 267(1):217–232, 11 2003. ISSN 00219797. doi: 10.1016/S0021-9797(03)00635-0.
- Christos D. Tsakiroglou. A methodology for the derivation of non-Darcian models for the flow of generalized Newtonian fluids in porous media. *Journal of Non-Newtonian Fluid Mechanics*, 105 (2-3):79–110, 2002. ISSN 03770257. doi: 10.1016/S0377-0257(02)00066-6.
- Takeshi Tsuji, Fei Jiang, and Kenneth T. Christensen. Characterization of immiscible fluid displacement processes with various capillary numbers and viscosity ratios in 3D natural sandstone. *Advances in Water Resources*, 95:3–15, 2016. ISSN 03091708. doi: 10.1016/j.advwatres.2016.03.005. URL <http://dx.doi.org/10.1016/j.advwatres.2016.03.005>.
- G. G. Tsyppkin and V. A. Shargatov. Influence of capillary pressure gradient on connectivity of flow through a porous medium. *International Journal of Heat and Mass Transfer*, 127:1053–1063, 2018. ISSN 00179310. doi: 10.1016/j.ijheatmasstransfer.2018.08.107. URL <https://doi.org/10.1016/j.ijheatmasstransfer.2018.08.107>.
- G. C. Tzimas, T. Matsuura, D. G. Avraam, W. Van Der Brugghen, G. N. Constantinides, and A. C. Payatakes. The combined effect of the viscosity ratio and the wettability during forced imbibition through nonplanar porous media. *Journal of Colloid and Interface Science*, 189(1):27–36, 1997. ISSN 00219797. doi: 10.1006/jcis.1996.4658.
- Kosta Urumović. The referential grain size and effective porosity in the Kozeny-Carman model. *Hydrology and Earth System Sciences*, 20(5):1669–1680, 2016. ISSN 16077938. doi: 10.5194/hess-20-1669-2016.
- Joost H. van der Linden, Antoinette Tordesillas, and Guillermo A. Narsilio. Preferential flow pathways in a deforming granular material: self-organization into functional groups for optimized global transport. *Scientific Reports*, 9(1):1–15, 2019. ISSN 20452322. doi: 10.1038/s41598-019-54699-6.
- P. Venkataraman and P. Rama Mohan Rao. Darcian, Transitional, and Turbulent Flow through Porous Media. *Journal of Hydraulic Engineering*, 124(8):840–846, 8 1998. ISSN 0733-9429. doi: 10.1061/(ASCE)0733-9429(1998)124:8(840). URL <http://ascelibrary.org/doi/10.1061/%28ASCE%290733-9429%281998%29124%3A8%28840%29>.
- Iris T.E. Verhagen, Adriana Crisóstomo-Figueroa, James E.P. Utley, and Richard H. Worden. Abrasion of detrital grain-coating clays during sediment transport: Implications for diagenetic clay coats. *Sedimentary Geology*, 403:105653, 2020. ISSN 00370738. doi: 10.1016/j.sedgeo.2020.105653. URL <https://doi.org/10.1016/j.sedgeo.2020.105653>.

- Maziar Veyskarami, Amir H. Hassani, and Mohammad Hossein Ghazanfari. Modeling of non-Darcy flow through anisotropic porous media: Role of pore space profiles. *Chemical Engineering Science*, 151:93–104, 2016. ISSN 00092509. doi: 10.1016/j.ces.2016.05.020.
- Benoit Vincent, Jen Waters, Francis Witkowski, Gautier Daniau, Norman Oxtoby, Stephen Crowley, and Rob Ellam. Diagenesis of Rotliegend sandstone reservoirs (offshore Netherlands): The origin and impact of dolomite cements. *Sedimentary Geology*, 373:272–291, 10 2018. ISSN 00370738. doi: 10.1016/j.sedgeo.2018.06.012.
- Kevin Vo, David M. Walker, and Antoinette Tordesillas. Transport pathways within percolating pore space networks of granular materials. *AIP Conference Proceedings*, 1542:551–554, 2013. ISSN 0094243X. doi: 10.1063/1.4811990.
- Harsh Biren Vora and Brandon Dugan. Porosity-Permeability Relationships in Mudstone from Pore-Scale Fluid Flow Simulations using the Lattice Boltzmann Method. *Water Resources Research*, 55(8):7060–7071, 2019. ISSN 19447973. doi: 10.1029/2019WR024985.
- Oliver J.W. Wakefield, Edward Hough, and Alex W. Peatfield. Architectural analysis of a Triassic fluvial system: The Sherwood Sandstone of the East Midlands Shelf, UK. *Sedimentary Geology*, 327:1–13, 2015. ISSN 00370738. doi: 10.1016/j.sedgeo.2015.07.006.
- Dayong Wang, Dongyan Han, Wenqiang Li, Zhanpeng Zheng, and Yongchen Song. L'imagerie par résonance magnétique et l'analyse du modèle simplifié de Kozeny-Carman de paquets de billes de verre comme cadre de référence pour étudier la perméabilité des roches réservoir. *Hydrogeology Journal*, 25(5):1465–1476, 2017. ISSN 14350157. doi: 10.1007/s10040-017-1555-7.
- Junjie Wang, Shenghe Wu, Qing Li, Jiajia Zhang, and Qiheng Guo. Characterization of the pore-throat size of tight oil reservoirs and its control on reservoir physical properties: A case study of the Triassic tight sandstone of the sediment gravity flow in the Ordos Basin, China. *Journal of Petroleum Science and Engineering*, 186(October 2019):106701, 2020a. ISSN 09204105. doi: 10.1016/j.petrol.2019.106701. URL <https://doi.org/10.1016/j.petrol.2019.106701>.
- Menghao Wang, Youming Xiong, Liming Liu, Geng Peng, and Zheng Zhang. Lattice Boltzmann Simulation of Immiscible Displacement in Porous Media: Viscous Fingering in a Shear-Thinning Fluid. *Transport in Porous Media*, 126(2):411–429, 2019a. ISSN 15731634. doi: 10.1007/s11242-018-1162-7. URL <https://doi.org/10.1007/s11242-018-1162-7>.
- Qian Wang, Shenglai Yang, Haishui Han, Lu Wang, Kun Qian, and Jieqiong Pang. Experimental investigation on the effects of CO<sub>2</sub> displacement methods on petrophysical property changes of ultra-low permeability sandstone reservoirs near injection wells. *Energies*, 12(2), 2019b. ISSN 19961073. doi: 10.3390/en12020327.
- Qiaochu Wang, Dongxia Chen, Xianzhi Gao, Fuwei Wang, Jinheng Li, Wenhao Liao, Ziyi Wang, and Guangjie Xie. Microscopic pore structures of tight sandstone reservoirs and their diagenetic controls: A case study of the Upper Triassic Xujiahe Formation of the Western Sichuan Depression, China. *Marine and Petroleum Geology*, 113(October 2019):104119, 2020b. ISSN 02648172. doi: 10.1016/j.marpetgeo.2019.104119. URL <https://doi.org/10.1016/j.marpetgeo.2019.104119>.
- Ren Wang, Wanzhong Shi, Xiangyang Xie, Wei Zhang, Shuo Qin, Kai Liu, and Arthur B. Busbey. Clay mineral content, type, and their effects on pore throat structure and reservoir properties: Insight from the Permian tight sandstones in the Hangjinqi area, north Ordos Basin, China.

- Marine and Petroleum Geology*, 115(February):104281, 2020c. ISSN 02648172. doi: 10.1016/j.marpetgeo.2020.104281. URL <https://doi.org/10.1016/j.marpetgeo.2020.104281>.
- Sen Wang, Qihong Feng, Yeliang Dong, Xiaodong Han, and Shoulei Wang. A dynamic pore-scale network model for two-phase imbibition. *Journal of Natural Gas Science and Engineering*, 26: 118–129, 2015. ISSN 18755100. doi: 10.1016/j.jngse.2015.06.005. URL <http://dx.doi.org/10.1016/j.jngse.2015.06.005>.
- Xin Wang, Chaohua Guo, Sheng He, Zeyun Jiang, and Yongjie Ma. Improved skeleton extraction method considering surface feature of natural micro fractures in unconventional shale/tight reservoirs. *Journal of Petroleum Science and Engineering*, 168(February):521–532, 2018. ISSN 09204105. doi: 10.1016/j.petrol.2018.05.040. URL <https://doi.org/10.1016/j.petrol.2018.05.040>.
- Xiukun Wang and James J. Sheng. A self-similar analytical solution of spontaneous and forced imbibition in porous media. *Advances in Geo-Energy Research*, 2(3):260–268, 2018. ISSN 22079963. doi: 10.26804/ager.2018.03.04.
- Yamin Wang, Muhan Yu, Zhenkai Bo, Pavel Bedrikovetsky, and Furqan Le-Hussain. Effect of temperature on mineral reactions and fines migration during low-salinity water injection into Berea sandstone. *Journal of Petroleum Science and Engineering*, 202(September 2020), 2021. ISSN 09204105. doi: 10.1016/j.petrol.2021.108482.
- Ying Wang, Changyong Zhang, Ning Wei, Mart Oostrom, Thomas W. Wietsma, Xiaochun Li, and Alain Bonneville. Experimental study of crossover from capillary to viscous fingering for supercritical CO<sub>2</sub>-water displacement in a homogeneous pore network. *Environmental Science and Technology*, 47(1):212–218, 2013. ISSN 0013936X. doi: 10.1021/es3014503.
- Edward A. Warren and Andrew J. Pulham. Anomalous porosity and permeability preservation in deeply buried tertiary and Mesozoic sandstones in the Cusiana field, llanos foothills, Colombia-reply. *Journal of Sedimentary Research*, 72(3):445–448, 2002. ISSN 15271404. doi: 10.1306/120701720445.
- Wei Wei, Xiaomin Zhu, Mingxuan Tan, Mengge Xue, Dianbin Guo, Hui Su, and Pengyu Wang. Diagenetic and porosity evolution of conglomerate sandstones in Bayingebi Formation of the Lower Cretaceous, Chagan Sag, China-Mongolia frontier area. *Marine and Petroleum Geology*, 66:998–1012, 2015. ISSN 02648172. doi: 10.1016/j.marpetgeo.2015.08.011. URL <http://dx.doi.org/10.1016/j.marpetgeo.2015.08.011>.
- R. Weibel, C. Kjølner, K. Bateman, L. H. Nielsen, P. Frykman, N. Springer, and T. Laier. Mineral changes in CO<sub>2</sub> experiments - Examples from Danish onshore saline aquifers. *Energy Procedia*, 4: 4495–4502, 2011. ISSN 18766102. doi: 10.1016/j.egypro.2011.02.405. URL <http://dx.doi.org/10.1016/j.egypro.2011.02.405>.
- Gert Jan Weltje and Luc J.H. Alberts. Packing states of ideal reservoir sands: Insights from simulation of porosity reduction by grain rearrangement. *Sedimentary Geology*, 242(1-4):52–64, 2011. ISSN 00370738. doi: 10.1016/j.sedgeo.2011.10.001. URL <http://dx.doi.org/10.1016/j.sedgeo.2011.10.001>.
- Zhang Wen, Guanhua Huang, and Hongbin Zhan. Non-Darcian flow to a well in a leaky aquifer using the Forchheimer equation. *Hydrogeology Journal*, 19(3):563–572, 2011. ISSN 14312174. doi: 10.1007/s10040-011-0709-2.

- Max Wigley, Benoît Dubacq, Niko Kampman, and Mike Bickle. Controls of sluggish, CO<sub>2</sub>-promoted, hematite and K-feldspar dissolution kinetics in sandstones. *Earth and Planetary Science Letters*, 362:76–87, 2013. ISSN 0012821X. doi: 10.1016/j.epsl.2012.11.045.
- L. Wilson, M. J. Wilson, J. Green, and I. Patey. The influence of clay mineralogy on formation damage in North Sea reservoir sandstones: A review with illustrative examples. *Earth-Science Reviews*, 134:70–80, 2014. ISSN 00128252. doi: 10.1016/j.earscirev.2014.03.005. URL <http://dx.doi.org/10.1016/j.earscirev.2014.03.005>.
- Yongli Wu, Qinfu Hou, and Aibing Yu. Pore-Scale Study of Fluid Flow and Drag Force in Randomly Packed Beds of Different Porosities. *Industrial and Engineering Chemistry Research*, 58(12):5041–5053, 2019. ISSN 15205045. doi: 10.1021/acs.iecr.8b06418.
- Kelai Xi, Yingchang Cao, Beyene Girma Haile, Rukai Zhu, Jens Jahren, Knut Bjørlykke, Xiangxiang Zhang, and Helge Hellevang. How does the pore-throat size control the reservoir quality and oiliness of tight sandstones? The case of the Lower Cretaceous Quantou Formation in the southern Songliao Basin, China. *Marine and Petroleum Geology*, 76:1–15, 2016. ISSN 02648172. doi: 10.1016/j.marpetgeo.2016.05.001. URL <http://dx.doi.org/10.1016/j.marpetgeo.2016.05.001>.
- Meng Xiao, Xuanjun Yuan, Dawei Cheng, Songtao Wu, Zhenglin Cao, Yong Tang, and Zongrui Xie. Feldspar Dissolution and Its Influence on Reservoirs: A Case Study of the Lower Triassic Baikouquan Formation in the Northwest Margin of the Junggar Basin, China. *Geofluids*, 2018, 2018. ISSN 14688123. doi: 10.1155/2018/6536419.
- Chiyu Xie, Ali Q. Raeini, Yihang Wang, Martin J. Blunt, and Moran Wang. An improved pore-network model including viscous coupling effects using direct simulation by the lattice Boltzmann method. *Advances in Water Resources*, 100:26–34, 2017. ISSN 03091708. doi: 10.1016/j.advwatres.2016.11.017. URL <http://dx.doi.org/10.1016/j.advwatres.2016.11.017>.
- Qi Xu, Xingwei Wang, and Jiajun Chen. Quantitative evaluation of pore-scale heterogeneity based on statistical analysis of a pore network model of unconsolidated porous media. *Hydrogeology Journal*, 28(5):1841–1852, 2020. ISSN 14350157. doi: 10.1007/s10040-020-02162-6.
- Benyamin Yadali Jamaloei, Riyaz Kharrat, and Koorosh Asghari. Pore-scale events in drainage process through porous media under high- and low-interfacial tension flow conditions. *Journal of Petroleum Science and Engineering*, 75(1-2):223–233, 2010. ISSN 09204105. doi: 10.1016/j.petrol.2010.11.006. URL <http://dx.doi.org/10.1016/j.petrol.2010.11.006>.
- Benyamin Yadali Jamaloei, Riyaz Kharrat, Koorosh Asghari, and Farshid Torabi. The influence of pore wettability on the microstructure of residual oil in surfactant-enhanced water flooding in heavy oil reservoirs: Implications for pore-scale flow characterization. *Journal of Petroleum Science and Engineering*, 77(1):121–134, 2011. ISSN 09204105. doi: 10.1016/j.petrol.2011.02.013. URL <http://dx.doi.org/10.1016/j.petrol.2011.02.013>.
- A. I. Yalysheva and A. V. Maslov. Upper Precambrian sandstones in the Volga-Ural region: Mineralogy, petrography, lithochemistry, and formation conditions. *Lithology and Mineral Resources*, 48(4):343–371, 2013. ISSN 00244902. doi: 10.1134/S0024490213040068.
- Hong Yan, Zhijun Dai, Jiufa Li, Jianchun Zhao, Xiaoling Zhang, and Junkai Zhao. Distributions of sediments of the tidal flats in response to dynamic actions, Yangtze (Changjiang) Estuary. *Journal of Geographical Sciences*, 21(4):719–732, 2011. ISSN 1009637X. doi: 10.1007/s11442-011-0875-0.

- Leilei Yang, Tianfu Xu, Keyu Liu, Bo Peng, Zhichao Yu, and Xiaomeng Xu. Fluid–rock interactions during continuous diagenesis of sandstone reservoirs and their effects on reservoir porosity. *Sedimentology*, 64(5):1303–1321, 2017. ISSN 13653091. doi: 10.1111/sed.12354.
- Shaochun Yang, Ya Wang, Shiqi Zhang, Yongchao Wang, Yifan Zhang, and Yongfu Zhao. Controls on Reservoirs Quality of the Upper Jurassic Mengyin Formation Sandstones in Dongying Depression, Bohai Bay Basin, Eastern China. *Energies*, 13(3):646, 2 2020. ISSN 1996-1073. doi: 10.3390/en13030646. URL <https://www.mdpi.com/1996-1073/13/3/646>.
- Yongfei Yang, Zhihui Liu, Jun Yao, Lei Zhang, Jingsheng Ma, S. Hossein Hejazi, Linda Luquot, and Toussaint Dono Ngarta. Flow simulation of artificially induced microfractures using digital rock and lattice boltzmann methods. *Energies*, 11(8):1–17, 2018. ISSN 19961073. doi: 10.3390/en11082145.
- Jun Yoneda, Motoi Oshima, Masato Kida, Akira Kato, Yoshihiro Konno, Yusuke Jin, Junbong Jang, William F. Waite, Pushendra Kumar, and Norio Tenma. Permeability variation and anisotropy of gas hydrate-bearing pressure-core sediments recovered from the Krishna–Godavari Basin, offshore India. *Marine and Petroleum Geology*, 108(June 2018):524–536, 2019. ISSN 02648172. doi: 10.1016/j.marpetgeo.2018.07.006. URL <https://doi.org/10.1016/j.marpetgeo.2018.07.006>.
- Jiahui You and Kyung Jae Lee. Pore-Scale Study to Analyze the Impacts of Porous Media Heterogeneity on Mineral Dissolution and Acid Transport Using Darcy–Brinkmann–Stokes Method. *Transport in Porous Media*, 137(3):575–602, 2021. ISSN 15731634. doi: 10.1007/s11242-021-01577-3. URL <https://doi.org/10.1007/s11242-021-01577-3>.
- Fang Yu and Allen Gerhard Hunt. Damköhler Number Input to Transport-Limited Chemical Weathering Calculations. *ACS Earth and Space Chemistry*, 1(1):30–38, 2017. ISSN 24723452. doi: 10.1021/acsearthspacechem.6b00007.
- Guang Hui Yuan, Ying Chang Cao, Jon Gluyas, Yan Zhong Wang, Ke Yu Liu, Ke Lai Xi, Tian Yang, and Jian Wang. How important is carbonate dissolution in buried sandstones: evidences from petrography, porosity, experiments, and geochemical calculations. *Petroleum Science*, 16(4): 729–751, 2019. ISSN 19958226. doi: 10.1007/s12182-019-0344-4. URL <https://doi.org/10.1007/s12182-019-0344-4>.
- Guanghai Yuan, Yingchang Cao, Jon Gluyas, and Zhenzhen Jia. Reactive transport modeling of coupled feldspar dissolution and secondary mineral precipitation and its implication for diagenetic interaction in sandstones. *Geochimica et Cosmochimica Acta*, 207:232–255, 2017. ISSN 00167037. doi: 10.1016/j.gca.2017.03.022. URL <http://dx.doi.org/10.1016/j.gca.2017.03.022>.
- Q. Yuan and J. Azaiez. Cyclic time-dependent reactive flow displacements in porous media. *Chemical Engineering Science*, 109:136–146, 2014. ISSN 00092509. doi: 10.1016/j.ces.2014.02.003. URL <http://dx.doi.org/10.1016/j.ces.2014.02.003>.
- I. Yusuf and E. Padmanabhan. Impact of rock fabric on flow unit characteristics in selected reservoir sandstones from West Baram Delta Offshore, Sarawak. *Journal of Petroleum Exploration and Production Technology*, 9(3):2149–2164, 2019. ISSN 21900566. doi: 10.1007/s13202-019-0617-x. URL <http://dx.doi.org/10.1007/s13202-019-0617-x>.
- Muhammad Aleem Zahid, Dong Chunmei, Alexandra N. Golab, Chengyan Lin, Xianguo Zhang, Xinmin Ge, Wu Songtao, Muhammad Jawad Munawar, Cunfei Ma, and Lydia Knuefing. Pore

- size distribution and reservoir characterization: evaluation for the Eocene beach-bar sequence, Dongying Depression, China. *Arabian Journal of Geosciences*, 12(21), 2019. ISSN 18667538. doi: 10.1007/s12517-019-4772-7.
- T. R. Zakirov and M. G. Khranchenkov. Prediction of permeability and tortuosity in heterogeneous porous media using a disorder parameter. *Chemical Engineering Science*, 227:115893, 2020. ISSN 00092509. doi: 10.1016/j.ces.2020.115893. URL <https://doi.org/10.1016/j.ces.2020.115893>.
- Marco Zecca, Sarah J. Vogt, Paul R.J. Connolly, Eric F. May, and Michael L. Johns. NMR Measurements of Tortuosity in Partially Saturated Porous Media. *Transport in Porous Media*, 125(2):271–288, 2018. ISSN 15731634. doi: 10.1007/s11242-018-1118-y. URL <https://doi.org/10.1007/s11242-018-1118-y>.
- Wenshu Zha, Daolun Li, Zhiwei Lu, and Bao Jia. An equivalent single-phase flow for oil-water two-phase flow and its potential application in well test. *Advances in Geo-Energy Research*, 2(2): 218–227, 2018. ISSN 22079963. doi: 10.26804/ager.2018.02.09.
- Bin Zhang, Jianting Kang, and Tianhe Kang. Monte Carlo simulations of methane adsorption on kaolinite as a function of pore size. *Journal of Natural Gas Science and Engineering*, 49(18): 410–416, 2018a. ISSN 18755100. doi: 10.1016/j.jngse.2017.11.026. URL <https://doi.org/10.1016/j.jngse.2017.11.026>.
- Changyong Zhang, Qinjun Kang, Xing Wang, Julie L. Zilles, Roland H. Müller, and Charles J. Werth. Effects of pore-scale heterogeneity and transverse mixing on bacterial growth in porous media. *Environmental Science and Technology*, 44(8):3085–3092, 4 2010. ISSN 0013936X. doi: 10.1021/es903396h.
- Changyong Zhang, Mart Oostrom, Thomas W. Wietsma, Jay W. Grate, and Marvin G. Warner. Influence of viscous and capillary forces on immiscible fluid displacement: Pore-scale experimental study in a water-wet micromodel demonstrating viscous and capillary fingering. *Energy and Fuels*, 2011a. ISSN 08870624. doi: 10.1021/ef101732k.
- Hao Zhang, Yushuang Zhu, Ningyong Ma, Chuangfei Zhou, Yongchao Dang, Fei Shao, Jun Jiao, Li Li, Hengli Wang, and Ming Li. Combined technology of PCP and nano-CT quantitative characterization of dense oil reservoir pore throat characteristics. *Arabian Journal of Geosciences*, 12(16), 2019. ISSN 18667538. doi: 10.1007/s12517-019-4684-6.
- Liang Zhang, Jiahao Chao, Songhe Geng, Zhen Zhao, Huijuan Chen, Yinfei Luo, and Guangxiong Qin. Particle migration and blockage in geothermal reservoirs during water reinjection: Laboratory experiment and reaction kinetic model. *Energy*, 206:118234, 2020a. ISSN 03605442. doi: 10.1016/j.energy.2020.118234. URL <https://doi.org/10.1016/j.energy.2020.118234>.
- Na Zhang, Manchao He, Bo Zhang, Fengchao Qiao, Hailong Sheng, and Qinhong Hu. Pore structure characteristics and permeability of deep sedimentary rocks determined by mercury intrusion porosimetry. *Journal of Earth Science*, 27(4):670–676, 2016. ISSN 1674487X. doi: 10.1007/s12583-016-0662-z.
- Na Zhang, Fangfang Zhao, Pingye Guo, Jiabin Li, Weili Gong, Zhibiao Guo, and Xiaoming Sun. Nanoscale pore structure characterization and permeability of mudrocks and fine-grained sandstones in coal reservoirs by scanning electron microscopy, mercury intrusion porosimetry, and low-field nuclear magnetic resonance. *Geofluids*, 2018, 2018b. ISSN 14688123. doi: 10.1155/2018/2905141.

- Qiulan Zhang, N. K. Karadimitriou, S. M. Hassanizadeh, P. J. Kleingeld, and A. Imhof. Study of colloids transport during two-phase flow using a novel polydimethylsiloxane micro-model. *Journal of Colloid and Interface Science*, 401:141–147, 7 2013. ISSN 00219797. doi: 10.1016/j.jcis.2013.02.041.
- Yang Zhang, Yuanfeng Cai, Yang Qu, Qin Wang, Lixin Gu, and Gaojun Li. Two-stage fluid pathways generated by volume expansion reactions: insights from the replacement of pyrite by chalcopyrite. *Scientific Reports*, 10(1):1–12, 2020b. ISSN 20452322. doi: 10.1038/s41598-020-76813-9. URL <https://doi.org/10.1038/s41598-020-76813-9>.
- Yanhua Zhang, J. Robinson, and P. M. Schaubs. Numerical modelling of structural controls on fluid flow and mineralization. *Geoscience Frontiers*, 2011b. ISSN 16749871. doi: 10.1016/j.gsf.2011.05.011.
- Jianlin Zhao, Feifei Qin, Dominique Derome, and Jan Carmeliet. Simulation of quasi-static drainage displacement in porous media on pore-scale: Coupling lattice Boltzmann method and pore network model. *Journal of Hydrology*, 588(January):125080, 2020. ISSN 00221694. doi: 10.1016/j.jhydrol.2020.125080. URL <https://doi.org/10.1016/j.jhydrol.2020.125080>.
- Yixin Zhao, Shanbin Xue, Songbai Han, Zhongwei Chen, Shimin Liu, Derek Elsworth, Linfeng He, Jianchao Cai, Yuntao Liu, and Dongfeng Chen. Effects of microstructure on water imbibition in sandstones using X-ray computed tomography and neutron radiography. *Journal of Geophysical Research: Solid Earth*, 122(7):4963–4981, 2017. ISSN 21699356. doi: 10.1002/2016JB013786.
- Tianqi Zhou, Chaodong Wu, Zhongkui Shi, Jialin Wang, Wen Zhu, Bo Yuan, and Disheng Yang. Multi-Scale Quantitative Characterization of Pore Distribution Networks in Tight Sandstone by integrating FE-SEM, HPMI, and NMR with the Constrained Least Squares Algorithm. *Energies*, 12(18):3514, 9 2019. ISSN 1996-1073. doi: 10.3390/en12183514. URL <https://www.mdpi.com/1996-1073/12/18/3514>.
- Yong Zhou, Youliang Ji, Liming Xu, Shiqi Che, Xiaobing Niu, Lu Wan, Yuqi Zhou, Zhicheng Li, and Yuan You. Controls on reservoir heterogeneity of tight sand oil reservoirs in Upper Triassic Yanchang Formation in Longdong Area, southwest Ordos Basin, China: Implications for reservoir quality prediction and oil accumulation. *Marine and Petroleum Geology*, 78:110–135, 2016. ISSN 02648172. doi: 10.1016/j.marpetgeo.2016.09.006. URL <http://dx.doi.org/10.1016/j.marpetgeo.2016.09.006>.
- Feng Zhu, Wenxuan Hu, Jian Cao, Funing Sun, Yifeng Liu, and Zhenmeng Sun. Micro/nanoscale pore structure and fractal characteristics of tight gas sandstone: A case study from the Yuanba area, northeast Sichuan Basin, China. *Marine and Petroleum Geology*, 98(April):116–132, 2018. ISSN 02648172. doi: 10.1016/j.marpetgeo.2018.08.013. URL <https://doi.org/10.1016/j.marpetgeo.2018.08.013>.
- Ali S. Ziarani and Roberto Aguilera. Pore-throat radius and tortuosity estimation from formation resistivity data for tight-gas sandstone reservoirs. *Journal of Applied Geophysics*, 83:65–73, 2012. ISSN 09269851. doi: 10.1016/j.jappgeo.2012.05.008. URL <http://dx.doi.org/10.1016/j.jappgeo.2012.05.008>.
- Horst Zwingmann, Norbert Clauer, and Reinhard Gaupp. Structure-related geochemical (REE) and isotopic (K-Ar, Rb-Sr,  $\delta^{18}\text{O}$ ) characteristics of clay minerals from Rotliegend sandstone reservoirs (Permian, northern Germany). *Geochimica et Cosmochimica Acta*, 63(18):2805–2823, 1999. ISSN 00167037. doi: 10.1016/S0016-7037(99)00198-2.



## Appendix A

# Results from the Pore-Scale Permeability Experiments

Table A.1: The data collected from the pore-scale permeability experiments. The values displayed are the mean values from a sampled time period after the pressure had stabilised and the period of sampled time differed between the different experiments. Note: Samples 6A, 7A, 8A and 9A correspond to sample results post acidic flow.

| Sample | Average Flow Rate (ml/min) | Average Inlet Pressure (bar) | Average Outlet Pressure (bar) |       |
|--------|----------------------------|------------------------------|-------------------------------|-------|
| 1      | 0.010                      | 0.529                        | 0.521                         |       |
|        | 0.010                      | 0.501                        | 0.496                         |       |
|        | 0.015                      | 0.163                        | 0.154                         |       |
|        | 0.015                      | 0.196                        | 0.185                         |       |
|        | 0.020                      | 0.544                        | 0.533                         |       |
|        | 0.020                      | 0.732                        | 0.721                         |       |
|        | 0.025                      | 0.175                        | 0.158                         |       |
|        | 0.025                      | 0.207                        | 0.191                         |       |
|        | 0.030                      | 0.872                        | 0.852                         |       |
|        | 0.030                      | 0.894                        | 0.874                         |       |
|        | 2                          | 0.010                        | 0.482                         | 0.477 |
|        |                            | 0.010                        | 0.508                         | 0.504 |
|        |                            | 0.015                        | 0.189                         | 0.184 |
|        |                            | 0.015                        | 0.236                         | 0.230 |
| 0.020  |                            | 0.592                        | 0.585                         |       |
| 0.020  |                            | 0.600                        | 0.591                         |       |
| 0.025  |                            | 0.199                        | 0.183                         |       |
| 0.025  |                            | 0.275                        | 0.262                         |       |
| 0.030  |                            | 0.294                        | 0.276                         |       |
| 0.030  |                            | 0.435                        | 0.416                         |       |
| 3      |                            | 0.010                        | 0.385                         | 0.384 |
|        |                            | 0.010                        | 0.395                         | 0.393 |
|        |                            | 0.015                        | 0.400                         | 0.392 |
|        |                            | 0.015                        | 0.414                         | 0.405 |
|        | 0.020                      | 0.338                        | 0.326                         |       |
|        | 0.020                      | 0.339                        | 0.325                         |       |
|        | 0.025                      | 0.380                        | 0.363                         |       |
|        | 0.025                      | 0.366                        | 0.349                         |       |
|        | 0.030                      | 0.393                        | 0.367                         |       |
|        | 0.030                      | 0.346                        | 0.319                         |       |

| Sample | Average Flow Rate (ml/min) | Average Inlet Pressure (bar) | Average Outlet Pressure (bar) |
|--------|----------------------------|------------------------------|-------------------------------|
| 4      | 0.010                      | 0.571                        | 0.568                         |
|        | 0.010                      | 0.744                        | 0.739                         |
|        | 0.015                      | 0.198                        | 0.194                         |
|        | 0.015                      | 0.219                        | 0.214                         |
|        | 0.020                      | 1.011                        | 1.005                         |
|        | 0.020                      | 0.801                        | 0.794                         |
|        | 0.025                      | 0.463                        | 0.458                         |
|        | 0.025                      | 0.195                        | 0.186                         |
|        | 0.030                      | 0.991                        | 0.981                         |
|        | 0.030                      | 0.725                        | 0.717                         |
| 7      | 0.010                      | 0.497                        | 0.493                         |
|        | 0.010                      | 0.625                        | 0.620                         |
|        | 0.015                      | 0.504                        | 0.498                         |
|        | 0.015                      | 0.569                        | 0.561                         |
|        | 0.020                      | 0.515                        | 0.506                         |
|        | 0.020                      | 0.523                        | 0.512                         |
|        | 0.025                      | 0.465                        | 0.453                         |
|        | 0.025                      | 0.537                        | 0.525                         |
|        | 0.030                      | 0.401                        | 0.388                         |
|        | 0.030                      | 0.540                        | 0.528                         |
| 8      | 0.010                      | 0.594                        | 0.582                         |
|        | 0.015                      | 0.539                        | 0.525                         |
|        | 0.015                      | 0.543                        | 0.528                         |
|        | 0.020                      | 0.525                        | 0.507                         |
|        | 0.020                      | 0.525                        | 0.507                         |
|        | 0.025                      | 0.478                        | 0.457                         |
|        | 0.025                      | 0.511                        | 0.484                         |
|        | 0.030                      | 0.481                        | 0.456                         |
|        | 0.030                      | 0.491                        | 0.460                         |
|        | 0.030                      | 0.540                        | 0.528                         |

| Sample | Average Flow Rate (ml/min) | Average Inlet Pressure (bar) | Average Outlet Pressure (bar) |
|--------|----------------------------|------------------------------|-------------------------------|
| 9      | 0.010                      | 0.519                        | 0.499                         |
|        | 0.010                      | 0.487                        | 0.470                         |
|        | 0.015                      | 0.471                        | 0.441                         |
|        | 0.015                      | 0.496                        | 0.453                         |
|        | 0.020                      | 0.522                        | 0.448                         |
|        | 0.020                      | 0.528                        | 0.448                         |
|        | 0.025                      | 0.580                        | 0.469                         |
|        | 0.025                      | 0.553                        | 0.449                         |
|        | 0.030                      | 0.522                        | 0.373                         |
|        | 0.030                      | 0.601                        | 0.454                         |
| 10     | 0.010                      | 0.464                        | 0.441                         |
|        | 0.010                      | 0.457                        | 0.432                         |
|        | 0.015                      | 0.428                        | 0.400                         |
|        | 0.015                      | 0.503                        | 0.470                         |
|        | 0.020                      | 0.514                        | 0.477                         |
|        | 0.020                      | 0.422                        | 0.411                         |
|        | 0.025                      | 0.501                        | 0.462                         |
|        | 0.025                      | 0.500                        | 0.451                         |
|        | 0.030                      | 0.482                        | 0.429                         |
|        | 0.030                      | 0.469                        | 0.416                         |
| 11     | 0.010                      | 0.602                        | 0.559                         |
|        | 0.010                      | 0.585                        | 0.539                         |
|        | 0.015                      | 0.599                        | 0.540                         |
|        | 0.015                      | 0.630                        | 0.570                         |
|        | 0.020                      | 0.563                        | 0.478                         |
|        | 0.020                      | 0.574                        | 0.483                         |
|        | 0.025                      | 0.594                        | 0.494                         |
|        | 0.025                      | 0.625                        | 0.476                         |
|        | 0.030                      | 0.747                        | 0.614                         |
|        | 0.030                      | 0.609                        | 0.487                         |

| Sample | Average Flow Rate (ml/min) | Average Inlet Pressure (bar) | Average Outlet Pressure (bar) |
|--------|----------------------------|------------------------------|-------------------------------|
| 8A     | 0.010                      | 0.492                        | 0.477                         |
|        | 0.010                      | 0.492                        | 0.478                         |
|        | 0.015                      | 0.547                        | 0.530                         |
|        | 0.015                      | 0.567                        | 0.546                         |
|        | 0.020                      | 0.593                        | 0.564                         |
|        | 0.020                      | 0.602                        | 0.570                         |
|        | 0.025                      | 0.563                        | 0.525                         |
|        | 0.025                      | 0.550                        | 0.515                         |
|        | 0.030                      | 0.214                        | 0.170                         |
|        | 0.030                      | 0.181                        | 0.136                         |
| 9A     | 0.010                      | 0.432                        | 0.408                         |
|        | 0.010                      | 0.466                        | 0.435                         |
|        | 0.015                      | 0.501                        | 0.461                         |
|        | 0.015                      | 0.578                        | 0.534                         |
|        | 0.020                      | 0.562                        | 0.503                         |
|        | 0.020                      | 0.569                        | 0.505                         |
|        | 0.025                      | 0.626                        | 0.540                         |
|        | 0.025                      | 0.571                        | 0.484                         |
|        | 0.030                      | 0.636                        | 0.535                         |
|        | 0.030                      | 0.653                        | 0.560                         |
| 10A    | 0.010                      | 0.601                        | 0.580                         |
|        | 0.010                      | 0.547                        | 0.528                         |
|        | 0.015                      | 0.496                        | 0.466                         |
|        | 0.015                      | 0.570                        | 0.535                         |
|        | 0.020                      | 0.550                        | 0.519                         |
|        | 0.020                      | 0.601                        | 0.565                         |
|        | 0.025                      | 0.498                        | 0.452                         |
|        | 0.025                      | 0.529                        | 0.481                         |
|        | 0.030                      | 0.498                        | 0.445                         |
|        | 0.030                      | 0.559                        | 0.504                         |

| Sample | Average Flow Rate (ml/min) | Average Inlet Pressure (bar) | Average Outlet Pressure (bar) |
|--------|----------------------------|------------------------------|-------------------------------|
| 11A    | 0.010                      | 0.416                        | 0.371                         |
|        | 0.010                      | 0.494                        | 0.457                         |
|        | 0.015                      | 0.460                        | 0.390                         |
|        | 0.015                      | 0.485                        | 0.411                         |
|        | 0.020                      | 0.468                        | 0.349                         |
|        | 0.020                      | 0.517                        | 0.354                         |
|        | 0.025                      | 0.451                        | 0.311                         |
|        | 0.025                      | 0.428                        | 0.272                         |

## Appendix B

# Input Parameters for the Avizo Fire Absolute Permeability Experimental Simulations

Table B.1: The inputs for the Avizo Fire Absolute Permeability Experimental Simulations for each sample. The inputs were based on the results from the pore-scale permeability experiments. The inputs for sample 12 were based on the results from sample 11 as experiments were not conducted on sample 12 due to experimental limitations. The inputs from sample 11 were used as it is the most similar sample in terms of composition.

| Sample | Inlet Pressure (Pa) | Outlet Pressure (Pa) | Viscosity (Pa.s) |
|--------|---------------------|----------------------|------------------|
| 1      | 52900               | 52100                | 0.001            |
| 2      | 48200               | 47700                | 0.001            |
| 3      | 38500               | 38400                | 0.001            |
| 4      | 57100               | 56800                | 0.001            |
| 7      | 49700               | 49300                | 0.001            |
| 8      | 54000               | 52800                | 0.001            |
| 9      | 51900               | 49900                | 0.001            |
| 10     | 46400               | 44100                | 0.001            |
| 11     | 60200               | 55900                | 0.001            |
| 12     | 60200               | 55900                | 0.001            |



# Appendix C

## CFD Results

Table C.1: The data collected from the CFD simulations.

| Sample                   | Zone       | Volumetric Flow Rate (m/s <sup>3</sup> ) | Pressure Difference (Pa) | Area (m <sup>2</sup> )  |
|--------------------------|------------|--|--------------------------|-------------------------|
| 1                        | 3          | 7.21 × 10 <sup>-11</sup>                 | 16.66                    | 1.63 × 10 <sup>-7</sup> |
|                          |            | 1.44 × 10 <sup>-10</sup>                 | 33.33                    |                         |
|                          |            | 1.73 × 10 <sup>-10</sup>                 | 39.99                    |                         |
|                          |            | 3.02 × 10 <sup>-10</sup>                 | 69.96                    |                         |
|                          |            | 4.16 × 10 <sup>-10</sup>                 | 96.60                    |                         |
|                          |            | 4.04 × 10 <sup>-9</sup>                  | 961.23                   |                         |
|                          |            | 2.87 × 10 <sup>-8</sup>                  | 9440.29                  |                         |
|                          |            | 1.27 × 10 <sup>-7</sup>                  | 92690.12                 |                         |
|                          |            | 4.87 × 10 <sup>-7</sup>                  | 911595.61                |                         |
|                          |            | 1.75 × 10 <sup>-6</sup>                  | 8970233.42               |                         |
| 2                        | 2          | 1.11 × 10 <sup>-10</sup>                 | 16.66                    | 1.62 × 10 <sup>-7</sup> |
|                          |            | 1.99 × 10 <sup>-10</sup>                 | 29.99                    |                         |
|                          |            | 4.21 × 10 <sup>-10</sup>                 | 63.30                    |                         |
|                          |            | 5.75 × 10 <sup>-10</sup>                 | 86.61                    |                         |
|                          |            | 5.56 × 10 <sup>-9</sup>                  | 861.60                   |                         |
|                          |            | 3.94 × 10 <sup>-8</sup>                  | 8448.53                  |                         |
|                          |            | 1.76 × 10 <sup>-7</sup>                  | 82613.31                 |                         |
|                          |            | 6.16 × 10 <sup>-7</sup>                  | 810551.02                |                         |
|                          |            | 2.36 × 10 <sup>-6</sup>                  | 7961594.28               |                         |
|                          |            | 3  | 3                        |                         |
| 1.17 × 10 <sup>-10</sup> | 16.66      |  |                          |                         |
| 2.10 × 10 <sup>-10</sup> | 29.98      |  |                          |                         |
| 4.43 × 10 <sup>-10</sup> | 63.26      |  |                          |                         |
| 6.06 × 10 <sup>-10</sup> | 86.54      |  |                          |                         |
| 5.75 × 10 <sup>-9</sup>  | 856.64     |  |                          |                         |
| 3.74 × 10 <sup>-8</sup>  | 8302.41    |  |                          |                         |
| 1.59 × 10 <sup>-7</sup>  | 80579.90   |  |                          |                         |
| 5.98 × 10 <sup>-7</sup>  | 782622.42  |  |                          |                         |
| 2.15 × 10 <sup>-6</sup>  | 7600105.11 |  |                          |                         |

| Sample | Zone                   | Volumetric Flow Rate (m/s <sup>3</sup> ) | Pressure Difference (Pa) | Area (m <sup>2</sup> ) |
|--------|------------------------|--|--------------------------|------------------------|
| 4      |                        | $2.14 \times 10^{-10}$                   | 9.99                     | $1.63 \times 10^{-7}$  |
|        |                        | $3.57 \times 10^{-10}$                   | 16.65                    |                        |
|        |                        | $6.43 \times 10^{-10}$                   | 29.96                    |                        |
|        |                        | $1.33 \times 10^{-9}$                    | 63.19                    |                        |
|        |                        | $1.82 \times 10^{-9}$                    | 86.40                    |                        |
|        |                        | $1.45 \times 10^{-8}$                    | 851.97                   |                        |
|        |                        | $7.25 \times 10^{-8}$                    | 8338.73                  |                        |
|        |                        | $2.74 \times 10^{-7}$                    | 82174.36                 |                        |
|        |                        | $9.95 \times 10^{-7}$                    | 809492.92                |                        |
|        |                        | $3.49 \times 10^{-6}$                    | 7969250.24               |                        |
| 3      | 2                      | $8.75 \times 10^{-11}$                   | 6.66                     | $1.62 \times 10^{-7}$  |
|        |                        | $5.63 \times 10^{-10}$                   | 43.23                    |                        |
|        |                        | $1.11 \times 10^{-9}$                    | 86.27                    |                        |
|        |                        | $1.58 \times 10^{-9}$                    | 122.56                   |                        |
|        |                        | $1.28 \times 10^{-8}$                    | 1188.29                  |                        |
|        |                        | $6.50 \times 10^{-8}$                    | 11274.85                 |                        |
|        |                        | $2.47 \times 10^{-7}$                    | 108576.31                |                        |
|        |                        | $9.28 \times 10^{-7}$                    | 1028317.41               |                        |
|        | 3                      | $3.17 \times 10^{-11}$                   | 6.66                     | $1.62 \times 10^{-7}$  |
|        |                        | $2.07 \times 10^{-10}$                   | 43.32                    |                        |
|        | $4.14 \times 10^{-10}$ | 86.62                                    |                          |                        |
|        | $5.88 \times 10^{-10}$ | 123.23                                   |                          |                        |
|        | $5.53 \times 10^{-9}$  | 1226.04                                  |                          |                        |
|        | $3.60 \times 10^{-8}$  | 12072.01                                 |                          |                        |
|        | $1.55 \times 10^{-7}$  | 118876.83                                |                          |                        |
|        | $5.93 \times 10^{-7}$  | 1170498.02                               |                          |                        |

| Sample | Zone | Volumetric Flow Rate (m/s <sup>3</sup> ) | Pressure Difference (Pa) | Area (m <sup>2</sup> ) |
|--------|------|--|--------------------------|------------------------|
| 4      | 4    | $2.37 \times 10^{-11}$                   | 6.66                     | $1.62 \times 10^{-7}$  |
|        |      | $1.54 \times 10^{-10}$                   | 43.33                    |                        |
|        |      | $3.08 \times 10^{-10}$                   | 86.64                    |                        |
|        |      | $4.38 \times 10^{-10}$                   | 123.28                   |                        |
|        |      | $4.22 \times 10^{-9}$                    | 1229.10                  |                        |
|        |      | $2.99 \times 10^{-8}$                    | 12151.92                 |                        |
|        |      | $1.35 \times 10^{-7}$                    | 119949.88                |                        |
|        |      | $5.22 \times 10^{-7}$                    | 1184399.23               |                        |
|        |      | $2.02 \times 10^{-10}$                   | 9.99                     | $1.62 \times 10^{-7}$  |
|        |      | $4.35 \times 10^{-10}$                   | 23.28                    |                        |
|        |      | $6.16 \times 10^{-10}$                   | 32.92                    |                        |
| 4      | 3    | $7.46 \times 10^{-10}$                   | 39.89                    |                        |
|        |      | $8.25 \times 10^{-10}$                   | 44.37                    |                        |
|        |      | $9.31 \times 10^{-10}$                   | 49.83                    |                        |
|        |      | $1.03 \times 10^{-9}$                    | 55.79                    |                        |
|        |      | $1.05 \times 10^{-9}$                    | 56.78                    |                        |
|        |      | $1.07 \times 10^{-9}$                    | 57.77                    |                        |
|        |      | $1.10 \times 10^{-9}$                    | 59.76                    |                        |
|        |      | $1.82 \times 10^{-9}$                    | 99.37                    |                        |
|        |      | $7.27 \times 10^{-9}$                    | 435.86                   |                        |
|        |      | $4.18 \times 10^{-8}$                    | 4182.72                  |                        |
|        |      | $1.69 \times 10^{-7}$                    | 40347.69                 |                        |
| 5      | 5    | $6.19 \times 10^{-7}$                    | 391027.49                |                        |
|        |      | $2.25 \times 10^{-6}$                    | 3742197.45               |                        |
|        |      | $1.40 \times 10^{-12}$                   | 20.83                    | $1 \times 10^{-8}$     |
|        |      | $1.63 \times 10^{-12}$                   | 24.16                    |                        |
|        |      | $1.85 \times 10^{-12}$                   | 27.50                    |                        |
|        |      | $2.08 \times 10^{-12}$                   | 30.83                    |                        |
|        |      | $2.30 \times 10^{-12}$                   | 34.16                    |                        |
|        |      | $2.30 \times 10^{-11}$                   | 341.62                   |                        |
|        |      | $2.29 \times 10^{-10}$                   | 3411.83                  |                        |
|        |      | $2.11 \times 10^{-9}$                    | 33810.33                 |                        |

| Sample | Zone | Volumetric Flow Rate (m/s <sup>3</sup> ) | Pressure Difference (Pa) | Area (m <sup>2</sup> ) |
|--------|------|--|--------------------------|------------------------|
| 5      |      | $1.24 \times 10^{-8}$                    | 331315.54                |                        |
|        |      | $5.09 \times 10^{-8}$                    | 3257263.50               |                        |
| 6      |      | $1.23 \times 10^{-12}$                   | 4.18                     | $1 \times 10^{-8}$     |
|        |      | $2.21 \times 10^{-12}$                   | 7.50                     |                        |
|        |      | $2.88 \times 10^{-12}$                   | 9.79                     |                        |
|        |      | $4.59 \times 10^{-12}$                   | 15.63                    |                        |
|        |      | $4.68 \times 10^{-11}$                   | 156.16                   |                        |
|        |      | $4.62 \times 10^{-10}$                   | 1553.80                  |                        |
|        |      | $3.72 \times 10^{-9}$                    | 15166.67                 |                        |
|        |      | $1.82 \times 10^{-8}$                    | 146437.86                |                        |
|        |      | $6.88 \times 10^{-8}$                    | 1428397.40               |                        |